Accretion processes of radio galaxies at high energies

Sandra de Jong

Observatoire de Paris
Ecole Doctorale
Astronomie et Astrophysique d' Ile-de-France
Doctorat
Astronomie et Astrophysique

Auteur: Sandra de Jong

Accretion processes of radio galaxies at high energies

Directeur de thèse: Volker Beckmann

Soutenue le 29 octobre 2013 devant le jury composé de:

Françoise Combes	Présidente
Jelle S. Kaastra	Rapporteur
Gilles Henri	Rapporteur
Thierry J.-L. Courvoisier	Examinateur
Sylvain Chaty	Examinateur
Volker Beckmann	Examinateur

Contents

1 Abstract

Keywords: Active Galaxies, Individual Galaxies: 3C 111, M87, Jets, Accretion disks/Accretion, X-rays and gamma-rays, Supermassive Black Holes
Mots clés: Galaxies Actifs, Galaxies Individuelles: 3C 111, M87, Jets, Disque d'accrétion/Accrétion, Rayons X, Rayons Gamma, Trous noirs Supermassifs

AGN are the luminous ($L \gtrsim 10^{42}\,\mathrm{erg\,s^{-1}}$) cores of active galaxies, powered by accretion onto the central super massive black hole, either via an accretion disk or via a radiatively inefficient accretion flow. There are still several open questions, for example on the launching of jets, which are present in about 10% of the AGN. Another question appeared with the *Fermi*/LAT gamma-ray survey, which detected many blazars but also a small group of radio galaxies. Radio galaxies are postulated to be blazars where the observer sees the jet at an angle $\theta > 10^{\circ}$ allowing a view of both jet and core, rather than only the jet as is the case with blazars. Radio galaxies are divided into two classes, depending on the radio luminosity of the jets. The Fanaroff-Riley I (FR-I) sources have jets that are bright near the core, where the FR-IIs display extended edge-brightened jets. The FR-I sources are connected to the BL Lacs, which are low-luminosity blazars. FR-II types are thought to be the parent population of the luminous FSRQ, which are also blazars.
This thesis presents a study of gamma-ray bright radio galaxies. By analysing X-ray and gamma-ray data in addition to creating broad-band spectral energy distributions (SEDs), we studied two examples of this new class of sources. For the FR-II source 3C 111 we analysed *Suzaku*/XIS and PIN and *INTEGRAL* IBIS/ISGRI observations to create a X-ray spectrum. We also used a *Swift*/BAT spectrum from the 58-month survey. The 0.4–200 keV spectrum of the source shows both thermal, Seyfert-like signatures such as an iron K-α line, and non-thermal jet features. We also analysed gamma-ray data from *Fermi*/LAT. The gamma-ray and X-ray data are combined with historical radio, infra red and optical to build the SED, which can be well represented with a non-thermal jet model. The bolometric luminosity of 3C 111 is rather low, and the SED model shows rather a BL Lac type than the expected FSRQ.
The next source we studied is the nearby FR-I M87. This source has been detected in gamma-rays and in the TeV band, but so far not in the hard X-rays ($> 10\,\mathrm{keV}$). The first part of our analysis was focussed on setting an upper limit to the hard X-ray emission of this source, using *INTEGRAL* IBIS/ISGRI observations. In addition to the standard method we applied several techniques in the analysis process, such as pointing selection and shadowgram treatment, in order to decrease the noise level of the result. Using 5.1 Ms of ISGRI data we determined a 3σ upper limit to the average 20–60 keV flux of $f < 3 \times 10^{-12}\,\mathrm{erg\,cm^{-2}\,s^{-1}}$. We have also analysed *Suzaku*/PIN observations, where we detected M87 for the first time in the hard X-ray band, with a flux of $f = 1.3^{+0.1}_{-0.2} \times 10^{-11}\,\mathrm{erg\,cm^{-2}\,s^{-1}}$ between 20 and 60 keV. This detection indicates a flare, since the flux is significantly higher than the derived average upper limit. We also analysed *Fermi*/LAT data and combined this with the X-ray

upper limits and historical radio, infrared and optical observations to build a SED. The SED can be modelled as a BL Lac source, which is expected since M87 is a FR-I type.
We then also examined the general aspects of gamma-ray bright radio galaxies. Most of these objects are of the FR-I type, and the core of at least one FR-II, 3C 111, is rather BL Lac-like than the expected FSRQ. For the other FR-II sources this might also be the case. The gamma-ray emission originates from the jet, similar as in the case of blazars. Due to the large jet angle, the emission is not observed to be boosted. However, since the gamma-ray emission originates near the black hole, either reflection or a large opening angle can explain the observations.
In addition, I contributed to the study of a possible dark matter halo observed with *Fermi*/LAT in the vicinity of the Virgo cluster. Our work has shown that a population of point sources contributes to this emission. In this thesis, the result of an extended emission analysis and the search for possible counter parts of new sources are presented.
Finally, the detection of two new X-ray sources using *Swift* is reported here for the first time. These sources, the BL Lac object BZB J1552+0850 and the Seyfert galaxy LSBC F727–V01, are both located within the 95% error circle of the *Fermi*/LAT source 2FGL J1551.9+0855. We analysed the X-ray data from the XRT and data from the UVOT. The likely counterpart of the *Fermi* source is rather the blazer BZB J1552+0850, since Seyfert galaxies are rarely gamma-ray emitters.
To understand the gamma-ray bright radio galaxies, X-ray observations can be used to can characterise these sources. Using for example the new generation of instruments, such as *NuSTAR* and *ASTRO-H*, will help with their superior resolution to distinguish between thermal and non-thermal emission in the X-ray spectrum. Additionally, by building SEDs from simultaneous multi-wavelength observations will help constrain the broad-band emission. This will also help to pinpoint the counter part of *Fermi*/LAT detected sources, which is not trivial due to the large uncertainty in position.

2 Résumé

Cette thèse présente le travail que j'ai effectué dans le domaine des noyaux actifs de galaxie (NAGs), en particulier sur les radiogalaxies.

2.1 Introduction

En 1943, Carl Seyfert découvre le premier NAG. Six galaxies sont observées dans la bande optique sur de large bandes d'émission (Seyfert 1943). Durant la fin des années 1950, plusieurs grandes campagne de surveillance radio ont été effectuées, comme le "Third Cambridge Survey" à 178 MHz (Edge et al. 1959). La plupart des objets détectés furent associés à des galaxies sur la bande visible. Quelques-uns d'entre eux furent identifiés comme des étoiles affichant des raies d'émission inconnues. Ces objets ont été surnommés "Presqu'étoiles" ou "Quasi-Stellar Objects" (QSO). 3C 273 est un QSO et Schmidt (1963), en utilisant un spectre sur l'optique, découvrit que ces raies correspondaient en fait à la série de Balmer du Magnésium II décalée vers le rouge avec z=0.158. Le décalage des raies vers le rouge ne pouvait pas avoir une origine gravitationnelle étant donné la largeur des raies et la présence de raies de transition interdites. L'éloignement de 3C 273 impliquait alors que l'objet était encore plus lumineux qu'on le pensait et les QSO ne pouvait plus être considéré comme des étoiles. Depuis cette découverte, les objets comme 3C 273 sont appelés Quasars.

Un NAG est caractérisée par la grande luminosité de son noyau, avec $L \gtrsim 10^{42}\,\mathrm{erg\,s^{-1}}$, provenant d'une région compacte. On pense que les NAGs sont alimentés par accrétion via un disque d'accrétion autour d'un trou noir central. Les sources moins lumineuses semblent généralement accompagnées d'un disque d'accrétion dominé par l'advection (ADAF). La luminosité maximale pouvant être obtenue par accrétion est la luminosité d'Eddington L_{Edd}, où la pression de radiation est équilibrée par la gravité. Elle est définie par:

$$L_{\mathrm{Edd}} = \frac{4\pi G M m_p c}{\sigma_{\mathrm{T}}} \simeq 1.3 \times 10^{38} \frac{M}{M_\odot}\,\mathrm{erg\,s^{-1}} \tag{2.1}$$

Ici m_p est la masse de proton, M la masse de l'objet centrale, G la constante gravitationelle et σ_{T} la section efficace de Thomson. Les NAGs peuvent être divisés en deux classes: les sources radio-silencieuses ou *radio-quiet*, comme les galaxies de Seyfert et les *Low-Ionisation Narrow Emission-Line Region* (LINERS), et les sources radio-bruyantes ou *radio-loud*, comme les blazars et les radiogalaxies. Cette dernière catégorie présente des jets pour approximativement 10% des NAGs. La distinction est basée sur la radio-bruyance R, définie comme $R = F_{5\,\mathrm{GHz}}/F_{\mathrm{B}}$, ici $F_{5\,\mathrm{GHz}}$ est le flux radio à 5 GHz et F_{B} est le flux optique à pour la bande B. Un NAG est radio-bruyant quand $R \geq 10$. Les mécanismes de formation du jet ne sont toujours pas complètement compris. La raison pour la quelle certains NAGs montrent des jets et d'autres non reste également à ce jour incertaine.

Des modèles d'unification (e.g. Antonucci 1993; Urry & Padovani 1995) ont été proposés, où il est supposé que tous les NAGs sont des objets intrinsèquement similaires, observés sous

différentes conditions, par exemple, d'orientation. Ce modèle de base suppose un trou noir supermassif entouré d'un disque d'accrétion. Les raies spectrales observées dans les bandes optiques et ultraviolettes proviennent des régions de gaz. Le *Broad Line Region* (BLR) est plus proche du trou noir et les larges raies spectrales proviennent de là. Le *Narrow Line Region* (NLR) est, quant à lui, plus loin du centre et sont à l'origine des raies spectrales fines. Un tore de matière opaque entoure le trou noir, le disque d'accretion et le BLR. Les objets radio-bruyants montrent aussi deux jets perpendiculaires au disque d'accrétion.

Quand un objet est observé *face-on*, cela signifie que la ligne de visée est perpendiculaire au disque d'accretion. L'observateur peut voir le disque d'accretion, le BLR et le NLR (en cas d'un objet radio-silencieux). Donc, les raies spectrales larges et fines sont visibles. Dans ce cas, le NAG est dit de Type 1. Pour un objet vu *edge-on*, la ligne de visée est parallèle au disque, le tore obscurcissant l'emission du disque et du BLR et permettant uniquement la visibilité des raies spectrales fines provenant de NLR. Ces NAGs entrent dans la classe Type 2. Le Type 2 contient un Type 1 core qui est obscurci. Des observations radio polarisées ont confirmées cette théorie (Antonucci & Miller 1985). Pour les sources radio-bruyantes, l'angle du jet θ avec la ligne de visée est important. Pour les radiogalaxies ayant un angle de jet tel que $\theta > 10°$, l'émission du jet et le noyau sont visibles. Deux types de radiogalaxies ont été distingués par Fanaroff & Riley (1974), en se basant sur la morphologie du jet, et la luminosité radio à 178 MHz (rest-frame). Les types FR-I sont moins lumineux, avec une luminosité à 178 MHz de $L_{\mathrm{FR-I}} < L_{\mathrm{FR}} \sim 2 \times 10^{25}\,\mathrm{W\,Hz^{-1}\,sr^{-1}}$. Les jets sont moins focalisés, et l'émission maximale est proche du noyau. Les jets de type FR-II sont plus lumineux, avec un luminosité à 178 MHz de $L_{\mathrm{FR-II}} > L_{\mathrm{FR}}$. Les jets sont très focalisés, plus long et sont le plus brillant sur les bords du jet. Si l'angle du jet est tel que $\theta < 10°$, l'émission est dominée par le jet relativiste et l'objet est identifié comme étant un blazar.
À cause du jet relativiste, l'émission des blazars est "Doppler boosté", et les photons peuvent atteindre de très hautes energies jusqu'au régime du TeV qui sont vus grâce au petit angle de jet. Par ailleurs, un plus grand angle de jet des radio galaxies empêche l'observateur de voir le jet intérieur et donc l'émission observée n'est plus "Doppler boosté". À cause de cela, les radiogalaxies n'ont pas été considérées comme sources de gamma et TeV. Cette idée a changé avec le premier catalogue de *Fermi*/LAT (Abdo et al. 2010a) qui permet d'observer les rayons gamma compris entre 20 MeV et 300 GeV (Atwood et al. 2009). La plupart des NAGs dans le catalogue sont des blazars, mais quelques radiogalaxies sont aussi incluses. Cela indique que notre compréhension des radiogalaxies et des NAGs n'est pas complète. Pour commencer à comprendre cette nouvelle classe de source et pour examiner l'origine des rayons gamma émis par les radiogalaxies, deux des radiogalaxies détectées par *Fermi*/LAT sont étudiées plus en détail sur la bandes X et gamma et par l'étude des distributions spectrale d'énergie ou *Spectral Energy Distributions* (SEDs).

2.2 Résultats

2.2.1 La radiogalaxie de type FR-II 3C 111

Dans la première partie de cette étude, on se concentre sur la radiogalaxie de type FR-II 3C 111. 3C 111 (z=0.049 Sargent 1977) est détectée par *Fermi*/LAT, et incluse dans le premier catalogue des sources (Abdo et al. 2010a). Le jet a une taille projetée de 78 kpc (Bridle & Perley 1984) et l'angle du jet est $\theta = 18°$ (Jorstad et al. 2005). Sur le spectre optique et

X, 3C 111 montre des signatures thermiques comme une galaxie de Seyfert. La recherche a débutée par une analyse des rayons X et gamma. L'analyse des données de *Fermi*/LAT, sensible entre 20 MeV–>300 GeV montre que 3C 111 est detecté entre 0.1–100 GeV, avec un significativité de $\sim 3\sigma$, un indice spectral de $\Gamma_\gamma = 2.4 \pm 0.2$ et un flux $f = 1.2 \times 10^{-8}\,\mathrm{ph\,cm^{-2}\,s^{-1}}$. Ensuite, les données de *Suzaku* XIS et PIN, de IBIS/ISGRI, un imageur sensible entre 15 keV et 10 MeV sur le observatoire spatial *INTEGRAL* sont analysés, et finalement, un spectre de *Swift*/BAT est ajouté pour créer le spectre de rayons X entre 0.4–200 keV.

Le meilleur ajustement (χ^2_ν=1.10, 1676 degrés de liberté) est obtenu avec une loi de puissance absorbée présentant une coupure exponentielle, une réflexion d'un matériau neutre (`pexrav`, Magdziarz & Zdziarski 1995) et un profile Gaussien pour la raie du Fer K-α sur 6.4 keV. La densité équivalente de la colonne d'hydrogène est $N_\mathrm{H} = (9.0 \pm 0.2) \times 10^{21}\,\mathrm{cm^{-2}}$, l'indice spectral est $\Gamma = 1.68 \pm 0.03$, la coupure d'énergie est $E_\mathrm{cut} = 227^{+143}_{-67}\,\mathrm{keV}$ et le facteur d'échelle de réflexion est $R = 0.7 \pm 0.3$. Les valeurs de la coupure d'énergie et du facteur d'échelle de réflexion sont dans la gamme prévue pour les galaxies de Seyfert. Pour la raie du Fer K-α, une largeur équivalente $EW = 85 \pm 11\,\mathrm{eV}$ est trouvée. La raie du Fer K-α est aussi une signature thermique, mais en utilisant des observations historiques, on trouve que le continuum émission est variable. En conclusion, l'émission dans la bande X de 3C 111 montre des signatures thermiques provenant du centre, proche du trou noir, et des signatures non-thermiques, provenant du jet.

En utilisant les résultats de cette analyse, un SED est construit. Pour représenter les basses énergies, les observations historiques sur les bandes radio, optique et ultraviolet sont utilisées. Le SED est sur le format $\nu f(\nu)$ pour pouvoir comparer un grand domain d'énergie. Pour un blazar, un SED a une forme caractéristique, qui s'explique par l'émission synchrotron et diffusion par effect Compton inverse. Ce modèle suppose une population d'électrons relativistes, sur une région sphérique avec rayon et champ magnétique, qui se déplacent dans le jet avec un facteur Doppler δ. Les électrons émettent un rayonnement synchrotron et les photons ainsi émis sont diffusés par effet Compton inverse (*Synchrotron self-Compton*, SSC). L'émission de 3C 111 est bien représentée par le SSC modèle, ce qui indique qu'une large bande de l'émission est dominée par le jet. Les paramètres utilisés pour la représentation indique que 3C 111 est plus proche d'un BL Lac (le type de blazar le moins lumineux). Ce qui n'est pas prévu dans le modèle d'unification qui connecte les FR-II radio galaxies avec les FSRQ.

2.2.2 La radiogalaxie de type FR-I M87

Tandis que la plupart des radiogalaxies detectées sur le bande gamma sont de types FR-I, la seconde source étudiée est la radiogalaxie de type FR-I M87. Cet objet est détecté du regime radio jusqu'à celui du TeV, mais pas sur les rayons X de $> 10\,\mathrm{keV}$. Notre recherche de M87 a deux objectifs: détecter ou déterminer une limite supérieure d'émission $> 10\,\mathrm{keV}$ grâce aux résultats des observations de *INTEGRAL* IBIS/ISGRI publiques et privées, puis étudier avec un SED l'émission en bande large. M87 est un objet proche, situé à un distance de 16 Mpc. Cela offre l'avantage de pouvoir observer les composantes individuelles de la source, comme les "hotspots" du jet, par exemple pour les rayons X avec *Chandra*. L'angle du jet de M87 est $\theta = 30°$ (Bicknell & Begelman 1996).

2 Résumé

INTEGRAL IBIS/ISGRI utilise la technique du masque codé, qui permet de faire converger les rayons X et gamma. Cette technique a l'avantage de permettre un large champ de vue et une imagerie des photons de haute énergie, à la différence de l'usage des miroirs. Cependant, la résolution angulaire est moins bonne et la déconvolution des images est complexe. Les données de *INTEGRAL* sont organisées sur une *revolution* (une orbite complète, environ 3 jours) et les *science windows* (scw, pointages individuels). Nous commençons avec un analyse standard utilisant les logiciels Offline Scientific Analysis (OSA) 9 sur toutes les données ISGRI sur M87 (duration on-time total 4.7 Ms). Parce que le flux sur la bande X est probablement faible, l'information du flux est extraite seulement dans la bande en énergie 20–60 keV. Pour chaque scw une image est crée, et ces images sont combinées en une mosaïque. Un significativité de 3.8σ est trouvée ainsi qu'un flux $f = 3.0 \times 10^{-12}\,\mathrm{erg\,cm^{-2}\,s^{-1}}$ entre 20 et 60 keV. Pourtant, la mosaïque montre de fortes structures de base, ce qui implique que la détection n'est pas fiable. Pour quantifier la qualité de la mosaïque, la moyenne quadratique des significativités de l'ensemble de l'image (*significance map*) est calculée. Idéalement, la moyenne quadratique pour cette *significance map* est $s_{\mathrm{rms}} = 1$. L'analyse standard avec OSA 9 rapporte une moyenne quadratique de $s_{\mathrm{rms}} = 1.85$. Pour étudier ces structures de base, deux nouvelles mosaïques sont crées, une première avec tous les scw situés avant décembre 2010 et une seconde avec tous les scw situé après. Toutes les deux mosaïques montrent des structures de base, elles ne sont donc pas dépendantes du temps. Après le calcul de la moyenne quadratique des significativités des scw individuelles, celles avec un moyenne quadratique de $s_{\mathrm{rms,scw}} > 1.2$ sont omises. Une nouvelle mosaïque est créée avec cette selection et le on-time totale a diminué jusqu'à 4.5Ms. La moyenne quadratique s'améliore avec $s_{\mathrm{rms}} = 1.35$, mais M87 n'est pas significativement détecté.

Aussi, l'analyse des données selectionnées incluant de nouvelles observations en total on-time 5.2 Ms effectuée à l'aide des nouveaux logiciels OSA 10 montre des structures de base sur la mosaïque, avec une moyenne quadratique de $s_{\mathrm{rms}} = 1.38$. M87 n'est pas significativement détectée, avec une 3σ limite supérieure de flux $f < 3.3 \times 10^{-12}\,\mathrm{erg\,cm^{-2}\,s^{-1}}$ entre 20–60 keV. Quelques autres techniques sont utilisées, comme la sélection des données ou des changements sur les logiciels d'analyse, pour trouver l'origine des structures de base et pour améliorer l'image. Les structures ne trouvent pas leur origine dans le *source cleaning* out de soustraction de fond. Enfin, le meilleur résultat affiche une moyenne quadratique de significativité de $s_{\mathrm{rms}} = 1.08$, et un 3σ limite supérieure de flux de $f < 3.3 \times 10^{-12}\,\mathrm{erg\,cm^{-2}\,s^{-1}}$ entre 20 et 60 keV.

L'analyse de données des moniteurs de rayons X JEM-X sur *INTEGRAL* ne montrent aussi aucune émission significative $> 10\,\mathrm{keV}$, avec un 3σ limite supérieure de flux $f < 1.2 \times 10^{-11}\,\mathrm{erg\,cm^{-2}\,s^{-1}}$ entre 10.2 et 25 keV. L'émission à plus basse énergie 3–10.2 keV est détectée avec 15.1σ, avec $f = (1.6 \pm 0.2) \times 10^{-11}\,\mathrm{erg\,cm^{-2}\,s^{-1}}$.
M87 est lumineux sur la bande d'énergie de *Fermi*/LAT, contrairement à 3C 111. L'analyse des données entre 100 MeV et 100 GeV montrent une significativité de 19σ, et un flux de $f = 2.2 \times 10^{-8}\,\mathrm{ph\,cm^{-2}\,s^{-1}}$.

Suzaku a observé M87 fin 2006. Les données du détecteur à rayons X durs PIN sont analysées pour comparaison avec la limite supérieure de flux trouvée avec ISGRI. Un spectre peut être extrait, et un 20–60 keV flux de $f = 1.3^{+0.1}_{-0.2} \times 10^{-11}\,\mathrm{erg\,cm^{-2}\,s^{-1}}$ est trouvé. C'est la première fois que M87 est observé dans les energies $> 10\,\mathrm{keV}$. Le spectre est representé

avec une loi de puissance absorbée dont l'indice spectral est $\Gamma = 2.8^{+0.5}_{-0.4}$.

En utilsant les observations historiques sur les bandes radio et optiques, deux SED sont construits; un pour l'état moyen (utilisant la limite supérieure de ISGRI) et un pour l'état éruptif 2006 (en utilisant la d'étection PIN). Les deux SEDs sont bien representés avec un modèle SSC. Les paramètres utilisés pour l'ajustement indiquent que M87 est comme un BL Lac avec un ADAF, prevu dans le modèle d'Unification. Pour l'état eruptif 2006, le SED est mal échantillonné ce qui rend difficile de trouver un bonne représentation.

2.2.3 Détection de deux nouvelles sources sur rayons X

Pour l'étude des radio galaxies détectées avec *Fermi*/LAT, nous avons demandé les droits des données *INTEGRAL* IBIS/ISGRI de trois sources détectées avec LAT. Pour une de ces sources, 2FGL J1551.9+0855, les observations de *Swift* sont demandées simultanément avec les observations d'ISGRI. Sur le catalogue de *Fermi*/LAT 2FGL J1551.9+0855 est associé avec une BL Lac à $z = 1.015$, CRATES J1552+0850 (Nolan et al. 2012). L'analyse des données de ISGRI met un 3σ limite supérieure de 20–60 keV flux, $f \lesssim 4 \times 10^{-11}\,\mathrm{erg\,cm^{-2}\,s^{-1}}$ et $f \lesssim 3 \times 10^{-10}\,\mathrm{erg\,cm^{-2}\,s^{-1}}$ pour les deux observations, en raison de la faible exposition de 89 ks et 7 ks, respectivement.L'analyse des données de *Swift*/XRT (le télescope des rayons X sensible entre 0.2–10 keV) montrent deux sources possibles. Les positions de ces sources sont compatibles avec un BL Lac BZB J1552+0850 ($z > 1.015$) et une galaxie de Seyfert LSBC F727-V01 ($z = 0.071$). Ces deux sources sont placées sur le cercle d'erreur à 95% de 2FGL J1551.9+0855. Ensuite, les données de *Swift*/UVOT (télescope UV/Optique de 170 à 650 nm) sont analysées. Les magnitudes derivées ne sont pas compatibles avec les résultats obtenus précédemment par SDSS. Les differences peuvent être introduites par la variabilité des sources ou à cause d'une difference sur le rayon d'extraction. Il est plus probable que le BL Lac BZB J1552+0850 soit le vrai assocation de 2FGL J1551.9+0855. Les BL Lacs sont connus pour être des émetteurs de rayons gamma, tandis que les galaxies de Seyfert ne le sont pas. Cette conclusion est supportée par un suivi en infrarouge (Massaro et al. 2012).

2.2.4 Halo de matière noire proche de M87

J'ai contribué à l'étude d'un possible halo de matière noire (*dark matter*, DM) observé avec *Fermi*/LAT à proximité de l'amas de la Vierge. Cette halo a montré un signal compatible avec une annihilation de DM avec un significativité de 4.4σ en utilisant 3 ans de données de *Fermi*/LAT (Han et al. 2012). 3.8 ans d'observations de LAT sont analysées et une analyse morphologique avec différents modèles spatiaux et spectraux a été effectuée. Le meilleur ajustement est une loi de puissance exponentielle de coupure. Le meilleur modèle spatial est asymétrique. Plusieurs nouvelles sources ponctuelles ont été trouvées (Macías-Ramírez et al. 2012), positionnées sur la structure du potentiel de DM. L'inclusion de ces sources dans l'analyse montrent une diminution de significativité jusqu'à $\sim 3\sigma$. Le signal attribué à DM est probable grâce aux nouvelles sources et aux incertitudes dans l'émission diffuse de la galaxie.

2.3 Conclusion

Dans cette thèse, l'origine de l'émission des rayons gamma pour deux sources, le FR-II 3C 111 et le FR-I M87 est étudiée par analyse spectrale dans les rayons X et gamma, et SEDs. Dans le

cas de 3C 111 des processus thermiques du noyau sont visibles sur la bande X, tandis que pour M87 sur les rayons X l'émission non-thermique du jet est visible. Sur le SE, les deux sources montrent un spectre de type BL Lac. Au total, l'échantillon de radiogalaxies détectées avec *Fermi*/LAT se compose de 15 sources. La plupart de ces objets sont de type FR-I, le noyau de FR-II 3C 111 est comme le type BL Lac et n'est pas la FSRQ prévue de l'Unification. Aussi les autres radio galaxies détectées par rayonnement gamma de type FR-II peuvent montrer un noyau BL Lac. L'émission de rayons gamma provient du jet, à l'image des blazars. Parce que l'angle du jet est grand sur les radio galaxies, l'émission n'est pas observée "boostée". Quand l'émission de rayons gamma trouve sa source proche du trou noir, une réflexion ou un grand angle d'ouverture du jet peut expliquer les observations. Pour continuer cette étude afin de comprendre le rayonnement gamma provenant des radio galaxies, des observations sur les rayons X peuvent être utilisées pour caractériser ces objets. Par exemple de nouveaux instruments comme *ASTRO-H* et *NuSTAR* vont aider, grâce à leur résolution supérieure, à distinguer l'émission thermique de l'émission non thermique dans le spectre des rayons X. Construire SED à partir d'observations multi-longueur d'onde simultanées aidera à limiter l'émission à bande large.

3 Introduction

The first Active Galactic Nuclei (AGN) were observed in the optical band, as extragalactic nebulae with particularly broad emission lines, in 1943 (Seyfert 1943). The first large radio surveys performed in the late 1950s showed more peculiar objects, the Quasi-stellar objects (QSOs), which appeared to be bright and point-like sources. The QSOs showed emission lines at unknown wavelengths, which was interpreted by Schmidt (1963) as caused by redshift, which placed the QSOs at large distances. Though the luminosities of the QSOs were initially thought to be due to starlight, the extragalactic nature of the sources ruled out this theory, and soon after it was established that accretion by a super massive black hole could produce the observed luminosities (e.g. Salpeter 1964). In Chapter 4 the history and anatomy of AGN is more extensively described.

Nowadays, our knowledge on AGN has improved (e.g. Beckmann & Shrader 2012). Both by theories, like the unification model (e.g. Urry & Padovani 1995) and by observations, such as performed by the *INTEGRAL* mission, which has observed hundreds of AGN in the hard X-ray band, increasing our understanding of the physics and the Unification model (e.g. Courvoisier 2013a).
Open questions remain. For example, it is thought that all galaxies harbour a super massive black hole in their centre, though not all galaxies are AGN. The exact accretion processes, which are the origin of the observed luminosity, are still a matter of debate. Also the launching of jets, present in about 10% of the AGN and in many other accreting objects such as microquasars (e.g. Chaty 2005), is not fully understood.

In this thesis the focus lies on a specific type of AGN: the radio galaxies. These sources have a prominent jet which is observed with an angle of $> 10^{\circ}$ to the line of sight. The radio galaxies show emission from thermal processes from the core, near the central black hole, and non-thermal synchrotron and inverse Compton emission from the jet. Radio galaxies are assumed to be the parent population of blazars, the type of radio-loud AGN where the observer looks directly into the jet. The relativistic jet swamps any thermal core emission and high energy photons up to TeV are expected due to Doppler boosting. Due to the relatively large angle of the jet with respect to the line of sight, gamma-ray emission was not expected from radio galaxies. This picture changed with the *Fermi* satellite, which operates between 30 MeV to 300 GeV. Many blazar sources were detected, but also a small group of gamma-ray bright radio galaxies.

Therefore, it seems that our understanding of radio galaxies is not complete. To understand the origin of the gamma-ray emission, we studied two gamma-ray detected radio galaxies in great detail, using X-ray spectra and performing broad band analysis (see Chapter 6 for the X-ray and gamma-ray instruments used). In the X-ray band we can observe both thermal, Seyfert-like and non-thermal, jet-like, signatures. Since AGN are observed in all wavelengths, from radio to TeV, and potentially even emit cosmic rays (Henri et al. 1999), it is important to observe, and model the emission processes in the full energy band.

Table 3.1: Sample of *Fermi*/LAT radio galaxies (Abdo et al. 2010e). 3C 120 was not included in the first catalogue but is detected using 15-months of *Fermi*/LAT data. Pictor A was detected using three years of *Fermi*/LAT observations (Brown & Adams 2012), but has not been included in either of the *Fermi*/LAT catalogues.

Object	FR type	redshift	Included in 1FGL	Included in 2FGL	VHE
3C 111	FR-II	0.049	yes	no	no
M87	FR-I	0.00436	yes	yes	yes
Cen A	FR-I	0.001825	yes	yes	yes
NGC 1275	FR-I	0.017559	yes	yes	yes
3C 78	FR-I	0.0288	yes	no	no
PKS 0625-354	FR-I?	0.054594	yes	yes	no
NGC 6251	FR-I	0.02471	yes	yes[a]	no
3C 207	FR-II	0.684	yes	yes	no
3C 380	FR-II	0.692	yes	yes	no
3C 120[b]	FR-I	0.03301	no	no	no
PKS 0943–76	FR-II	0.27	yes	yes	no
Cen B	FR-I	0.01215	no	yes	no
IC 310	FR-I	0.018940	no	yes	yes
Fornax A	FR-I	0.005871	no	yes	no
Pictor A[c]	FR-II	0.035	no	no	no

[a] Associated position changed.

[b] Included in Abdo et al. (2010e)

[c] Brown & Adams (2012)

The first radio galaxy to be detected in gamma-rays was the nearby Fanaroff-Riley (FR, see Section 4.2.2) 1 object Centaurus A. This nearby source, $z = 0.001825$, was observed by the early gamma-ray observatory *CGRO*/EGRET (Hartman et al. 1999). Also 3C 111 and NGC 6251 were shown to have a potential *CGRO*/EGRET counter part. The first *Fermi*/LAT catalogue, using 11 months of observations, has detected a total of 1451 sources, among which 569 blazars and 10 non-blazar AGN (Abdo et al. 2010a). In a *Fermi*/LAT paper dedicated to misaligned blazars, the source 3C 120 has been detected using 15 months of observations (Abdo et al. 2010e). In total the sample consists now of 11 radio galaxies, 7 FR-I galaxies and 4 FR-II sources. In the second *Fermi*/LAT catalogue, the LAT-detected sources 3C 111, 3C 120 and 3C 78 sources are no longer significantly detected. but there were several new sources found: IC 310, Centaurus B and Fornax A. Centaurus A, included in the first catalogue, was split into two gamma-ray sources for the second catalogue, as significant gamma-ray emission from the core and from the radio lobes was observed (Nolan et al. 2012). In Table 3.1 all gamma-ray bright radio galaxies detected so far can be found. The majority of the sources are of the FR-I type, and all observed sources are at redshifts $z < 0.69$.

In addition to gamma-ray emission, four gamma-ray bright radio galaxies have also been detected in the TeV band. While in the gamma-ray band we observe a majority of FR-I sources, in the TeV band only FR-I sources are observed.

To understand the differences between FR-I and FR-II sources in the high energy band,

we have chosen to take a closer look at both an FR-I source (M87, see Chapter 8) and an FR-II object (3C 111, see Chapter 7). In Chapter 11 we tie our results into a larger sample, and compare with blazars and other radio galaxies to understand these enigmatic sources.

In addition to this work on gamma-ray bright radio galaxies as a group, a potential dark matter halo around M87 was studied using *Fermi*/LAT observations, described in Chapter 10. Finally, observations from *Swift*/XRT near the *Fermi*/LAT detected source 2FGL J1551.9+0855 led to the discovery of X-ray emission from two AGN, the blazar BZB J1552+0850 and the Seyfert 1 galaxy LSBC F727-V01, see Chapter 9.

4 Active Galactic Nuclei

4.1 Introduction

An Active Galactic Nucleus (AGN) is the core of an active galaxy, and the term is used for a broad variety of objects. The first class of AGN that was discovered are the Seyfert galaxies. Seyfert (1943) used optical observations of 6 galaxies which showed redshifted broad emission lines in their spectrum. Taking into account the large distance of the galaxies which can be deduced from the redshift, these objects had to be very luminous. While the common understanding at that time was that the emission results from a large number of stars, later observations indicated that the nucleus, where the emission arises, has a diameter less than 100 pc. However, concentrating individual stars with a total mass of a few times $10^8\,\mathrm{M}_\odot$, within a volume $\ll 0.0005\,\mathrm{kpc}^3$ seemed not feasible, as Woltjer (1959) pointed out. Soon after it was established that only accretion onto a super massive black hole could produce this kind of energy output within such a small volume (Salpeter 1964; Lynden-Bell 1969).

The first radio surveys were performed in the late 1950s, for example the third Cambridge survey, at 178 MHz (Edge et al. 1959) and the Parkes survey of the southern sky at 408 MHz, 1410 MHz and 2650 MHz (Ekers 1969). Most of the radio sources could be identified with resolved galaxies, but the position of several radio sources coincided with optical point sources, and these sources were thus called QSOs or *Quasi-Stellar Objects*. The QSOs showed strong emission lines, but at unidentified wavelengths. For example, using radio observations, the position of the QSO 3C 273 was determined with an accuracy of 1 arcsecond using the lunar occultation method (Hazard et al. 1963). The radio position coincides with a star-like optical counter part, which showed unidentified emission lines. Schmidt (1963) showed that the unidentified lines observed were the hydrogen Balmer series and the magnesium II line, redshifted with $z = 0.158$. This redshift could be of gravitational origin, or of cosmological origin (Greenstein & Schmidt 1964). The gravitational explanation is excluded, assuming a galactic object yields a density which can not be reconciled with the width of the emission lines and the presence of forbidden lines. Similarly, assuming an extra-galactic object also could not reconcile the densities with the lines present. Assuming a cosmological redshift, caused by the expansion of the Universe, places 3C 273 at a distance of $D = 649\,\mathrm{Mpc}$ via $D = cz/H_0$, with z the redshift and H_0 the Hubble constant[1]. The large distance indicates that these QSO are not stars, but rather star-like, and were renamed quasi-stellar radio sources or quasars. In addition, the distance also implies that the luminosity of these objects is much larger than previously assumed, and also about 100 times as luminous as known spiral galaxies.

In the years following this discovery several more quasars were observed, with a redshift up to about $z \sim 2$. The objects were characterised by broad emission lines, a large redshift,

[1] A recent study using HII regions yielded a Hubble parameter of $H_0 = 74.3 \pm 3.1\,(\mathrm{statistical}) \pm 2.9\,(\mathrm{systematic})\,\mathrm{km\,s^{-1}\,Mpc^{-1}}$, a measurement which is in agreement with independent measurements of type Ia supernovae (Chávez et al. 2012).

Figure 4.1: Optical spectrum for the BL Lac RX J1517.7+6525(Beckmann et al. 1999).

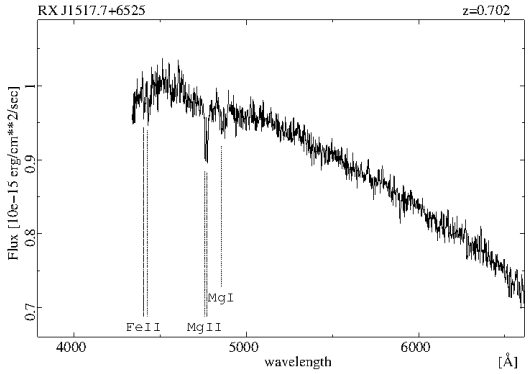

a variable continuum flux, and a UV excess, when compared to stars in a colour-colour diagram (Matthews & Sandage 1963). This latter property was used to identify new quasars candidates (Ryle & Sandage 1964). This lead to the discovery of the radio-quiet quasar-like objects, that showed a similar UV excess as the quasars but were not detected in the radio band (Sandage 1964).

Nowadays a different terminology is used. The whole class of active galaxies is called AGN. The radio-loud sources are divided into blazars and radio galaxies, where the blazars are more luminous and highly variable. The blazar class is subdivided into BL Lac-type objects, after the prototype BL Lacertae, and into the bright FSRQ and SSRQ (flat and steep spectrum radio quasars, respectively). The difference between these groups is the equivalent width (EW) of the emission lines, where BL Lacs do not display lines with EW$\geq$ 5Å. An example of the optical spectrum of a BL Lac source, RX J1517.7+6525, can be found in Figure 4.1. Figure 4.2 shows a spectrum for a FSRQ source, 3C 273.

The radio-quiet group consists of Seyfert galaxies and LINERs (Low-Ionisation Narrow Emission-line Regions), where the Seyfert class is more luminous. The Seyfert galaxies can be divided into different groups, depending on the presence of broad and narrow emission lines, where type 1 Seyferts show both narrow and broad emission lines and type 2 Seyferts show only narrow emission lines. There are also intermediate types of Seyferts, which are classified based on the broadness of the Balmer lines (see for example Winkler 1992).

4.2 Components

4.2.1 Core

It is thought that AGN are fuelled by a super massive black hole (SMBH) in their centre (Salpeter 1964; Lynden-Bell 1969). This explains the high luminosity output, $L \gtrsim 10^{42}\,\mathrm{erg\,s^{-1}}$, by accretion of matter onto the SMBH, and the variability in the emission on short time scales of $\Delta t \sim$ minutes in the X-rays and in the TeV band, which indicates that the emission arises in a compact region. The central black hole can be fuelled by gas from nearby dense stellar clusters via tidal distortions and stellar collisions, providing sufficient fuel for low-luminosity AGN (Combes 2001). For high-luminosity AGN, a high accretion rate is needed. Large-scale

Figure 4.2: Optical spectrum for the FSRQ 3C 273, the spectrum shows several strong emission lines (Yates & Garden 1989).

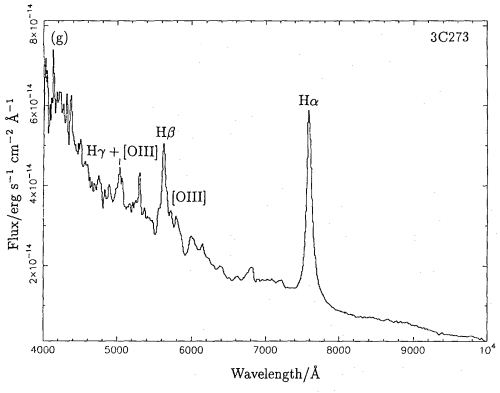

gravitational instabilities can drive gas towards the accreting object.

The maximum luminosity that can be achieved by spherical accretion onto a mass M is the Eddington luminosity L_{Edd}, where the radiation pressure balances the gravitational force. The Eddington luminosity is expressed as:

$$L_{\mathrm{Edd}} = \frac{4\pi G M m_p c}{\sigma_{\mathrm{T}}} \simeq 1.3 \times 10^{38} \frac{M}{M_\odot} \,\mathrm{erg\,s^{-1}} \tag{4.1}$$

Here, m_p is the mass of a proton, M the mass of the central object and σ_{T} the Thomson cross-section, see equation (5.2).

Since the central SMBH does not emit radiation, it can not be directly observed. There are several techniques which allow us to determine the mass of the central BH indirectly, for example the $M_{\mathrm{BH}} - \sigma$ relation. This connects the black hole mass M_{BH} with the stellar velocity distribution σ in the bulge of the host galaxy (Magorrian et al. 1998). It is now assumed that all galaxies harbour a central SMBH, however these are generally not active, such as the SMBH in our own galaxy, Sagittarius A* (Sgr A*, Balick & Brown 1974). This compact and bright radio source lies at the centre of the Milky Way, and the stars within 0.01 pc of Sgr A* were observed to move very fast, $v > 1000\,\mathrm{km\,s^{-1}}$ (Eckart & Genzel 1997; Ghez et al. 1998). These stellar motions indicated the mass of the radio source to be large. Later work by Ghez et al. (2008) and Gillessen et al. (2009) confirmed this by tracking the stars near Sgr A* for 12 years, showing that they indeed orbit around a central BH with a mass estimate of $M_{\mathrm{BH}} \backsimeq 4.3 \times 10^6 M_\odot$. Due to the angular resolution necessary to track the stars near the centre this technique can not be applied to other galaxies to infer the mass of their central SMBH. To measure the black hole mass in other galaxies, reverberation mapping can be used, or tracking water masers in the accretion disk near the central object to create rotation curves (see for example Moran et al. 1999). Reverberation mapping measures the structure near the central BH by monitoring the continuum emission and the emission of the broad-line region (see Section 4.2.3). The broad-line region clouds are assumed to follow Keplerian orbits, and the clouds are illuminated by the central engine. Doppler effects cause the emission line profiles arising in the broad-line region to broaden, which gives the

root-mean-square velocity of these clouds. The variations in the continuum influence the line emission, with a certain time delay which depends on the distance of the emission region. From the velocity variations and the radius of the emission region the mass of the compact object can be calculated. Masses between $M_{\rm BH} \approx 10^6 - 10^{10} M_\odot$ have been derived.

In the process of accretion, the infalling gas rotates around the SMBH in tightening Keplerian orbits, forming a geometrically thin but optically thick accretion disk. The material gradually loses its angular momentum, due to viscous processes produced by turbulent effects and magnetic instabilities (Shakura & Sunyaev 1973). The heat created in the disk is radiated away via black body emission, which depends on the radius R. The effective temperature is:

$$T(R) = T_*(R/R_{\rm BH})^{-3/4} \tag{4.2}$$

where $R_{\rm BH}$ is the radius of the SMBH, R the radius where the radiation is emitted, and T_* is defined as:

$$T_* = \left(\frac{G M_{\rm BH} \dot{M}}{4\sigma\pi R_{\rm BH}^3} \right)^{1/4} \tag{4.3}$$

where $M_{\rm BH}$ is the mass of the SMBH, and $\dot{M}$ the accretion rate. The overall disk spectrum is approximately the sum of the black body emission at each radius R. Here losses due to disk Compton scattering are not taken into account. The thin disk scenario breaks down if the accretion rate exceeds significantly the Eddington value or cooling becomes inefficient, such that the disk cannot be vertically confined.

For some low-luminous sources the thin accretion disk approximation does not properly explain the luminosity based on the measured black hole mass. In these cases an accretion flow emerges which is cooled by advection rather than radiation. In these models, which are called advection dominated accretion flow (ADAF, Ichimaru 1977) or radiatively inefficient accretion flow (RIAF, Ptak et al. 2004), the accreting matter is heated viscously, and since the radiative cooling is inefficient, heat is stored as entropy (Narayan & Yi 1994). One of the results of this type of flows is that the accreting matter forms a corona rather than a disk. Due to the low efficiency, sources with an ADAF will be less luminous than sources that have a radiatively efficient accretion flow.

There exist other alternative models for the accretion onto the central black hole. For example, an inhomogeneous accretion flow where collisions between the clumpy matter creates shocks could give rise to the observed optical to X-ray emission (Courvoisier & Türler 2005; Ishibashi & Courvoisier 2009). However, such a model is not able to explain the observed jets in AGN.

4.2.2 Jets

Radio lobes have first been reported by Jennison & Das Gupta (1953), who analysed radio observations of the nearby radio galaxy Cygnus A. Initially it was thought that the jets were ejected and not attached to the host galaxy. Later it was shown that the radio lobes could be powered by the jets originating from the centre of the galaxy (Rees 1966). With radio interferometry techniques, many more jetted sources have been discovered, and it is even possible to resolve the inner parts of the jet. For the nearby galaxy M87 for example, Hada

et al. (2011) have used observations between 2.3 and 43.2 GHz to image the jet base down to $\sim 0.01\,\mathrm{pc}$ (see also Section 8.2). Nowadays it is possible to resolve jets also in other bands, such as in the optical and soft X-rays.

Jets can extend from parsec scale out to hundreds of kiloparsecs in luminous sources. For radio galaxies, the Fanaroff-Riley classification is used (Fanaroff & Riley 1974). The FR-I types are less luminous, often show two symmetric jets, and most of the jet emission originates close to the core (see Figure 4.3 for example). The FR-II sources are more luminous, do not always show an equally bright counter jet and show edge-brightened extended jets (see Figure 4.4). In this case the difference in luminosity in both jets, or the absence of the counter jet, is connected to the Doppler boosting and viewing angle, such that the jet pointed towards the observer appears brighter. This also explains the apparent super luminal motion of jet knots (parts of the jet which display higher luminosity, possibly due to shocks) which have been observed in several sources (e.g. Wehrle et al. 2001).

FR-I and FR-II sources can be discriminated based on their radio luminosity. Sources with a luminosity higher than a monochromatic luminosity of $L_{\mathrm{FR}} \sim 2 \times 10^{25}\,\mathrm{W\,Hz^{-1}\,sr^{-1}}$ at a rest-frame frequency of 178 MHz are classified as FR-II, and sources with luminosities below the luminosity L_{FR} are classified as FR-I (Fanaroff & Riley 1974). In the optical band there is no distinction between both types of radio sources (Owen & Ledlow 1994). At low redshift ($z < 0.5$) FR-I galaxies tend to be in galaxy clusters, while FR-II sources are more often hosted by isolated galaxies. At higher redshifts both FR types are found in rich environments (Hill & Lilly 1991).

The mechanism responsible for launching the jet is still under discussion. For example, the driver can be disk accretion energy and angular momentum (Blandford & Payne 1982) or the black hole spin (Blandford & Znajek 1977). The latter, also known as the Blandford-Znajek mechanism, is often used to explain the powering of the jet. In this model, an accretion disk with a strong magnetic field can extract spin energy from the rotating central black hole. As accreted matter from the disk falls into the SMBH, the magnetic field lines are carried along with the matter. The spin of the SMBH then drags the field lines, twisting the lines and generating a toroidal component. This induces a poloidal electric current, which follows the field lines into the poles of the SMBH. The energy transported via the currents into the poles is expelled and forms a jet.

Another theory shows that it is possible to extract energy from the rotating SMBH via frame dragging (Penrose process, Penrose 1969). It is assumed that the rotational energy of the SMBH is not located inside the event horizon, where the escape velocity exceeds the speed of light, but rather outside of it in the ergosphere. Within the ergosphere spacetime is dragged along with the SMBH rotation (frame-dragging, or Lense-Thiring effect, Lense & Thirring 1918). Then, an infalling piece of matter which enters the ergosphere can be split into two pieces, such that one falls into the event horizon and the other can escape to infinity. Due to the conditions in the ergosphere, the particles can have a negative energy as long as conservation of energy holds. This way, the escaping matter can have a larger energy than the original infalling matter.

AGN jet observations suggest the jets might precess either due to the Lense-Thirring effect or the accretion disk viscosity. The jet can interact with the intra-cluster medium surround-

Figure 4.3: An example of a FR-I galaxy, M84, at 5GHz (Laing & Bridle 1987). Both the jets are visible, and most jet luminosity is emitted near the core.

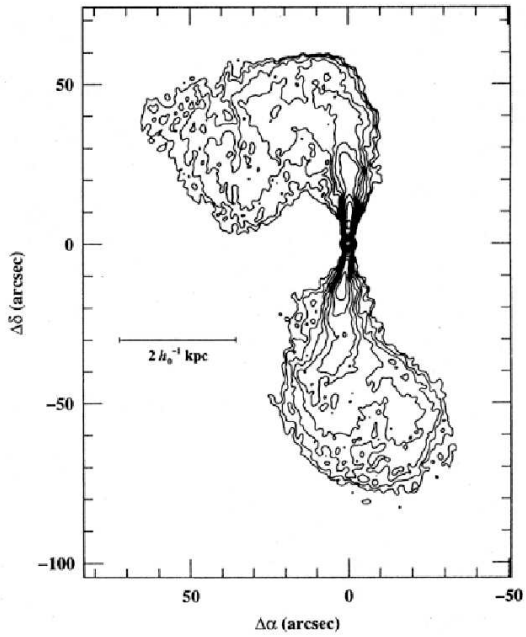

ing the galaxy and form cavities or inflate bubbles. For example near the elliptical galaxy NGC 1275, multiple cavities mis-aligned with a jet have been observed, which might indicate a strong precession of the jet (Falceta-Gonçalves et al. 2010). However, later work by Nixon & King (2013) showed that the Lense-Thirring effect alone can not be responsible for repeated jet precession, since the angular momentum of the accretion disk is small compared to that of the SMBH, which restricts the motion of the jet. In AGN the angular momentum of the disk is constrained. The angular momentum of the disk J_d is related to the disk radius R_d via $J_d \propto R_d^{1/2}$. The radius of the disk is limited, the disk will fragment into stars due to self-gravity if the radius is too large. It is possible for the jet direction to change slightly on time scales of $\gtrsim 10^7$ yr due to random accretion events.

4.2.3 Extended emission

The optical and UV spectra of AGN show the presence of both broad and narrow lines. These lines are thought to arise in different regions, the broad and narrow line region (BLR and NLR, respectively), since the properties of the gas which causes the emission lines appear to be different. The broad lines are Doppler-broadened, showing a typical full-width half-maximum velocity of $\Delta v_{\mathrm{FWHM}} \approx 5000\,\mathrm{km\,s^{-1}}$. The temperature of the gas as derived from the emission lines is $T \simeq 10^4\,\mathrm{K}$ with a density of $n > 10^9\,\mathrm{cm^{-3}}$. The overall mass of the BLR can be calculated from the C IV emission line, and is found to be low even for luminous sources, $M_{\mathrm{BLR}} \sim 1 - 10 M_\odot$. Reverberation mapping (see Section 4.2.1) is used to probe the BLR (e.g. Clavel et al. 1991), and it has been shown that the BLR is close to the central engine, at a radius of ∼0.01–1 pc.

The narrow lines show a full-width half-maximum velocity of $\Delta v_{\mathrm{FWHM}} \approx 400\,\mathrm{km\,s^{-1}}$, and

Figure 4.4: The FR-II radio galaxy 3C 175 at 5GHz (Bridle et al. 1994). The jet which is pointed towards the observer is visible, and, while the radio lobes of the counter jet can be observed, the jet itself is not visible due to Doppler boosting away from the observer.

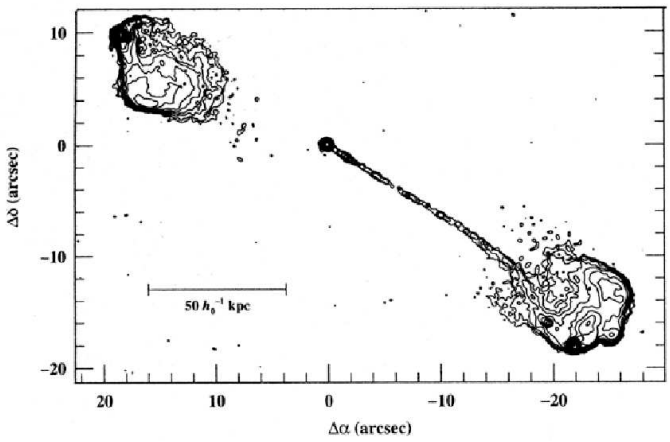

the presence of forbidden lines indicates that the gas density is low. An average density of the emitting gas can be derived with about $\bar{n} \simeq 2000\,\mathrm{cm}^{-3}$ (Koski 1978). The NLR extends beyond the BLR, out to a distance from the central black hole of about 100–10,000 pc. Smaller distances have been reported, for example for the Seyfert 2 galaxy NGC 5548 a much smaller distance of 1–15 pc from the central source was deduced (Detmers et al. 2009). The total mass of the NLR is larger than that of the BLR, of the order of $M_{\mathrm{NLR}} \sim 10^6 M_\odot$. In both cases the gas is thought to be contained in optically thin clouds, photoionised by UV radiation, which causes the observed lines.

Surrounding the accretion disk and the BLR is thought to be a dusty torus. This was proposed initially to explain the polarized emission lines in the optical spectrum observed in the nearby (distance 14.4 Mpc) Seyfert 2 galaxy NGC 1068 (Antonucci & Miller 1985), but now forms a key element to the Unified scheme (see Section 4.3). Infrared observations of the torus show that the structure should be geometrically thick, obscuring and of parsec size. Interferometry observations of the torus of NGC 1068 with the VLTI at 8μm showed warm ($T \simeq 320\,\mathrm{K}$) dust in a 2.1 pc thick structure which is 3.4 pc in diameter, surrounding a smaller, hotter ($T > 800\,\mathrm{K}$) structure, confirming earlier constraints (Jaffe et al. 2004). It is likely that the dust and gas in the torus are not smoothly distributed but rather located in clumpy clouds (e.g. Elitzur & Shlosman 2006). This can explain the velocity dispersion observed in the centres of galaxies, which overestimates the temperature if the distribution would be of thermal origin, the different critical densities indicated by different emission lines and the long-term variability of the column density of certain AGN (Krolik & Begelman 1988, 1986).

4.3 Unified scheme

Antonucci (1993) introduced a simplified model to unite AGN, which assumed all AGN are in-

trinsically similar objects. In this model, AGN are divided into two basic types: a radio-quiet and radio-loud group. Sources in both groups can have a range of intrinsic luminosities, but all other properties, such as the observed spectral lines, result solely from orientation effects. The basic model for the radio-quiet sources assumes a broad-line region (BLR) and an optical featureless continuum which originates from the central source. This is surrounded by an obscuring torus and a narrow-line region (NLR), and a weak jet is present, perpendicular to the torus. If the source is observed face-on, emission lines from both the NLR and the BLR can be observed, and the source is classified as a Type 1. Objects which are observed edge-on will show only emission from the NLR since the BLR is obscured. These AGN are classified as Type 2 objects. In the case of a Type 2 source, reflected light can reveal the emission from the BLR near the nucleus. This has been shown for example using radio polarization observations, where the Type 2 source NGC 1068 showed a Type 1 core with broad emission lines in polarized light (Antonucci & Miller 1985). In case of radio-loud sources there are additional twin jets emitting relativistically boosted synchrotron radiation.

Urry & Padovani (1995) expanded on this model to unify the radio-loud sources, again assuming that the appearance of a source is strongly dependent on the orientation, which is based on the strong anisotropic radiation caused by beaming and obscuration by the dust torus. Figure 4.5 shows a diagram of this model. In this model, the radio galaxies are the parent population of the blazars, which have beamed emission with respect to the observer. FR-II radio galaxies appear as luminous quasars when the jet is close to the line of sight, and FRI type radio galaxies would be seen as BL Lac objects. This distinction is based on observational characteristics, such as radio and IR properties, host galaxies, and statistical properties from X-ray and radio surveys.

In a spectral energy distribution (SED), the frequency times flux ($\nu f(\nu)$) or the frequency times luminosity ($\nu L(\nu)$) is plotted versus the frequency ν (or wavelength λ or energy E), both on a logarithmic scale, enabling a broad view over decades in frequency and flux. The SED of a source is influenced by its beaming factor and jet presence. For example, Figure 4.6 shows the SED of the blazar Markarian 421, which has a redshift of $z = 0.031$ (Abdo et al. 2011). The emission from this source is dominated by non-thermal, Doppler-boosted jet emission, resulting in a typical double-humped shape. In Figure 4.7 the SED of a radio-quiet, non-beamed source is shown, of the Seyfert Type 1 galaxy Markarian 509 at $z = 0.034$ (Kaastra et al. 2011). Since the emission is not dominated by a relativistic jet, features from the central engine can be observed, such as the infrared emission from dust heated by the central engine and the thermal emission of the accretion disk.

About 10% of AGN show jets and it is not clear why some sources do exhibit significant jets and some do not. In order to distinguish between sources with significant jet emission, the term of *radio loudness* has been introduced. Radio loudness is commonly defined as the ratio between the radio flux at 5 GHz $F_{5\mathrm{GHz}}$ and the optical flux in the B-band F_{B}, where an object with $F_{5\mathrm{GHz}}/F_{\mathrm{B}} \geq 10$ is considered radio-loud (Kellermann et al. 1989). A connection to the SMBH spin was postulated as an explanation for jet presence, where fast rotating SMBH could drive a jet (see for example Wilson & Colbert 1995). Radio-loud sources are commonly found in elliptical host galaxies which show merger activity, whereas radio-quiet sources are found in less luminous spiral hosts (Smith et al. 1986). This might link recent ($t \leq 10^9\,\mathrm{yr}$) merger activity to radio-loudness. Here it is expected that after the two galaxies collide,

Figure 4.5: Schematic depiction of the AGN unified model (Urry & Padovani 1995, adapted). The upper half of the diagram shows the radio-loud case, the lower half the radio-quiet version. The small dots represent the broad-line region, the larger dots the narrow-line region. The torus, surrounding the central super-massive black hole and accretion disk, is shown in orange.

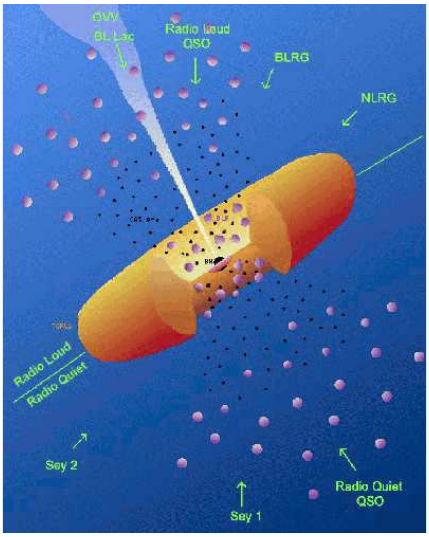

both the central SMBHs will coalesce on a time scale less than the Hubble time. Wilson & Colbert (1995) have shown that in the event of a merger, if both SMBH are of equal mass a high-spin SMBH can result. But King et al. (2013) showed by modeling the X-ray spectra of a sample of 37 Seyfert sources that a majority of these radio-quiet sources show a high spin.

A correlation was found by Laor (2000) between the mass of the SMBH and the radio-loudness. In a sample of 87 quasars, all sources with a SMBH mass of $M_{\mathrm{BH}} > 10^9\,\mathrm{M}_\odot$ are radio-loud, whereas all sources with a SMBH mass of $M_{\mathrm{BH}} < 3 \times 10^8$ are radio-quiet. This lead to the idea that the unification of AGN could be summed up in 3 parameters: inclination angle, SMBH mass, and Eddington ratio $L_{\mathrm{bol}}/L_{\mathrm{Edd}}$, which is a tracer of the mass accretion rate. Using a sample of 80 sources with known SMBH mass, Ho (2002) showed that the radio loudness-SMBH mass division as deduced by Laor (2000) did not hold, as radio-loud sources with SMBH masses in the range $\sim 10^6 - 10^9\,\mathrm{M}_\odot$ were found. In addition, the sample yielded an inverse correlation between the radio luminosity at 5 GHz and the Eddington ratio, which would indicate that the radio luminosity increases as the mass accretion rate decreases.

Other theories on why some sources are radio loud and can therefore be considered to host a strong jet include other characteristics of the AGN. For example, Sikora & Begelman (2013) argued that the magnetic flux threading the SMBH is most important to launch a jet, rather than the SMBH spin or the Eddington ratio. According to this theory a jet can be produced if enough flux can be accumulated to form a magnetically chocked accretion flow (see Narayan et al. 2003). This can be achieved by a hot accretion flow, followed by a massive cold accretion event, which can be caused by a merger event for example. Here, the hot accretion flow drags the magnetic flux in, which is compressed by the cold accretion flow, invoking a magnetically

Figure 4.6: SED of Markarian 421, a high-synchrotron peaked BL Lac object (Abdo et al. 2011). This SED has been modelled with three different one-zone synchrotron self-Compton models (see also Section 7.6.1 for these types of models).

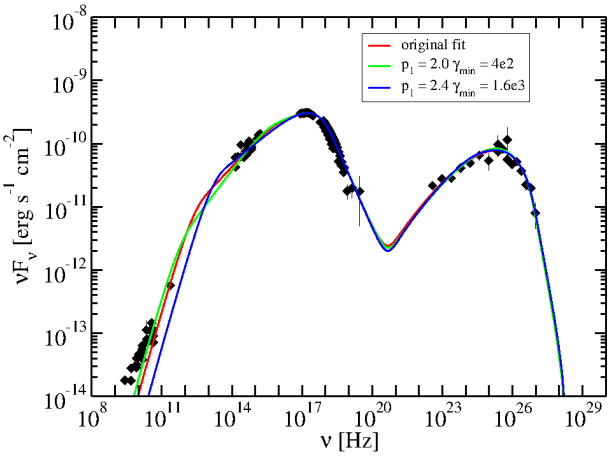

choked flow necessary to launch a jet.

4.3.1 The blazar sequence

The spectral energy distribution (SED) of blazars tends to have a typical shape, which can be seen for example in Figure 4.6. This particular double-hump structure is often explained using synchrotron self-Compton (SSC) of a population of electrons in the jet, where synchrotron emission forms the low-energy branch and inverse Compton (IC) emission accounts for the second feature (see Section 7.6.1 for a more extensive description of this mechanism).
Blazars can be subdivided into two groups, depending on the equivalent width (EW) of the emission lines in the optical band. Flat Spectrum Radio Quasars (FSRQ) have emission lines with an equivalent width EW$>$ 5Å, and BL Lac show emission lines that have EW$<$ 5Å. The BL Lac objects are then subdivided into three classes, based on the peak frequency of the synchrotron branch in the SED (Padovani & Giommi 1995a). The low-frequency peaked BL Lac objects (LBL) show a synchrotron peak frequency in infrared, the intermediate-frequency peaked (IBL) have a synchrotron peak in optical or UV, and the high-frequency peaked objects (HBL) display a synchrotron peak frequency in UV or soft X-rays (Padovani & Giommi 1995b; Bondi et al. 2001). This distinction was initially based on sources being either radio or X-ray selected, with the radio selected BL Lacs belonging to the LBL class and the X-ray selected ones to the HBL class. With advancing observational techniques and using surveys with different sensitivity, the distinction based on the peak frequency, and thus on the overall spectral energy distribution, appeared more physical, though. Apart from the difference in peak frequency, HBL and LBL tend to have different physical parameters, for example the HBL are on average less powerful, show a lower degree of polarisation and variability.

When studying the X-ray spectra of 114 FSRQ sources, Padovani et al. (1997) found a mean spectral energy index of $\alpha_x \sim 1$ in the 0.4–2.0 keV band. This spectral index is similar to the index of $\alpha_x \sim 1.1$ found for LBL sources in this band. The HBL sources show a spectral

Figure 4.7: The SED of Seyfert 1 object Markarian 509, based on simultaneous data from the infrared up to the hard X-ray domain (Kaastra et al. 2011). The data has been corrected for both Galactic and intrinsic absorption. A radio measurement at 30 GHz gives a flux level of only $\nu f_\nu = 4.6 \times 10^{-18}\,\mathrm{erg\,cm^{-2}\,s^{-1}\,Hz^{-1}}$, and is therefore not included in the SED.

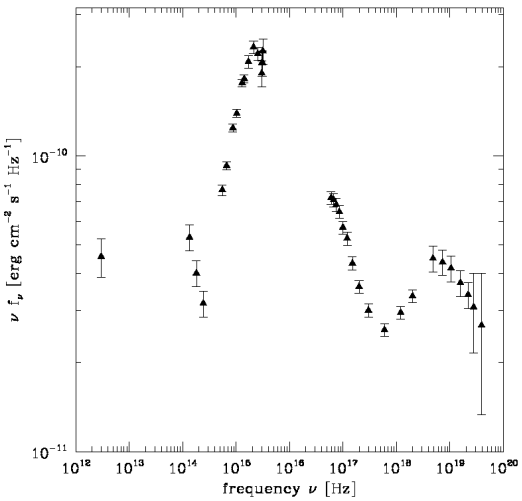

energy index closer to $\alpha_\mathrm{x} \sim 1.5$. The FSRQ also show a concave shape of the optical-to-X-ray continuum, implying that inverse Compton processes dominate the emission in the X-ray band. Similar results were found for LBL sources, whereas for HBL sources the X-ray band is part of the synchrotron branch.

Fossati et al. (1998) showed that a correlation exists between the luminosity of a source and the peak frequency of the synchrotron branch, using a sample of 126 blazars from different surveys. This blazar sequence can be seen in Figure 4.8 which shows average SEDs for FSRQ and the three BL Lac types. A correlation between the peak frequencies of both synchrotron and inverse Compton component was found as well, suggesting a similar origin of the emission for the different blazar classes. The ratio between the luminosities in the inverse Compton branch and the synchrotron branch (the Compton dominance), increases for more luminous sources, indicating the broad-band emission of these sources is more dominated by inverse Compton emission. An explanation for this behaviour is possibly the cooling of radiating electrons in the jet. The cooling depends on the jet power and the strength of the diffuse radiating field, such as the BLR, surrounding the jet (Ghisellini et al. 1998). A powerful jet will have a larger electron density compared to a weak jet, allowing efficient cooling of the electrons. The strong external radiation field is also contributes to the cooling of electrons. In BL Lac sources the emission lines originating from the BLR are either weak or absent, supporting the theory of a weaker external photon field in less luminous sources. Later work has shown that this theory does not hold for all individual sources but rather for large samples. For example, Padovani et al. (2002) showed a FSRQ where the emission in the X-ray band was due to synchrotron processes, rather than caused by the expected inverse Compton emission.

Figure 4.8: Average SEDs for different blazar types (Fossati et al. 1998). The most powerful sources are the Flat Spectrum Radio Quasars (FSRQ), which show a synchrotron peak at radio to infrared, and the peak of the inverse Compton branch in the X-ray to soft gamma-ray branch. The high-frequency peaked BL Lac objects (HBL) are the least powerful in this sequence and show a synchrotron peak in the X-ray band and a peak of the inverse Compton emission in the VHE domain.

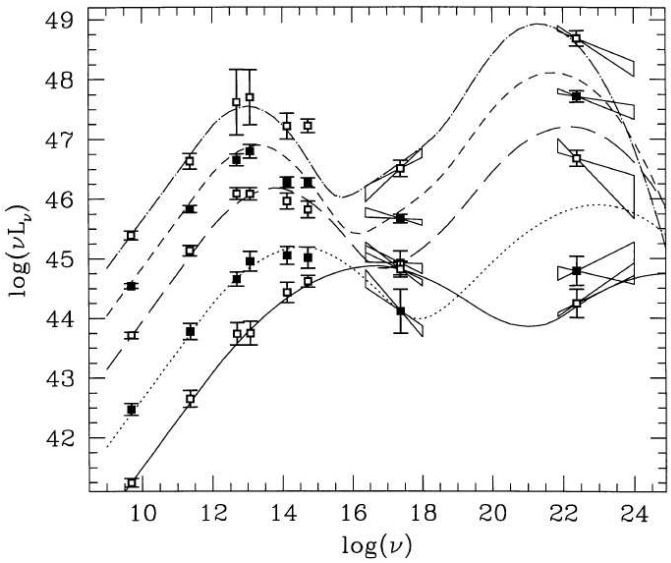

More recent theories to explain the blazar sequence connect the behaviour of different source classes to accretion rate, which is linked to the jet power, and the black hole mass, as it is proportional to the dissipation region of the jet (Ghisellini & Tavecchio 2008). In this scenario BL Lac objects tend to have central black holes of lower mass, and a lower accretion rate than FSRQ. Meyer et al. (2011) proposed a scenario which divides the blazar population into two categories based on jet power. Using a sample of 216 blazars and 41 radio galaxies, the peak frequency of the synchrotron branch and luminosity at the peak frequency were calculated. The resulting synchrotron peak luminosity versus peak frequency diagram can be found in Figure 4.9, which shows two different branches. The tracks A and B demonstrate the path of a source in progressive misalignment, for a powerful source (track A) and a weak source (track B). Weak sources, which includes most BL Lac objects and the FR-I radio galaxies, show a decelerating, low power jet which can be connected to radiatively inefficient accretion. The sources which display a strong jet, most FSRQ and FR-II radio galaxies, show radiatively efficient accretion.

Using Compton dominance, a quantity not altered by redshift, Finke (2013) found a correlation between Compton dominance and the synchrotron peak frequency for a sample with 886 blazars from the 2LAC catalogue. This sample does not show the two branches found by Meyer et al. (2011) in the plot of the synchrotron peak luminosity versus the peak frequency, as can be seen in the right panel of Figure 4.9. A simple model is constructed where the differences between blazar classes are introduced by the magnetic field of the emitting region,

Figure 4.9: Plot of synchrotron peak luminosities versus the peak frequencies showing results from different samples.

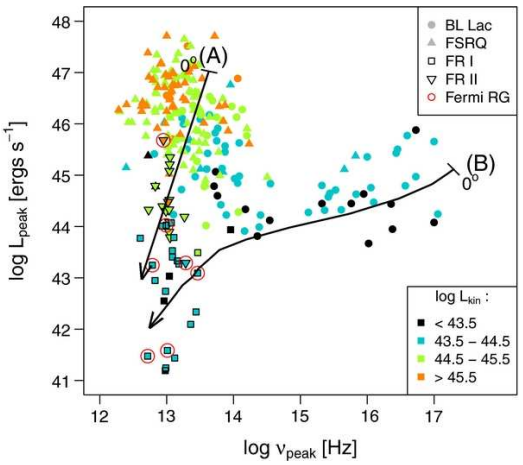

(a) Results found by Meyer et al. (2011) using 257 blazars.

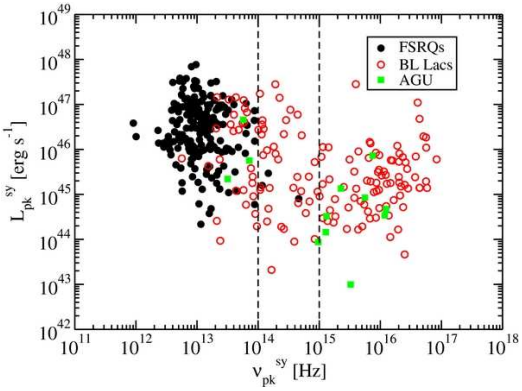

(b) Results found by Finke (2013), using a sample of 886 blazars.

the external radiation field density and the jet angle. The HBL with a low magnetic field and a weak external radiation field will show a synchrotron peak at a high frequency due to the lack of cooling either by synchrotron emission or Thomson scattering. If the magnetic field and external radiation field increase, cooling will play a more important role, decreasing the synchrotron peak frequency, and if the cooling increases to a certain level it will enter a fast- cooling regime for the FSRQ. In this scenario an external Compton component, using seed photons from a source outside the jet, is used, in addition to the SSC process. When only the SSC process is assumed, the Compton dominance is not dependent on the jet angle. However, if external Compton scattering is assumed, the Compton dominance becomes angle-dependent. This is particularly important for FSRQ, since a correlation between angle and Compton dominance was found, implying a necessity for an external Compton component in the SED. For BL Lac objects, the SSC process alone provides a good fit for the SED.

Zhang et al. (2013) postulated the jet launching mechanism to be different in the different blazar classes, based on SED fits. No statistical difference was found in the Doppler factors of the jet emission for either BL Lacs or FSRQ. It was found that the jet emission from FSRQ is dominated by the Poynting flux[2] and the jets have a high radiative efficiency. For FSRQ the jet power is proportional to the SMBH mass, and FSRQ jets are highly magnetized, which would indicate the jets are produced by the Blandford-Znajek mechanism, which relies on the black hole spin (see Blandford & Znajek 1977). The jets from BL Lac objects are rather dominated by particles and have lower radiation efficiency. For BL Lac objects there is an anti-correlation between the jet power and the SMBH mass, indicating a different launching mechanism, such as for example the Blandford-Payne mechanism (see Blandford & Payne 1982), where angular momentum is extracted from the accretion disk.

[2]It is assumed the jet power is carried by the bulk motion power of particles (relativistic electrons and cold protons), the Poynting flux (dominated by magnetic fields) and emitted radiation.

5 Radiative processes

In this Chapter several astrophysical radiative processes relevant to this work are described. More extensive discussions can be found in for example Rybicki & Lightman (1979) or Courvoisier (2013b).

5.1 Thomson and Compton scattering

Non-relativistic interaction between a charged particle and a photon, where the photon energy E is much smaller than the rest mass of the particle $E = h\nu \ll mc^2$, will cause coherent, elastic scattering, referred to as Thomson scattering. The differential cross-section $d\sigma$ for scattering $d\Omega$ is defined as:

$$\frac{d\sigma}{d\Omega} = \frac{e^4}{m^2c^4}\sin^2\Theta = r_0^2\sin^2\Theta \tag{5.1}$$

Here Θ is the scattering angle, and r_0 is the classical electron radius with $r_0 \equiv \frac{e^2}{mc^2}$. The total cross-section for Thomson scattering σ_T is found by integrating over solid angle:

$$\sigma_{\mathrm{T}} = \frac{8\pi}{3}r_0^2 \simeq 6.652 \times 10^{-25}\,\mathrm{cm}^2 \tag{5.2}$$

At higher photon energies the relativistic effects can no longer be ignored, and the photon will carry momentum. Therefore the scattering is no longer elastic and energy exchange is possible. The scattering process is now referred to as Compton scattering when the photon transfers energy to the electron. After the scattering, a photon with initial energy E_1 will have an energy of

$$E_2 = \frac{E_1}{1 + \frac{E_1}{mc^2}(1 - \cos\theta)} \tag{5.3}$$

Here θ is the angle between the photon's original path and the deviation.
With increasing photon energy the cross-section for the interaction to happen decreases, so the scattering process is less efficient at higher energies. At low energies, $\frac{h\nu}{mc^2} \ll 1$, the cross-section is the Thomson cross-section $\sigma = \sigma_{\mathrm{T}}$. For the extreme relativistic case, where $\frac{h\nu}{mc^2} \gg 1$, the Klein-Nishina formula which is derived from quantum electrodynamics is used:

$$\sigma \simeq \sigma_{\mathrm{T}}\frac{3}{8}\frac{mc^2}{h\nu}(\ln 2\frac{h\nu}{mc^2} + \frac{1}{2}) \tag{5.4}$$

5.1.1 Inverse Compton scattering

In the case of Inverse Compton scattering energy is transferred from a relativistic electron to a low-energy photon (see Figure 5.1 for a diagram). Therefore, since $h\nu \ll mc^2$, the Thomson

Figure 5.1: Diagram of the inverse Compton scattering process. The observers frame is K, the electron rest-frame is K'. (Image based on Figure 7.2 in Rybicki & Lightman 1979).

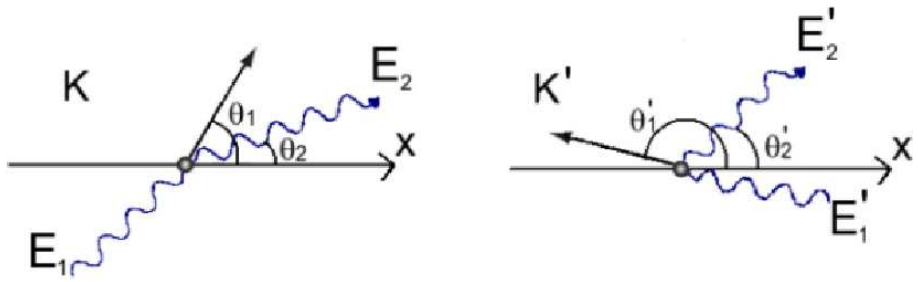

cross-section can be used. In the rest-frame K' of the relativistic electron, the energy of the photon $h\nu$ is transformed via Doppler shift formula to

$$h\nu' = \gamma h\nu(1 - \beta\cos\theta) \tag{5.5}$$

then θ is the angle between the direction of the photon and the electron, and the Lorentz factor $\gamma \equiv (1-\beta^2)^{-1/2}$ and $\beta \equiv v/c$. Since Thomson scattering is elastic, the energy in the electron rest-frame K' is elastic: $E'_1 = E'_2$. Transforming to the observer frame K this gives

$$E_2 \backsimeq \gamma^2 E_1 \tag{5.6}$$

The process is less effective for higher energy photons, as quantum effects reduce the cross-section. From conservation of energy, the maximum photon energy increase in the observer frame K is

$$E_2 \leq E_1 + \gamma mc^2 \tag{5.7}$$

.

Assuming an isotropic distribution of electrons and photons, where the photons have a density vdE_1 in the range dE_1. The total luminosity emitted in the electron rest-frame is then

$$\frac{d\epsilon'_2}{dt'} = c\sigma_{\rm T} \int E'_2 v' dE_1 \tag{5.8}$$

Assuming the energy change of the photon in the electron rest-frame compared to the energy change in the observer frame of $\gamma E_1 \gg mc^2$, gives $E'_2 = E'_1$. Then applying the Doppler shift formula, the emitted luminosity in the observer frame can be described as:

$$\frac{d\epsilon_2}{dt} = c\sigma_{\rm T}\gamma^2(1 + \frac{1}{3}\beta^2)U_{\rm ph} \tag{5.9}$$

The initial photon density $U_{\rm ph}$ is defined as $U_{\rm ph} \equiv \int E_1 v dE_1$. From here, the luminosity can be calculated using the radiated energy (assuming scattering takes place in Thomson regime):

$$L_{\rm IC} = \frac{dE_{\rm rad}}{dt} = \frac{4}{3}c\sigma_{\rm T}\gamma^2\beta^2 U_{\rm ph} \tag{5.10}$$

Figure 5.2: Electron spiralling around a magnetic field line. The emission is radiated in the direction of the electron velocity, in a beam with opening angle $\simeq \frac{1}{\gamma}$.

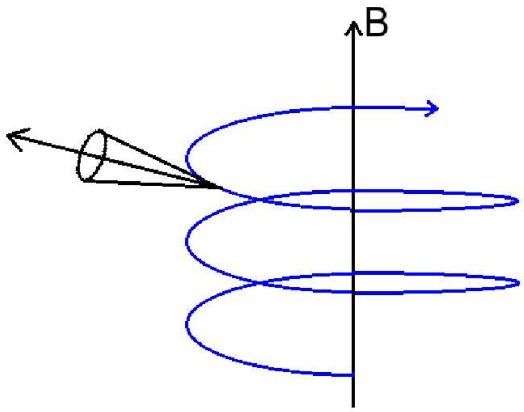

5.2 Synchrotron radiation

Synchrotron emission occurs when charged relativistic particles are accelerated by a magnetic field. For a particle with mass m and charge q moving through a magnetic field with strength $\mathbf{B}$ we can express the motion of the particle as

$$\frac{d}{dt}(\gamma m\mathbf{v}) = \frac{q}{c}\mathbf{v} \times \mathbf{B} \tag{5.11}$$

$$\frac{d}{dt}(\gamma mc^2) = q\mathbf{v} \cdot \mathbf{E} \tag{5.12}$$

where γ is the Lorentz factor of the particle. Equation 5.12 is equal to 0, and as such implies that $\gamma = 0$ and v are constant. We can separate v into two perpendicular components $v_\perp$ perpendicular to the field lines and $v_\parallel$, which is parallel to the field lines. Since $|v|$ is constant, and with $dv_\parallel/dt = 0$ due to the force being perpendicular to the magnetic field, $v_\parallel$ is constant, and so $v_\perp$ is also constant. This equates to a helical motion: a uniform motion in the direction of the magnetic field, and a uniform circular motion with a constant radius r_g and pitch angle α (angle between field and velocity). The gyroradius r_g is defined as:

$$r_\mathrm{g} = \frac{v_\perp \gamma mc}{qB} \tag{5.13}$$

The frequency of the rotation is dependent on the magnetic field, via:

$$\omega_\mathrm{B} = \frac{qB}{\gamma mc} \tag{5.14}$$

The acceleration is perpendicular to the velocity, with $a_\perp = \omega_\mathrm{B} v_\perp$. The total emitted radiation is then

$$L = \frac{2q^2}{3c^3}\gamma^4 \omega_\mathrm{B}^2 v_\perp^2 = \frac{2}{3} r_0^2 c v_\perp^2 \gamma^2 B^2 \tag{5.15}$$

If the velocity distribution is isotropic, it is necessary to average Eq. 5.15 over all pitch angles for a given velocity $v_\perp$:

$$< v_\perp^2 >= \frac{v^2}{4\pi} \int \sin^2 \alpha d\Omega = \frac{3v^2}{3} \tag{5.16}$$

which gives a synchrotron luminosity of

$$P = \frac{4}{3}\sigma_\mathrm{T} \frac{v^2}{c} \gamma^2 U_\mathrm{B} \tag{5.17}$$

Here, σ_T is the Thomson cross-section and U_B the magnetic energy density, defined as $U_\mathrm{B} = B^2/8\pi$.
The radiation is not emitted isotropically due to relativistic effects, but rather in a narrow cone with opening angle $\simeq \frac{1}{\gamma}$ in the direction of the velocity of the particle, see Figure 5.2. Therefore the emission can only be observed when the cone is pointed along the line of sight, such that the emission is pulsed. The width of the observed pulses is dependent on the Lorentz factor γ and the frequency of rotation ω_B with $\Delta t \approx (\gamma^3 \omega_\mathrm{B} \sin\alpha)^{-1}$ with α the pitch angle. The produced spectrum will cut off at a critical frequency ω_c, which is defined as

$$\omega_\mathrm{c} \equiv \frac{3}{2}\gamma^3 \omega_\mathrm{B} \sin\alpha \tag{5.18}$$

The time averaged luminosity per unit frequency derived from the Fourier transform of the electric field, and can be expressed as:

$$\frac{dW}{dt\, d\omega} \equiv L(\omega) = C_1 F\left(\frac{\omega}{\omega_\mathrm{c}}\right) \tag{5.19}$$

with F a dimensionless function and C_1 a constant which can be evaluated by integrating the luminosity per unit frequency:

$$L = \int_0^\infty L(\omega) d\omega = C_1 \int_0^\infty F\left(\frac{\omega}{\omega_\mathrm{c}}\right) d\omega = \omega_\mathrm{c} C_1 \int_0^\infty F(x) dx \tag{5.20}$$

Here x is defined as ω/ω_c. Since the luminosity L and the critical frequency ω_c are known (Eq. 5.15, Eq. 5.18), the luminosity per unit frequency in the highly relativistic case where $v/c \sim 1$ is:

$$L(\omega) = \frac{4}{9} \frac{q^3 B \sin\alpha}{mc^2} F\left(\frac{\omega}{\omega_\mathrm{c}}\right) \tag{5.21}$$

The synchrotron spectrum can then be approximated by a power law over a limited range of frequencies, with a spectral index s via

$$L(\omega) \propto \omega^{-s} \tag{5.22}$$

Assuming a population of electrons, with a number density $n(\gamma)d\gamma$ for particles with energies between γ and $\gamma + d\gamma$, the particle distribution as a function of energy can be described as

$$n(\gamma)d\gamma = C\gamma^{-p} d\gamma,\ \gamma_1 < \gamma < \gamma_2 \tag{5.23}$$

The parameter C is the normalisation of the power law. The total luminosity radiated per unit volume per unit frequency is then the integral over all energies γ of the number density times the single particle radiation formula (which only depends on γ via $\omega_\mathrm{c} \propto \gamma^2$, Eq. 5.21):

$$L_\mathrm{tot}(\omega) = C \int_{\gamma_1}^{\gamma_2} L(\omega) \gamma^{-p} d\gamma \propto \int_{\gamma_1}^{\gamma_2} F\left(\frac{\omega}{\omega_\mathrm{c}}\right) \gamma^{-p} d\gamma \tag{5.24}$$

Changing variables to $x = \omega/\omega_c$:

$$L_{\rm tot} \propto \omega^{-(p-1)/2} \int_{x_1}^{x_2} F(x) x^{(p-3)/2} dx \tag{5.25}$$

Assuming wide energy limits, such that $x_1 \to 0$ and $x_2 \to \infty$ leaves the integral approximately constant,

$$L_{\rm tot} \propto \omega^{-(p-1)/2} \tag{5.26}$$

This relates the spectral index s (Eq. 5.22) to the particle distribution index (Eq. 5.23) with

$$s = \frac{p-1}{2} \tag{5.27}$$

Using this relation, a measurement of the power law index of a synchrotron spectrum can be related directly to the slope of the underlying particle distribution.

5.2.1 Synchrotron self-absorption

The derivation for synchrotron emission in the previous chapter assumed that all emitted synchrotron photons will reach the observer. However, it is possible that the photons will be absorbed by the same population of electrons that emit the synchrotron radiation leading to a break in the spectrum. The absorption is most efficient near the turn-over frequency $\nu_{\rm SSA}$ where the transition from optically thick to optically thin takes place. At higher frequencies $\nu > \nu_{\rm SSA}$ the electron density has a power law index of $-p$, increasing the chance of escape for the produced photons. The observed intensity of the emission is proportional to the emission function (see Eq. 5.26)

$$I_\nu \propto \nu^{-(p-1)/2} \tag{5.28}$$

At frequencies below $\nu_{\rm SSA}$, the emitting material will be optically thick. The observed intensity is then proportional to the source function S_ν:

$$S_\nu = \frac{L(\nu)}{4\pi\alpha_\nu} \tag{5.29}$$

α_ν is the absorption coefficient which is dependent on ν via $\alpha_\nu \propto \nu^{(-p+4)/2}$ in this case (see for full derivation of the absorption coefficient Rybicki & Lightman 1979). So, in the optically thick case the observed intensity is related to the frequency via

$$I_\nu \propto \nu^{5/2} \tag{5.30}$$

Synchrotron self-absorption is important in bright sources with high electron densities or large magnetic fields, in most sources the turn-over frequency $\nu_{\rm SSA}$ is too low to be observed in most sources. Therefore, in case of the sources analysed in this work, which have low magnetic fields and low electron densities, synchrotron self-absorption will not play an important role.

5.2.2 Synchrotron self-Compton

The process where synchrotron photons are used as seed photons for inverse Compton scattering using the same electron population is called synchrotron self-Compton (SSC). The medium has to be optically thick for the photons can interacted with the electron population.

The luminosity of the inverse Compton scattering is dependent on the energy density of the initial photon field (Eq. 5.10). The synchrotron luminosity, which is the initial photon field in the case of SSC, depends on the energy density of the magnetic field (Eq. 5.17), so therefore the ratio of the SSC luminosity to the synchrotron this model luminosity is:

$$\frac{L_{\mathrm{SSC}}}{L_{\mathrm{Sy}}} = \frac{U_{\mathrm{rad}}}{U_{\mathrm{B}}} \tag{5.31}$$

The product of the inverse Compton process can contribute to the energy density of the photon field U_{rad}, as such contributing to another SSC process. Due to the synchrotron self-absorption the brightness temperature of the synchrotron process can not exceed T_{max}, which is $\sim 10^{12}\,\mathrm{K}$. If the brightness temperature T_{b} exceeds this threshold, the inverse Compton process will dominate the emission. Then, the luminosity ratio of the inverse Compton and synchrotron emission goes as $\frac{L_{\mathrm{IC}}}{L_{\mathrm{sy}}} \propto T_{\mathrm{b}}^{10}$, reducing greatly the synchrotron emission. This effect is known as the inverse Compton catastrophe. For the sources studied in this work, the brightness temperature is sufficiently low, so the catastrophe is avoided.
The broad-band emission of blazars is often modelled as SSC emitted by relativistic electrons located in a region in the jet which moves towards the observer, in Section 7.6.1 this process is described in more detail. Also for several gamma-ray bright radio galaxies such as those treated in this thesis, this model can be applied succesfully.

6 The High-Energy Domain

6.1 History

Even though X-ray emission (100 eV–100 keV) has first been detected in 1895 by Wilhelm Röntgen, X-ray astronomy only started in the 1960s. Due to the Earth's atmosphere being opaque to X-ray and gamma-ray emission, the emission can not be observed from the ground. In the early 1960s Giacconi et al. (1962) observed the first object outside the solar system in X-rays, the microquasar Scorpius X-1. This was done using a detector consisting of three Geiger counters on a sounding rocket. About a decade later dedicated X-ray satellites were launched, such as *Uhuru* (launched in 1970, Forman et al. 1978) and *SAS-3* (launched in 1975, Mayer 1975). These instruments detected many more X-ray sources, both Galactic and extra-galactic.

Through the years the sensitivity of the instruments improved, allowing for better localization of sources, for example by the use of grazing incidence mirrors[1]. The X-ray observatory *HEAO-2*, better known as the *Einstein Observatory*, launched in 1978, used this mirror technique. Some of the results are the detection of X-ray jets from Centaurus A and M87, and the detection of many Seyfert galaxies and blazars, allowing for population studies. *EXOSAT* (Taylor et al. 1981), an observatory with several instruments allowing observations between 0.1–50 keV, was launched in 1983. This satellite was one of the first to carry an on-board computer, such that data could be processed before transmitting. This also allowed for changes in the data handling programs in-flight. Due to its highly eccentric 90.6-hour orbit, uninterrupted observations were possible for 76 hours each orbit, which led to new insights in AGN X-ray variability (e.g. Barr et al. 1986) and the discovery of quasi-periodic oscillations in Galactic compact sources (e.g. Lewin et al. 1985).
The number of known X-ray sources expanded to more than 10^5 with the all-sky surveys (e.g. Voges et al. 1999) of the *ROSAT* observatory (Truemper 1982), which was launched in 1990. Detectors aboard *ROSAT* were sensitive in X-rays from 0.1–2.4 keV, and in the UV-band.
The X-ray band, around 10 keV, was studied intensely by *ASCA*, launched in 1993 and sensitive between 0.5–10 keV (Tanaka et al. 1994). It was the first X-ray mission to carry charge-coupled devices (CCDs), to study the detailed spectra of both Galactic and extra-galactic objects. A combination of imaging and spectroscopy allowed detailed studies of the iron K-α complex (see Section 7.2.1), which revealed asymmetrical broadening possibly due to a strong gravitational field (e.g. Nandra et al. 1997).

In 1999 two new satellites, *Chandra* and *XMM-Newton*, were launched. The *Chandra* observatory provides the highest spatial resolution in X-rays < 10 keV of 0.5 arcseconds, allowing for extremely detailed observations in this band (Weisskopf et al. 2000). In Section 6.2.4

[1] Due to the energies of X-ray photons, significant reflection can only be achieved by using several mirrors which each reflect the photons with a small, "grazing" angle.

more information about this satellite can be found. *XMM-Newton* also operates in X-rays $< 12\,\mathrm{keV}$, and has the largest collecting area to date, of $1500\,\mathrm{cm}^2$ at 2 keV, due to the 58 mirrors for each of the three detectors, allowing for detection and spectroscopy of faint sources (Jansen et al. 2001). The angular resolution for this telescope is 6 arcseconds and it provides a field of view of 30'.
In 1991 the *Compton Gamma-Ray Observatory* (*CGRO*) was launched, which carried several detectors sensitive between 20 keV and 30 GeV. In the case of hard X-ray detectors, it is often not possible to use grazing incidence mirrors, as focal lengths $> 10\,\mathrm{m}$ would be needed. The hard X-ray instrument OSSE on *CGRO* is a collimated instrument, which detected photons within an energy range of 50 keV to 10 MeV. Collimated instruments have limited imaging capabilities. Detectors such as *BeppoSAX*/PDS (launched 1996, Boella et al. 1997; Frontera et al. 1997) or *Suzaku*/PIN (Takahashi et al. 2007, see Section 6.2.2) are also collimated instruments. Instruments such as *INTEGRAL*/IBIS (Ubertini et al. 2003, see Secton 6.2.1) and *Swift*/BAT (see Section 6.2.3) use a coded-mask, which does allow for imaging but the coded-mask absorbs part of the flux, and the large field of view collects background as well, and as such the detectors are less sensitive than a telescope with focussing optics.
The new mission *NuSTAR* (launched 2012, Harrison et al. 2010) is a hard X-ray (5–80 keV, energy resolution FWHM of 0.9 keV at 60 keV) imager which uses a mirror with a focal length of 10 m, achieved by a mast which was extended after launch in orbit. *NuSTAR*, together with *XMM-Newton*, has measured the spin of the supermassive black hole in the galaxy NGC 1365, using the relativistically broadened iron K-α line (Risaliti et al. 2013). This was possible due to *NuSTAR*'s energy range which covers the hard X-ray band which constrains the continuum emission.
An upcoming high-energy mission is *Astro-H*, which is planned to be launched in 2014, and which will have detectors in the 0.3 to 600 keV range (Takahashi et al. 2010). This mission will have a high spectral resolution of $\Delta E \sim 7\,\mathrm{eV}$ between 0.3–12 keV. At 30 keV an effective area of $300\,\mathrm{cm}^2$ is expected and an angular resolution of 60–90 arcseconds, a major improvement compared to current hard X-ray detectors.

Observation of gamma-rays ($> 100\,\mathrm{keV}$) is more complex compared to X-ray detection. Gamma-ray photons are more rare than X-ray or lower energy photons. Due to their high energy, it is not possible to focus gamma-ray photons, even with grazing incidence mirrors. The existence of cosmic gamma-rays, due to for example Compton scattering, was postulated before the emission was detected (e.g. Feenberg & Primakoff 1948). The first gamma-ray detector, *Explorer-11* (Kraushaar et al. 1965), which operated $> 50\,\mathrm{MeV}$, was launched in 1961 and detected 22 gamma-rays and 22,000 cosmic ray events in the 7-month lifetime of the mission. The gamma-ray events seemed to have an asymmetrical distribution, and no significant clustering near the Galactic plane was observed. *OSO-3*, launched in 1967, was sensitive to emission at energies $E >$50 MeV (Kraushaar et al. 1972). This satellite observed solar flares, the diffuse X-ray background, a flare from the microquasar Scorpius X-1, and gamma-rays from the Galactic plane.
The *SAS-2* satellite, operating between 20–300 MeV, was launched in 1972 (e.g. Kniffen et al. 1973) and detected the neutron star Geminga. A few years later, in 1975, *COS-B* was launched, which was sensitive to gamma-rays with energies $E >$30 MeV (Bignami et al. 1975). *COS-B* made a point source catalogue, containing about 25 objects, and a full map of the Galactic plane. It also observed the first extragalactic source in gamma-rays, the blazar 3C 273 (Swanenburg et al. 1978). Both *SAS-2* and *COS-B* used a spark chamber to detect

the gamma-ray emission via pair-conversion.
In the late 1960s and early 1970s, the military *Vela* satellites from the US, built to detect gamma-ray emission from nuclear testing, observed the first gamma-ray bursts, though at that time the origins of the emission were unknown.
The *CGRO* observatory, launched in 1991 as mentioned above, carried also two gamma-ray instruments, COMPTEL (0.75–30 MeV, Schönfelder et al. 1984) and EGRET (20 MeV-30 GeV Nolan et al. 1992). The COMPTEL detector consists of two parts and works by Compton scattering. Incoming photons are scattered in the first detector, where energy is lost and transferred to electrons. Then the decreased photon energy is measured in the second detector, and the original energy can be inferred. Using COMPTEL a sky-map between 1–30 MeV was created, and performed a study of ^{26}Al, by the 1.81 MeV line.
EGRET, a pair-production detector, performed several sky surveys at $E >$100 MeV, discovering almost 300 new sources (e.g. Hartman et al. 1999). Due to the large positional error of $\sim 1°$, not all sources can be identified since several counterparts are present in the error circle.
The *Fermi* satellite was launched in 2008, carrying its main instrument, the Large Area Telescope (LAT), which operates between 30 MeV to 300 GeV (see Section 6.7). The LAT has a better sensitivity and angular resolution compared to EGRET, and in survey mode many more sources have been detected: the first catalogue contained 1451 sources (Abdo et al. 2010g). *Fermi* also discovered e.g. two large gamma-ray emitting bubbles around the Milky Way (Su et al. 2010), several new milli-second pulsars (Abdo et al. 2010b) and the first pulsar which only emits pulses in gamma-rays (Abdo et al. 2008).

6.2 Instruments

In this section the instruments used in this thesis will be described in more detail.

6.2.1 INTEGRAL

The INTErnational Gamma-Ray Astrophysics Laboratory (INTEGRAL, Winkler et al. 2003) was launched 17th of October 2002 into an eccentric orbit with a period of 72 hours. The eccentric orbit guarantees a stable background environment while the satellite moves outside the Earth's van Allen radiation belts, allowing $\sim 90\%$ of the revolution to be used for scientific operations.
INTEGRAL carries several detectors: the Imager-on-board of the Integral Satellite (IBIS, 15 keV to 10 MeV, Ubertini et al. 2003), the Spectrometer for Integral (SPI, 20 keV to 8 MeV, Vedrenne et al. 2003), the Joint European Monitor in X-rays (JEM-X, 3–35 keV, Lund et al. 2003), and the Optical Monitoring Camera (OMC, V-band 500–600 nm, Mas-Hesse et al. 2003). In the next few sections the instruments used in this work will be discussed in more detail.

The *INTEGRAL* mission uses a coded mask to image the hard X-ray and soft gamma-ray sky. The advantages of the coded-mask technique is a much larger field of view compared to grazing incidence detectors, such as XMM-Newton. It is also easier to observe high-energy photons using a coded-mask, since the mirrors for high-energy photons have focal lengths of > 10 m, and mirrors become transparent above $\sim$MeV energies. In addition there is no need for additional background observations as both background and source are simultaneously

Figure 6.1: The *INTEGRAL* satellite, artist representation (ESA).

observed (Caroli et al. 1987). On the other hand, the angular resolution for coded-mask detectors is less good compared to grazing-incidence detectors, and due to absorption of photons by the mask, coded-mask instruments are less sensitive as focussing detectors. The angular resolution depends only on the size of the mask elements H and the distance between the mask and the detector L, via

$$\theta = \arctan\left(\frac{H}{L}\right) \tag{6.1}$$

Another drawback of using a coded mask is the complicated reconstruction of the sky, where complete knowledge of the mask and background are necessary. All sources in the field cast a shadow of the mask on the detector, which is called the shadowgram (see Figure 6.2). The sky image S can be reconstructed from the shadowgram image D via

$$D = S \times A + B \tag{6.2}$$

Here A is the known coded mask geometry and B the additional background which is not influenced by the mask. Noise can be introduced by the imperfections of the detector, such as the internal background of the instrument, and deformation and tilting of the mask with respect to the detector. Also, the the screws, and glue deposits between the coded mask elements and the supporting structure need to be taken into account in the deconvolution.

IBIS

The imager IBIS consists of two detectors. For lower energies there is ISGRI, the INTEGRAL Soft Gamma-Ray Imager which operates between 15-22 keV (evolution with time) to 1 MeV, is an 128x128 pixel array made of cadmium telluride crystals, arranged in eight independent modules (Lebrun et al. 2003). PICsIT, the Pixellated Imaging Caesium Iodide Telescope, works at higher energies and is sensitive between 200 keV to 10 MeV, this detector uses 64x64 thallium activated caesium iodide scintillator crystals (Labanti et al. 2003).
IBIS uses a tungsten coded mask to reconstruct the sky image, see Figure 6.3, left. The mask consists of transparent and opaque elements, with a size of 94x94 elements where each element is 11.2x11.2 mm. The sources in the field of view illuminate the mask, and project a shadow on the detectors. The detectors are surrounded by an active bismuth germanium oxide (BGO) scintillator, to shield the detectors from photons coming in from other directions.
The field of view is 9° x9° (fully-coded[2]) with an angular resolution of ∼12 arcmin.

[2]The region of the sky for which the source modulated by the mask totally illuminates the detector plane (Caroli et al. 1987).

Figure 6.2: This diagram shows the imaging of two sources, red and blue, using a coded mask. Image from ISDC/Marc Türler.

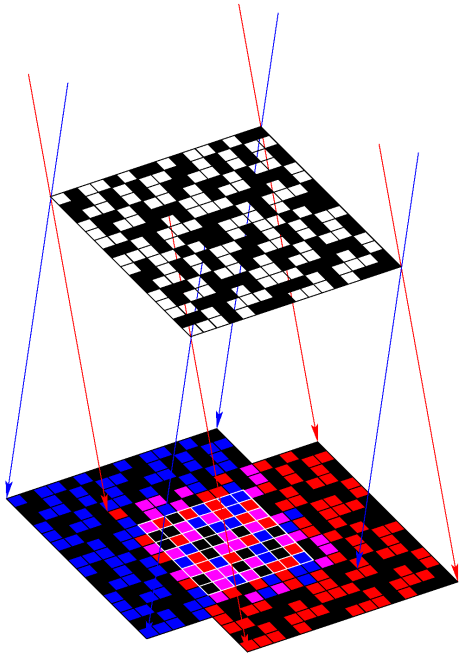

Figure 6.3: Coded masks of the *INTEGRAL* mission: IBIS and JEM-X (images from ISDC).

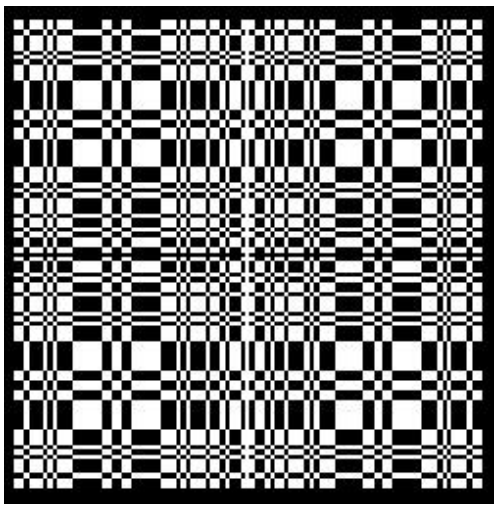

(a) The tungsten coded mask of IBIS with the transparent elements in white and the opaque elements in black. Half of the elements are opaque. The size of the mask is about 1.1 m by 1.1 m.

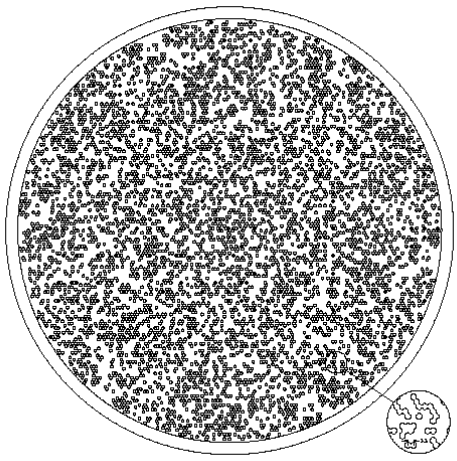

(b) JEM-X coded mask where the pattern is composed out of 22,501 elements and which is open for 25%. The mask diameter is 535 mm.

JEM-X

The X-ray monitor JEM-X consists of two aligned identical Microstrip Gas Chambers with a sensitive area of $500\,\mathrm{cm}^2$, filled with a xenon (90%)-methane(10%) mixture at 1.5 bar pressure. JEM-X uses the coded mask technology as well, see Figure 6.3 on the right, the mask is cut into a 0.5mm thick tungsten plate, with an opening fraction of 25%. The low open area increases the sensitivity, particularly in fields with many sources, or for the study weak sources in a field with strong sources. Both detectors have an identical mask that is inverted with respect to each other to minimize common side lobes in the image. The field of view is circular with a diameter of 4.8°(fully coded), and the angular resolution 3.25'.
After launch it became clear that anodes of the JEM-X detectors were eroded, possibly due to cosmic-rays which can initiate short-circuits at the root of the strips, with a rate of one strip a day, for 256 detectors, in JEM-X2. To reduce this damage, the gain of both detectors was reduced, and to increase the lifetime of the instrument, usually only one JEM-X detector is operating at a time.

6.2.2 Suzaku

The X-ray satellite *Suzaku* has been launched in 2005 July 10 (Mitsuda et al. 2007) as *ASTRO-EII*, see Figure 6.4. The mission was a replacement of the *ASTRO-E* mission which was lost due to failure at launch 5 years prior. The spacecraft has a near-circular, 96-minute, orbit with an inclination of 31 degrees.
Suzaku contains three different detectors; the X-Ray Imaging Spectrometer (XIS, ∼0.2–12 keV), a Hard X-ray Detector (HXD, ∼10 keV – 600 keV) and a X-Ray Spectrometer (XRS). The last instrument, a high-resolution spectrometer ($\Delta E \sim 7\,\mathrm{eV}$ achieved in orbit), was the primary instrument on *Suzaku*. After three weeks of observations, the cooling system failed and the liquid helium was lost a few weeks after the launch, rendering the instrument unable to perform. In addition there are five grazing incidence X-ray telescopes, of which four are used for XIS and 1 for XRS, which is no longer in use.

HXD

The HXD is a collimated instrument, sensitive between ∼10 keV and 600 keV (Takahashi et al. 2007). The detectors are placed in a 4x4 grid, and each unit consists of two detectors, PIN diodes and a GSO phoswich counter. At low energies, 10–70 keV, silicon PIN diodes are most effective, with an energy resolution of $\sim 4\,\mathrm{keV}$ (FWHM). At high energies, 40–600 keV, Gadolinium Silicate crystal (GSO) scintillators, placed behind the PIN diodes, are more effective. The energy resolution of the GSO is $7.6/\sqrt{E_{\mathrm{MeV}}}\%$ (FWHM). The detectors are surrounded by 20 crystal scintillators for active shielding.
The effective area for the HXD is $\sim 160\,\mathrm{cm}^2$ at 20 keV, and $\sim 260\,\mathrm{cm}^2$ at 100 keV. The field of view is for the PIN is collimated by the passive fine collimator into 34x34 arcmin squares, similar to the GSO below 100 keV. Above 100 keV, the collimator is transparent, and the field of view is 4.5°x4.5°.

XIS

The XIS instrument consists of four charge-coupled devices (CCD) detectors, three, XIS0,2 and 3, are front-illuminated (FI) and the last, XIS-1, is back-illuminated (BI) (Koyama et al.

Figure 6.4: Schematic overview of the *Suzaku* satellite, on top are the XRTs (Uchiyama et al. 2008).

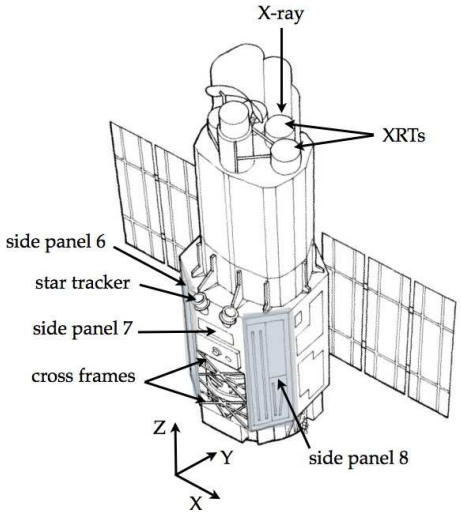

2007). A third FI, the XIS2 unit, was lost 9th November 2006, due to catastrophic damage, possibly due to a micro-meteorite, and the data taken by this detector after the incident can not be used.
Each XIS has an optical blocking filter, made from polyimide coated with aluminium on both sides, in front of it, to reduce contamination by optical and UV light. To reduce thermal noise, the sensors are kept at ∼-90°C during observations.
The FI detectors are less sensitive than the BI detector to the softest X-rays, due to inactive volume of the Si and SiO_2 grid at the front side of the CCD. The energy resolution is ∼ 130 eV at 6 keV. The CCD for each XIS has 1024x1024 pixels. For the FI detectors, the effective area is 340 cm^2, and for the BI the effective area is 390 cm^2. The XIS field of view is 17.8'x17.8'.

6.2.3 Swift

The *Swift* Gamma-ray Burst Mission was designed as a multi-wavelength observatory for gamma-ray burst science (Gehrels et al. 2004). *Swift* was launched at 20 November 2004 into a low Earth orbit (altitude 600 km), with an inclination of ∼ 20° and an orbital period of 90 minutes. The observatory, see Figure 6.5, is equipped with three detectors: the Burst Alert Telescope (BAT), the X-ray Telescope (XRT) and an Ultra-violet and Optical Telescope (UVOT). *Swift* scans the sky continuously, and it can quickly, and autonomously, slew to the direction of a possible gamma-ray burst using momentum wheels.

BAT

The BAT instrument (Barthelmy et al. 2005) is a coded-mask instrument similar to *INTEGRAL*. The mask is composed of ∼54000 lead elements with a size of 5x5x1mm placed in a random 50% open-50% closed pattern. The detector has a large field of view of 1.4 sr (half-coded), monitoring the sky for gamma-ray bursts and repointing to the position of a burst as it is observed with a precision of 1–4' within 20 seconds. The energy range for imaging is

Figure 6.5: A diagram of the *Swift* satellite. On top, the D-shaped coded mask of BAT is visible (image from UK Swift Science Data Centre).

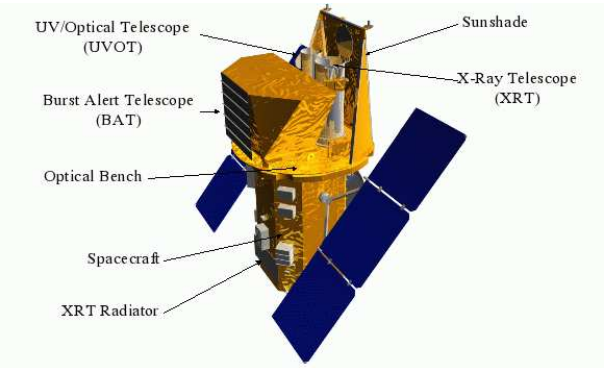

14–195 keV, with a non-coded response up to 500 keV, since the mask is transparent above 195 keV. In addition to gamma-ray burst detection and localization, BAT is also used for hard X-ray surveys, accumulating sky images every 5 minutes. For example, the 70-month hard X-ray survey contains over 1100 sources, of which more than 500 are AGN (Baumgartner et al. 2013).

XRT

The XRT (Burrows et al. 2005) has a smaller field of view, of 23 arcmin, and a resolution of 18" (half-power diameter). After the satellite has slewed in the direction of a possible burst, the XRT can localize the burst location to 5" accuracy, within 100 seconds after the burst start. XRT is sensitive between 0.2–10 keV, with a resolution of $\sim 140\,\mathrm{eV}$ at 6 keV (at launch). This instruments utilizes a grazing incidence mirror to focus the X-rays onto a CCD, rather than a coded-mask. XRT provides light curves and spectra of the late prompt emission and afterglow. XRT is also used to observe other astrophysical phenomena, for example, it has also observed the X-ray flash from the shock break-out from a supernova.

UVOT

Co-aligned with the XRT is the UVOT (Roming et al. 2005), which observes the optical prompt emission and afterglow of the gamma-ray bursts. The emission is focussed onto a CCD with modified Ritchey-Chrétien optics (a system with a hyperbolic primary and secondary mirror), using a 30 cm primary and 7.2 cm secondary mirror. The detector is sensitive between 170—650 nm, and the field of view of the UVOT is 17" by 17", with a point-spread function of 0.9" (FWHM) at 350 nm.

6.2.4 Chandra

The *Chandra* X-ray observatory, originally AXAF (for Advanced X-ray Astrophysics Facility, Weisskopf et al. 1996), is an X-ray imager which provides a high spatial resolution of 0.5 arcsec, a large improvement compared to previous instruments. *Chandra* was launched on 23 July 1999 in an elliptical high-earth orbit (perigee 16 000 km, apogee 133 000 km) with an

Figure 6.6: *Chandra* satellite overview (credit: NASA).

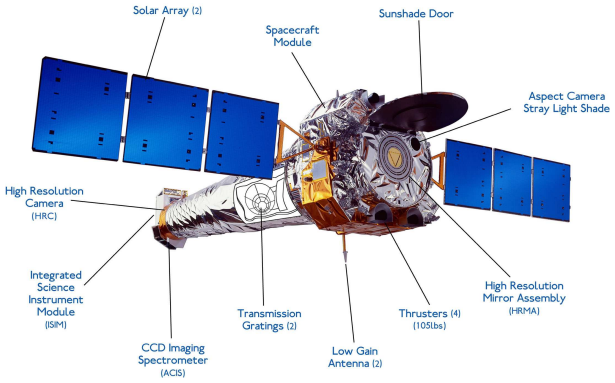

inclination of $\sim 28.5°$, and an orbital period of 64 hours. The highly elliptical orbit allows a high observation efficiency, of >70%, since the fraction of time in the van Allen radiation belts is small, and the fraction of the sky occulted by the Earth is also low (Weisskopf et al. 2000). The observatory, see Figure 6.2.4, contains two instruments, the Advanced CCD Imaging Spectrometer (ACIS, 0.2–10 keV) and the High Resolution Camera (HRC, 0.1–10 keV). HRC consists of two detectors, one for imaging and one for spectroscopy(e.g. Murray et al. 2000). HRC is not used in this work. *Chandra* also contains two transmission gratings, one for low (LETGS, 0.07–10 keV) and one for high energy (HETGS, 0.4–10 keV), which can be placed behind the mirror and work with either HRC or ACIS.

ACIS

ACIS (e.g. Plucinsky et al. 2003) is composed of two arrays of CCDs, with 1026 rows and 1024 columns of pixels, which operate simultaneously. For ACIS-I the array consists of four CCDs placed in a square, which gives the largest field of view and is optimal for imaging. ACIS-S is optimized for spectroscopy and consists of a linear array of six CCDs. The spatial resolution of the CCDs is limited by the pixel size, which are 24 μm square with no spacing between the pixels. Since these CCDs are also sensitive to UV and optical photons, polyimide/aluminum meshless films are placed above the CCD to block these unwanted signals.

6.2.5 Fermi

The *Fermi* Gamma-ray Space telescope, formerly known as Gamma-ray Large Area Space Telescope or GLAST, was launched 11th of June 2008 into a circular low Earth orbit (565 km altitude, inclination $\sim 25.6°$) with an orbital period of ∼95 minutes. The observatory contains two instruments: the Large Area Telescope, LAT (Atwood et al. 2009), and the Gamma-ray Burst Monitor, GBM (Meegan et al. 2009). The GBM consists of two sets of detectors sensitive between ∼8 keV to ∼40 MeV, and has a large field of view of almost the entire sky. GBM data are not used in the work presented here.

Figure 6.7: Artist representation of the *Fermi* satellite (Credit: NASA E/PO, Sonoma State University, Aurore Simonnet).

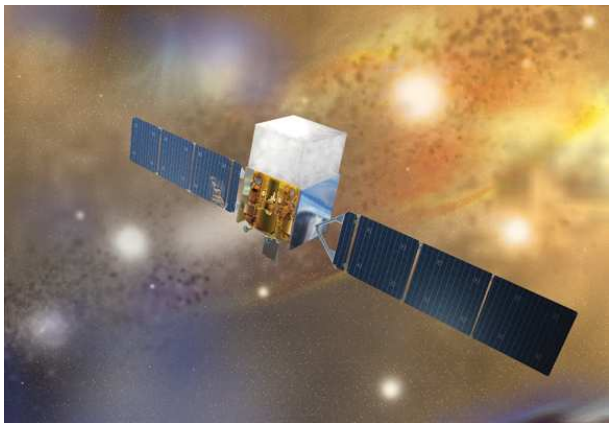

LAT

The primary instrument aboard the *Fermi* satellite is the Large Area Telescope (LAT), which has an energy range of 20 MeV to >300 GeV and is used to survey the sky (field of view 2.4 steradians, ∼20% of the sky). Since high energy gamma-rays cannot be reflected or refracted, the LAT detects electron-positron pairs produced by incoming photons. LAT contains a 4x4 array of identical modules, each consisting of a tracker, calorimeter and data acquisition module. In the tracker photons hit thin metal sheets, 16 in total, and are converted to electron-positron pairs. The tracks of the charged particles are measured to reconstruct the directions of the incoming gamma-ray photon. After the tracker the particles enter a caesium iodide calorimeter, which estimates the energy of the gamma-ray photon by measuring the energy deposition of the electromagnetic particle shower that results from the electron-positron pair. The calorimeter also images the shower development profile, which can be used to estimate shower leakage fluctuations and also to reject cosmic rays. The data acquisition module then distinguishes between gamma-rays signals and cosmic rays, and transmits the information to the ground segment. Surrounding the modules is an anti-coincidence detector consisting of plastic tiles, which rejects charged-particles, such as cosmic rays.

7 3C 111: An FR-II source with a hybrid BL Lac core

In this chapter I will describe the work performed on the radio galaxy 3C 111. This FR-II source has been included in the first *Fermi*/LAT catalogue. Preliminary results of this work have been presented as a poster at the *X-ray Universe 2011*, and also at the *INTEGRAL* conference *The Extreme and Variable High Energy Sky* in Chia Laguna in 2011, and subsequently have been published in the conference proceedings (de Jong et al. 2011). This work was published July 31, 2012 in Astronomy & Astrophysics (de Jong et al. 2012b). A copy of the published paper can be found at the end of this chapter on page 79.

7.1 Introduction

We have initiated this study on 3C 111 because it is one of the few gamma-ray bright radio galaxies, and of those sources, it is one of the few with an FR-II type morphology. In Table 3.1 all gamma-ray detected radio galaxies included in the first *Fermi*/LAT catalogue are listed. The scientific motivation for this study is to determine what physical processes are responsible for the high-energy emission, i.e. whether the broad-band emission in the X- and γ-ray domain is dominated by thermal processes from the core, similar to the situation in Seyfert type AGN, or by non-thermal processes from the jet, like blazars. For the latter the observer looks directly into the jet, which has an angle $\theta < 10^\circ$ to the line of sight, and any emission from the core is swamped by the boosted emission from the relativistic jet. In the case of radio galaxies, the angle of the jet to the line of sight is $\theta > 10^\circ$, and one does not look directly down into the jet, so both core and jet emission can be observed. The gamma-ray emission in blazars due to the relativistic beaming in the jet is easily explained. For radio galaxies the origin of the gamma-ray emission is not yet understood.

To further our understanding of the gamma-ray emission in radio galaxies, we study the X-ray spectrum and the broad-band emission of 3C 111. The X-ray spectra for Seyfert galaxies and blazars are different, so by analysing the X-ray data for the radio galaxy 3C 111 we can determine whether the emission in this band arises rather from a Seyfert galaxy, or from a blazar. The results of this analysis are presented in Section 7.5.

The difference between blazars and Seyferts can also be seen in the spectral energy distribution (SED), see for example Figures 4.7 and 4.6. Therefore, in order to understand the physical processes responsible for the broad-band emission, we also made an SED for 3C 111 and applied physical models to it, as can be seen in Section 7.6.

Figure 7.1: Radio image of 3C 111 at 1.4 GHz, observed with the VLA in June 1982 (Linfield & Perley 1984). The core is visible in the centre with the jet extending to the upper left corner.

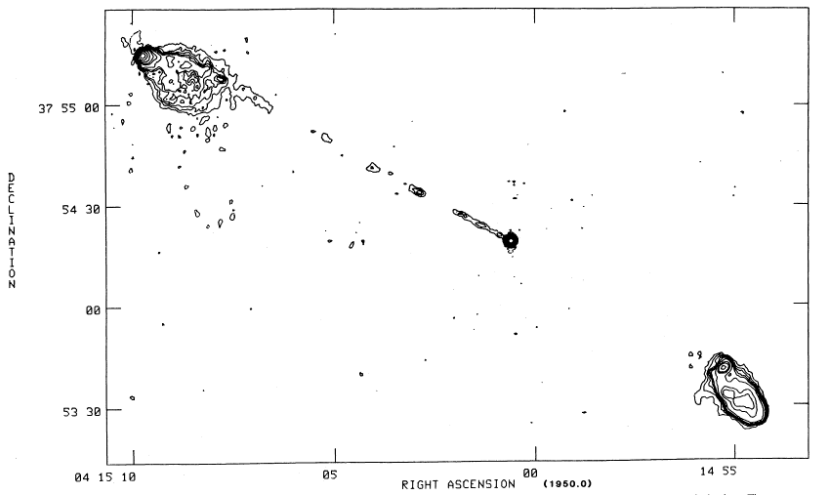

7.2 About the source

3C 111 is a nearby (z=0.049, Sargent 1977) radio galaxy with a FR-II morphology (FR for Fanaroff-Riley), meaning that the radio image is lobe dominated, i.e. the termination shocks of the jet are brighter than the core and the confined jet itself (Fanaroff & Riley 1974; Linfield & Perley 1984). In Figure 7.1 the radio map of 3C 111 is shown, with the core of the galaxy in the middle. The jet, which has a projected size of 78 kpc (Bridle & Perley 1984) and an angle to the line of sight of $\theta = 18°$ (Jorstad et al. 2005), can be seen extending to the upper left corner of the image. There is no visible counter jet, but a bright lobe is detected in the opposite direction of the detected jet, which is likely fed by the undetected counter jet, see the lower right corner of Figure 7.1.

The jet dominates the emission in the radio domain by synchrotron processes. In the optical domain 3C 111 shows strong broad emission lines, typical for Seyfert I-type galaxies (Sargent 1977). Also the X-rays, 3C 111 shows Seyfert properties by displaying a redshifted iron K-α line at 6.1 keV (Lewis et al. 2005).

7.2.1 X-ray features

It is interesting to study the core of radio galaxies in the X-ray band, since there is a difference between the spectra of Seyfert galaxies, which show many thermal components, and blazars, which do not. A beamed source like a blazar will only show a spectrum which follows a power law, since only the jet emission will be contributing to the X-ray spectrum. For non-beamed sources, different features originating close to the black hole can be observed. A schematic representation can be found in Figure 7.2. The accretion disk around the black hole produces a thermal spectrum which can be observed in the optical/UV domain. The photons emitted by the disk can then be up-scattered to X-rays by relativistic electrons, which might be

Figure 7.2: Schematic diagram of a Type 1, non-beamed AGN (Beckmann & Shrader 2012). The soft excess is present in some radio-quiet sources. (See section 4.3 for the distinction between type 1 and type 2 AGN).

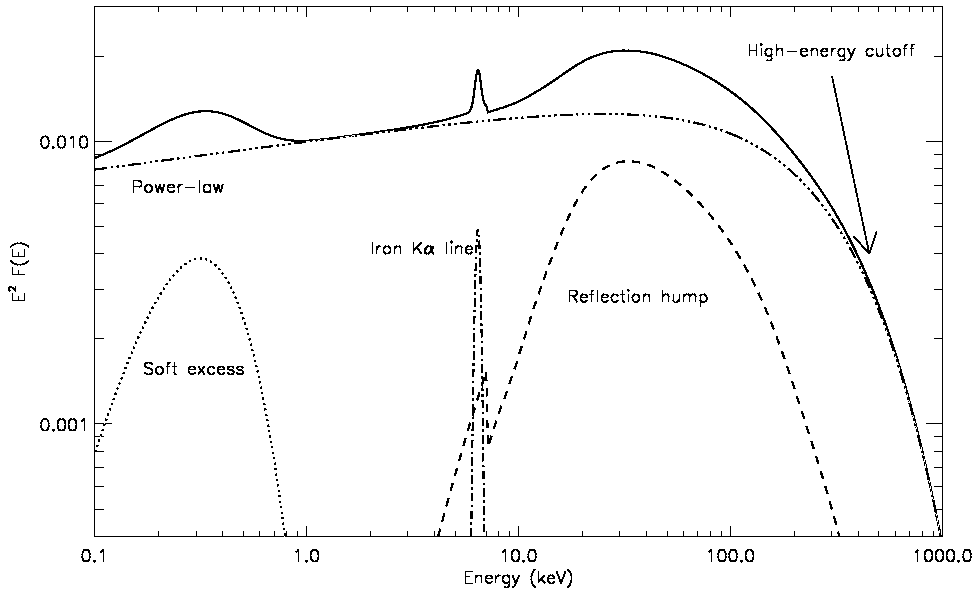

present in a corona above the disk through inverse Compton processes (see Section 5.1)). Since the disk temperature and the relativistic electron energy distribution are limited, the resulting inverse Compton spectrum shows a power law shape and a high-energy cut-off. In addition the emission is re-processed due to absorption, which leads to a reflection hump with a peak at maximum reflection efficiency (around 30 keV, depending on geometry, Beckmann & Shrader 2012; Ishibashi & Courvoisier 2010). In more luminous sources the amount of reflection is weaker (Ishibashi & Courvoisier 2010). This is thought to be due to luminous AGN expelling the reflecting material due to radiative pressure.

At $E = 6.4\,\mathrm{keV}$, the Fe-Kα fluorescence line can be observed in many AGN with a 2–10 keV luminosity $L_X \lesssim 10^{45}\,\mathrm{erg\,s^{-1}}$. The iron line is thought to arise from cool material close to the central engine and is connected to reflection. The hot corona above the accretion disk irradiates the outer disk (or some other cold gas). In this cooler medium the X-ray photons can be absorbed, followed by fluorescent line emission, or absorbed followed by Auger de-excitation which destroys the photon, scatters it out of the disk or reprocesses it into a fluorescence line photon which escapes (Fabian et al. 2000). Other iron fluorescent lines, such as the iron K-β line at 7.06 keV, can be observed nearby the K-α line, but in general these other lines are much weaker. In some objects, broadening of the iron K-α line is observed, which can occur due to relativistic effects or turbulence in the disk (Pariev & Bromley 1998). Iwasawa & Taniguchi (1993) found an anti-correlation between the strength of the iron line and the 2–10 keV luminosity, which is also called the *X-ray Baldwin effect*, after the anti-correlation between the UV continuum luminosity and the strength of the C IV λ1550 line (Baldwin 1977). This might have an explanation similar to the anti-correlation between reflection and

luminosity, where a more active core might blow the nearby matter away via radiation pressure or thermal dissipation. Also, in a more active AGN, the matter might be ionized to a higher degree, so there is less low-ionized material to produce the iron line (Shu et al. 2010).

3C 111 has been observed by several X-ray instruments, and the iron K-α fluorescence line is visible at 6.1 keV (the line energy is slightly changed due to the redshift of 3C 111, via $\lambda_{\rm obs} = (1+z)\,\lambda_{\rm em}$, see also Section 7.5.1). The equivalent width (EW) of this line has been measured several times and might be variable. *BeppoSAX* shows an $EW < 72\,$eV (Dadina 2007). Using *Suzaku*/XIS, Tombesi et al. (2010) found an $EW = 86 \pm 16\,$eV , and Ballo et al. (2011) report a similar value of $EW = 75 \pm 13\,$eV using both *Suzaku*/XIS and PIN. Observations taken two years later with *Suzaku*/XIS show a smaller equivalent width with measurements $EW = 40 \pm 7\,$eV, $EW = 33 \pm 6\,$eV, and $EW = 38 \pm 10\,$eV for each data set, respectively (Tombesi et al. 2011). *XMM-Newton* observations between 0.4–10 keV also show a lower value of the equivalent width of $EW = 38^{+11}_{-9}\,$eV (Ballo et al. 2011).
In addition to the iron line, 3C 111 also shows a high-energy cut-off in the X-ray spectrum. Previous studies have have shown a cut-off energy of 146^{+224}_{-68} keV using *BeppoSAX* data (Grandi et al. 2006) and $E_{\rm cut} = 126^{+193}_{-50}\,$keV using data from *XMM-Newton*, *INTEGRAL* and *Swift* (Molina et al. 2009). Lower limits to the cut-off have been derived too, of $E_{\rm cut} \geq 82\,$keV using *BeppoSAX* (Dadina 2007) and a lower limit of $E_{\rm cut} \geq 75\,$keV using *XMM-Newton* and *Suzaku*/XIS and PIN (Ballo et al. 2011).
Some observations seem to suggest that a reflection component is visible in the X-ray spectrum. The reflection is expressed with the relative reflection scaling factor R, the solid angle of the cold reflecting material visible from the Comptonizing source, in units of 2π. A reflection scaling factor between $0 < R < 1$ can be understood as an isotropic source above a disk, whereas a reflection scaling factor $R = 0$ implies no reflection, and a reflection of $R = 1$ the reflected component is as strong as the direct component. Upper limits have been reported of $R \leq 2.25$ (Dadina 2007), but also of $R < 0.3$ (Grandi et al. 2006), both using *BeppoSAX* data. Constraints on the reflection of $R = 0.19^{+0.05}_{-0.04}$ with *XMM-Newton*, $R = 0.35 \pm 0.06$ using *Suzaku*/XIS and PIN (Ballo et al. 2011) and $R = 0.9 \pm 0.6$ using data from *XMM-Newton*, *INTEGRAL* and *Swift* (Molina et al. 2009) have been reported. Rivers et al. (2011) show no detection of reflection between 3 keV and $\gtrsim$ 100 keV, using data from *RXTE*.

7.2.2 Gamma-ray detections

3C 111 has been detected in gamma-rays with *CGRO*/EGRET, a high energy gamma-ray telescope covering the energy range from 30 MeV to ∼30 GeV, which was operational between 1991 and 2000 (Kanbach et al. 1988). Initially the connection between the EGRET source 3EG J0416+3650 and 3C 111 was tentative. The distance between the objects is 1.2 °, and thus 3C 111 is located outside of the 99% probability region of 3EG J0416+3650 (Hartman et al. 1999). The 95% confidence contour radius for 3EG J0416+3650 is large, at 38'. Counterparts are identified using information from other wavebands, particularly radio, since most identified EGRET sources are blazars which are also strong radio sources. In the 99.9% confidence region there are 12 radio sources, of which only 3C 111 is also identified as an X-ray source, making it a strong potential counter part (Sguera et al. 2005). Later work supports this conclusion. EGRET data have been re-analysed, showing that the original source 3EG J0416+3650 is likely a blend of several sources, of which one has a good positional agreement with 3C 111 (Hartman et al. 2008).

Figure 7.3: Light curve of 3C 111 data with a bin of 1 month between 1-100 GeV.

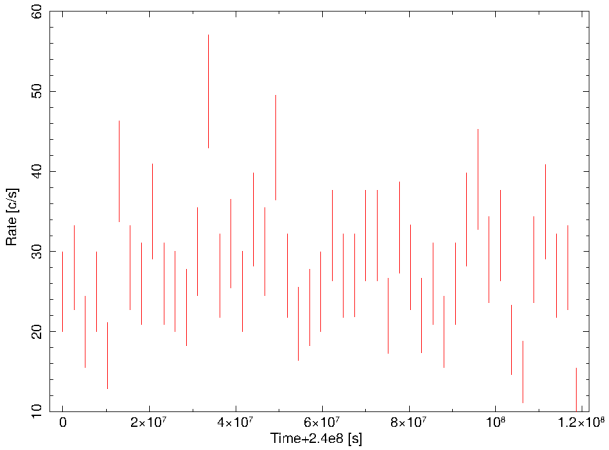

In the first *Fermi*/LAT catalogue, which uses 11 months of data, 3C 111 was reported among the few non-blazar AGN (Abdo et al. 2010e), with a significance of 4.3σ between 100 MeV to 100 GeV, and a flux of $f = 4.5 \times 10^{-8}\,\mathrm{ph\,cm^{-2}\,s}$ between 100 MeV and 100 GeV. In Table 7.1 the spectral information of the source in bins between 100 MeV to 100 GeV can be found. As can be seen in this table, 3C 111 is not bright at the highest gamma-rays, the significance peaks between 1-3 GeV.

In the second *Fermi*/LAT catalogue, which uses 24 months of data since the launch, 3C 111 is no longer included, indicating the significance of the source dropped below the threshold of TS=25, which can be due to several reasons, like variability or to the change in analysis procedures (Nolan et al. 2012). In addition, 3C 111 has a low Galactic latitude, complicating the analysis by possible source confusion and the strong Galactic plane diffuse emission (Ackermann et al. 2011a). 3C 111 is likely to be variable in gamma-rays, as found in a re-analysis of the data (Kataoka et al. 2011). Confirming this is another study of the 24 months of *Fermi*/LAT data showing that 3C 111 was detectable during a short time period of $\Delta t \sim 30 - 60$ days. Using causality arguments, this variability limits the radius of the emission region to $R < 0.1\,\mathrm{pc}$, assuming a Doppler factor of $\delta \sim 3$ (Grandi et al. 2012). The detectability of 3C 111 in the GeV range coincided with an increase in flux in other energy bands: millimetre, optical and X-rays, which indicates that the emission is likely to emerge from the same region. In gamma-rays 3C 111 can not be resolved, however, in the radio images it could be seen that a new knot in the jet emerged during the flaring episode. This constrains the gamma-ray emission of the source to a region within 0.3 pc of the central super massive black hole.

7.3 Gamma-ray detection: Fermi analysis

During the nominal all-sky survey mode of *Fermi*/LAT, a total effective exposure time of 83.7 Ms was accumulated in the direction of 3C 111 between 4 August 2008 and 20 April 2011 (see section 6.2.5 for a description of the satellite, and Figure 7.3 for a light curve of the data).

We selected diffuse-event-class photons (P6_V3 instrument response functions) between 100 MeV and 300 GeV in a circular region of interest with a radius of 15° around the source, the standard region recommended to include all photons from the source. Events with a zenith angle of more than 105° were excluded (Abdo et al. 2009a), if the region of interest is too close to the Earth's edge, the background emission will increase due to atmospheric gamma-rays. We also used the standard cuts proposed by the instrument team based on the data quality of the events and the instrument configuration. After filtering the data with these cuts, an exposure map is made, which is necessary for the likelihood analysis. First a live time cube was generated, which is a table covering the full sky, using the time range covered by the spacecraft file. The exposure depends on the time the detector observed the source, but also the inclination angle between the source direction and the LAT normal. Next the exposure map, which consists of an integral of the total response over the region of interest, was generated using the lifetime cube. Since the response function depends on the photon energy, the exposure map is also dependent on the energy.
We then used the likelihood analysis to determine the flux of the source. Since the event file included the flux of 3C 111 and the nearby sources, the model needs to contain several sources. In addition the galactic and extra galactic diffuse emission has to be modelled. If the field is not properly modelled, the flux attributed to the source of interest can be too high.

The goodness of the fit is expressed in $L = -\log\text{Likelihood}\, l$. The likelihood l is the product of the probabilities of observing the detected counts in each bin. The observed number of counts per bin is characterised by a Poisson distribution, since even in the cases where there are many counts, they are binned into a large number of bins resulting in a small number of counts per bin. If the expected number of counts in a bin i is m_i (dependent on the model), the probability of detecting n_i counts in that bin, is $p_\mathrm{i} = m_\mathrm{i}^{n_\mathrm{i}} \exp[-m_\mathrm{i}]/n_\mathrm{i}!$. Then, the likelihood l is the product of p_i, for all i:

$$l = \exp[-N_\mathrm{exp}]\Pi_\mathrm{i} m_\mathrm{i}^{n_i}/n_\mathrm{i}! \tag{7.1}$$

Here, $-N_\mathrm{exp}$ is the sum of m_i. Now, assuming all bins get infinitesimally small, such that the number of bins is $N_\mathrm{bins} \gg N_\mathrm{exp}$, the detected counts n_i is either 0 or 1. This is the unbinned likelihood l, and the formula becomes:

$$l = \exp[-N_\mathrm{exp}]\Pi_\mathrm{i} m_\mathrm{i} \tag{7.2}$$

The unbinned likelihood is more accurate than the binned likelihood, since the expected counts m_i are compared to each count n_i, and not over an average per bin i. However, for sources with a high count rate, the unbinned likelihood might not be performed due to time or computing constraints.
The use of Likelihood l means it can be compared with other fits but does not state a goodness on itself, like for example the χ^2-statistic. For each model, the maximum likelihood shows the best fit. Comparing the likelihood of different models needs to take into account the degrees of freedom, as well as the likelihood value. A model with more parameters will fit at least as well, and thus has a equal or greater likelihood, as a model with less parameters.

The significance of the source, as a test statistic value TS, is calculated with the likelihood statistic following:

$$TS = -2\ln(l_{\mathrm{max},0}/l_{\mathrm{max},1}) \tag{7.3}$$

Table 7.1: The spectral results for the 3C 111 analysis, taken from the first *Fermi* source catalogue (Abdo et al. 2010a). The photon spectral index between 100 MeV-100 GeV is $\Gamma_\gamma = 2.6 \pm 0.2$.

Energy band	significance [σ]	flux [$\mathrm{ph\,cm^{-2}\,s^{-1}}$]
100 MeV – 300 MeV	0.8	3.5×10^{-8}
300 MeV – 1 GeV	2.1	0.9×10^{-8}
1 GeV – 3 GeV	3.9	1.4×10^{-9}
3 GeV – 10 GeV	0.7	3.2×10^{-10}
10 GeV – 100 GeV	0	0.9×10^{-10}

Here $l_{\mathrm{max},0}$ is the maximum likelihood for the so-called null hypothesis, a model which does not include the source for which the significance is calculated, and $l_{\mathrm{max},1}$ is the maximum likelihood for a model that does include the source.

7.3.1 First analysis

The significance found for 3C 111 has a slight dependence on the model, and which sources are included in the model, but overall the results on the flux and power law index are in agreement among the different models applied to the data. We used the unbinned analysis for the Pass 6 data, as advised by the *Fermi* team, since 3C 111 is not a bright source in gamma-rays.
First we used a model containing 10 sources: the sources closest to 3C 111, and the bright sources in the field, such as the Crab Pulsar (distance to 3C 111: 23°) and the Geminga Pulsar (distance to 3C 111: 36°), taken from the first *Fermi* catalogue. We found a significance of TS=12.4 for 3C 111, a flux of $f = 1.3 \times 10^{-8}\,\mathrm{ph\,cm^{-2}\,s^{-1}}$ and a power law index of $\Gamma_\gamma = 2.4 \pm 0.4$. The overall goodness of the fit is expressed in a -log likelihood of $L = 7093218$. To improve the goodness of the fit, and thus our representation of the data, we removed a source in the field of view with a low significance to test a different model. This results in a fit with -log likelihood $L = 7093261$, and the likelihood decreased, showing an improvement in the fit. The significance of 3C 111 is lower, TS=12.0, with a flux of $f = 1.2 \times 10^{-8}\,\mathrm{photons\,cm^{-2}\,s^{-1}}$ and a power law index of $\Gamma_\gamma = 2.4 \pm 0.4$. Creating a model omitting 3 of the low-significance sources in the field and including 2 more bright sources (called model 1 afterwards), yielded a -log likelihood of $L = 7093294$. This model is not nested, meaning that, due to the addition of new sources and removal of previous sources, the parameters can not be adjusted to get the base model again. Therefore, it can not be directly compared to the previous models. The significance of 3C 111 decreased slightly to TS=11.3, the flux $f = 1.2 \times 10^{-8}\,\mathrm{ph\,cm^{-2}\,s^{-1}}$ and a power law index of $\Gamma_\gamma = 2.4 \pm 0.2$.

7.3.2 Second run: reprocessed data

After we performed this analysis the *Fermi* team released reprocessed data, where the old event class 3 has been split into two parts. We re-analysed the data using these event classes, see Figure 7.4 for the countmap. Using model 1 as described in the previous paragraph, the new data yielded a -log likelihood of $L = 8163485$, a TS of 12.5 for 3C 111 between 100 MeV and 300 GeV, and a power law index of $\Gamma_\gamma = 2.4 \pm 1.5$ and a flux of

Figure 7.4: The countmap of *Fermi*/LAT, centred on 3C 111 with a radius of 15 degrees. The other bright sources in the field are indicated. The region around 3C 111 has about 15 counts per pixel. The bright source NGC 1275 has $\sim$ 100 counts.

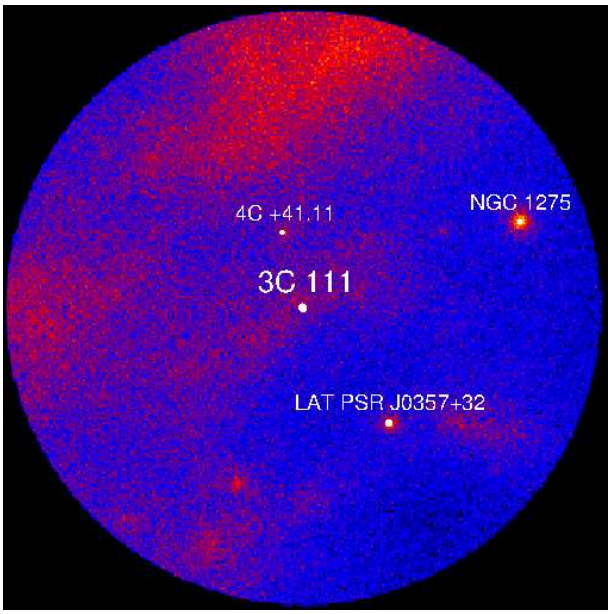

$f = (1.3 \pm 4.3) \times 10^{-8}\,\mathrm{ph\,cm^{-2}\,s^{-1}}$. Due to the large error on the flux this result cannot be trusted. However, the derived error on the flux is an estimate from the covariance matrix. Also for weak sources the flux error will be asymmetric and will not include 0. We have tried different models to understand the dependency of the flux on different assumptions. We also applied this model 1 on the first year of data, to look for variability. This fit resulted in similar values as for the whole data set; a TS value of 13.0 for 3C 111, with a flux of $f = (1.3 \pm 4.3) \times 10^{-8}\,\mathrm{ph\,cm^{-2}\,s^{-1}}$ and a power law index of $\Gamma_\gamma = 2.4 \pm 1.4$.

We also used a model which included all 34 sources from the first catalogue within 20° of 3C 111, where all parameters have been fixed to catalogue values except for the normalization of each source, and for 3C 111 both the normalization and power law index have been left free. This fit resulted in a very low significance for 3C 111 of TS=-0.14, and a flux of $f = 2.5 \times 10^{-11}\,\mathrm{ph\,cm^{-2}\,s^{-1}}$. In this case the flux was very low due the many sources used in the model. Since the resulting flux and significance were much lower than what is expected from the *Fermi* catalogue value the model used appears not to be a good representation of the gamma-ray emission of the source.

We created a new model, called model 2 afterwards, which included 4 close sources and the bright source NGC 1275, which is at a 12° separation with 3C 111. Using model 2 we found that 3C 111 has a significance of TS=12.3, with a flux of $f = (1.3 \pm 4.3) \times 10^{-8}\,\mathrm{ph\,cm^{-2}\,s^{-1}}$ and a power law index of $\Gamma_\gamma = 2.4 \pm 1.5$. The -log likelihood for this fit is $L = 8163569$.

Since 3C 111 is less bright at higher gamma-rays, we tried to improve the significance of the detection by applying this model to the same region but in different energy ranges. This

requires complete reanalysis of the data in these other energy ranges[1].

In the energy range from 100 MeV to 100 GeV, the fit using model 2 yielded a significance for 3C 111 of TS=11.3, with a flux of $f = 1.2 \times 10^{-8}\,\mathrm{ph\,cm^{-2}\,s}$, and a power law index of $\Gamma_\gamma = 2.4 \pm 0.2$. An increased energy range of 100 MeV to 200 GeV gives a TS=12.4 for 3C 111, with a flux of $f = 1.2 \times 10^{-8}\,\mathrm{ph\,cm^{-2}\,s}$, the power law index being $\Gamma_\gamma = 2.4 \pm 0.2$. This is the same significance and flux as for the full energy range, implying the flux between 200 and 300 GeV is very low. We have also analysed the data between 200 MeV to 300 GeV to see the influence of the first 100-200 MeV flux. This gave a TS=10.4 for 3C 111, a flux of $f = 4.8 \times 10^{-9}\,\mathrm{ph\,cm^{-2}\,s}$, and a photon index of $\Gamma_\gamma = 2.5 \pm 0.2$.

We also tried to analyse the data between 1-100 GeV, but this yielded a test statistic of TS$\sim$33 for both the model 1 and model 2. The flux found is $f = 3 \times 10^{-8}\,\mathrm{ph\,cm^{-2}\,s}$ and a power law index of $\Gamma_\gamma = 2.7$. The flux of this detection was higher than the flux taken over a larger energy range, and the detection significance was also much higher than expected. The *Fermi*/LAT catalogue shows a significance of 4.3σ for 3C 111 in this energy range, whereas the TS value of 33 would indicate 5.8σ. To investigate this curious detection we compared with the bright source NGC 1275, which has a test statistic of TS=160 with the model in this energy range, which is $\sim 13\sigma$, whereas the *Fermi*/LAT catalogue shows a much higher significance of 59.3σ. Since both these values were quite different from the catalogue, we omitted this result since it is not trustworthy.

The result of the analysis in the energy range 100 MeV to 300 GeV is similar using either model 1 and model 2, and for either the previous Pass 6 or the reprocessed data. The results are also similar to the *Fermi* catalogue, the flux found in our analysis is lower since we use a longer time and, due to the variability of the source, the source was less bright in the second year of *Fermi* observations. Therefore we decided the result we found can be used in the spectral energy distribution.

Using GTBIN we created a spectrum to be used in XSPEC in the PHA1 format, with 4 logarithmic bins. The background is created with GTBKG, which uses the spectrum, the livetime cube, the exposure map and the model used in the likelihood analysis, to estimate the total counts in the energy bands takes from the spectrum. A response matrix file is created with GTRSPGEN, which uses the detailed response functions provided by the *Fermi* team. The elements of the response matrix relate directly to the probability of an incident photon with a true energy E being detected with an apparent energy E' by the instrument. The source position, observation time and energy grid are taken from the input spectrum file, and the instrument orientation was taken from the pointing/livetime history file. The spectrum created yielded two significant data points, which is not enough to fit any model to, but it can be used in the SED.

7.3.3 Pass 7 data

We also used the new Pass 7 data released by the *Fermi*/LAT team at 5 August, 2011. Using a new classification of LAT data, the effective area is increased at low energies, and more

[1] Since there is only one model applied to different cuts of the data, the likelihood does not give any information about the fit and shall therefore not be quoted here.

Table 7.2: The parameters for the individual power-law fits of the data for 3C 111 and their 90% confidence levels.

Instr.	Epoch	Exposure	PL index	f [erg cm^{-2} s^{-1}]	Energy range
XIS0	22-25 August 2008	95.4 ks	1.60 ± 0.02	$(2.20 \pm 0.02) \times 10^{-11}$	0.4–10 keV
XIS1	22-25 August 2008	95.4 ks	1.59 ± 0.02	$(2.24^{+0.03}_{-0.02}) \times 10^{-11}$	0.4–10 keV
XIS3	22-25 August 2008	95.4 ks	1.63 ± 0.02	$(2.20 \pm 0.02) \times 10^{-11}$	0.4–10 keV
PIN	22-25 August 2008	101.9 ks	1.52 ± 0.14	$(4.8 \pm 0.4) \times 10^{-11}$	12–60 keV
ISGRI	24 March 2003-19 August 2009	508 ks	1.90 ± 0.20	$(1.2 \pm 0.2) \times 10^{-10}$	20–200 keV
BAT	December 2004-May 2009	54 months[a]	1.99 ± 0.09	$(1.05 \pm 0.05) \times 10^{-10}$	15–150 keV
LAT	4 August 2008-20 April 2011	83.7 Ms	2.4 ± 0.2	$(6 \pm 2) \times 10^{-12}$	> 100 MeV

[a] Elapsed time

accurate in the GeV energy range. The photon classes have been redefined, so we re-analysed the data using the new photon class P7SOURCE_V6. In addition new software is released. Using one year of data between 100 MeV and 100 GeV, and the model with 4 close sources and the bright source NGC 1275 as used before, a TS value of 20 was found for 3C 111, a flux of $f = 3 \times 10^{-8}\,\mathrm{ph\,cm^{-2}\,s^{-1}}$ and a photon index of $\Gamma_\gamma = 2.5$. The flux found is 3 times as large as before, and the index is consistent with the value found with the Pass 6 data. With this analysis, the significance found for NGC 1275 is $\sim 59\sigma$, similar to the catalogue value of 65σ, and the flux is similar to catalogue value ($f \sim 2 \times 10^{-7}\,\mathrm{ph\,cm^{-2}\,s^{-1}}$).
The significance and flux of 3C 111 were higher as before, but still close to the catalogue value. For the spectral energy distribution the difference will not be significant.

7.4 X-ray Analysis

In addition to the gamma-ray analysis we analysed X-ray data from 3C 111. To create the spectrum we used several instruments to cover a large energy band. The fluxes, elapsed time and power law indices of the individual spectra can be found in Table 7.2.

7.4.1 Suzaku analysis

We analysed data from the *Suzaku* satellite (description in Section 6.2.2). The observations were made from 22 to 25 August 2008 with a total elapsed time of 236.9 ks in HXD nominal pointing mode. We used data from both the XIS and HXD/PIN detector.

Soft X-rays: XIS

For the XIS we used the clean events as provided by the instrument team to create three spectra for the three XIS detectors between ∼0.2–12 keV. The cleaned event files were screened by event, for example flickering pixels are removed, and by GTI, for example to exclude the passage through the South Atlantic anomaly where the inner van Allen radiation belt comes down to 200 km above the Earth's surface. The cleaned files come in both the 5x5 and 3x3 models, the difference is only in the number of pixels read out around the centre of each event, which is 25 or 9. We use only the 3x3 mode.
Since the XIS is an imaging instrument the background spectra can be taken from the same

Figure 7.5: XIS0 count map, with the source, circle, and background, polygon at the top, regions. An extraction radius of about 250 pixels is recommended to include 99% of the source flux. The cross denotes the position of 3C 111. The image is overexposed to show details. At the exact position of 3C 111 the count rate is ∼1000 counts/s, at the edges of the source region the count rate drops to about 10 counts/s. In the background, the count rate is 0–4 counts/s.

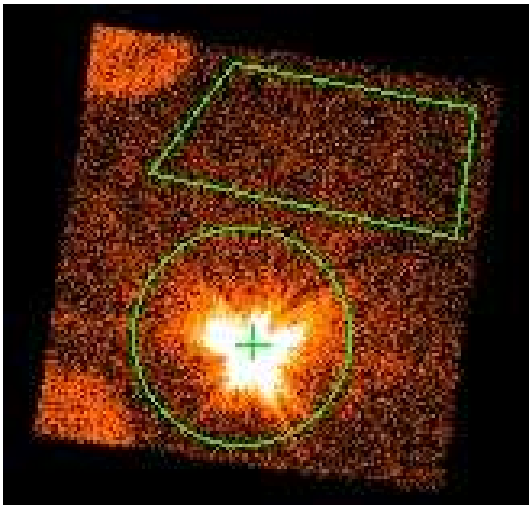

data files. Using a imaging software, like DS9, regions for the background and source were defined, see for example Figure 7.5. Then we used XSELECT to extract the spectra in each region.

The response files were created for the source spectrum and the background with XISRMFGEN. For this only the spectral file was necessary since it contains the necessary information about the instrument, observation data and clock mode, which determines the exposure time and region, and the time resolution.

After this the spectra are binned applying GRPPHA, using the criterion of a minimum of 100 counts per bin to increase the statistics, especially below ∼0.6 keV and above ∼8 keV. The back-illuminated XIS-1 detector has an energy range down to ∼0.2 keV, whereas the front-illuminated XIS-0 and XIS-3 have an energy range starting at ∼0.4 keV. At energies above 10 keV, the spectrum has less significant bins, especially for XIS-1. We used the energy range between 0.4–10 keV for all XIS spectra.

It is possible to add the three spectra, using for example MATHPHA. When treating the overall spectrum we have chosen to keep the different XIS spectra separate, since the detectors have slightly different power law indices (see Table 7.2), so they influence the overall power law differently.

To find the specifics of the iron line at 6.4 keV we chose to add the spectra, to get a more accurate observation, since for the three spectra the iron line has the same energy E_{line}, but slightly different equivalent widths. By adding the three spectra any fluctuations caused by

the detector differences are averaged out.

Hard X-rays: PIN and GSO

We also used data from the HXD, which consists of the PIN (sensitive below 60 keV) and GSO detectors (sensitive above 30 keV). PIN is a collimated instrument, so it is not possible to get background information from the data itself. The non X-ray background (NXB) is provided by the instrument team. The Cosmic X-ray background (CXB) is about 5% of the PIN background, so it needs to be taken into account. The CXB is not distributed, but can be simulated in XSPEC (Arnaud 1996) using the flat response file. The typical CXB is based on the *HEAO* results, assuming uniform emission from a region of 2°x2°(Boldt 1987):

$$CXB(E) = 9.0 \times 10^{-9} \times \left(\frac{E}{3\,\mathrm{keV}}\right)^{-0.29} \times \exp\left(\frac{-E}{40\,\mathrm{keV}}\right) \mathrm{erg\,cm^{-2}\,s^{-1}\,str^{-1}\,keV^{-1}} \quad (7.4)$$

This has to be corrected for the 4 square degree field of view for the flat PIN response files by multiplying by $4\mathrm{deg}^2/1\mathrm{sr}$. Then, XPSEC assumes the power law is normalized at 1 keV, and given in units of photons instead of ergs, so we obtain:

$$CXB(E) = 9.412 \times 10^{-3} \times \left(\frac{E}{1\,\mathrm{keV}}\right)^{-1.29} \times \exp\left(\frac{-E}{40\,\mathrm{keV}}\right) \mathrm{ph\,cm^{-2}\,s^{-1}FOV^{-1}keV^{-1}} \quad (7.5)$$

Then the CXB and NXB are added into a single background spectrum using MATHPHA. Both the source and background files were filtered using the good time intervals. The source file was dead-time corrected (this is not necessary for the background file). Then the exposure of the background spectrum has to be multiplied by 10, since, the backgrounds have been scaled up by 10 to suppress Poisson noise. The response file was also distributed by the instrument team. The response files that are needed depend on when the data were taken, since the high-voltage setting of the PIN diodes and the low energy threshold has been adjusted several times, and the pointing, which can be either XIS or HXD. The resulting spectrum was rebinned to increase the count rate in the channels. The channels below 12 keV were not used because the PIN response matrix needs improvements in this energy range. Since the channels above 60 keV were not significant they are ignored in the analysis.

We reprocessed the raw GSO event files, and screened it with the standard criteria for pulse and event height and corrected for dead-time. Since the NXB distributed by the Suzaku team is binned, the GSO spectrum has to be rebinned accordingly. The resulting spectrum has only a few significant bins and is noise dominated, so we decided not to use it.

7.4.2 INTEGRAL analysis

To get a better coverage at higher energies we added *INTEGRAL*/ISGRI data to the spectrum (see Section 6.2.1 for the instrument description). We used data since the launch on 17 October 2002 up to 19 August 2009, with an exposure time of 508 ks. For the analysis we used the Offline Scientific Analysis (OSA) version 9.0 as provided by the ISDC (Courvoisier et al. 2003). The 411 individual science windows (individual spacecraft pointings) were processed one by one, creating a directory with an image and a spectrum for each pointing, using IBIS_SCIENCE_ANALYSIS. The raw data were processed, for example by applying dead-time

Figure 7.6: INTEGRAL/ISGRI significance map around 3C 111, between 20 and 200 keV. 3C 111 has a significance of 22σ. The grid shows J2000.0 coordinates.

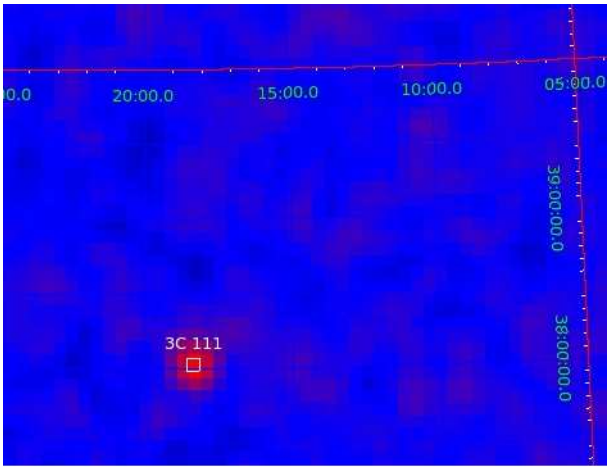

correction and tagging of noisy pixels. After corrections the data were sorted in energy bins, choosing 3 bins, 20–50 keV, 50–100 keV and 20–200 keV. Re-binned background maps were also created and subtracted from the image. After this a search for sources was performed and a list of detected sources created. Then, each image was summed into a total mosaic, see Figure 7.6 for the significance map of the mosaic. 3C 111 has a significance of 23σ between 20–50 keV, of 9σ between 50 and 100 keV and over the whole 20–200 keV band a significance of 22σ, indicating the source is slightly brighter at lower energies.

The individual spectra were also summed together, using SPE_PICK, yielding a spectrum with 13 bins. The ancillary response file was created together with the spectrum. The response file was provided by the *INTEGRAL* team. There was no background file necessary since the background has been taken into account during the imaging analysis.
We ignored the first two ($< 20\,\mathrm{keV}$) and last two ($> 200\,\mathrm{keV}$) channels of the spectrum, since these were not significant. See Figure 7.7 for the resulting spectrum fit with a simple power law model, with a power law index of $\Gamma = 1.9 \pm 0.2$ between 20–200 keV (see also Table 7.2).

7.4.3 Swift/BAT

Lastly we added *Swift*/BAT data (see Section 6.2.3) from the 58-month survey (Tueller et al. 2010; Baumgartner et al. 2010), December 2004 to May 2009, to the spectrum. Since the BAT detector has a large field of view of 1.4 sr partially coded (Barthelmy et al. 2005), it has regularly observed 3C 111.
We downloaded the spectrum and response matrix from the HEASARC website[2]. The detected flux for 3C 111 in this survey is $1.2 \times 10^{-10}\,\mathrm{ergs\,cm^{-2}\,s^{-1}}$ between 14 keV and 195 keV. The spectrum has 8 channels, and we ignored the first channel ($< 15\,\mathrm{keV}$), since due to varying thresholds in the individual detectors, channels below 14 keV should not be used for spectral analysis. There are 2 channels above 150 keV which were also ignored, because

[2] http://heasarc.nasa.gov/docs/swift/results/bs58mon/

Figure 7.7: *INTEGRAL* IBIS/ISGRI data of 3C 111, unfolded spectrum and power law model with index $\Gamma = 1.9 \pm 0.2$.

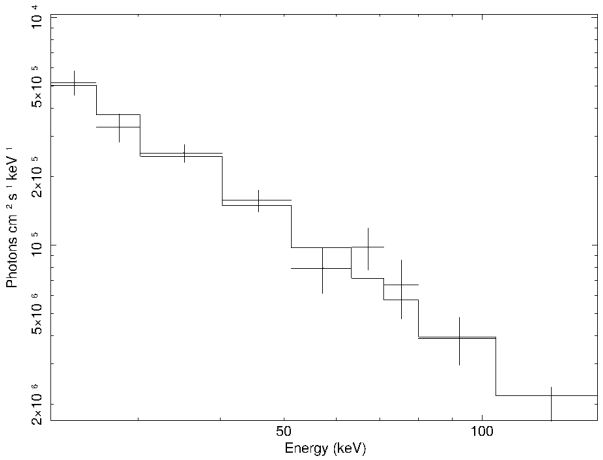

channels above 150 keV are unreliable due to a lack of calibration data at those energies, and should therefore not be used in spectral analysis. The *Swift* spectrum can be seen in Figure 7.8. The spectrum follows a simple power law with photon index $\Gamma = 1.99 \pm 0.09$ (see also Table 7.2).

7.5 X-ray spectrum

We combined the X-ray data in a spectrum between 0.4 and 200 keV. To analyse the spectrum we used XSPEC, version 12.7, and tested several models. All errors quoted in this section are 90% confidence, unless stated otherwise.
We started with a simple absorbed power law and a Gaussian component for the iron line (see end of this section). The fit gives a reduced $\chi^2_\nu = 1.14$ for 1678 degrees of freedom (d.o.f.). The equivalent hydrogen column-density was $N_\mathrm{H} = (8.8 \pm 0.1) \times 10^{21}\,\mathrm{cm}^{-2}$ and the power law index $\Gamma = 1.63 \pm 0.01$.

To improve the fit we added a cut-off to the power law. A break or cut-off of some kind can be expected from Table 7.2, where the power law index of the lower energy is $\Gamma \sim 1.6$ and for the higher energies the power law index is $\Gamma \sim 2$. The goodness of the fit improved when applying a cut-off power law: $\chi^2_\nu = 1.12$ for 1677 d.o.f. and the F-test probability is 5×10^{-8}, showing that the addition of a cut-off improved the model. The equivalent hydrogen column-density was $N_\mathrm{H} = (8.7 \pm 0.1) \times 10^{21}\,\mathrm{cm}^{-2}$, the power law index $\Gamma = 1.60 \pm 0.02$ and the cut-off energy was $E_\mathrm{cut} = 138^{+56}_{-32}\,\mathrm{keV}$. A broken power law gave a similar result, with $\chi^2_\nu = 1.11$ for 1676 d.o.f., an equivalent hydrogen column-density $N_\mathrm{H} = (8.8 \pm 0.1) \times 10^{21}\,\mathrm{cm}^{-2}$, first power law index of $\Gamma_1 = 1.63 \pm 0.01$, second power law index $\Gamma_2 = 2.0 \pm 0.1$ and a break energy of $E_\mathrm{br} = 22^{+7}_{-3}\,\mathrm{keV}$. The break energy is very close to the lower energy limit of the hard X-ray spectrum, so the break might also be caused by intercalibration issues between the soft and hard X-ray data.

Figure 7.8: *Swift*/BAT data, unfolded spectrum and power law model with index $\Gamma = 1.99 \pm 0.09$.

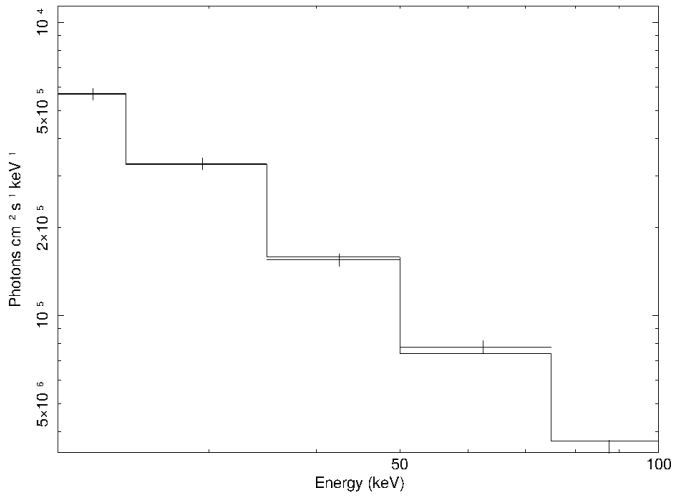

Figure 7.9: The count spectrum of the combined *Suzaku*/XIS (0.4–10 keV), *Suzaku*/PIN (12-60 keV), *INTEGRAL* IBIS/ISGRI (20-200 keV), and *Swift*/BAT (15-150 keV), with the fitted `pexrav` model: an absorbed cut-off power-law with reflection from neutral material. In addition there is a Gaussian component for the iron line at 6.4 keV. The bottom panel shows the residuals in terms of the standard deviation with error bars of size 1σ.

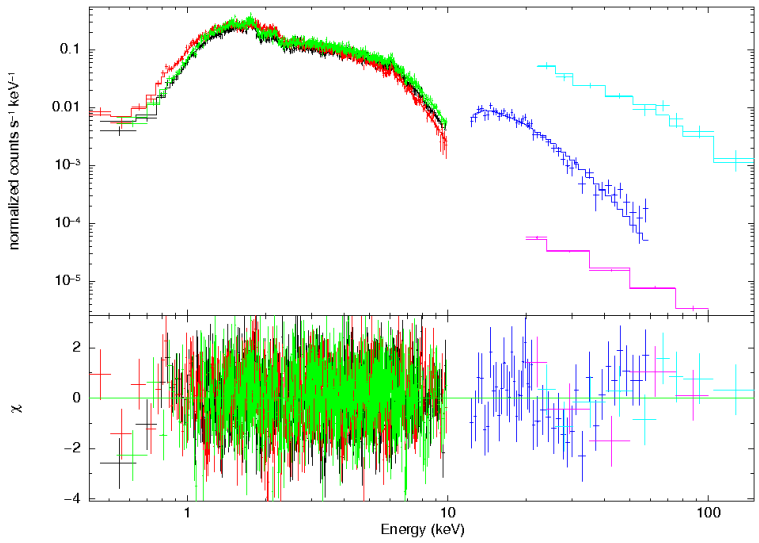

Figure 7.10: Error contours for the best-fit `pexrav` model, the reflection component R against the high-energy cut-off $E_{\rm cut}$. The contour levels correspond to a $\Delta\chi^2$ of 68%, 90% and 99.7% statistical confidence levels.

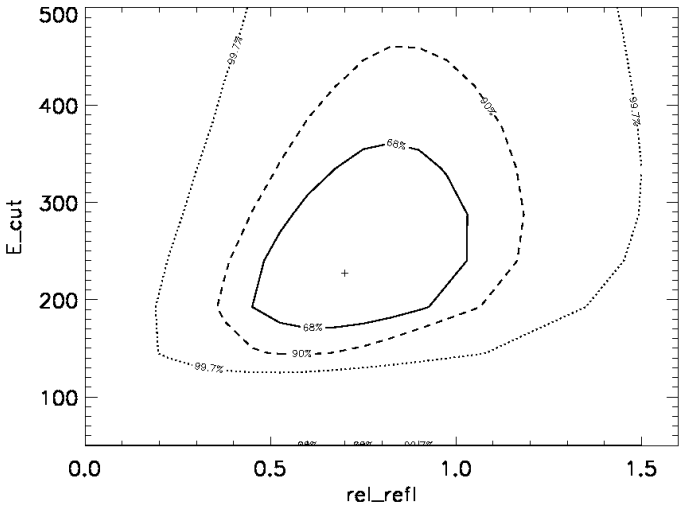

Next, we have applied a reflection component to the fit, using the `pexrav` model (Magdziarz & Zdziarski 1995). The model has an exponentially cut off power law with reflection from neutral material. The reflection component improved the fit to $\chi^2_\nu = 1.10$ (1676 d.o.f.), see Figure 7.9. For the equivalent hydrogen column-density we found $N_{\rm H} = (9.0 \pm 0.2) \times 10^{21}\,{\rm cm}^{-2}$, a power law index of $\Gamma = 1.68 \pm 0.03$, a cut-off energy of $E_{\rm cut} = 227^{+143}_{-67}\,{\rm keV}$ and a reflection scaling factor of $R = 0.7 \pm 0.3$. We also made an error contour plot, by using the steppar command in XSPEC. This routine performed a fit while stepping through parameter values of a certain range. This resulted in an confidence contour map, as seen in Figure 7.10. Based on this analysis, a cut-off below 130 keV can be excluded at a 99.7% (3σ) confidence level.

In addition to this analysis, we also applied the `compPS` model, which describes thermal Comptonization (Poutanen & Svensson 1996). In this model, seed photons from the cold thick accretion disk are injected into the electron plasma, which can have several different geometries. The electrons in the plasma cloud have a Maxwellian distribution with a temperature $T_{\rm e}$ and optical depth τ, related to the Compton parameter $y = 4\tau k T_{\rm e}/(m_e c^2)$. The seed photons are upscattered by the electrons from their initial energy E_i to $E_f = e^y E_i$. This produces a spectrum, which is afterwards reflected from a cool medium (e.g. the outer accretion disk) and smeared out by the rotation of the disk.
There are different geometries possible for the electron cloud, and for its distribution. The disk can be either black body or a multicolour disk, which produces a different seed photon spectrum, and the injection method can vary. We have tried to vary some of these parameters. For the geometry, we tried the plane slab and a sphere, where the photons are injected at the bottom of the slab and at the centre of the sphere. The plane slab gave a better fit of $\chi^2_\nu = 1.10$ for 1676 d.o.f., with the sphere $\chi^2_\nu = 1.11$ for 1676 d.o.f., indicating the electron plasma is rather in a plane above the accretion disk than in a corona around in the accretion

Figure 7.11: Unfolded spectrum of 3C 111, see Figure 7.9 for data description, and the best-fit `compps` model and the Gaussian component for the iron line. The bottom panel shows the residuals in terms of the standard deviation with error bars of size 1σ.

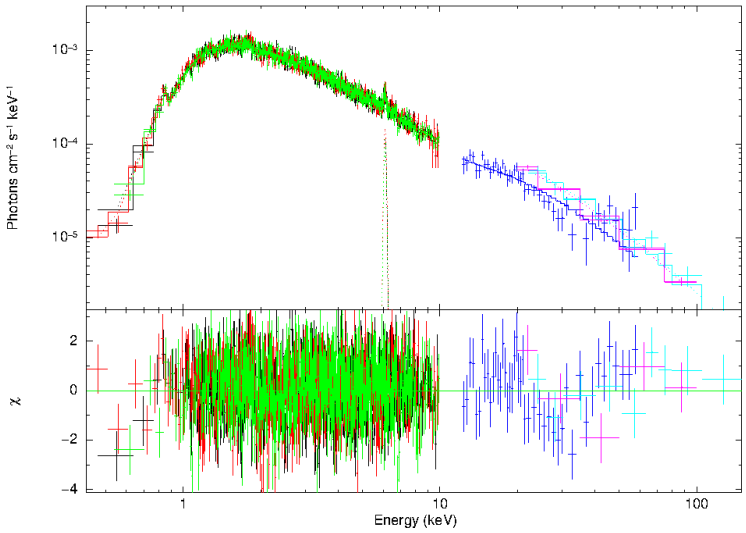

disk. We also used the model of a sphere where the source of the seed photons is distributed according to the eigenfunction of the diffusion equation, which gave a fit of $\chi^2_\nu = 1.11$ for 1676 d.o.f. For the reflection emissivity law, r^β, we tried using an emissivity of $1 - \sqrt{(6/r_g)}/r_g^3$, which gave a $\chi^2_\nu = 1.12$ for 1676 d. o.f., whereas a non-rotating disk gave a better fit of $\chi^2_\nu = 1.10$ with 1676 d.o.f.

The best-fit model, using a plane slab, with injection of photons at the bottom, a Maxwellian electron distribution and a non-rotating multi-colour disk, gave a fit with $\chi^2_\nu = 1.10$, 1676 d.o.f., with an equivalent hydrogen column density of $N_\mathrm{H} = (9.0 \pm 0.2) \times 10^{21}\,\mathrm{cm}^{-2}$, an electron temperature of $kT_\mathrm{e} = 91^{+22}_{-48}\,\mathrm{keV}$, a reflection component $R = 1.8^{+0.5}_{-0.7}$ and a Compton parameter $y = 0.6 \pm 0.1$, which corresponds to an optical depth $\tau = 0.8$, see Figure 7.11.

7.5.1 Iron line

The iron line energy E_line does not vary significantly among the models, we found a line energy of $E_\mathrm{line} = 6.11\,\mathrm{keV}$, and the equivalent width between 85–107 eV for the different XIS detectors. The line energy is redshifted due to the distance to 3C 111, in the rest-frame the line energy is $E_\mathrm{line} = 6.404\,\mathrm{keV}$. To connect the redshift with the observed and the emitted wavelength, the following formula can be used:

$$\lambda_\mathrm{obs} = (1 + z)\lambda_\mathrm{em} \tag{7.6}$$

where z is the redshift of the object, λ_obs is the observed and redshifted wavelength, and λ_em the wavelength of the emission. For the energy in keV the formula becomes:

$$E_\mathrm{em}/(1 + z) = E_\mathrm{obs} \tag{7.7}$$

since $E = hc/\lambda$. So using an emitted line energy of $E_\mathrm{em} = 6.404\,\mathrm{keV}$ and the redshift of 3C 111 $z = 0.049$, we find that the observed line energy should be $E_\mathrm{obs} = 6.101\,\mathrm{keV}$, consistent with

the line energy found.
There was a slight variation between the XIS detectors, resulting in different values for the EW per detector. To get a good measurement of the iron line, we added the three XIS-spectra using MATHPHA. The line energy was $E_{\rm line} = 6.11 \pm 0.02\,\mathrm{keV}$ and the equivalent width $EW = 85 \pm 11\,\mathrm{eV}$.

7.6 SED modelling

After the analysis of the X-ray spectrum we wanted to study the broad-band emission of 3C 111, to put the X-ray spectrum in a wider perspective.

7.6.1 Synchrotron self-Compton

To model the spectral energy distribution (SED) we used a synchrotron self-Compton (SSC) model, which is often used for blazar SEDs. This simple model assumes that the emission arises from a spherical plasma volume that travels down the relativistic jet, which has an angle to the line of sight of θ with a bulk Lorentz factor Γ (see for a diagram Figure 7.12). The spherical volume with radius R_s, with a randomly orientated magnetic field B contains an isotropic population of high-energy electrons that emit synchrotron radiation. The synchrotron photons are then inverse Compton scattered to higher energies (SSC, Maraschi et al. 1992). The emitted radiation is Doppler-shifted with a Doppler factor of $\delta = [\Gamma(1 - \beta\cos\theta)]^{-1}$. The energy distribution of the electrons can be parametrised in several ways, but often a broken power law is used:

$$N(E) = \begin{cases} kE^{-p_1} \text{ if } & E_{\rm min} < E < E_{\rm br} \\ kE^{-p_2} \text{ if } & E_{\rm br} < E < E_{\rm max} \end{cases} \tag{7.8}$$

Here, k is the electron normalization factor, $E_{\rm min}$ is the minimum energy of the electrons, due to self-absorption, and $E_{\rm max}$ the maximum energy attained by the electrons. Electrons with the break energy $E_{\rm br}$, where the cooling time (the minimum between synchrotron and Compton cooling time) equals the escape time, emit the dominant synchrotron power output. The first power law index $p_1 < 3$ and the second one is steeper, with $p_2 > 3$.
The output spectrum shows two peaks, a synchrotron branch, which covers the radio to X-ray band, and the inverse Compton branch, in gamma-rays and VHE. The frequencies of the peaks, $\nu_{\rm S}$ for the synchrotron peak and $\nu_{\rm IC}$ for the inverse Compton peak, are correlated via the break energy of the electron energy distribution, via

$$\gamma_{\rm br} = \left(\frac{3\nu_{\rm IC}}{4\nu_{\rm S}}\right)^{1/2} \tag{7.9}$$

where $\gamma_{\rm br} = E_{\rm br}/mc^2$. This makes the break energy $E_{\rm br}$ one of the few parameters that can be directly inferred from the SED. Since the synchrotron peak frequency can be expressed as $\nu_{\rm S} = 3.7 \times 10^6 \gamma_{\rm br}^2 B\delta(1+z)^{-1}$, the magnetic field B and Doppler factor δ can be

$$B\delta = (1+z)\frac{\nu_{\rm S}^2}{2.8 \times 10^6 \nu_{\rm IC}} \tag{7.10}$$

This equation is not valid in the Klein-Nishina limit (Tavecchio et al. 1998), where the quantum electrodynamics start to affect the cross-section of the scattering process (see equation

Figure 7.12: Schematic overview of the synchrotron and inverse Compton processes in the jet. The volume travels down the jet with a certain bulk Lorentz factor. The electrons contained in the volume emit synchrotron emission, which are used as seed photons for the inverse Compton processes (SSC). Also depicted are possible inverse Compton processes via seed photons from the broad-line region or accretion disk (Beckmann & Shrader 2012).

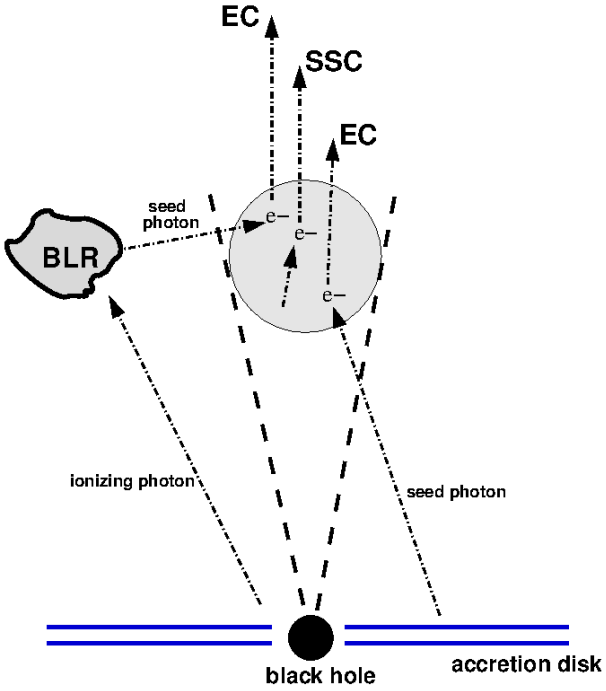

5.4)). Lastly, the radius of the emitting region R_s might be derived from observations. If the variability time scale $t_{\rm var}$ is known,

$$R_s = ct_{\rm var}\frac{\delta}{1+z} \tag{7.11}$$

In addition to the SSC processes, an external Compton (EC) component might be necessary to accurately represent the high-energy part of the SED, for example for the luminous FSRQ class of sources (see section 4.3.1). The seed photons for this process can come for example from the accretion disk or the broad line region. Since there is no need for an external Compton component in the case of the sources discussed in this chapter and the next, EC will not be discussed beyond this.

7.6.2 Data preparation

We used the X-ray spectrum, were we omitted the *Suzaku*/XIS data below 1 keV to avoid contamination by possible starburst emission, and the *Suzaku*/PIN data above 50 keV are not used due the low statistics between 50–60 keV. To use the X-ray spectrum from XSPEC we plotted the data with `eufspec`, to extract the unfolded spectrum and model in Ef(E) and wrote the spectrum to a data file. Then, we converted the photon spectrum into $\log(\nu f\nu)$

format. A similar procedure was used for the *Fermi* spectrum. Correcting for the Galactic absorption does not change the spectrum, at these high energies the absorption is less important.
Since all the data we analysed were in the high energy range, it is not possible to model the entire SED. Therefore we used also historical data from NED[3] to represent the low energy branch, where we omitted observations that only included the core, since with X-rays and gamma-rays the source cannot be resolved. NED provides data points in a convenient $\nu F\nu$ format, albeit it is in Jy Hz units. The X-ray and gamma-ray data are in $\mathrm{ergs\,cm^{-2}\,s^{-1}}$, but the transformation between between these units is linear: $1\,\mathrm{Jy} = 10^{-23}\,\mathrm{ergs\,cm^{-2}\,s^{-1}\,Hz^{-1}}$. Using a small script, the SI units of the NED data are changed to cgs.

The infrared and optical data points needed to be absorption corrected. For this we used the column density $N_\mathrm{H} = 9.0 \times 10^{21}\,\mathrm{cm^{-2}}$ which was found in the X-ray spectrum. The extinction in the V-band can be calculated using the column density via:

$$A_\mathrm{V} = N_\mathrm{H}/(1.79 \times 10^{21}\,\mathrm{cm^{-2}}) \tag{7.12}$$

Then, using the extinction in the V-band A_V, the relative extinctions in other bands can be calculated via $A_\mathrm{i}/A_\mathrm{V}$ for band i, which can be found for example in Schlegel et al. (1998). The correction factor per bandpass can be calculated by multiplying the flux in band i with 2.5^{A_i}, since the correction relative to A_V is in units of magnitude. The difference in magnitude $\Delta m = m_1 - m_2$ is related to the flux ratio $f_r = f_1/f_2$ via $\Delta m = -2.5 \log_{10} f_r$.

7.6.3 The SSC code

To model the SED of 3C 111 we used the public code by Krawczynski et al. (2004)[4]. This code follows a one-zone SSC, as described before. The input parameters are the radius R_s and magnetic field B of a volume, which moves with angle θ and bulk Lorentz factor Γ. The electrons confined in the sphere have an energy distribution which can be approximated with a broken power law as described, with energies E_min, E_max, E_br and power law indices p_1 and p_2. The external Compton parameters are the black hole mass M_bh, accretion rate $\dot{M}$ and the height of the blob above the accretion disk d_b. Additional parameters in this model are the redshift and jet-frame energy density of the electrons.

The code has no complete model-fitting implementation, it returns a spectrum for a set of input parameters, leaving the parameter estimation to the user. Due to the parameters being interlinked, improving the fit is not straightforward. In addition, by using a fitting algorithm the model will be dominated by the lower energies due to the large error in flux for the high energies.

7.6.4 Results

To start the SED modelling we used as input parameters the standard parameters of the code, without the external Compton component, which are tuned for a blazar, with a jet angle $\theta = 5°$ and a Doppler factor of $\delta = 10$. The magnetic field is $B = 0.025\,\mathrm{G}$, the radius of the emitting region $R_s = 10^{14}\,\mathrm{cm}$ and the electron energy distribution is characterized with a

[3] http://ned.ipac.caltech.edu/
[4] This code is no longer available online.

Figure 7.13: SED of 3C 111 plotted with crosses, green points are historical radio data, blue are IR/optical points, red points data analysed in this work. The model plotted with a line is for a typical HBL blazar model, with scaled down jet power.

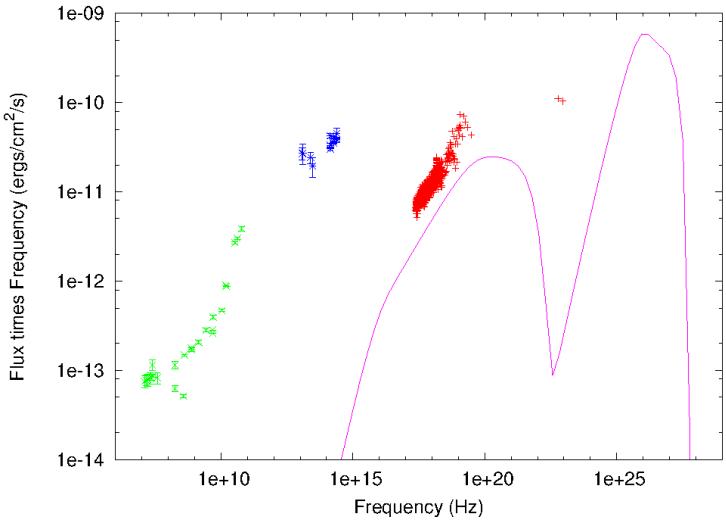

broken power law with index $p_1 = 2$ between $E_{\rm min} = 3.9 \times 10^{10}\,{\rm eV}$ and $E_{\rm br} = 3.2 \times 10^{12}\,{\rm eV}$, and an index $p_2 = 3$ between $E_{\rm br}$ and $E_{\rm max} = 3.2 \times 10^{13}\,{\rm eV}$. The parameters are used for a HBL blazar object, a low luminous blazar. These type of objects show a SED with the peak of the synchrotron branch in the X-ray band, the peak frequency is $\nu_{\rm S} = 2 \times 10^{20}\,{\rm Hz}$, and the inverse Compton branch peaks in the VHE, the peak frequency in this case is $\nu_{\rm IC} = 4 \times 10^{26}\,{\rm Hz}$. The spectrum which was produced with these parameters can be found in Figure 7.13.

To change the overall power in the SED the Doppler factor δ was adjusted, since a lower Doppler factor means the emission is less boosted and as such appears less energetic. Since the Doppler factor is connected to the angle θ and bulk Lorentz factor of Γ via $\delta = [\Gamma(1 - \beta\cos\theta)]^{-1}$, the larger jet angle $\theta = 18°$ of 3C 111 naturally decreases the Doppler factor δ. The dependence on most parameters, for the SSC process, is on the Doppler factor rather than the bulk Lorentz factor Γ or the jet angle θ. The jet power, the radius of the emitting region R_s, which defines the amount of particles, and the magnetic field B, which increases as the flux increases due to the dependence of the synchrotron power, can be adapted to change the overall power. The shapes of the synchrotron and inverse Compton branches and peak frequencies depend strongly on the energies that define the electron population.

Another well-documented gamma-ray bright radio galaxy, Centaurus A has been similarly modelled. Although this source is a FR-I type source, and less luminous, the SED is closer to 3C 111 (see Figure 5, Abdo et al. 2010c). To model the SED of Cen A, Abdo et al. (2010c) used a Doppler factor $\delta = 1$, a magnetic field $B = 6.2\,{\rm G}$ and a radius of $R_s = 3 \times 10^{15}\,{\rm cm}$. The electron energy distribution shows a first power law index of $p_1 = 1.8$ between the minimum energy of $E_{\rm min} = 1.5 \times 10^8\,{\rm eV}$ and the break energy of $E_{\rm br} = 4 \times 10^8\,{\rm eV}$. Between the break energy $E_{\rm br}$ and the maximum energy $E_{\rm max} = 5 \times 10^{13}\,{\rm eV}$ the power law index is $p_2 = 4.3$. Using these parameters in the model did not give a good representation for the data of 3C 111,

Figure 7.14: Same SED as in Figure 7.13, the line shows a SSC model for the FR-I radio galaxy Cen A (parameters from Abdo et al. 2010c).

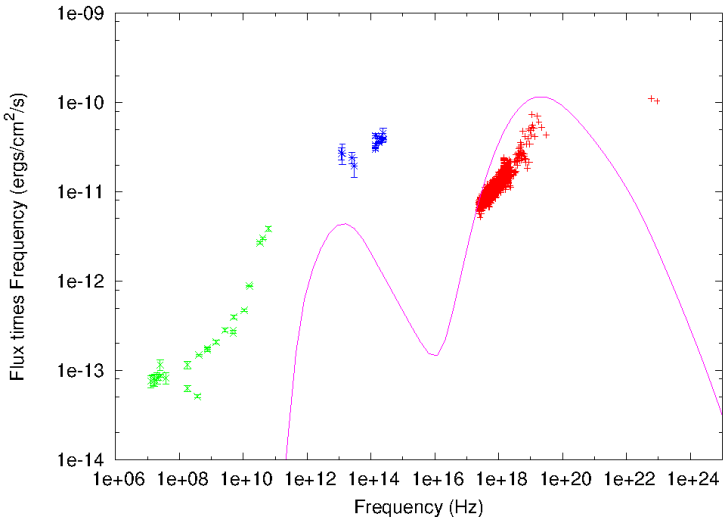

see Figure 7.14. This model shows the synchrotron peak frequency is at $\nu_{\rm S} = 1 \times 10^{14}$ Hz and the inverse Compton peak frequency is $\nu_{\rm IC} = 12 \times 10^{19}$ Hz, while for 3C 111 the synchrotron peak should be closer to $\nu_{\rm S} \sim 10^{15}$ Hz and the inverse Compton peak should be $\nu_{\rm IC} \sim 10^{21}$ Hz. The synchrotron branch does not have enough power, and the inverse Compton branch does not represent the *Fermi*/LAT data.

Starting from the parameters found for Cen A by Abdo et al. (2010c), we started to modify the input parameters to increase the peak frequencies and to better represent the shapes of the branches. The indices of the power law are tied to the power law index of the X-ray spectrum, via $s_X = (p-1)/s$, where $s_X \sim 1.6$, which would give for the first spectral index $p_1 \sim 2$ (since the X-ray spectrum is not purely non-thermal). We found for the broken power law which represents the electron energy distribution, indices of $p_1 = 2$ and $p_2 = 2.2$, which is not a significant break. Therefore, the electron energy distribution is represented by the index $p = 2$, and the minimum energy $E_{\rm min} = 5.6 \times 10^6$ eV and the maximum energy $E_{\rm max} = 6.8 \times 10^9$ eV. For the magnetic field we found $B = 4 \times 10^{-2}$ G, for the radius $R_s = 2 \times 10^{16}$ cm and a Doppler factor of $\delta = 14$. This model, see Figure 7.15, has a synchrotron peak frequency of $\nu_{\rm S} = 10^{14}$ Hz and a inverse Compton peak frequency at $\nu_{\rm IC} = 10^{22}$ Hz. The parameters used are summarized in Table 7.3, where also the parameters for Cen A and the blazar Mrk 421 are shown for comparison.

Figure 7.15: Same SED as in Figure 7.13, the line shows the model found for 3C 111.

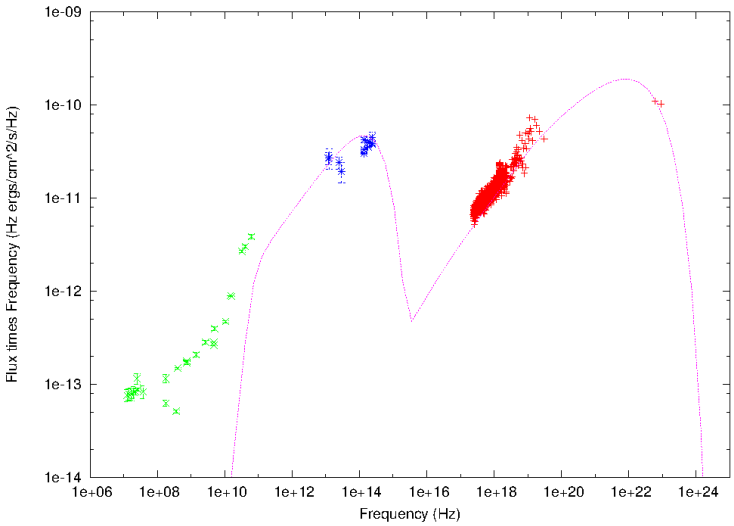

Table 7.3: Parameters used to model the SED of 3C 111 using the code by Krawczynski et al. (2004). For comparison, we include the fit parameters for the core of Centaurus A (Abdo et al. 2010c) and Markarian 421 (low flux state, Błażejowski et al. 2005).

Symbol	Description	3C 111	Cen A	Mrk 421
δ	Doppler factor	14	1.0	10.0
R_s	Radius of the emission volume [cm]	2×10^{16}	3.0×10^{15}	7.0×10^{15}
B	Magnetic field of emission volume [G]	4×10^{-2}	6.2	0.405
E_min	Minimum energy of the electron distribution [eV]	5.6×10^{6}	1.5×10^{8}	3.2×10^{6}
E_max	Maximum energy of the electron distribution [eV]	6.8×10^{9}	5.0×10^{13}	1.7×10^{11}
E_br	Break energy of the electron distribution [eV]	-	4.0×10^{8}	2.2×10^{10}
p_1	Spectral index of electron spectrum (E_min to E_br)	2	1.8	2.05
p_2	Spectral index of electron spectrum (E_br to E_max)	-	4.3	3.6
$\log L$	Bolometric luminosity (3-200 keV) [erg s^{-1}]	44.7	42.5[a]	45.5[b]

[a]Beckmann et al. (2011)
[b]Lichti et al. (2008)

7.7 Discussion

7.7.1 X-ray spectral features

High-energy cut-off

For 3C 111 we found a high-energy cut-off of $E_{\rm cut} = 227^{+143}_{-67}$ keV, using data from different instruments in a combined spectrum and the `pexrav` model, which describes an exponential cut-off power law reflected from neutral material. An indication for a turn-over can be seen in the power law indices for the different instruments in Table 7.2. At low energies between 0.4–10 keV the power law index is $\Gamma \sim 1.6$, and for the higher energies, the power law slope becomes steeper, between 15–200 keV the power law index is closer to $\Gamma \sim 1.9$. Using the `compPS` model, a Comptonization model which includes reflection, to this same data set we derived an electron temperature of $kT_{\rm e} = 91^{+22}_{-48}$ keV, which is consistent with the value derived using `pexrav`, via $E_{\rm cut} \simeq 3kT_{\rm e}$.

The value we derived for the high-energy cut-off is consistent with previous reported values of $E_{\rm cut} = 126^{+193}_{-50}$ keV (Molina et al. 2009), and $E_{\rm cut} = 146^{+224}_{-68}$ keV (Grandi et al. 2006), and lower limits of $E_{\rm cut} \geq 82$ keV (Dadina 2007), and $E_{\rm cut} \geq 75$ keV (Ballo et al. 2011). Earlier work by Rivers et al. (2011) using *RXTE* data between 3 keV and $\gtrsim$ 100 keV showed that the addition of a cut-off did not improve the fit. This might be due to the combination of different instruments used, and the wider energy range of the spectrum that was used in our case.

A high-energy cut-off is a typical property of the high-energy spectra of Seyfert galaxies, and is determined by the cut-off of the electron energy distribution. Typical values derived for the cut-off of Seyfert galaxies using *BeppoSAX* data are $E_{\rm cut} = 287 \pm 24$ keV (Dadina 2008) or using *INTEGRAL* IBIS/ISGRI stacked spectra $E_{\rm cut} = 85^{+16}_{-17}$ keV (Beckmann et al. 2009). The value of the cut-off found for 3C 111 can be considered in the expected range for Seyferts.

Centaurus A, a nearby gamma-ray bright FR-I radio galaxy, shows a cut-off at $E_{\rm cut} = 549^{+387}_{-168}$ keV, using the `pexrav` model on a spectrum based on *INTEGRAL* data between 3–1000 keV (Beckmann et al. 2011). Cen A shows a large angle to the line of sight, of ∼50–80°, and is classified as a Seyfert 1.5 type object. 3C 111 would be classified as a Seyfert 1. In these terms the lower cut-off energy of 3C 111 can be explained, since it is postulated Seyfert 1 objects have a lower cut-off energy than Seyfert 2 ($E_{\rm cut} = 230 \pm 22$ keV for Seyfert 1 and $E_{\rm cut} = 376 \pm 42$ keV, Dadina 2008). However, the difference can also be introduced in a variety of other ways (luminosity, FR-type). Due to the small sample of gamma-ray detected radio galaxies, an extensive study of their X-ray properties as a class of objects is not yet possible.

In X-ray spectra of AGN a high-energy cut-off can be observed, which can either have a thermal or non-thermal origin (see Section 7.2.1). The cut-off measured in 3C 111 can be interpreted as Seyfert-like, since it is in the range comparable to Seyfert galaxies. However, the cut-off can also be the result of non-thermal inverse Compton processes, and is in fact a smooth turn-over towards higher energies. Thermal processes cause an exponential cut-off, and the non-thermal turn-over curves in such a way to not exclude the gamma-ray and possible VHE emission. In the case of 3C 111, the current data do not allow to differentiate between these two types of cut-offs.

Reflection

Adding a reflection component to the model during the analysis of 3C 111 showed an improvement in the fit. Using `pexrav` we found a reflection of $R = 0.7 \pm 0.3$. Using the `compPS` model we confirmed a reflection component, with $R = 1.8^{+0.5}_{-0.7}$. The reflection scaling factor of $R > 1$ would indicate a specific geometry, for example a large covering fraction of cold disk material (Malzac 2001). The results from these two different models were not in agreement. Since the models were very different, `pexrav` is a descriptive model and `compPS` is a physical model, it is not unexpected to find different results. Similarly, both models were applied to the X-ray spectrum of Cen A, showing that the reflection derived with `compPS` is higher, but consistent, with the reflection derived using `pexrav` (Beckmann et al. 2011).

Earlier studies on the presence of a reflection component yielded different results, for example, using *BeppoSAX* data an upper limit of $R \leq 2.25$ (Dadina 2007) was found, which agrees with our result. Using the same *BeppoSAX* data, an upper limit to the reflection is $R < 0.3$ is found, which is inconsistent with our measurement (Grandi et al. 2006). A possible discrepancy might be introduced by a difference in the analysis, or different instruments of *BeppoSAX* being used: in the case of $R \leq 2.25$ the Low Energy Instrument LECS was not used, and so the energy range between ∼0.4–2 keV is excluded from the analysis.
Measurements of $R = 0.9 \pm 0.6$ using *XMM-Newton* and *Suzaku* (Molina et al. 2009), and $R = 0.35 \pm 0.06$ using *Suzaku* (Ballo et al. 2011) are in agreement with our findings. Other results, such as a reflection component of $R = 0.19^{+0.05}_{-0.04}$ using *XMM-Newton* (Ballo et al. 2011) are not consistent. In this case it is possible that difference is introduced due to fact that the spectrum used to find this value was between 0.4–10 keV, where our spectrum has a higher energy range, from 0.4–200 keV, and the reflection component depends on the energy band used to observe it.

Seyfert galaxies show a typical reflection of $R = 1.3^{+0.7}_{-0.4}$, as found from stacked *INTEGRAL* observations (Beckmann et al. 2009). The reflection observed in 3C 111, using either `pexrav` or `compPS` is consistent with this value.
The reflection observed in 3C 111 points to a thermal component in the X-ray spectrum, and the reflection scaling factor R found is in the expected range for Seyfert galaxies.

Iron line

The iron K-α line is thought to arise in the outer disk (or some other cold gas in the vicinity of the AGN core), and has a rest-frame energy of 6.4 keV. For the iron K-α line in the spectrum of 3C 111 we found a line energy of $E_{\rm line} = 6.11 \pm 0.02\,{\rm keV}$ ($z = 0.049$) and an equivalent width of $EW = 85 \pm 11\,{\rm eV}$, consistent with earlier reports of $EW = 60^{+20}_{-10}\,{\rm eV}$(Eracleous et al. 2000), $EW = 75 \pm 13\,{\rm eV}$(Ballo et al. 2011) and $EW = 86 \pm 16\,{\rm eV}$ (Tombesi et al. 2010), and $EW =\sim 40 - 100\,{\rm eV}$ (Lewis et al. 2005). Smaller values of $EW = 38.2^{+10.7}_{-9.2}\,{\rm eV}$ (Ballo et al. 2011) and $EW > 33 - 40\,{\rm eV}$ (Tombesi et al. 2011) have also been reported, and a larger value of $EW = 180 \pm 60\,{\rm eV}$(Rivers et al. 2011). These different measurements might be the result of variability. We plotted the correlation between the 4-10 keV flux and the EW of the iron line for several observations, see Figure 7.16. We used several statistical tests to verify if there is a significant correlation. The correlation has a Pearson's test coefficient of $r = -0.3$ and a Spearman's rank correlation coefficient of $r_s = -0.7$ with 7 d.o.f., which indicates a

Figure 7.16: Flux between 4–10 keV, in units of $10^{-11}\,\mathrm{ergs\,cm^{-2}\,s^{-1}}$, plotted against the EW in eV, data taken from this work and additional papers, see text. Using a linear regression fit a correlation between the two parameters was derived, the grey dashed line indicates the $1-\sigma$ error region on this correlation.

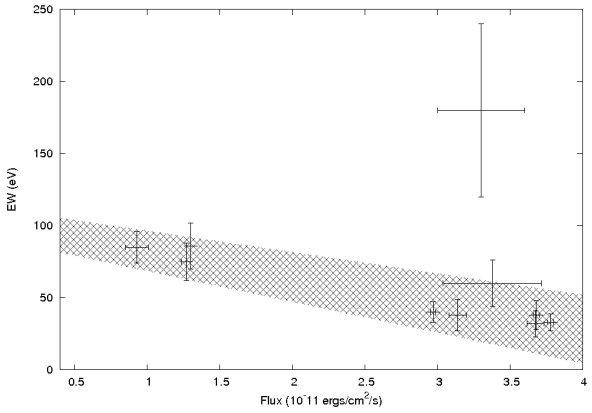

believable correlation between the 4–10 keV flux and the EW. When the large measurement of $EW = 180 \pm 60\,\mathrm{eV}$ is omitted, the correlation significance increases to $> 99\%$.
It is likely that the strength of the iron line is not variable, but the underlying flux is variable with a factor of ~ 5. The variability indicates that this continuum flux is produced in a non-thermal, variable process. This variability results in the iron line being more or less visible depending on the continuum flux. This explains the measurements of a low EW: at the moment the source was observed the continuum flux was at a higher state, drowning out the iron line flux.

Earlier surveys of Seyfert galaxies showed that the average EW is $EW = 450 \pm 70\,\mathrm{eV}$, where the Seyfert 1 objects have a slightly smaller average of $EW = 220 \pm 30\,\mathrm{eV}$ and the Seyfert 2 objects showed an average larger $EW = 700 \pm 200\,\mathrm{eV}$ (Dadina 2008). Compared to this 3C 111 shows a much weaker iron line, which could be evidence for a non-thermal component in the spectrum. However, recent work with high spectral resolution has shown that the EW of the iron K-α line in Seyferts is much lower on average, $EW = 53 \pm 3\,\mathrm{keV}$. This would indicate that the iron line measurement for 3C 111 is similar to Seyfert sources, and is an argument for a thermal core. However, the continuum flux of 3C 111 is partly variable in the X-ray band, which indubitably points to a non-thermal contribution.

CompPS

Fitting the spectrum of 3C 111 with the `compPS` model yielded a temperature for the electron cloud of $kT_\mathrm{e} = 91^{+22}_{-48}\,\mathrm{keV}$, a Compton parameter of $y = 0.6 \pm 0.1$ ($\tau = 0.8$) and a reflection scaling parameter of $R = 1.8^{+0.5}_{-0.7}$. This model has also been applied to other radio galaxies, such as Cen A, and NGC 4151, an optically thick Seyfert 1.5 galaxy. The hard X-ray spectrum of Cen A shows a cut-off of $kT_\mathrm{e} = 206 \pm 62\,\mathrm{keV}$, a Compton parameter of $y = 0.42^{+0.09}_{-0.06}$, which corresponds to an optical depth of $\tau = 0.26$, and a reflection scaling component of $R = 0.12^{+0.09}_{-0.10}$. The Compton y-parameter derived for Cen A is similar to 3C 111, but the

optical depth and the electron temperature are much lower.

NGC 4151 shows a dependence on the flux state for the optical thickness, which can decrease to $\tau \sim 0.3 - 0.6$ in the dim state to $\tau \sim 2.6$ in the bright state. In the dim state the electron temperature is $kT_{\rm e} \sim 180 - 230\,{\rm keV}$, and the reflection $R \sim 0.75 - 1$. In the bright state the electron temperature drops to $kT_{\rm e} \sim 54 - 73\,{\rm keV}$, and the reflection to $R \sim 0.4 - 0.55$. 3C 111 can be compared with the dim state optical depth, and the high state electron temperature of NGC 4151. The reflection we derived for 3C 111 is higher than both the reflection found in Cen A and NGC 4151.

7.7.2 Gamma-ray emission from 3C 111

3C 111 is included in the first *Fermi*/LAT source catalogue (Abdo et al. 2010a) based on 11 months of data, but is excluded in the second source catalogue where two years of data have been used (Nolan et al. 2012). This might be due to the likely variability of the source, but also to the change in analysis procedure. Since 3C 111 has also been observed with *CGRO*/EGRET, and associated with the source 3EG J0416+3650 (see Section 7.2.2), we pose that the gamma-ray detection of this source is significant.

We analysed 2 years *Fermi*/LAT, which yielded a $TS \sim 12.5$ for 3C 111, which is $\sim 3.5\sigma$. For the flux above 100 MeV we found $f = 1.3 \times 10^{-8}\,{\rm ph\,cm^{-2}\,s^{-1}}$, and a power law index of $\Gamma_\gamma = 2.4$. The first *Fermi*/LAT catalogue yielded for 3C 111 a significance of 4.3σ, a flux above 100 MeV of $f = 4.5 \times 10^{-8}\,{\rm ph\,cm^{-2}\,s^{-1}}$ and a power law index $\Gamma_\gamma = 2.6 \pm 0.2$, using 11 months of data. Since the source is variable in gamma-rays (see Section 7.2.2, Kataoka et al. 2011; Grandi et al. 2012), the lower detection significance and flux found in this work compared to the catalogue is likely due to the source being less bright in the second year. The power law index for both years is consistent, so the origin of the emission might not have changed. The variability is connected to the expulsion of knots from the core into the jet, so it is likely that during a new knot expulsion the gamma-ray brightness of the source will increase again.

7.7.3 SED

For variable sources, having a SED using simultaneously acquired data is important, to avoid mixing different spectral states. Multi-wavelength campaigns as organised for very variable objects give an unbiased view. In the SED presented here, the observations are not simultaneous. For example, the historical data has been taken over different years. Also, the X-ray and gamma-ray observations are the result of accumulated data taken over several years. 3C 111 is only moderately variable at most wavelengths. For example, hard X-ray studies showed no significant variability using 9 months of *Swift*/BAT data (Beckmann et al. 2007). In the radio domain, Grossberger et al. (2012) present decade-long light curves at 4.8 GHz, showing variations up to a factor of 2, which can be considered insignificant in the context of the SED. This can also be seen in the SED, the radio observations used here have been made over several decades, yet the SED does not show much variation. Other radio galaxies, such as Pictor A (Brown & Adams 2012) and NGC 1275 (Antón et al. 2004) have been analysed as well using time-averaged SEDs, confirming that gamma-ray detected radio galaxies are much

less variable than the *Fermi* detected blazers.

In the final model of the SED of 3C 111 the radio points were not properly accounted for. For observatories that operate at different wavebands there are large differences in the field of view and resolution of the acquired data. This is partially a technical problem (for example angular resolution at hard X-rays and beyond is much coarser than at radio and optical), but the resolution RL that can be achieved also depends on the wavelength λ and the dish diameter D, via $RL = \lambda/D$. At long radio wavelengths it is likely that we probe different regions of the source, such as the core, the jet with the knots, and the radio lobe and the hot spots. Obviously, this is not accounted for in the one-zone model, which instead assumes a single emission site. The SSC model likely overestimates the X-ray emission since we know from the spectrum that a thermal component is present and contributes in this energy range. The SSC emission in the X-ray band should therefore be considered to be an upper limit. Emission from the host galaxy is not taken into account in this model. However, as can be seen from the SED, in the wavebands where the host galaxy would provide a contribution (infrared to UV) the jet model gives a proper representation of the data.

The model parameters for 3C 111 can be found in Table 7.3. Compared with the low luminosity FR-I radio galaxy Cen A (Abdo et al. 2010c) the parameters used are quite different. The Doppler factor used to model Cen A, $\delta = 1.0$, is much lower than the one used in 3C 111, $\delta = 14$. Similarly the radius of the emitting region R_s is smaller for Cen A, $R_s = 3.0 \times 10^{15}$ cm, and for 3C 111 we found a radius of $R_s = 2 \times 10^{16}$ cm. The magnetic field of emitting region used for Cen A, $B = 6.2$ G, and for 3C 111 the magnetic field is less strong, $B = 4 \times 10^{-2}$ G. Since 3C 111 is a more luminous source, it is expected that the Doppler factor δ, which boosts the emission, the radius of the emitting region R_s, which defines the amount of particles, and/or the magnetic field B, which is related to the synchrotron power, is larger, since these parameters influence the overall power in the SED. For 3C 111 we used a simple power law for the electron energy distribution with power law index $p = 2$, while for Cen A a more complex broken power law is used, with first power law index $p_1 = 1.8$ and second power law index $p_2 = 4.3$. This is mainly due to the better sampling of the SED in the case of Cen A, which allows for more complex modelling. Overall, the physical properties of the X-ray emitting plasma in 3C 111 and Cen A appear rather similar, although Cen A is less luminous which can be seen in the lower Doppler factor and smaller emission region size.

When comparing 3C 111 with the blazar Mrk 421, both objects shows a similar Doppler factor δ. For Mrk 421 the Doppler factor is $\delta = 10$ and for 3C 111 we found $\delta = 14$. The magnetic field is 10 times stronger for Mrk 421, $B = 0.405$ G, whereas the radius of the emitting region is larger for 3C 111, $R_s = 2 \times 10^{16}$ cm and for Mrk 421 $R_s = 7 \times 10^{15}$ cm was used. Since Mrk 421 is a more powerful source than 3C 111, the smaller radius of the emitting region is countered by the stronger magnetic field.

SSC modelling is not possible on all gamma-ray detected radio galaxies. For example, the nearby FR-II radio galaxy Pictor A hinted at gamma-ray detection with a $TS = 20$ from two years of observation in the second *Fermi*/LAT catalogue, which was confirmed by using 3 years of observations by Brown & Adams (2012). The authors also applied a SSC model to the emission of the radio lobes, as has been done for Cen A (Abdo et al. 2010c), which are resolved in X-ray, optical and radio wavelengths. SSC modelling showed that it was not

possible to account for both the gamma-ray emission and the X-ray emission at the same time, which hints at other processes, or a different origin such as the core or relativistic jets for the gamma-ray emission.
The Unified theory assumes that the powerful FR-II radio galaxies are off-axis FSRQ blazars which have efficient accretion, and the less luminous FR-I galaxies are comparable to the BL Lac objects, which have inefficient accretion. In the SED FSRQs show a need for an external Compton component in addition to the SSC, whereas BL Lacs can be modelled with only a SSC component. In the SED for 3C 111 we show we can model the broad-band emission with only an SSC component, there is no need for an additional EC component. This might be physical, and thus showing a discrepancy in this Unification theory. However the lack of data in the inverse Compton branch might also not allow us to properly model the SED, and thus conceal the need for additional external Compton emission.

7.8 Conclusion

The first *Fermi*/LAT catalogue showed that not only blazars, but also a few radio galaxies show gamma-ray emission. For blazars the emission is thought to originate in the relativistic jet, where the Doppler boosting explains the bright emission. Radio galaxies are viewed with an angle to the jet, exposing the core. For these objects the origin of the gamma-ray emission is not clear. In addition, most high energy instruments have a large angular resolution, which does not allow to distinguish between separate components for most objects.

For 3C 111 the gamma-ray emission is variable, and Grandi et al. (2012) has shown, using multi-wavelength analysis, that the GeV emission appears to originate from a compact knot which appeared in the jet. This knot is separated from the core, and is placed 0.3 pc from the central engine. In this work we have analysed the X-ray spectrum of gamma-ray bright object 3C 111 between 0.4–200 keV to study the high energy emission of this object. For this we used data from several instruments, to get a spectrum as unbiased as possible. We found the best-fit model to be an absorbed cut-off power law with a reflection component and a Gaussian component for the 6.4 keV iron K-α line. The iron line and reflection originate in the core near the compact object, and are seen in Seyfert galaxies. We found that the iron line equivalent width is variable depending on the continuum flux, which points to a non-thermal contribution. The high-energy cut-off can be the result of either thermal or non-thermal processes, and with the data at hand it is not possible to distinguish between these types of cut-off.

We also modelled the broad-band SED, using the analysed X-ray data and gamma-ray data from *Fermi*/LAT, and historical radio, infrared and optical observations. Using a single zone SSC code we find that we can represent the overall emission from 3C 111 quite well, which implies that the underlying broad-band emission from the source is rather non-thermal. In the Unified theory FR-II radio galaxies are thought to be misaligned FSRQ blazars, objects with strong jets. FR-I objects are thought to be connected to the BL Lac type blazars, which are less luminous and are thought to have weak jets and inefficient accretion. We show in the SED that there is no need for an external Compton component, which is necessity for FSRQ blazars. This also points to the low accretion scenario in this source: in external Compton (EC) scenarios often the broad line region or the accretion disk itself are thought to be the source of the seed photons of the EC process. But because the accretion flow is low in 3C 111,

the disk luminosity is low and so is the luminosity of the broad line region.

A&A 545, A90 (2012)
DOI: 10.1051/0004-6361/201219302

Astronomy & Astrophysics

The nature of the multi-wavelength emission of 3C 111

S. de Jong, V. Beckmann, and F. Mattana

François Arago Centre, APC, Université Paris Diderot, CNRS/IN2P3, CEA/Irfu, Observatoire de Paris, Sorbonne Paris Cité, 10 rue Alice Domon et Léonie Duquet, 75205 Paris Cedex 13, France
e-mail: dejong@in2p3.fr

Received 28 March 2012 / Accepted 12 July 2012

ABSTRACT

Aims. We attempt to determine the nature of the high energy emission of the radio galaxy 3C 111, by distinguishing between the effects of the thermal and non-thermal processes.
Methods. We study the X-ray spectrum of 3C 111 between 0.4 keV and 200 keV, and its spectral energy distribution, using data from the *Suzaku* satellite combined with INTEGRAL, *Swift*/BAT data, and *Fermi*/LAT data. We then model the overall spectral energy distribution by including radio and infrared data.
Results. The combined *Suzaku*, *Swift* and INTEGRAL data are represented by an absorbed exponentially cut-off power-law with reflection from neutral material with a photon index $\Gamma = 1.68 \pm 0.03$, a high-energy cut-off $E_{\rm cut} = 227^{+143}_{-67}$ keV, a reflection component with $R = 0.7 \pm 0.3$ and a Gaussian component to account for the iron emission-line at 6.4 keV with an equivalent width of $EW = 85 \pm 11$ eV. The X-ray spectrum appears dominated by thermal, Seyfert-like processes, but there are also indications of non-thermal processes. The radio to γ-ray spectral energy distribution can be fit with a single-zone synchrotron-self Compton model, with no need for an additional thermal component.
Conclusions. We suggest a hybrid scenario to explain the broad-band emission, including a thermal component (iron line, reflection) that dominates in the X-ray regime and a non-thermal one to explain the spectral energy distribution.

Key words. galaxies: active – gamma rays: galaxies – X-rays: galaxies – galaxies: individual: 3C 111

1. Introduction

Radio galaxies are a subclass of active galactic nuclei (AGNs) and in the unification model of AGN radio galaxies are the radio-loud counterparts of Seyfert galaxies (Antonucci 1993; Urry & Padovani 1995). For both of these classes, it is thought that the inclination is large, such that the observer views the core, which is dominated by thermal processes through absorbing material. This differs from blazars, where the inclination angle is very small. The observed emission originates in the relativistic jet, which is dominated by non-thermal processes. Owing to the Doppler boosting of the emission in the jet, the energy of the observed emission from blazars can reach the γ-ray regime, even up to TeV energies. Several non-blazar AGNs have also been found to emit significantly in the γ-ray regime (Hartman et al. 2008; Abdo et al. 2010c; Ackermann et al. 2011). Although there have been several theories (i.e. misaligned jet, shocks in the radio lobes) about the origin of this high-energy radiation, conclusive support of any of these theories is yet to be found.

3C 111 is a nearby ($z = 0.049$, Sargent 1977) flat-spectrum FR-II radio galaxy (Fanaroff & Riley 1974; Linfield & Perley 1984) that displays strong, broad emission-lines in the optical (Sargent 1977) and an iron-emission line in the X-ray regime (Lewis et al. 2005), similar to Seyfert galaxies. In the radio regime, the galaxy's emission is dominated by the relativistic jet, which has an angle of 18° to our line of sight (Jorstad et al. 2005). The projected size of the jet is 78 kpc (Bridle & Perley 1984). There is no visible counter-jet, although a bright lobe is detectable in the opposite direction of the observed jet, which is likely fed by the undetected counter-jet (Linfield & Perley 1984).

Earlier studies of 3C 111 in the X-ray band have identified the high energy cut-off of the spectrum. Dadina (2007) found a lower limit of $E_{\rm cut} \geq 82$ keV using *BeppoSAX* data and Ballo et al. (2011) derived a similar lower limit to the cut-off of $E_{\rm cut} \geq 75$ keV, using data from *XMM-Newton* and *Suzaku*/XIS and PIN. Molina et al. (2009), using *XMM-Newton*, *Swift*, and INTEGRAL data, constrained the cut-off energy to be $E_{\rm cut} = 126^{+193}_{-50}$ keV. It is uncertain whether a reflection component is present in the X-ray spectrum. An upper limit of $R \leq 2.25$ was found by Dadina (2007) using *BeppoSAX* data and constraints of $R = 0.9 \pm 0.6$ were derived by Molina et al. (2009) and $R = 0.35 \pm 0.06$ by Ballo et al. (2011) using *Suzaku*/XIS and PIN data. Ballo et al. (2011) used *XMM-Newton* data to find the reflection in the energy range 0.4–10 keV to be $R = 0.19^{+0.05}_{-0.04}$. Rivers et al. (2011) did not detect a reflection component, using RXTE data between 3 keV and ≥100 keV. The equivalent width (EW) of the iron line at 6.1 keV has been measured several times and is likely variable. Ballo et al. (2011) and Tombesi et al. (2010) found similar values of $EW = 75 \pm 13$ eV (*Suzaku*/XIS and PIN) and $EW = 86 \pm 16$ eV (*Suzaku*/XIS), respectively. Using *Suzaku*/XIS data of three different observations taken two years later, Tombesi et al. (2011) found a smaller EW of between $EW > 33$ eV and $EW > 40$ eV. Similarly, Ballo et al. (2011) used *XMM-Newton* data to fit the 0.4–10 keV spectrum and found an $EW = 38^{+11}_{-9}$ eV.

3C 111 has been detected in γ-rays by CGRO/EGRET (Hartman et al. 1999; Sguera et al. 2005; Hartman et al. 2008), and was included in the first *Fermi*/LAT catalogue (Abdo et al. 2010a). In the second *Fermi*/LAT catalogue, the source was omitted since it had no longer been significantly detected

(Nolan et al. 2012). 3C 111 is likely variable in the γ-ray regime (Ackermann et al. 2011). Using 24 months of *Fermi*/LAT data, Grandi et al. (2012) found 3C 111 to be detectable during a short time-period ($\Delta t \sim 30$–60 days), limiting the radius of the emission region to be $R < 0.1$ pc (assuming a Doppler factor of $\delta = 3$) based on causality arguments. The detectability of the source in the GeV energy range coincided with an increase in the flux in the millimeter, optical and X-rays regimes, indicating the emission is likely to emerge from the same region. Since the outburst in millimeter, optical, and X-rays is associated with the ejection of a bright radio knot, this indicates that the GeV emission originates from the radio core within 0.3 pc of the central supermassive black hole.

To understand the physical processes causing the emission in 3C 111, we first study the X-ray to γ-ray spectrum to find whether the emission is the product of thermal (Seyfert-like) or non-thermal processes (blazar-like) or a combination of both. We then model the spectral energy distribution (SED) to understand the processes dominating the broad-band radiation of 3C 111 from radio to high energies.

2. Observations and data reduction

To cover a large energy band from X-rays to γ-rays and study the high-energy emission from 3C 111, we used data from several different instruments.

2.1. Suzaku-XIS/PIN

3C 111 was observed by *Suzaku* from 22 August 2008 to 25 August 2008 with a total elapsed time of 236.9 ks in HXD nominal pointing mode. We analysed data from the X-ray Imaging Spectrometer (XIS, Koyama et al. 2007) and Hard X-ray Detector (HXD, Takahashi et al. 2007). The XIS instrument consists of three separate CCD detectors and has an energy range of ~0.2–12.0 keV. The HXD is a collimated instrument, consisting of two independent detector systems, silicon PIN diodes that function in the range ~10–60 keV and GSO scintillation counters covering the energy range ~30–600 keV.

For the observations made with the XIS, we used the clean events provided by the instrument team where the standard event cuts had been applied.

The flux of 3C 111 is too low above 70 keV to extract a significant spectrum from the HXD/GSO detector, hence we used only HXD/PIN data. The *Suzaku* team provides a response file for the PIN, which depends on both the epoch in which the data were taken and the pointing mode. In addition a non X-ray background (NXB) per observation is available for the PIN analysis. After filtering the source and background files in time using the good time intervals, we extracted the source and background spectra. The source spectrum needed to be corrected for dead-time events, which we achieved using HXDDTCOR. The NXB was simulated with ten times more counts to suppress statistical errors. We therefore needed to increase the exposure time of the background spectrum by a factor of ten. Using XSPEC, we simulated the cosmic X-ray background (CXB) using the PIN response file for the flat emission distribution in the proper epoch and point mode. We combined the NXB and CXB files and used this as a background in our analysis.

2.2. INTEGRAL IBIS/ISGRI

The International Gamma-Ray Astrophysics Laboratory (INTEGRAL; Winkler et al. 2003) is a γ-ray observatory with several instruments on board. We used the INTEGRAL Soft Gamma-Ray Imager (ISGRI), which is part of the Imager on Board INTEGRAL Spacecraft (IBIS), a coded-mask detector. ISGRI is sensitive between 15 keV to 1 MeV (Lebrun et al. 2003).

We used all data collected by INTEGRAL since the launch of the satellite up to August 2009, with a total exposure time of 508 ks. We first created individual spectra for all science windows (a science window is all data produced during one pointing) using the IBIS_SCIENCE_ANALYSIS routine. We then summed all the individual spectra to achieve a higher signal-to-noise ratio.

2.3. Swift-BAT

The Burst Alert Telescope (BAT) aboard the *Swift* satellite is a coded-aperture camera with an energy range of 14–195 keV for imaging (Barthelmy et al. 2005). Since the BAT telescope monitors the sky continuously and has a large field of view (1.4 sr, partially coded), it has regularly observed 3C 111.

We used data from the 58-month hard X-ray survey, from 2004 December to the end of 2009 May (see Tueller et al. 2010; Baumgartner et al. 2010). The detected flux for 3C 111 in this survey is 1.2×10^{-10} erg cm^{-2} s^{-1} between 14 keV and 195 keV.

2.4. Fermi-LAT

The Large Area Telescope (LAT) aboard the *Fermi* satellite operates in an energy range between 20 MeV and 300 GeV (Atwood et al. 2009). The LAT is a pair-conversion telescope with a very wide field of view that scans the sky continuously. During the nominal all-sky survey observing mode of *Fermi*/LAT, a total effective exposure time of 83.7 Ms was accumulated in the direction of 3C 111 between 4 August 2008 and 20 April 2011.

We selected diffuse-event-class photons (P6_V3 instrument response functions) between 100 MeV and 200 GeV in a circular region of interest with radius of 15° around the source. Events with a zenith angle of more than 105° were excluded (Abdo et al. 2009). We used the standard cuts proposed by the *Fermi* team based on the data quality of the events and the instrument configuration.

The maximum-likelihood analysis tool GTLIKE models all the emission in a given region, which can contain several sources. The goodness of fit is expressed as the log-likelihood value which is the probability of obtaining the data given an input model. After creating a model including all detectable sources in the field, we used GTLIKE to fit the model until the log-likelihood value was maximised. We found the test statistic value of 3C 111 to be $TS = 12.8$, which corresponds to a significance of ~3σ. The data provided only two significant points so it is impossible to fit the spectrum in e.g. XSPEC. However, when creating the spectrum, GTLIKE gives a spectral slope of $\Gamma_\gamma = 2.41 \pm 0.17$ across the range 0.1–200 GeV and a flux of $f = 1.2 \times 10^{-8}$ ph cm^{-2} s^{-1}.

3. Results

3.1. X-ray spectrum

We simultaneously fitted the X-ray spectra between 0.4 keV and 200 keV, in XSPEC (Arnaud 1996). We started our analysis by fitting the spectrum with an absorbed power-law and a

Table 1. Parameters for the individual power-law fits of the data, and their 90% confidence levels.

Instrument	Epoch	Exposure time	PL index	f [erg cm^{-2} s^{-1}]	Energy range
XIS0	22–25 August 2008	95.4 ks	1.60 ± 0.02	$(2.20 \pm 0.02) \times 10^{-11}$	0.4–10 keV
XIS1	22–25 August 2008	95.4 ks	1.59 ± 0.02	$(2.24^{+0.03}_{-0.02}) \times 10^{-11}$	0.4–10 keV
XIS3	22–25 August 2008	95.4 ks	1.63 ± 0.02	$(2.2 \pm 0.02) \times 10^{-11}$	0.4–10 keV
PIN	22–25 August 2008	101.9 ks	1.52 ± 0.14	$(4.8 \pm 0.4) \times 10^{-11}$	12–60 keV
ISGRI	24 March 2003–19 August 2009	508 ks	1.90 ± 0.20	$(1.2 \pm 0.2) \times 10^{-10}$	20–200 keV
BAT	December 2004–May 2009	54 months[a]	1.99 ± 0.09	$(1.05 \pm 0.05) \times 10^{-10}$	15–150 keV
LAT	4 August 2008–20 April 2011	83.7 Ms	2.4 ± 0.2	$(6 \pm 2) \times 10^{-12}$	>100 MeV

Notes. [(a)] Elapsed time.

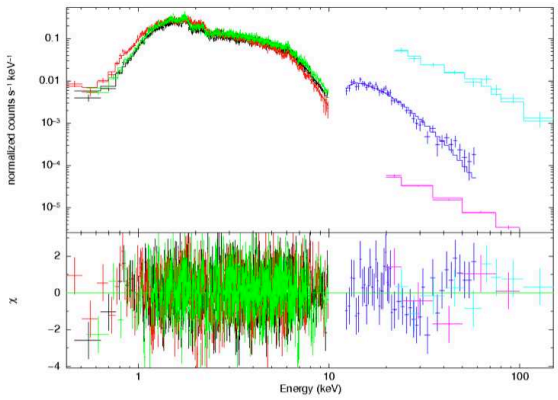

Fig. 1. Count spectrum of the combined *Suzaku*/XIS (0.4–10 keV), *Suzaku*/PIN (12–60 keV), INTEGRAL ISGRI (20–200 keV), and *Swift*/BAT (15–150) data with the fitted model: an absorbed cut-off power-law with reflection from neutral material and a Gaussian component to account for the iron line at 6.4 keV. The bottom panel shows the residuals in terms of the standard deviation with error bars of size one sigma.

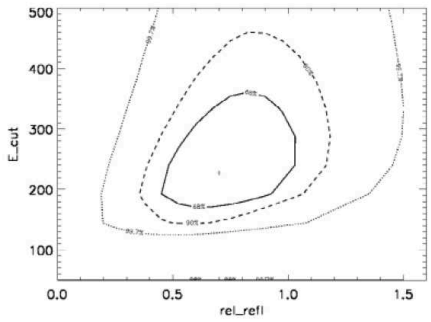

Fig. 2. Error contours for the best-fit `pexrav` model, reflection component R vs. the high-energy cut-off $E_{\rm cut}$. The contour levels correspond to $\Delta\chi^2$ of the 68%, 90%, and 99.7% statistical confidence regions. A cut-off below 130 keV is excluded at a 99.7% level.

Gaussian component at 6.1 keV to account for the redshifted iron emission-line. The fit resulted in a reduced chi-squared of $\chi^2_\nu = 1.14$ (1678 d.o.f.). We tried to improve our fit by using a cut-off power-law, which yielded a better fit with $\chi^2_\nu = 1.12$ (1677 d.o.f.). We explored the possibility of a broken power-law, but with a $\chi^2_\nu = 1.14$ (1676 d.o.f.), this gave no improvement in the fit. Adding a reflection component did further improve the fit, $\chi^2_\nu = 1.10$ (1676 d.o.f., F-test probability 4×10^{-8}). The resulting fit and the residuals are shown in Fig. 1. We derived the following best-fit parameters and 90% errors: the value for the equivalent hydrogen column-density $N_{\rm H} = (9.0 \pm 0.2) \times 10^{21}$ cm^{-2}, a power-law index of $\Gamma = 1.68 \pm 0.03$, a high-energy cut-off $E_{\rm cut} = 227^{+143}_{-67}$ keV and a reflection scaling factor of $R = 0.7 \pm 0.3$. Figure 2 shows the confidence contours of the reflection component versus the cut-off energy with $\Delta\chi^2$ of 68%, 90%, and 99.7%. We can exclude a cut-off below 130 keV at the 99.7% confidence level.

We fitted the data with a more physical model, `compPS` (Poutanen & Svensson 1996), which describes the process of thermal Comptonization. In this model, seed photons from the cool, thick accretion disc are injected into the electron plasma. The electron cloud can have several geometries, and we chose a plane-parallel slab: we also applied other geometries but found that they neither influenced the parameter values nor improved the fit. The electrons in the cloud have a Maxwellian distribution with an electron temperature $T_{\rm e}$ and an optical depth τ related to the Compton parameter $y = 4\tau kT_{\rm e}/(m_{\rm e}\,c^2)$. The seed photons are up-scattered from their initial energy $E_{\rm i}$ to $E_{\rm f} = {\rm e}^y E_{\rm i}$. The Compton scattering of the seed photons with the electrons in the plasma results in a spectrum that is afterwards reflected from a cool medium and then smeared out by the rotation of the disc.

The best-fit model gave a $\chi^2_\nu = 1.10$ (1676 d.o.f.). The values that we found for this model are an equivalent hydrogen column-density $N_{\rm H} = (9.0 \pm 0.2) \times 10^{21}$ cm^{-2}, a temperature of the electrons $kT_{\rm e} = 91^{+22}_{-48}$ keV, a reflection component $R = 1.8^{+0.5}_{-0.7}$, and a Compton parameter of $y = 0.6 \pm 0.1$, which corresponds to an optical depth $\tau = 0.8$.

We also fitted all data sets individually with an absorbed power-law and a Gaussian component. The values of the flux levels and power-law indices for these individual best fits to the data can be found in Table 1.

The measurements of the iron line at 6.4 keV are consistent in all three *Suzaku*/XIS spectra. After adding the three spectra together, we derived a line energy $E_{\rm line} = 6.11 \pm 0.02$ keV and an $EW = 85 \pm 11$ eV.

3.2. Fitting of the time-averaged SED

After we had created a SED based on our data, we modelled it with a public synchrotron self-Compton (SSC) code developed by Krawczynski et al. (2004)[1]. The SSC mechanism assumes an isotropic population of high-energy electrons that emit synchrotron radiation followed by inverse Compton scattering of the

[1] http://jelley.wustl.edu/multiwave/spectrum/?code

Table 2. Parameters used to model the SED of 3C 111 using the code by Krawczynski et al. (2004).

Symbol	Description	3C 111	Cen A	Mrk 421
δ	Doppler factor	14	1.0	10.0
R_s	Radius of the emission volume [cm]	2×10^{16}	3.0×10^{15}	7.0×10^{15}
B	Magnetic field of emission volume [G]	4×10^{-2}	6.2	0.405
E_{min}	Minimum energy of the electron distribution [eV]	5.6×10^{6}	1.5×10^{8}	3.2×10^{6}
E_{max}	Maximum energy of the electron distribution [eV]	6.8×10^{9}	5.0×10^{13}	1.7×10^{11}
E_{br}	Break energy of the electron distribution [eV]	–	4.0×10^{8}	2.2×10^{10}
p_1	Spectral index of electron spectrum (E_{min} to E_{br})	2	1.8	2.05
p_2	Spectral index of electron spectrum (E_{br} to E_{max})	–	4.3	3.6
$\log L$	Bolometric luminosity (3–200 keV) [erg s^{-1}]	44.7	42.5[a]	45.5[b]

Notes. For comparison, we include the fit parameters for the core of Centaurus A (Abdo et al. 2010b) and Markarian 421 (low flux state, Błażejowski et al. 2005). [(a)] Beckmann et al. (2011); [(b)] Lichti et al. (2008)

synchrotron photons to higher energies (Maraschi et al. 1992). The inverse Compton component may also include a thermal component of external seed photons (e.g. from the broad-line region or accretion disc) that are also Compton upscattered to high energies (external Compton component, Dermer & Schlickeiser 1993). The electron population is located in a spherical volume of radius R_s with a randomly orientated magnetic field B that moves relativistically towards the observer with a bulk Lorentz factor of Γ and an angle between the jet and the line of sight of θ. Thus, the radiation is Doppler-shifted with a Doppler factor $\delta = [\Gamma(1-\beta\cos\theta)]^{-1}$. The electron energy spectrum in the jet-frame follows a broken power-law, with indices p_1 and p_2, and is characterised by a minimum and maximum energy (E_{min}, E_{max}) and a break energy (E_{br}). The power in the SED is mostly influenced by the Doppler factor and both the radius and magnetic field of the emitting region. The shapes of the synchrotron and inverse Compton peaks and the peak frequencies depend strongly on the energies that define the electron population.

Since we only had data in the X-ray and γ-ray regimes, it was impossible to model the entire SED. We therefore added archival radio data, neglecting the observations that only included the core, and infrared data from the NED archive[2]. Assuming that the infrared emission is produced in the same region as the X-rays (the accretion disc or inner jet), we were able to use the column density found in the X-ray spectra, $N_H = 9.0 \times 10^{21}$ cm^{-2} to calculate the extinction in the V-band $A_V = N_H/(1.79 \times 10^{21}$ cm$^{-2})$ (Predehl & Schmitt 1995). From the extinction in the V-band, we calculated the extinction in the near-infrared bands J, H, and K using the correction factors from Schlegel et al. (1998). We removed the *Suzaku*/XIS data below 1 keV to avoid possible contamination by starburst emission.

Using our best fit of the X-ray spectrum, we were able to constrain some of the parameters. The indices of the power-law are tied to the power-law index of the X-ray spectrum: the first power-law index is $p_1 = 2$ (below E_{br}). Starting with this parameter and the initial parameters of the code, we optimised the model. We focused on the energies that characterise the electron population to define the shape of the peaks, and to change the overall energy output in the SED we adjusted the radius of the emitting region and its magnetic field, and the Doppler factor.

We found that the break in the electron power-law is insignificant and we therefore used a single power-law with index $p_1 = p_2$. Furthermore, we found the minimum energy of the electron distribution to be $E_{min} = 5.6 \times 10^6$ eV and the maximum energy $E_{max} = 6.8 \times 10^9$ eV. The Doppler factor is $\delta = 14$, the radius of the spherical emission-volume is $R_s = 2 \times 10^{16}$ cm, and the magnetic field is $B = 4 \times 10^{-4}$ G. The parameters that we used to fit the data can be found in Table 2, and the resulting plot is presented in Fig. 3. The addition of an external Compton component does not improve the model fit.

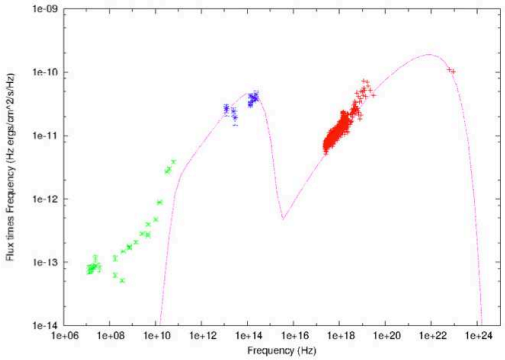

Fig. 3. SED showing 3C 111 unabsorbed fluxes and the SSC one-zone model. Crosses indicate data extracted and analysed in this work. We have added archival and deabsorbed IR and radio points from NED. The line shows the SSC model. See Table 2 for the values used.

4. Discussion

To evaluate the physical processes that dominate the high-energy emission from X-ray to γ-rays in 3C 111, we studied the X-ray spectrum and the broad-band SED.

4.1. X-ray spectrum

We constrained the high-energy cut-off of 3C 111 by applying the `pexrav` model, which describes an exponentially cut-off power-law spectrum reflected from neutral material (Magdziarz & Zdziarski 1995) in XSPEC. We found a cut-off $E_{cut} = 227^{+143}_{-67}$ keV using data from INTEGRAL/ISGRI, *Suzaku*/XIS and PIN, and *Swift*/BAT. An indication of the cut-off can already be seen in the power-law indices of the individual fits, which go from $\Gamma \sim 1.6$ in the soft X-rays to ~1.9 in the hard band (Table 1). We also applied the physical `compPS` model to

[2] http://ned.ipac.caltech.edu/

the same data, which yielded an electron temperature $kT_e = 91^{+22}_{-48}$ keV that can be related to the cut-off energy via $E_{cut} \simeq 3kT_e$. The electron temperature that we found using the compPS model is consistent with the cut-off energy that we derived using the pexrav model.

The value we found for the high-energy cut-off is consistent with the upper limits reported by Dadina (2007) and Ballo et al. (2011) and the measurement by Molina et al. (2009). Rivers et al. (2011) found, using data from RXTE from 3 keV to ≳100 keV, that the addition of a cut-off does not improve their fit of 3C 111. This might be because we used a combination of different instruments and a wider energy range for the spectrum presented here.

A high-energy cut-off is a typical property of the high-energy spectra of Seyfert galaxies, and the value we derived for 3C 111 is in the expected range for cut-off energies observed in Seyferts (Beckmann et al. 2009; Dadina 2008).

We measured the reflection in 3C 111 using both the compPS and the pexrav model to be $R = 1.8^{+0.5}_{-0.7}$ and $R = 0.7 \pm 0.3$, respectively. Since these models are very different (pexrav is a descriptive model and compPS is a physical model), we expect to find different measures of the reflection. Beckmann et al. (2011) applied both models to the hard X-ray spectrum of the radio galaxy Cen A and found that the reflection in the case of compPS is also slightly higher though consistent with the reflection found using the pexrav model.

The reflection scaling factor we derived, $R = 0.7 \pm 0.3$, using the pexrav model can be compared to earlier work using the same model. Our results are consistent with an upper limit reported by Dadina (2007), as well as with the constraints obtained by Molina et al. (2009) and Ballo et al. (2011). The latter also reported a significantly lower result, $R = 0.19^{+0.05}_{-0.04}$, when using only soft X-ray data between 0.4 keV and 10 keV. This is to be expected since the reflection component depends on the energy band used to observe it. In addition Rivers et al. (2011) did not detect a reflection component when applying the pexrav model between 3 keV and ≳100 keV. They constrained the model so as to avoid a high-energy cut-off, which might explain the difference from our result.

The value we measured is also consistent with the average Seyfert properties values of $R = 1.2^{+0.6}_{-0.3}$ for Seyfert 1 and $R = 1.1^{+0.7}_{-0.4}$ for Seyfert 2 galaxies (Beckmann et al. 2009).

For the iron line at 6.11 keV, we found that its $EW = 85 \pm 11$ eV, which is similar to the results of Ballo et al. (2011) and Tombesi et al. (2010). Smaller values between $EW > 33$ eV and $EW > 40$ eV were reported by Tombesi et al. (2011). Since the source is variable, it is likely that the iron line EW varies depending on the continuum. Figure 4 shows the correlation between the flux between 4 keV and 10 keV and the EW of the iron line for several observations. The correlation between the flux and the EW has a significance of >95%, a Pearson's test coefficient of $r = -0.3$, and a Spearman's rank correlation coefficient $r_s = -0.7$, showing a believable correlation between the flux level and the EW. When we did not consider the large EW measurement based on RXTE data presented by Rivers et al. (2011), we get a highly significant correlation with a probability of >99%. Tombesi et al. (2010, 2011) also report the power-law indices changing for the different data sets. Similarly, using a different data set, Ballo et al. (2011) derived an $EW = 38^{+11}_{-9}$ eV. Since there is a difference of several months between both data sets this value can again be explained by the source variability.

We found that the EW is smaller than the average value for Seyfert galaxies Dadina (2008), at $EW = 448 \pm 67$ eV, which

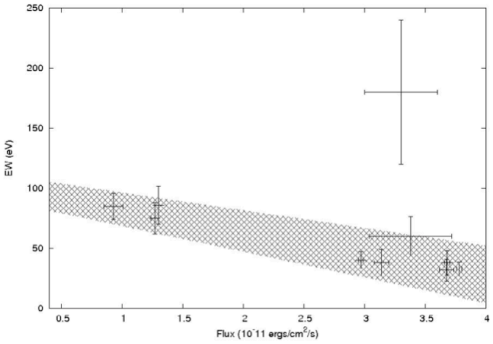

Fig. 4. Flux of the source versus the EW of the iron line. Data taken from Tombesi et al. (2010, 2011), Ballo et al. (2011), Rivers et al. (2011), Lewis et al. (2005), and Eracleous et al. (2000) and this work are plotted as points with error bars. We used a linear regression fit to derive a correlation between the two parameters. The fit is plotted with grey dashed lines indicating the 1σ error region.

can be compared to the average for Seyfert 1 galaxies of $EW = 222 \pm 33$ eV and for Seyfert 2 galaxies of $EW = 693 \pm 195$ eV. The correlation between EW of the iron line and the underlying power-law flux indicates that the line flux does not vary significantly, whereas the continuum varies by a factor of ~5. This can be naturally explained if the majority of the continuum flux is produced in a non-thermal and variable process. The small value of the EW of the iron line may indicate that the X-ray spectrum of 3C 111 does not only contain a thermal, but also a non-thermal contribution.

We also fitted the spectrum with the physical compPS model, deriving a temperature for the electron cloud $kT_e = 91^{+22}_{-48}$ keV, a Compton parameter $y = 0.6 \pm 0.1$ (which corresponds to an optical depth of $\tau = 0.8$), and a reflection component $R = 1.8^{+0.5}_{-0.7}$.

NGC 4151 is a well-studied case of a Seyfert core at hard X-rays. Beckmann et al. (2005) fitted the compPS model to the spectrum of the Seyfert galaxy NGC 4151 across the range 2–300 keV. They found for the electron plasma temperature $kT_e = 94^{+4}_{-10}$ keV, a reflection component $R = 0.72 \pm 0.14$ and an optical depth of $\tau = 1.3^{+0.13}_{-0.05}$. The hard X-ray spectrum (3–1000 keV) of Centaurus A, which is another nearby γ-ray detected radio galaxy, was also modelled with compPS by Beckmann et al. (2011). This yielded an electron plasma temperature of $kT_e = 206 \pm 62$ keV, a Compton parameter $y = 0.42^{+0.09}_{-0.06}$ (which corresponds to an optical depth of $\tau = 0.26$), and a reflection component of $R = 0.12^{+0.09}_{-0.10}$. NGC 4151 is optically thick, whereas both Cen A and 3C 111 are not. The optical thickness of NGC 4151 depends on the flux state and can decrease to $\tau =\sim 0.3$–0.6 in the dim state (Lubiński et al. 2010), when the electron temperature can increase to $T_e \sim 180$–230 keV. The optical depth of 3C 111 is similar to that of the dim state of NGC 4151, but the electron temperature is closer to the electron temperature of the brighter state. The reflection measured in 3C 111 is higher than those found in both NGC 4151 and Cen A.

Chatterjee et al. (2011) concluded that the X-ray spectrum of 3C 111 is of thermal inverse Compton origin, based on a correlation between the optical and X-ray fluxes, as well as a weak optical polarisation and a smaller variance in the optical than X-ray flux on shorter timescales. They concluded that these findings are consistent with a reprocessing model where the X-rays are mostly produced by inverse Compton scattering of thermal optical/UV seed photons from the accretion disc.

The cut-off we measured using the `pexrav` model may have either a thermal or a non-thermal origin. It can be interpreted as a high-energy cut-off measured in Seyfert galaxies. In the case of 3C 111, the cut-off value is also comparable to the typical cut-offs found in Seyfert galaxies. The cut-off observed in the `pexrav` model can also be caused by non-thermal inverse-Compton scattering processes. In this case, the smooth turnover of the inverse Compton branch towards higher energies appears as a cut-off in the `pexrav` model. While in the thermal inverse-Compton case the cut-off is exponential, the non-thermal spectrum is curved in such a way that γ-ray and VHE emission cannot be excluded. It is impossible to differentiate between an exponential and a simple cut-off in the hard X-rays based on the data at hand, thus both the non-thermal and the thermal interpretations of the curved X-ray spectrum are still valid. The reflection component is a property of Seyfert galaxies and a result of thermal processes. The value of the one we detect is in the typical range for reflection in Seyfert galaxies. The EW of the observed iron line is smaller than expected for Seyfert galaxies and is also variable, implying that the continuum is similarly variable. We therefore suggest that, while the thermal processes in the X-ray band in 3C 111 seem to dominate, we cannot exclude a non-thermal contribution.

4.2. γ-rays

3C 111 was proposed as a counterpart of the γ-ray source 3EG J0416+3650 in the third CGRO/EGRET catalogue, even though it fell outside the 99% probability region (Hartman et al. 1999). A re-analysis of the data (Sguera et al. 2005) concluded that 3EG J0416+3650 is likely associated with 3C 111. There are no other plausible counterparts in the EGRET error region, which is also larger than previously thought because the quoted errors were statistical only and did not take into account the larger systematic errors caused by inaccuracies in the Galactic diffuse model. The EGRET data were re-analysed (Hartman et al. 2008) when it was found that 3EG J0416+3650 is likely the result of the blending of more than one source. One of these components (detected only above 1 GeV) can be associated with 3C 111. Furthermore, 3C 111 was included in the first *Fermi*/LAT source catalogue (Abdo et al. 2010a) with a significance of 4.3σ. In the second *Fermi*/LAT source catalogue, 3C 111 was excluded because the source was no longer significantly detected (Nolan et al. 2012). However, 3C 111 is very likely to be variable (Ackermann et al. 2011) and therefore no longer detectable in the second year. This was also confirmed by Kataoka et al. (2011), who found a significance $>5\sigma$ for 3C 111 using 24 months of *Fermi*/LAT data and by Grandi et al. (2012) who found that the γ-ray emission is not persistent, but flaring and associated with the ejection of bright radio knots.

Since 3C 111 was detected by CGRO/EGRET and *Fermi*/LAT at different epochs, we assumed that the source is a variable γ-ray emitter. We included data from the first *Fermi*/LAT catalogue where the source was detected significantly. Our analysis gives a power-law index similar to that given in the first catalogue with a comparable flux level (Abdo et al. 2010a).

4.3. Spectral energy distribution

To construct the SED of a variable source, simultaneously acquired data are necessary in order to ensure that we make an unbiased measurement. The data used in the SED of 3C 111 were not acquired simultaneously, which can affect the results in the sense that the SED is composed of measurements from different spectral states. This effect is more severe for very variable objects, whereas at most wavebands 3C 111 is moderately variable. We refer, for example to Beckmann et al. (2007) who found no significant variability in hard X-rays for their study of 9 months of *Swift*/BAT data. For the radio domain, Grossberger et al. (2012) present decade-long light curves showing variations of up to a factor of 2 which we can consider as insignificant variability in the context of the SED. For other radio galaxies, it has also been shown that the use of non-simultaneous data to construct the SED does not introduce any significant bias. For example, the radio galaxies NGC 1275 (Antón et al. 2004) and Pictor A (Brown & Adams 2012) were also similarly analysed using time-averaged SEDs. The results for the physical parameters should thus not be significantly affected by the moderate variability of 3C 111.

The archival radio data that we used to model the SED were not well-represented by our SSC model. For observatories that operate at different wavebands, there are large differences in the data acquired in terms of the field of view and resolution. The resolution depends on the wavelength via $RL = \lambda/D$, where RL is the resolution, λ the wavelength, and D the dish diameter. It is therefore possible that we probe different regimes in the broad-band SED, something that the one-zone model does not account for.

In SSC models, the relativistic electron-energy distribution is often assumed to be a broken power-law with a break energy $E_{\rm br}$, a power-law index before the break of $p_1 < 3$ and a power-law index after the break of $p_2 > 3$ (see for example Ghisellini et al. 1996; Tavecchio et al. 1998; Krawczynski et al. 2004). The electron population is confined to region of radius $R_{\rm s}$ and a magnetic field B that moves with a Doppler factor δ along the jet. The electrons emit synchrotron radiation and inverse Compton radiation using the synchrotron photons as seed photons. For electrons with energies below the break energy $E_{\rm br}$, cooling of the electrons is the dominant emission source and in the regime after the break, the escape of electrons from the source dominates. The peak synchrotron power is emitted by electrons at the break energy (Tavecchio et al. 1998). In the case of 3C 111, we found that using a broken power-law gave a break energy of $E_{\rm br} = 1.6$ GeV and power-law indices of $p_1 = 2$ and $p_2 = 2.2$. The break between the two power-laws is insignificant. We therefore applied a single power-law with an index $p = 2$, based on the power-law index of the X-ray spectrum. In the case of a single power-law, the maximum synchrotron power is emitted near the maximum energy of $E_{\rm max} \simeq 7$ GeV.

The energies that define the electron distribution, $E_{\rm min}$ and $E_{\rm max}$ influence the shape of the synchrotron and inverse Compton peak and were chosen by ourselves empirically. If the minimum energy, $E_{\rm min}$, decreases, the maximum of the peak occurs at lower frequency and the slopes are less steep. Increasing the $E_{\rm min}$ increases the depth between the synchrotron and inverse Compton peak and steepens the rise and fall of the peaks. The maximum energy, $E_{\rm max}$, is tied to the peak frequencies of both the synchrotron and inverse Compton peak: increasing this value would increase the peak frequencies.

Abdo et al. (2010b) modelled the SED of the core of the radio galaxy Cen A, using simultaneous data from the radio up to the γ-ray regime, applying a single-zone SSC. Comparing the parameters for this model and our own (see Table 2), it is clear that the models have significantly different parameter values. The magnetic field has a much higher value in the case

of Cen A ($B = 6.2$ G), than the value we found for 3C 111 ($B = 0.04$ G). The higher magnetic field increases the resulting flux because the synchrotron power depends on the magnetic field. In contrast, the Doppler factor used to model Cen A is low ($\delta = 1$) compared to the value we found for 3C 111, $\delta = 14$. A lower Doppler factor means that the emission is less boosted and therefore appears less energetic. There are also three orders of magnitude difference between the emission volumes: for Cen A, $R_s = 3 \times 10^{15}$ cm was used, whereas we assumed $R_s = 2 \times 10^{16}$ cm for 3C 111. Since this defines the amount of particles this also causes the flux to be lower for Cen A than for 3C 111. The higher value used for the magnetic field is attenuated by the lower Doppler factor and radius for Cen A, which causes the overall output to be lower, as expected for the less luminous source.

Pictor A is another FR-II radio galaxy that was detected by *Fermi*/LAT as reported by Brown & Adams (2012), who modelled the SED of one of the hot-spots in the radio-lobe of Pic A with a one-zone SSC model using the same code that we applied. They concluded that it is impossible to describe both the X-ray and γ-ray emission using the SSC model. Since the γ-ray emission is very variable it is likely to originate from the jet, whereas the X-rays originate from the hot-spot. This appears to indicate that more than one zone is needed to model the entire SED.

Błażejowski et al. (2005) also used the Krawczynski code to model the high-energy peaked BL Lac object Mrk 421, assuming only an SSC component. The parameter values they derived are shown in Table 2. Both the Doppler factor ($\delta = 10$) and the emitting region radius ($R_s = 7 \times 10^{15}$ cm) chosen for Mrk 421 are smaller than those chosen for 3C 111, but are larger than those of Cen A. Similar to Cen A, the magnetic field value for Mrk 421, $B = 0.4$ G, is a factor of 10 stronger than for 3C 111. The smaller radius and Doppler factor decrease the flux, but owing to the strong magnetic field the flux in the SED for Mrk 421 is higher than the flux of 3C 111.

We conclude that the overall emission from 3C 111 can be modelled with a simple synchrotron self-Compton model, where no additional thermal Compton component is needed. Since the X-rays appear to be (mostly) of thermal origin, the SED provides an upper limit to the non-thermal emission in the X-ray band. There may be a thermal component in the SED, but with the current data we are unable to disentangle the possible thermal component from the overall non-thermal emission.

5. Conclusion

The origin of the high-energy emission from non-blazar AGNs remains unclear. Marscher et al. (2002) suggested that with the acceleration of the inner regions of the accretion disc a shock front will stream along the jet and the expulsion of a superluminal bright knot will follow. Grandi et al. (2012) show, using *Fermi*/LAT data, that the GeV emission of 3C 111 appears to originate from a compact knot confined to within 0.1 pc. This knot is clearly separate from the core and placed 0.3 pc from the central engine.

By analysing the X-ray spectrum and the broad-band SED, we have studied the nature of the high-energy emission of the radio galaxy 3C 111. We have presented an X-ray spectrum between 0.4 keV and 200 keV using data of 3C 111 acquired by several instruments and showed that the best-fit model is an absorbed cut-off power-law with both a reflection component and a Gaussian component to account for the iron line at 6.4 keV. The values we found for the reflection and high-energy cut-off are similar to those found in Seyfert galaxies, which would indicate that there is a thermal core visible. The cut-off can also originate from non-thermal processes and the EW of the iron line is variable and smaller than expected for Seyfert galaxies. We therefore conclude that the X-ray spectrum is mainly of thermal origin, but there may be a small non-thermal contribution.

Using the X-ray spectrum, together with γ-ray data from *Fermi*/LAT and archival deabsorbed radio and infrared data, we modelled the broad-band SED of 3C 111 using a single-zone synchrotron self-Compton model. This model is non-thermal and we also did not need to include an additional thermal component to model the SED. Since the X-ray emission is likely to have a combined thermal and non-thermal origin, the SSC model we used may overestimate the non-thermal contribution in the X-ray band and should therefore be considered an upper limit.

In conclusion, it seems that the high-energy emission from 3C 111 consists of both thermal and non-thermal components. In the X-ray spectrum, the thermal components manifest themselves in terms of an iron line and reflection. The non-thermal component is visible through the variability in the EW of the iron line. The high-energy cut-off can be the result of either thermal or non-thermal inverse Compton scattering, but our present spectrum does not allow us to distinguish which process is occurring. The broadband SED can be modelled with a non-thermal model, but it is possible there is a thermal component that we are unable to discern with the current data set.

Acknowledgements. Based on data provided by INTEGRAL, an ESA project funded by ESA member states (especially the PI countries: Denmark, France, Germany, Italy, Spain, Switzerland), Czech Republic, Poland, and with the participation of Russia and the USA. We acknowledge the use of public data from the *Swift* data archive. This research has made use of the NASA/IPAC Extragalactic Database (NED), which is operated by the Jet Propulsion Laboratory, California Institute of Technology, under contract with the National Aeronautics and Space Administration. This research has made use of NASA's Astrophysics Data System Bibliographic Services. We thank the anonymous referee for the comments that helped to improve the paper.

References

Abdo, A. A., Ackermann, M., Ajello, M., et al. 2009, ApJS, 183, 46
Abdo, A. A., Ackermann, M., Ajello, M., et al. 2010a, ApJS, 188, 405
Abdo, A. A., Ackermann, M., Ajello, M., et al. 2010b, ApJ, 719, 1433
Abdo, A. A., Ackermann, M., Ajello, M., et al. 2010c, ApJ, 720, 912
Ackermann, M., Ajello, M., Allafort, A., et al. 2011, ApJ, 743, 171
Antón, S., Browne, I. W. A., Marchã, M. J. M., Bondi, M., & Polatidis, A. 2004, MNRAS, 352, 673
Antonucci, R. 1993, ARA&A, 31, 473
Arnaud, K. A. 1996, in Astronomical Data Analysis Software and Systems V, eds. G. H. Jacoby, & J. Barnes, ASP Conf. Ser., 101, 17
Atwood, W. B., Abdo, A. A., Ackermann, M., et al. 2009, ApJ, 697, 1071
Ballo, L., Braito, V., Reeves, J. N., Sambruna, R. M., & Tombesi, F. 2011, MNRAS, 418, 2367
Barthelmy, S. D., Barbier, L. M., Cummings, J. R., et al. 2005, Space Sci. Rev., 120, 143
Baumgartner, W. H., Tueller, J., Markwardt, C., & Skinner, G. 2010, BAAS, 42, 675
Beckmann, V., Shrader, C. R., Gehrels, N., et al. 2005, ApJ, 634, 939
Beckmann, V., Barthelmy, S. D., Courvoisier, T. J.-L., et al. 2007, A&A, 475, 827
Beckmann, V., Soldi, S., Ricci, C., et al. 2009, A&A, 505, 417
Beckmann, V., Jean, P., Lubiński, P., Soldi, S., & Terrier, R. 2011, A&A, 531, A70
Błażejowski, M., Blaylock, G., Bond, I. H., et al. 2005, ApJ, 630, 130
Bridle, A. H., & Perley, R. A. 1984, ARA&A, 22, 319
Brown, A. M., & Adams, J. 2012, MNRAS, 421, 2303
Chatterjee, R., Marscher, A. P., Jorstad, S. G., et al. 2011, ApJ, 734, 43
Dadina, M. 2007, A&A, 461, 1209
Dadina, M. 2008, A&A, 485, 417
Dermer, C. D., & Schlickeiser, R. 1993, ApJ, 416, 458
Eracleous, M., Sambruna, R., & Mushotzky, R. F. 2000, ApJ, 537, 654
Fanaroff, B. L., & Riley, J. M. 1974, MNRAS, 167, 31

Ghisellini, G., Maraschi, L., & Dondi, L. 1996, A&AS, 120, C503
Grandi, P., Torresi, E., & Stanghellini, C. 2012, ApJ, 751, L3
Grossberger, C., Kadler, M., Wilms, J., et al. 2012, Acta Polytech., 52, 010000
Hartman, R. C., Bertsch, D. L., Bloom, S. D., et al. 1999, ApJS, 123, 79
Hartman, R. C., Kadler, M., & Tueller, J. 2008, ApJ, 688, 852
Jorstad, S. G., Marscher, A. P., Lister, M. L., et al. 2005, AJ, 130, 1418
Kataoka, J., Stawarz, Ł., Takahashi, Y., et al. 2011, ApJ, 740, 29
Koyama, K., Tsunemi, H., Dotani, T., et al. 2007, PASJ, 59, 23
Krawczynski, H., Hughes, S. B., Horan, D., et al. 2004, ApJ, 601, 151
Lebrun, F., Leray, J. P., Lavocat, P., et al. 2003, A&A, 411, L141
Lewis, K. T., Eracleous, M., Gliozzi, M., Sambruna, R. M., & Mushotzky, R. F. 2005, ApJ, 622, 816
Lichti, G. G., Bottacini, E., Ajello, M., et al. 2008, A&A, 486, 721
Linfield, R., & Perley, R. 1984, ApJ, 279, 60
Lubiński, P., Zdziarski, A. A., Walter, R., et al. 2010, MNRAS, 408, 1851
Magdziarz, P., & Zdziarski, A. A. 1995, MNRAS, 273, 837
Maraschi, L., Ghisellini, G., & Celotti, A. 1992, ApJ, 397, L5
Marscher, A. P., Jorstad, S. G., Gómez, J.-L., et al. 2002, Nature, 417, 625
Molina, M., Bassani, L., Malizia, A., et al. 2009, MNRAS, 399, 1293
Nolan, P. L., Abdo, A. A., Ackermann, M., et al. 2012, ApJS, 199, 31
Poutanen, J., & Svensson, R. 1996, ApJ, 470, 249
Predehl, P., & Schmitt, J. H. M. M. 1995, A&A, 293, 889
Rivers, E., Markowitz, A., & Rothschild, R. 2011, ApJS, 193, 3
Sargent, W. L. W. 1977, ApJ, 212, L105
Schlegel, D. J., Finkbeiner, D. P., & Davis, M. 1998, ApJ, 500, 525
Sguera, V., Bassani, L., Malizia, A., et al. 2005, A&A, 430, 107
Takahashi, T., Abe, K., Endo, M., et al. 2007, PASJ, 59, 35
Tavecchio, F., Maraschi, L., & Ghisellini, G. 1998, ApJ, 509, 608
Tombesi, F., Sambruna, R. M., Reeves, J. N., et al. 2010, ApJ, 719, 700
Tombesi, F., Sambruna, R. M., Reeves, J. N., Reynolds, C. S., & Braito, V. 2011, MNRAS, 418, L89
Tueller, J., Baumgartner, W. H., Markwardt, C. B., et al. 2010, ApJS, 186, 378
Urry, C. M., & Padovani, P. 1995, PASP, 107, 803
Winkler, C., Courvoisier, T. J.-L., Di Cocco, G., et al. 2003, A&A, 411, L1

8 M87: a weak BL Lac core in a nearby radio galaxy

This chapter describes the case of the radio galaxy M 87 and the work done within the course of this thesis. This nearby source has a FR-I morphology, and is detected both in gamma-rays and at very high energies, but had so far escaped a detection in hard X-rays. In the following Chapter the source is described, followed by the details on the analysis done based on X-ray and gamma-ray data, leading to the first detection of M87 in the hard X-ray band. Finally, the spectral energy distribution is discussed and it is shown that M87 hosts a weak BL Lac type AGN core at its centre. This work in progress was presented as a poster at the 9^{th} *INTEGRAL workshop*, and was published in the proceedings of this conference (de Jong et al. 2012c). A paper to be submitted to A&A is being prepared, as can be found at the end of this chapter on page 126.

8.1 Introduction

We started the study on M87 with two goals in mind. First we wanted to detect, or set an upper limit to the hard X-ray emission using the public, and private data we have with *INTEGRAL* IBIS/ISGRI. Second we wanted to analyse the spectral energy distribution (SED) in order to understand the physical processes responsible for the high-energy emission, and thus determine the nature of the central engine. This was done in a similar fashion to the case of 3C 111 in the previous chapter. The work on the SED of M87 is particularly interesting due to the lack of a hard X-ray detection, which would imply that if a synchrotron self-Compton (SSC) model is applied to the spectral energy distribution (SED), the inverse Compton branch would peak in gamma-rays (see Section 7.6.1), similar to a high-peaked BL Lac object such as Mrk 421, see Figure 4.6 for a broad band spectrum of this source (Abdo et al. 2011).

In addition, due to the small distance to M87 ($D = 16\,\mathrm{Mpc}$) we can image the different components of the source, such as the core, the jet and the hotspots, in soft X-rays for example with *Chandra*. Understanding the place of origin of the soft X-ray emission will help to study the hard X-rays and gamma-rays. In 3C 111 for example, it is possible to resolve the jet and core in for example radio but in the X-ray and gamma-ray band it is observed as a point source. Finally our study of M87 is complementary to our study of 3C 111 since, even though both sources are gamma-ray bright radio galaxies, the objects are very different: M87 is a low luminous FR-I source whereas 3C 111 is a bright FR-II source. Comparing them will help us understand the class of gamma-ray bright radio galaxies, and how to put them in the framework of the Unification theory (see Section 4.3).

8.2 Introduction to the source

M87 is a FR-I radio galaxy (Fanaroff & Riley 1974; Laing et al. 1983), meaning that the jets are brightest close to the core of the AGN. FR-I type sources often show symmetric jets, and the jets are less powerful than in the FR-II types. The jet of M87 has an apparent angle of $\theta = 30^{\circ}$ with respect to the line of sight (Bicknell & Begelman 1996). The central super massive black hole has a mass of $M_{BH} = (3-6) \times 10^9\, M_{\odot}$ (Macchetto et al. 1997; Gebhardt & Thomas 2009). M87 has a distance of 16 Mpc (Tonry 1991), due to its proximity it is possible to discern the different components of the source, such as the hotspots in the jet, in for example radio and optical (See Figure 8.1). The jet base has been imaged down to $40\,\mu$as resolution, corresponding to ~ 0.01 pc or ~ 5 Schwarzschild radii, using radio observations at 6 frequencies between 2.3 and 43.2 GHz. At the higher frequencies the jet base becomes more transparent due to the synchrotron emission becoming optically thin, and using observations at different frequencies allows to probe deeper into the jet. The observations at 43 GHz revealed that the jet base is located within 14–23 Schwarzschild radii from the central engine of the source, the super massive black hole (Hada et al. 2011). Doeleman et al. (2012) used radio interferometry at 1.3 millimetre to resolve the jet base in M87, and showed the base to have a size of ∼5.5 Schwarzschild radii. The size of the jet base can be correlated to the inner most stable orbit of the black hole, and the observations exclude a retrograde disk, in which the accretion disk and the super massive black hole have anti-parallel orbital angular momentum. This result agrees with the paradigm that the spin axes of the accretion disk and black hole will align due to angular momentum transfer from the disk (Gammie et al. 2004).

M87 has been observed in the VHE range the HEGRA array of Cherenkov telescopes (Aharonian et al. 2003). This detection has been confirmed by other TeV experiments, such as H.E.S.S. (Aharonian et al. 2006). The early gamma-ray mission *CGRO*/EGRET did not detect M87, with a 2σ upper limit of $f < 4 \times 10^{-8}\,\mathrm{ph\,cm^{-2}\,s^{-1}}$ above 100 MeV (Sreekumar et al. 1996). *Fermi*/LAT detected M87 using 6 months of observations, with a Test Statistic $TS \sim 60$, which corresponds to a significance of $\sim 7.7\sigma$(Abdo et al. 2009c). The first *Fermi*/LAT source catalogue includes M87 with a significance of 10.8σ between 100 MeV–100 GeV, an energy flux of $S = 1.75 \pm 0.38 \times 10^{-11}\,\mathrm{erg\,cm^{-2}\,s^{-1}}$ and a power law index of $\Gamma_{\gamma} = 2.33 \pm 0.12$ in the same energy range (Abdo et al. 2010a). This gamma-ray detection made M87 the third TeV gamma-ray detected radio galaxy, after Centaurus A, which is the only radio galaxy detected by *CGRO*/EGRET, and NGC 1275, a radio galaxy in the centre of a galaxy cluster (Abdo et al. 2009b).
Continuous monitoring using H.E.S.S. between 2003 and 2006 showed fast variations in the TeV band ($> 730\,$GeV), on time scales of days (Aharonian et al. 2006). The observations show an upper limit to the angular size is ∼3 arcmin, while the time scale of the fluctuations constrain the emission region to a very compact region, of $R_{\mathrm{TeV}} \sim 5 \times 10^{15} \delta\,\mathrm{cm}$, with δ the Doppler factor. A possible emission region could be the jet, particularly the knot HST-1, or the nucleus of the source. Neronov & Aharonian (2007) argue that the TeV emission originates in the core. Due to low bolometric luminosity of the nucleus ($L_{\mathrm{bol}} \sim 10^{40} - 10^{41}\,\mathrm{erg\,s^{-1}}$), the central engine can be transparent for photons with an energy up to 10 TeV. In addition, the low magnetic field near the nucleus might point to a TeV mechanism in which the electrons are being accelerated in strong, rotation induced electric field, which can be present in the vacuum gaps of the black hole magnetosphere.

Figure 8.1: Radio image of M87, at $\lambda = 90\,\mathrm{cm}$. The central region, in orange, contains the jet and inner radio lobes (Owen et al. 2000).

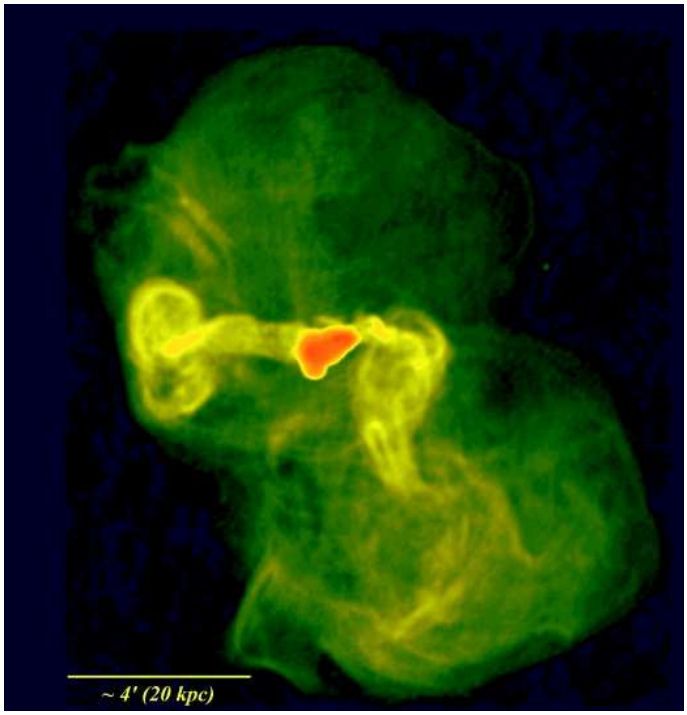

8.3 M87 in hard X-rays

Even though M87 is observed in the high energy domain, there has not yet been a detection in the hard X-rays ($\gtrsim 10\,\mathrm{keV}$). For example, high-flux states observed by *Chandra* show a flux of $f \backsimeq 2{\times}10^{-12}\,\mathrm{erg\,cm^{-2}\,s^{-1}}$ between 2 and 10 keV (González-Martín et al. 2009). Extrapolating this using a power law index of $\Gamma = 2$ would show a flux of $f \sim 10^{-12}\,\mathrm{erg\,cm^{-2}\,s^{-1}}$ between 20 and 60 keV. Since hard X-ray instruments are generally less sensitive than soft X-ray observatories, due to technical differences, this flux level might not be detected. For example, *INTEGRAL* IBIS/ISGRI has a sensitivity of 1 milliCrab for an observation of 1 Ms, which is $f_{\mathrm{mCrab}} \sim 1.2 \times 10^{-11}\,\mathrm{erg\,cm^{-2}\,s^{-1}}$ (Lebrun et al. 2003). Similarly, during the 70 month *Swift*/BAT survey a sensitivity of $f_{\mathrm{BAT}} \sim 1.3 \times 10^{-11}\,\mathrm{erg\,cm^{-2}\,s^{-1}}$ was reached (Baumgartner et al. 2013). Also, many of the earlier hard X-ray observatories (such as *Ginga*, Makino 1987) suffered from a low angular resolution, and as such were unable to distinguish between the emission from M87 and the nearby ($\sim 1.2°$) source NGC 4388.

RXTE/PCA (Jahoda et al. 1996) was one of the first detectors to observe M87 without contamination from NGC 4388. Using observations taken in January 1998, with an on-time of ∼167 ks, Reynolds et al. (1999) set an upper limit to the 20–60 keV non-thermal flux of M87 of $f < 3 \times 10^{-12}\,\mathrm{erg\,cm^{-2}\,s^{-1}}$, using a power law index of $\Gamma = 2$.

Walter & Neronov (2008) report preliminary results, showing a possible detection of M87, using *INTEGRAL* IBIS/ISGRI observations. The detection has a significance of 5.1σ and shows a flux of $f = (8.6 \pm 1.8) \times 10^{-12}\,\mathrm{erg\,cm^{-2}\,s^{-1}}$ between 20 and 60 keV, assuming a power law index of $\Gamma = 2.15$. To achieve this significance they used several analysis selections,

for example by removing the pointings which have background fluctuations > 1.1, and by removing the borders of the individual pointings. The position of the fit shows a slight displacement comparing to the nucleus of M87, of ∼3.3 arcminutes. The full-width half-maximum (FWHM) of IBIS/ISGRI is ∼12', so it is not possible to discern whether this emission arises from the core or the jet.

8.4 Data analysis

8.4.1 INTEGRAL/ISGRI data analysis

OSA 9 Analysis

We analysed data from *INTEGRAL* IBIS/ISGRI (see Section 6.2.1). We selected pointings with a direction within a radius of 8 degrees around the source. In addition to the publicly available data we also have private data rights on this source from several years of observations. In total we have observations made during 70 different revolutions (one revolution is a complete orbit, lasting for about 3 days) from the beginning of the mission.

We started by analysing all available data with the Offline Scientific Analysis (OSA) software (version 9). We used the standard input catalogue, where we added M87 and removed the source IGR J12310+1221. The addition of the source of interest in the catalogue is necessary in order to force the software to extract flux and significance information for M87. On the other hand, IGR J12310+1221 had been reported to be a potential counter part of M87 (Walter & Neronov 2008), located 3.3' away from the position of M87, but it is likely to be a false detection (see Section 8.3). If we do not remove this source from the catalogue the software will attempt to fit a source at this position and might contribute some of M87 flux to it.

The corrected data, COR, has been processed from the raw observations, i.e. by converting the housekeeping parameters to physical units, a processing step which is done by the ISDC Data Centre for Astrophysics (Courvoisier et al. 2003). We processed the science windows (scw, i.e. the individual pointings) one by one from the COR level, to the reconstructed image (IMA) level using `ibis_science_analysis`. This analysis chain takes into account the good time intervals, the dead-time is calculated, the events are binned and a re-binned background is created and subtracted from the image. In the next step the sources from the input catalogue are matched to the sources located in the field and an output file with the historic fluxes of these sources is created. In the last step the shadowgrams, the shadow of the coded mask on the detector, are deconvolved and the sky image is produced. A source search in the image is executed and the sources detected, with a signal-to-noise ratio $\geq 5\sigma$, are listed. Since the hard X-ray flux of M87 is likely to be low, we extracted flux information only in one energy band, from 20–60 keV, which has been shown to have the highest sensitivity for sources with a typical power law spectrum with $\Gamma \simeq 2$. Then we combined all 1481 individual images into a mosaic with a total on-source time of 4.7 Ms (see Figure 8.2 for the significance map). We found an excess of 3.8σ at the position of M87. There exist two methods of extracting the source flux in ISGRI images. One is by creating spectra in every scw and summing them by using `spe_pick`. For M87 this is not a good method, due to the source being weak. The other method is `mosaic_spec`, which creates a spectrum by extracting flux from the mosaic in specific energy bands, in this case the 20-60 keV band. The flux found is $f = 3.0 \times 10^{-12}\,\mathrm{erg\,cm^{-2}\,s^{-1}}$ between 20 and 60 keV (OSA 9-Full in Table 8.1).

Figure 8.2: The significance map of the sky region (30°x19°) around M87, analysed with OSA 9. M87 is located in the middle, next to the bright Seyfert 2 galaxy NGC 4388, which has a detection significance of 148σ in this analysis and a 20-60 keV flux of $f = 1.2 \times 10^{-10}\,\mathrm{erg\,cm^{-2}\,s^{-1}}$. NGC 4388 is located at a distance of 1.2°from M87. The contrast of this image has been increased for clarity.

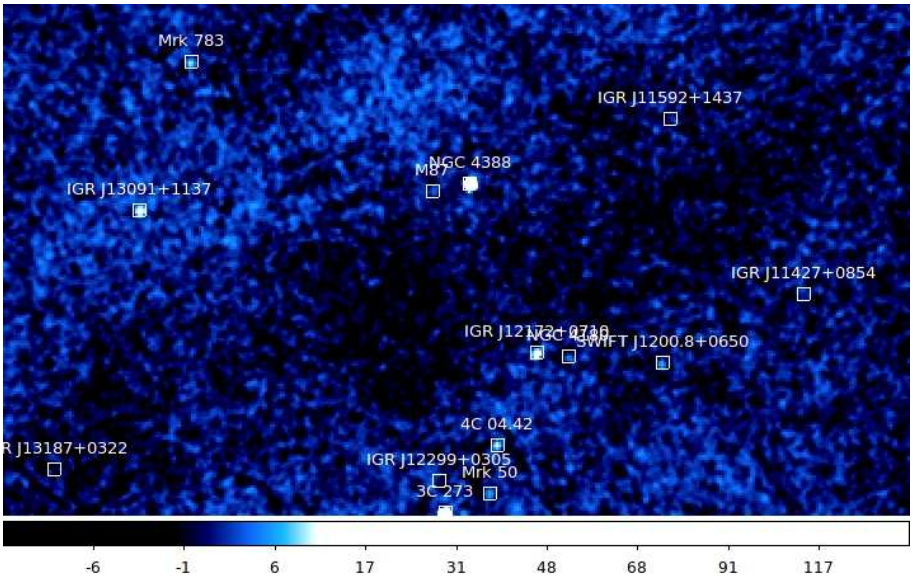

As it can be seen in Figure 8.2, M87 seems to be located in a significance 'trough'. In Figure 8.4 the entire count map of the region can be seen, rescaled to a scale of -7 to 7, smoothed with a Gaussian blur and with increased contrast, to visualize the underlying structure present in the region around M87. There appear to be two bands with a higher than average significance and in the middle a trough with a lower than average significance. To investigate these structures, we created two different mosaics, one for the revolutions with number < 1000, total of 1247 scw, and one with the revolutions > 1000, with 227 scw, to track if the significance maps would change over time. An evolution in time could for example be expected in case the features are due to an energy calibration drift (which indeed affects the OSA 9 software; Caballero et al. 2012) or a degradation of the IBIS/ISGRI detector. We found that the structure is visible in both mosaics, suggesting that the features are not time dependent.

Then a python code was developed to estimate the quality of the mosaics. This code calculates for each significance map the mean significance μ and the root mean square (rms) s_{rms}, as $s_{\mathrm{rms}} = \sqrt{(\sum_i s_i^2)/n}$ with n the number of pixels in the image, and s_i the values of the significance map. In case there are no significant sources detectable in the images, the mean of the significance should ideally be $\mu = 0\sigma$ and the rms should be $s_{\mathrm{rms}} = 1$. This assumption is also true for the case of the M87 field, because statistically the contribution of the few astrophysical sources to the significance map is negligible. Figure 8.3 shows the pixel distribution for the full mosaic.

Applying this code to the mosaic created with the OSA 9 software we find an rms $s_{\mathrm{rms}} = 1.75$, a significant deviation from the ideal case of the rms of $s_{\mathrm{rms}} = 1$. The mean μ found for

Figure 8.3: Distribution of the pixel values in the significance map of the ISGRI mosaic of the M87 field. Most of the pixels have a value between -7σ and $+7\sigma$, while the outliers indicate the bright sources in the field.

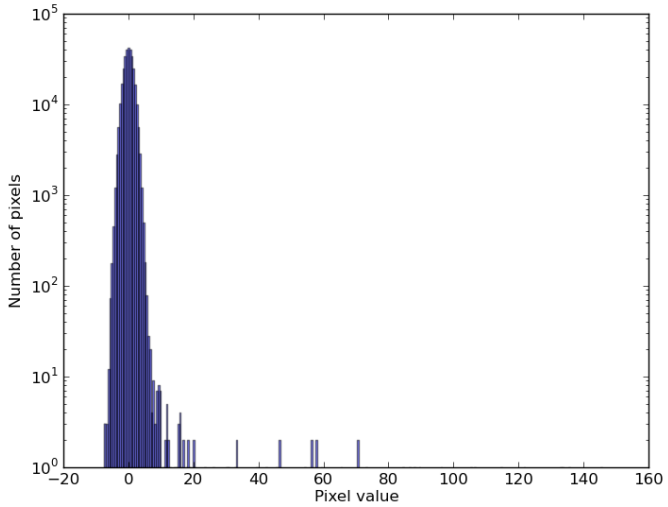

this mosaic is $\mu = 0.0129\sigma$ for a total of $\sim 3 \times 10^5$ pixels.

Applying this code to the two mosaics created with the revolutions above and below 1000 gave a similar rms: for both mosaics the rms of the significance is $s_{\rm rms} = 1.64$, which is only slightly better than for the full mosaic. The mean for the mosaic with revolutions below < 1000 is $\mu = 0.0158\sigma$, for $\sim 3 \times 10^5$ pixels, and the mosaic containing the revolutions above 1000 the mean is $\mu = -0.0440\sigma$, for $\sim 2 \times 10^5$ pixels. Therefore, the distributions of the significance have a lower rms variance $s_{\rm rms}$, but the mean value is shifted farther from $\mu = 0\sigma$ compared to the full mosaic.

Since the observed noise might originate from several scw which have not been corrected properly (for example they might have an unusually high background noise) we have computed the mean and the rms of the single scw. Then, we choose to filter out the scw that have an rms of $s_{\rm rms} > 1.2$, which corresponds to about 4% of the total number of scw (see Figure 8.5 for examples of scw of different quality).

Finally a new mosaic was made with the scw that have $s_{\rm rms} < 1.2$, which has a total on-time of 4.5 Ms. This mosaic has a rms for the significance map of $s_{\rm rms} = 1.35$ and a mean of $\mu = 0.0073\sigma$ (for $\sim 3 \times 10^5$ pixels), showing that the mosaic improved with this analysis. In this mosaic M87 is not detected, and a significance of 1.3σ is found at the coordinates of the source. Using `mosaic_spec`, we find a raw count rate of $r = 2.45 \pm 0.02\,{\rm c/s}$ (this is not corrected for systematic errors), which corresponds to a $3-\sigma$ upper limit of $f < 3.4 \times 10^{-12}\,{\rm erg\,cm^{-2}\,s^{-1}}$ between 20–60 keV (OSA 9-selected Table 8.1).

OSA 10 Analysis

The new version of the *INTEGRAL* analysis software, OSA 10, provides improvements to the IBIS/ISGRI energy calibration (Caballero et al. 2012). The reconstruction of the pho-

Figure 8.4: Significance mosaic of the region around M87 (59°by 37°), indicated in the centre of the image. This image is scaled between -7 and $+7\sigma$/pixel and smoothed with Gaussian blur.

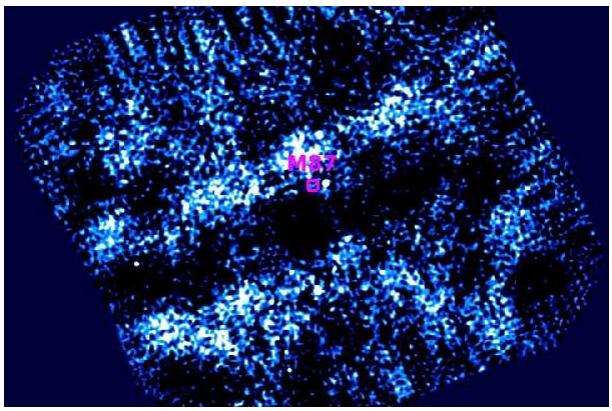

Figure 8.5: Significance maps of two different science windows. The images have been rescaled to -2σ to 2σ, and smoothed to better visualize the differences. The left image shows the map of scw number 032100600010, which has an rms of $s_{\rm rms} = 1.00$, and a pixel distribution within [-4,+4]. The right image shows scw 100600620010, which has an rms of $s_{\rm rms} = 1.31$, and the pixel distribution within [-5.4,+5.3].

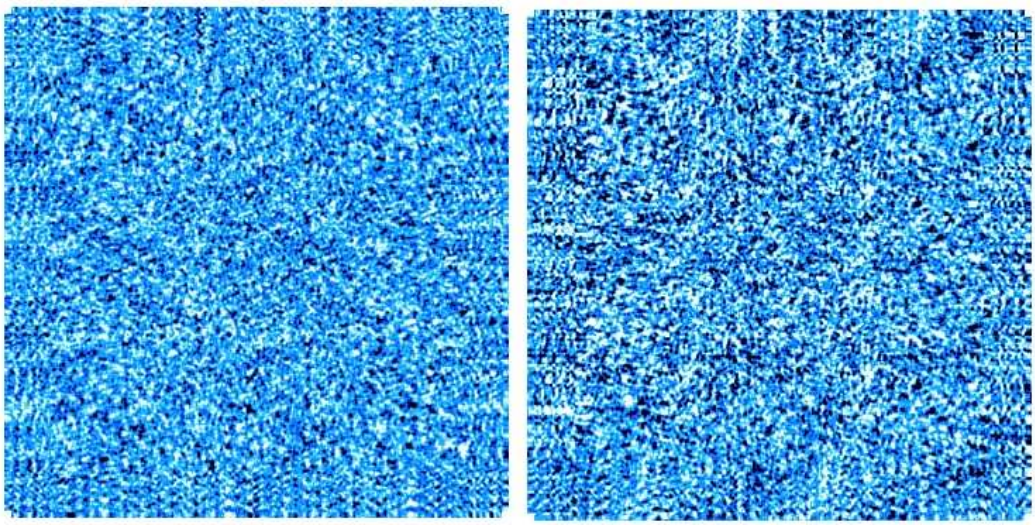

Table 8.1: Results of the mosaic analysis using different configurations as described in the text. The rms and mean are calculated over the full significance map of the mosaic. Detsig M87 is the significance at the position of M87, and the 3σ flux upper limit (UL) is derived using `mosaic_spec`. We also give the detection significance of the bright Seyfert 2 galaxy NGC 4388 for comparison.

Configuration	rms $s_{\rm rms}$	mean μ	Detsig M87 [σ]	20-60 keV UL flux [$10^{-12}\,{\rm ergs\,cm^{-2}\,s^{-1}}$]	On-time	Detsig NGC 4388[σ]
OSA 9-Full	1.85	0.0129	3.8	3.0	4.67 Ms	149.0
OSA 9-Selected	1.35	0.0073	1.3	3.4	4.47 Ms	114.1
OSA 10-Selected	1.38	-0.0103	1.6	3.3	5.23 Ms	113.5
OSA 10-Rev1	1.18	0.0204	1.7	4.2	2.78 Ms	89.4
OSA 10-Rev2	1.39	-0.0501	0.0	5.0	2.45 Ms	70.2
OSA 10-SG cut	1.22[a]	0.0628	0.9	3.4	5.13 Ms	108.2
OSA 10-SG comb	1.08[a]	0.0447	1.2	3.3	5.13 Ms	111.3

[a] See Figure 8.11 and Table 8.3.

ton energy in IBIS/ISGRI is improved significantly compared to OSA 9[1]. The gains and offsets of the rise time and pulse height are dependent on the temperature of the detector, and in the new OSA 10 temperatures of the thermal probes are used instead of assuming a constant temperature gradient between the different detector modules. In addition, also the pulse height and gain depend on the time and the events rise time. By following the stable instrumental background lines produced on board by the radio-active sodium, ^{22}Na, and tungsten fluorescence line, it is possible to follow and model the drift in the gain. This decreased the degradation of the energy resolution with time from a factor of ~ 3 (OSA 9) to a factor of ~ 2 (OSA 10) compared to the beginning of the mission. In addition the lower energy threshold has been updated, following the new energy reconstruction. Lastly a set of new ancillary response files, for different epochs, has been produced using Crab observations.

Meanwhile, *INTEGRAL* made new observations of M87 for which we successfully applied for the data rights. Using the selected set of scw (science windows) with an rms $s_{\rm rms} < 1.2$, and the new private data, we created a new mosaic using the OSA 10 software, and a similar analysis of the scw as for OSA 9. The resulting mosaic has a rms of the significance of $s_{\rm rms} = 1.38$, and a mean of $\mu = -0.0103\sigma$ with $\sim 3\times10^5$ pixels. For an on-time of 5.2 Ms, this mosaic gives a detection significance of 1.4σ at the position of M87, which corresponds to a 3σ flux upper limit of $f < 3.3\times10^{-12}\,{\rm erg\,cm^{-2}\,s^{-1}}$ to between 20–60 keV (OSA 10-Selected in Table 8.1). The longer exposure time enables us to set a slightly lower upper limit compared to before. However, the mosaic rms $s_{\rm rms}$ is not improved by either the increased exposure time nor the new software.

The use of a selected group of scw improved the mosaic, in the sense that the fluctuations in the significance map decreased. We decided to make a mosaic for each revolution, in total 70, to study the fluctuations and structures, and their temporal evolution. The revolutions we used contain between 4 and 55 science windows. After creating these mosaics, we applied the python code to find the statistics of the significance map. We find that revolutions early in

[1] http://www.isdc.unige.ch/integral/download/osa/doc/10.0/isgri_energy_calib.pdf

Figure 8.6: The rms of the significance map of each mosaic per revolution is plotted versus the revolution number with red triangles. The horizontal green line plotted at rms $s_{\rm rms} = 1.1$ shows the divide between the rms of the earlier revolutions and the higher rms of the later revolutions. Also the number of scw per revolution is shown with blue circles.

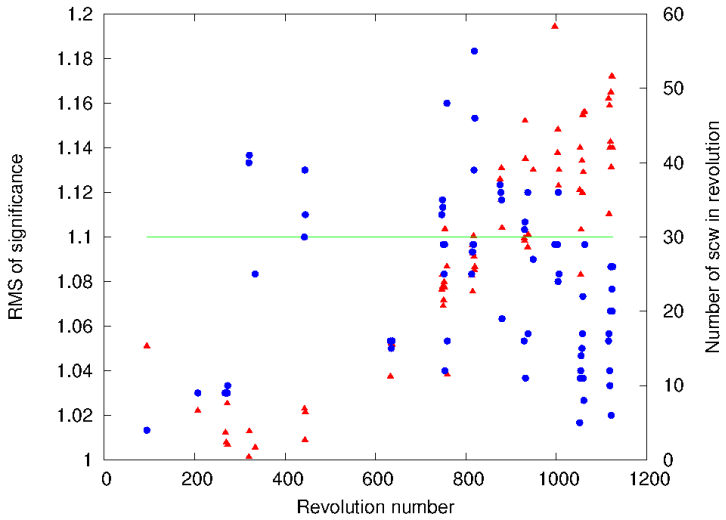

the mission, up to about rev 800 in May 2009, seem to have mosaics with an rms $s_{\rm rms} < 1.1$. Almost all revolutions after this date have an rms $s_{\rm rms} > 1.1$ (see Figure 8.6). The observed trend is not dependent on the amount of science windows per revolution, as can be seen in the same Figure. The structures might be caused by the background correction, since the background changes over time.

To study how the underlying structure propagates from a single revolution to the mosaic of several revolutions we created two mosaics. The first mosaic consists of revolutions that have a significance rms of $s_{\rm rms} < 1.1$ (OSA 10-Rev1 in Table 8.1). In total 939 science windows were used here. The produced mosaic appears indeed to be more regular (see left panel of Figure 8.7). This mosaic has an rms for the significance of $s_{\rm rms} = 1.18$, for $\sim 3 \times 10^5$ pixels, and M87 has a significance of 1.7σ, and a 3σ flux upper limit of $f < 4.2 \times 10^{-12}\,{\rm erg\,cm^{-2}\,s^{-1}}$ between 20 and 60 keV (on-time 2.7 Ms). We also made a mosaic with all the revolutions with a higher rms of $s_{\rm rms} > 1.1$, using 706 science windows (OSA 10-Rev2 in Table 8.1). The resulting mosaic shows clear structures, as it can be seen in Figure 8.7 (right panel). The rms of the significance is $s_{\rm rms} = 1.39$ (for $\sim 2 \times 10^5$ pixels) and M87 has a detection significance of 0σ (on-time 2.5 Ms). For comparison, the nearby bright Seyfert 2 galaxy NGC 4388 has a significance of 70.2σ in this mosaic, and in the mosaic with revolutions which have $s_{\rm rms} < 1.1$ the significance of this source is 89.4σ. Using `mosaic_spec` we extracted a count rate at the position of M87, which yielded an upper limit to the flux of $f < 5.0 \times 10^{-12}\,{\rm erg\,cm^{-2}\,s^{-1}}$ between 20 and 60 keV.

Figure 8.7: The left image shows the OSA 10 mosaic created from the revolutions with a significance rms of $s_{\rm rms} < 1.1$. For the right image the revolutions with a rms of $s_{\rm rms} > 1.1$ are used. Both images are scaled to [-5,5] to visualize the structure. The size of the images is $\sim 40^\circ$ by $\sim 40^\circ$.

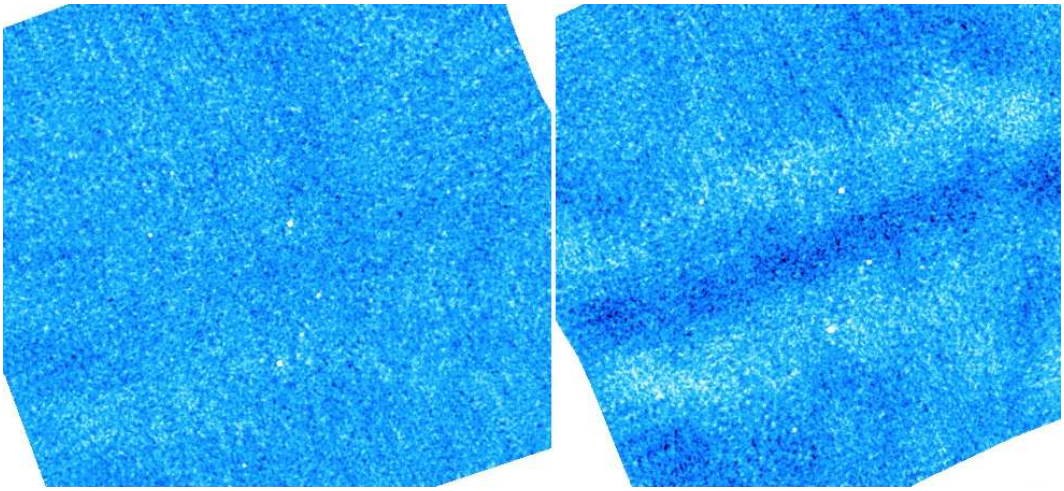

Ghostbusters

To continue the testing we chose two revolutions, one with a significance rms of $s_{\rm rms} < 1.1$ and one with a rms of $s_{\rm rms} > 1.1$, with a sufficient number of scw, so that the mosaics will not be noise-dominated. We chose two revolutions that are in the middle of the mission: revolution 0758, which was performed during December 2008, has 48 scw and the mosaic has a rms of the significance of $s_{\rm rms} = 1.09$. At the position of M87 the significance is 0.5σ (on-time 158 ks). The revolution 0876, performed a year later in December 2009, has 37 scw. The mosaic has a rms of $s_{\rm rms} = 1.13$ for the significance map, and on-time is 130 ks. No significance for M87 could be extracted in this mosaic. On a revolution level, in both mosaics, only the bright sources NGC 4388 and the blazar 3C 273 have been detected (see Figure 8.8 for the mosaics of these revolutions). The pixel distribution of the significance map for revolution 0758 shows that most pixels have a value between -4.6σ and $+4.6\sigma$, with outliers for the bright sources at 16σ. For the mosaic of revolution 0876, the distribution of the pixel values is slightly asymmetric and shows that most pixels have a value between -4.6σ to $+5\sigma$, with outliers of 32σ for the bright source 3C 273. The dramatic increase of significance of this bright quasar is likely due to a flaring episode in 2009 (see for example Abdo et al. 2010f; Chatterjee et al. 2012).

The structures that seem present in some of the mosaics might be related to possible ghosts, artefacts of bright sources, introduced in the image by the repeating pattern of the mask (see Figure 6.3). These spurious detections can be distinguished from the sources producing them, since the real sources are expected to have a higher significance, due to the only partial repetition of the mask pattern. When the mask model included in the software is a sufficiently accurate representation of the actual mask, ghosts are identified and cleaned by the software. However, the presence of mask defects like screws and glue fixing the mask to its support,

Figure 8.8: The left image shows the significance mosaic of revolution 0758, which contains 48 scw. The right side shows the mosaic of revolution 0876, containing 37 scw. Both images have been scaled to [-2,2] to visualize the structures, and are centred around the same position. The black circle denotes the position of M87. The mosaic of revolution 0876 shows the significance trough diagonally with the brighter bands on top and bottom. The mosaic of 0758 has a smoother appearance.

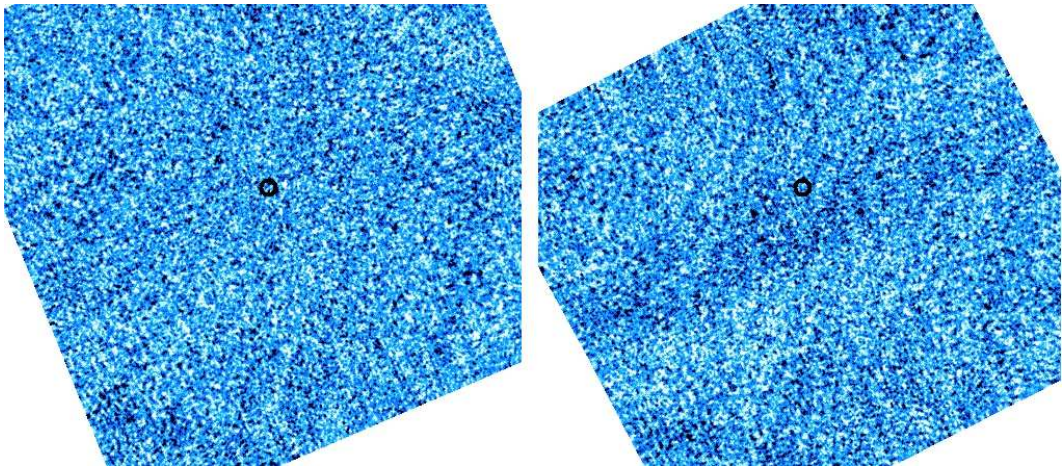

are not correctly modelled in the software, causing an incorrect reconstruction of the shadowgram and therefore strong residuals at the position of the ghosts might no be correctly cleaned (Soldi et al. 2012).

This influences the shadowgrams of strong sources, and creates artefacts in the images. In order to correct for these artefacts, the ghost_buster routine has been developed by Dominique Eckert (ISDC), and the algorithm has been included in the *INTEGRAL* software since OSA 9. The routine is activated for several bright sources and excludes the affected pixels in order to correct the artefacts. If ghost_buster is applied to many sources in the field, too many pixels might be excluded, decreasing dramatically the detector effective area. It is therefore important to apply ghost_buster only to bright sources whose ghost would otherwise not be properly corrected. To use ghost_buster we change the catalogue settings, choosing ISGRI_FLAG2=5, for the bright sources NGC 4388 and 3C 273. Then, we redid the analysis from the scw-level. The resulting mosaics can be found in Figure 8.9. The mosaic of revolution 0758 shows a smoother significance map compared to the mosaic of revolution 0876. For revolution 0758 the rms of the significance map is not changed, $s_{\mathrm{rms,ghost}} = 1.09$, but the significance at the position of M87 decreased to 0.03σ. For revolution 0876 the rms slightly decreased to $s_{\mathrm{rms,ghost}} = 1.12$, but the significance at the position for M87 remains 0. The pixel distribution for the significance map of 0758 is narrower, most pixels have a value between -4.7σ and 4.5σ. The bright sources in the field have a slightly lower significance, a difference of a few percent being due to the loss of effective area. Similarly, the pixel distribution is also narrower for revolution 0876, with most counts between -4.6σ and 4.9σ, and the bright sources have a slightly lower significance due to the ghost_buster routine. In conclusion, there are no significant improvements in the image quality when applying the ghost_buster in the M87 field. Therefore in the following of our analysis, we did not use this routine.

Figure 8.9: Significance maps of revolutions 0758 (left) and 0876 (right), when ghost_busters is applied to reduce the artefacts in the image caused by the bright sources. The mosaics are centred at the same position, and have been scaled to a range of -2 to 2 for the pixel values. The black circle shows the position of M87.

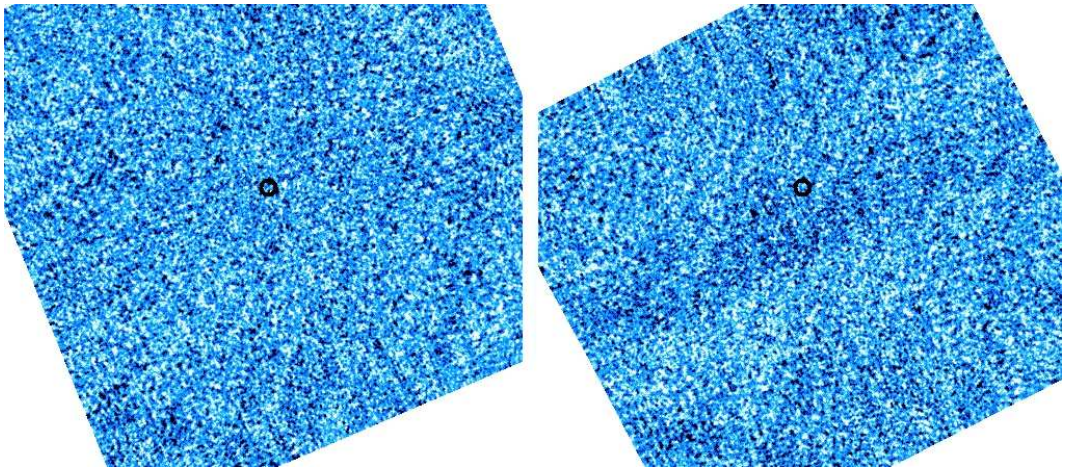

Shadowgram borders

It is possible that the structure which appears in the mosaics is connected to the coded mask, which we will investigate in this section.

The coded mask technique, which allows IBIS to image the sky at hard X-rays has several advantages, but also drawbacks, as discussed in Section 6.2.1. Additional instrumental background noise can determine an imperfect reconstruction of the sky image following the deconvolution of the detector shadowgrams. Since the detectors borders contain the least predictable instrumental background. Therefore, to decrease this source of additional noise, we decided to ignore the borders of the shadowgrams. To do this, we adapted accordingly part of the OSA software[2]. The routine ii_shadow_ubc reads the raw detector shadowgrams and their corresponding efficiency, and performs background correction on the shadowgrams, correcting for uniformity defects and non-uniform spatial distribution. By setting some of the pixels at the border of the whole detector, or at the borders of the 8 modules, to 0 efficiency, these pixels are effectively 'cut' from the analysis. In Figure 8.10 the difference between the standard shadowgram efficiency and one of the adapted cases is shown.

Due to the removal of the shadowgram edges in each science window, the outer parts of the mosaics are unnaturally smooth, as can be seen in Figure 8.11. Since we are interested in the region around M87, we adapt the python routine used to calculate the rms to select the 10°by 10°region around M87 and compute the rms in this region.

In the $10° \times 10°$ region around M87 the bright source NGC 4388 is present (see Figure 8.12). When calculating the full rms we did not remove the sources, since they did not influence the distribution significantly. However, here we chose to remove the bright source, partly because the total number of pixels we use is lower, about $\sim 2 \times 10^4$, but also since the improvements

[2]Aleksandra Gros, private communication

Figure 8.10: Efficiency maps, where black pixels correspond to 0 efficiency.

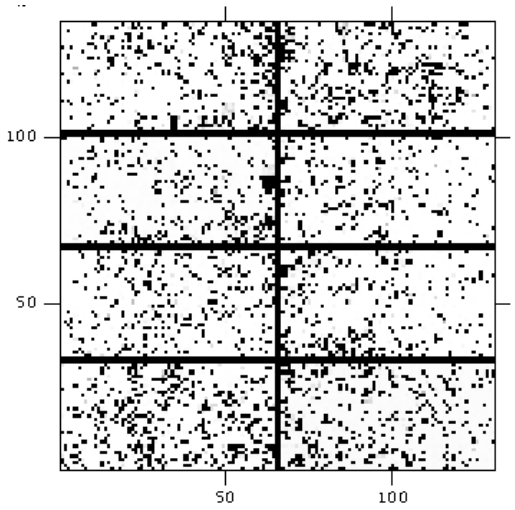

(a) Efficiency of the shadowgram for the standard case.

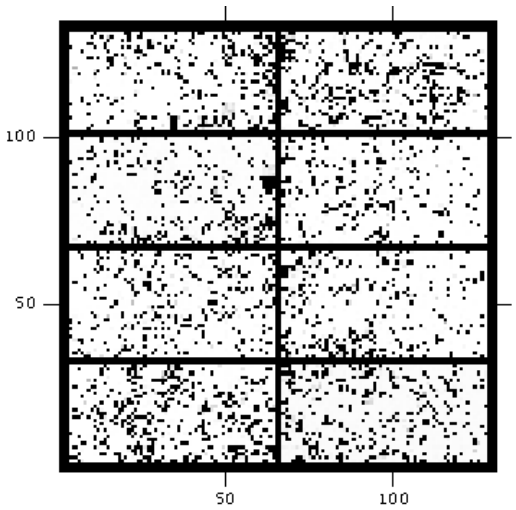

(b) Efficiency of the shadowgram where the detector borders have been 'cut', i.e. put to zero efficiency. For this case 3 pixels around the border have been excluded.

Figure 8.11: The left image shows the edge of the mosaic of revolution 0758, when no cuts on the shadowgrams have been applied. The right image shows the same edge, of the mosaic of revolution 0758 where a cut of 3 pixels is applied to the shadowgram of each science window. Both images have been scaled to [-2,2].

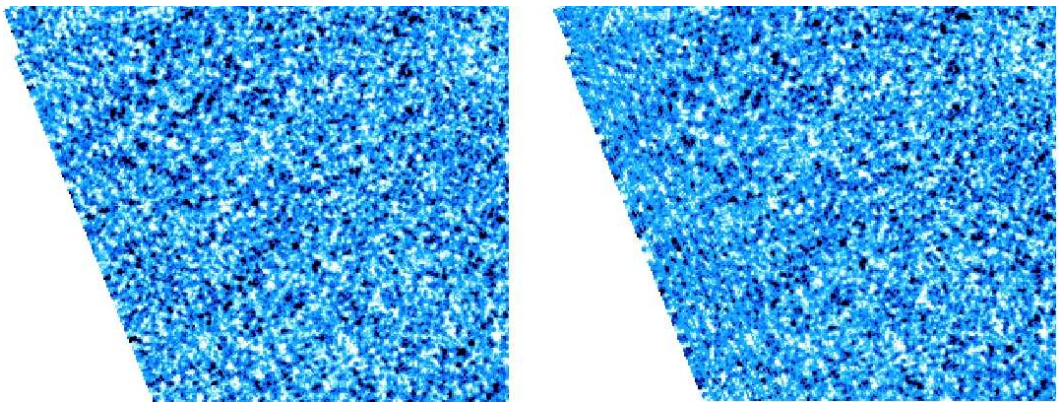

Figure 8.12: Full mosaic of revolution 0758, with coordinate grid (J2000.0 coordinates). The black box shows the inner $10° \times 10°$, which includes M87 and NGC 4388.

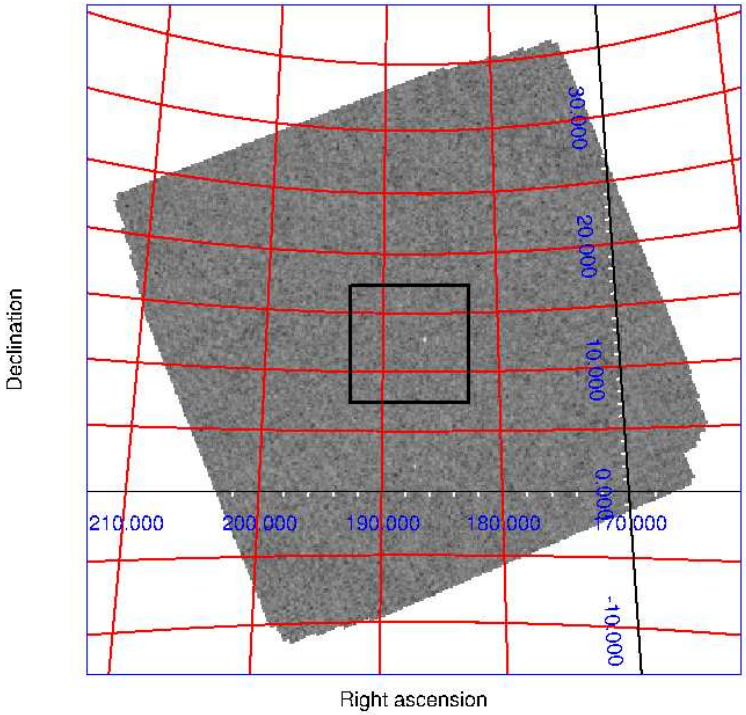

of the mosaic might be very subtle.

We found the position of the source in xy detector coordinates by using `xy2sky`, and removed a region with a radius of 5 pixels around this position. As a check to see if all the source pixels are removed, we inspected the rest of the image to find any pixels with a value smaller than -4, and -3, and with values larger than +3 and +4, and their location. Since the sources are removed from the region, single excesses are expected to be background fluctuations. However, if there is a clustering of points with higher significance in a region, this might suggest that either not all sources are properly removed, or that there is a background feature that is not properly accounted for.

In the mosaics where no cuts to the shadowgrams are applied (Table 8.2), revolution 0758 shows a rms for the inner $10° \times 10°$ of $s_{\mathrm{rms,10deg}} = 1.066$. The distribution of the significance is slightly asymmetric, as there are more pixels with a significance below -3σ, 51 pixels, than pixels with a value $> 3\sigma$, 39 pixels. The mosaic of revolution 0876 has a larger width of the significance distribution in the inner $10° \times 10°$ region, of $s_{\mathrm{rms,10deg}} = 1.152$, and shows a very asymmetric distribution, with 116 pixels of a value $< -3\sigma$ and 45 pixels with a value $> 3\sigma$. As it can be seen in Figure 8.8, the region around M87 is in the significance trough in the revolution 0876, which explains the asymmetrical pixel distribution.

We have tested five different configurations of the shadowgram, cutting either 1, 3 or 5 pixels from the shadowgram border, and by cutting 1 pixel around each module, in combination with a cut of either 1 or 5 pixels around the border. We started by using cuts on the border of the shadowgrams (see Table 8.2). The mosaics with 1 pixel cut from the border show a slight

Table 8.2: Results of the border cutting on revolutions 0758 and 0876. The quoted rms is computed on the significance map, taking into account only the innermost 10°x10°and excluding the bright source NGC 4388 ('rms inner 10°x10°'). The 'rms total' is the total mosaic rms. The significance at the position of M87 and the significance of NGC 4388 are taken from the source significance list produced with the mosaic. The columns 'No< -3σ' and 'No> 3σ' show the amount of pixels with a significance below -3σ or above 3σ, in the $10^\circ \times 10^\circ$ region.

Cut	rms inner $10^\circ \times 10^\circ$	rms total	detsig M87 [σ]	detsig NGC 4388 [σ]	No $< -3\sigma$	No $> 3\sigma$
None 0758	1.066	1.095	0.38	18.60	51	39
Border 1 0758	1.071	1.095	0.47	18.51	44	46
Border 3 0758	1.075	1.013	0.81	17.66	54	46
Border 5 0758	1.075	0.863	0.76	16.86	57	39
Border module 1 0758	1.079	1.094	0.34	18.40	66	41
Border 5 module 1 0758	1.086	0.808	0.35	16.58	64	56
None 0876	1.152	1.133	0	16.97	116	45
Border 1 0876	1.147	1.130	0	16.79	116	37
Border 3 0876	1.140	1.051	0	15.67	102	39
Border 5 0876	1.142	0.920	0.06	15.73	106	56
Border module 1 0876	1.157	1.130	0.21	15.90	123	48
Border 5 module 1 0876	1.152	0.874	0.21	14.75	101	46

difference for the rms of the full significance map for revolution 0876, but for revolution 0758 there seems to be no change. The rms of the inner $10^\circ \times 10^\circ$ is increased for revolution 0758, from $s_{\mathrm{rms,10deg}} = 1.066$ to $s_{\mathrm{rms,10deg}} = 1.071$, whereas for revolution 0876 this decreased from $s_{\mathrm{rms,10deg}} = 1.152$ to $s_{\mathrm{rms,10deg}} = 1.147$. The significance at the position of M87 increased slightly for revolution 0758, from 0.38σ to 0.47σ, and the significance of the near by bright source NGC 4388 decreased from 18.60σ to 18.51σ. The increase of the significance at the position of M87 is not necessarily due to the image improvement, due to its dimness level in the 20–60 keV energy band and to the change of effective area. The significance is $< 3\sigma$, indicating we probe the background rather than a source, and any increase or decrease is more likely due to background fluctuations. The decrease of the rms of the significance in the region near the source for revolution 0876 might indicate that using an adapted version of the shadowgram will indeed decrease the noise in the mosaic.

We also did tests with cutting 3 and 5 pixels from the border. For revolution 0758, the rms of the $10^\circ \times 10^\circ$ region around the source continues to increase, to $s_{\mathrm{rms,10deg}} = 1.075$. This might indicate that for revolutions that initially showed a mosaic with no significant structure, this treatment is not beneficial, since the noise increases rather than decreases due to the loss of effective area. For revolution 0876, the rms of the inner 10 degrees is lowest for a cut with 3 pixels, $s_{\mathrm{rms,10deg}} = 1.140$. A cut of 5 pixels of the borders yields an rms of $s_{\mathrm{rms,10deg}} = 1.142$. The total rms for these mosaics is decreases for both revolutions, this is likely due to the smoothing of the edges as it can be seen in Figure 8.11. For revolution 0758 the detection significance of the position of M87 peaks with the border cut of 3 pixels to 0.8σ.

The detection unit of IBIS/ISGRI consists of 8 separate modules, which causes the grid

Table 8.3: Details of the three mosaics created to test the shadowgram border cutting technique. The mosaic with no scw cut has no changes to the shadowgrams, and the mosaic with all scw cut has a border of 3 pixels cut around the shadowgrams. For the combined mosaic we used the shadowgram cut of 3 pixels for the revolutions which have a rms of the significance of $s_{\mathrm{rms}} > 1.1$, while for the rest we use the scw without any cuts. We also show the amount of pixels with a value below -5σ. The 5σ excesses are not associated with sources, but are the result of the structures visible in the mosaic image.

Configuration	rms inner $10^\circ \times 10^\circ$	rms total	M7 detsig [σ]	detsig NGC 4388 [σ]	No $< -5\sigma$	No $> 5\sigma$
No scw cut	1.543	1.393	1.5	113.2	7	12
All scw cut	1.397	1.215	0.9	108.2	2	3
Combined	1.412	1.083	1.2	111.3	4	1

on the shadowgrams corresponding to the zero efficiency region between the modules (see for example on Figure 8.10). The borders of the modules might also introduce additional noise, so we have also tried a configuration where we set 1 pixel around the modules to 0 efficiency, combined with a border cut of either 1 or 3 pixels. The results can be found in Table 8.2. Using a cut of 1 pixel on both the borders around the entire shadowgram and the modules, the rms in the inner 10 degrees increases in both cases, to $s_{\mathrm{rms,10deg}} = 1.079$ for revolution 0758 and $s_{\mathrm{rms,10deg}} = 1.157$ for revolution 0876. The significance at the position of M87 is decreased slightly for revolution 0758, compared to the significance found using no additional changes. For revolution 0876 in both cases a significance of 0.21σ was found at the position of M87. The amount of pixels with a value below -3 and above $+3$ increased for both revolutions, which also shows that this configuration does not decrease the stronger noise in the image. The detection significance of NGC 4388 is decreased for both revolutions, due to the loss of effective area. A cut of 5 pixels around the border and of 1 pixel around the modules yields an rms for the inner $10^\circ \times 10^\circ$ of $s_{\mathrm{rms,10deg}} = 1.086$ for revolution 0758, the highest among all configurations, and $s_{\mathrm{rms,10deg}} = 1.152$ for revolution 0876, similar to the no-change case. The amount of pixels with values below -3 and above $+3$ for 0758 is higher than for the case where no changes are made. For revolution 0876, the amount of pixels with a value below -3 is the lowest among all configurations, but the pixel value distribution is asymmetric around 0.

To summarize, the removal of 3 pixels around the shadowgram shows the largest improvement in the image, when comparing the deviance of the rms of the significance maps to the ideal case of $s_{\mathrm{rms}} = 1$, for the rms of the inner $10^\circ \times 10^\circ$. The cut of 5 pixels also shows an improvement of the image, but the 3-pixel cut has the further advantage of reducing the number of pixels with $|\sigma| > 3$ to a minimum, while minimizing also the excluded detector area.

To see if cutting the shadowgrams significantly improves the imaging results when using the full set of science windows, 1614 in total, we made three full mosaics. One where no changes have been made to the shadowgrams, one where we use a cut of 3 pixels on the borders of the shadowgrams of all scw and one where we use the cut of 3 pixels only on the revolutions that have a rms of $s_{\mathrm{rms}} > 1.1$. The results for these full mosaics can be found in Table 8.3,

and the pixel value distributions of the three mosaics are plotted in Figure 8.13. Since in the total mosaic the exposure time is increased, in the inner $10^\circ \times 10^\circ$ now three sources are significantly detected; NGC 4388, IGR 12172+0710, and the blazar 4C 04.42. We excluded the pixels at the position of these sources, with a radius of 6 pixels for NGC 4388 and a radius of 5 pixels for IGR 12172+0710 and 4C 04.42. To check if all sources are removed, we checked the amount and location of pixels with a value above 5σ. We did find excesses above this threshold not associated with sources, but rather with background structures in the mosaic. We also counted the number of pixels with a value below -5σ, to study the deviation of significance compared to the normal distribution (skewness) and excesses caused by the structure. We chose pixels with a value excess of 5σ here since due to the larger number of scw the natural spread will be larger and excesses of 3σ, or 4σ can be expected.

For the mosaic where no changes to the shadowgrams are applied, the rms of the inner $10^\circ \times 10^\circ$ significance map is largest, with $s_{\mathrm{rms,10deg}} = 1.543$, and the detection significance of NGC 4388 is largest with 113.2σ. The large rms is also reflected in the pixel distribution, which shows the largest amount of points with values below -5σ and above 5σ of all three mosaics. The mosaic where all scw have shadowgrams with a border cut of 3 pixels shows the lowest rms in the inner $10^\circ \times 10^\circ$, $s_{\mathrm{rms,10deg}} = 1.397$, and also the amount of 5σ excess pixels is lower than for the mosaic where no cuts have been applied. The detection significance of NGC 4388 is lowest among these mosaics, with 108.2σ (OSA 10-SG cut in Table 8.1). The combined mosaic has a rms of the inner $10^\circ \times 10^\circ$ in between the previous configurations of $s_{\mathrm{rms,10deg}} = 1.412$, and has the same number pixels with a value $|\sigma| > 5\sigma$ as the mosaic where all scw have been adapted (OSA 10-SG comb in Table 8.1). As it can be seen in Figure 8.13 the negative tail of the pixel distribution of the combined mosaic seems to extend beyond that of the mosaic where all scw have been adapted. It would be expected that the combined mosaic would be in between the other mosaics, but it seems to follow the distribution of the mosaic with all scw cut, except for the tails of the distribution. This would indicate that the outliers are more influenced by the non-adapted scw.
Using `mosaic_spec` we extracted a count rate at the position of M87, which is $2.23 \pm 0.02\,\mathrm{c\,s^{-1}}$ for both the mosaic with no cuts and the combined mosaic, and gives an upper limit flux of $f < 3.3 \times 10^{-12}\,\mathrm{erg\,cm^{-2}\,s^{-1}}$ between 20 keV and 60 keV. For the mosaic where we applied cuts to all scw we find a count rate of $2.21 \pm 0.02\,\mathrm{c\,s^{-1}}$, which translates to an upper limit to the flux of $f < 3.4 \times 10^{-12}\,\mathrm{erg\,cm^{-2}\,s^{-1}}$ between 20 and 60 keV (for all mosaics the on-time is 5.1 Ms).

As an additional check we used `mosaic_spec` on the pixels surrounding the position of M87, at a distance of $\sim 0.5^\circ$, to see if the error is similar and not a very local fluctuation. We made spectra at 4 different positions around M87, which all yielded a similar count rate, so the upper limit found is not a local fluctuation.

Background Subtraction

Even though we have been able to slightly improve the quality of the images, so far we have not been able to pin down the origin of the structures seen in the mosaic. Since they might be introduced by features of the imaging process, for example by the background correction or source cleaning, we run two more tests on revolutions 0758 and 0876.

To check the cleaning in the image, we made a custom catalogue with one weak source outside the field. We chose 3C 111, which has a distance of 107° to M87. Then, we put the `ibis_science_analysis` parameter OBS_SearchMode to 1, so that the software searches for

Figure 8.13: Histograms of the pixel values in the inner 10x10 degrees of the full mosaics, where the bright sources have been removed. The blue line shows the distribution when no cuts are applied, the green line shows the mosaic where a cut of 3 pixels has been applied to all shadowgrams, and the red line shows the mosaic where a cut has been applied only to the shadowgrams in revolutions with a rms of $s_{\mathrm{rms}} > 1.1$.

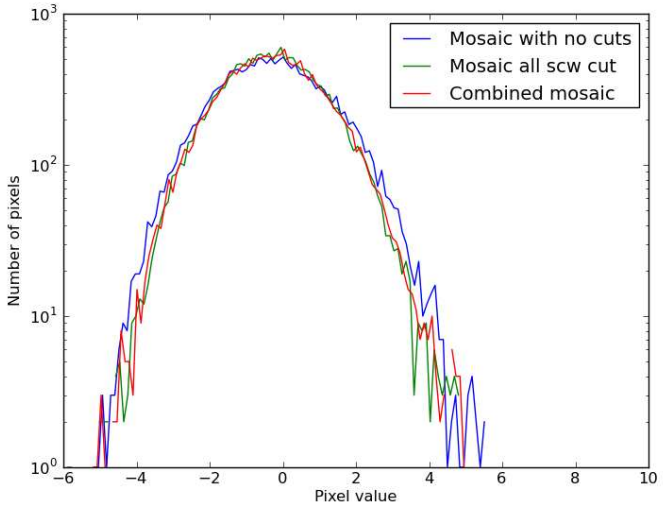

all the catalogue sources. The default value for this parameter is 3, a search for all catalogue sources plus a number of significant excesses. Since in the catalogue there are no sources within the M87 field, the software will not perform any cleaning of the image, resulting in ghosts from the bright undetected sources. This influences the rms of the significance, for revolution 0758 the rms is $s_{\mathrm{rms}} = 1.12$ and for revolution 0876 the rms if $s_{\mathrm{rms}} = 1.18$. As it can be seen in Figure 8.14, revolution 0876 shows the bar-like structure, whereas the mosaic of revolution 0758 does not, indicating that the structure does not arise from the source cleaning in the imaging process.

Since the presence of the bar in the significance map occurs mostly in the later revolutions (rev>800), and indeed the rms changes over time, there might be a dependence on the background correction. In fact, while the background shape and intensity evolves with time, the ISGRI background correction is based on a map with a fixed shape, where the normalization only changes with time. We have therefore made mosaics where we did not correct for the background, by changing the input to the parameter SCW1_BKG_I_isgrBkgDol of the `ibis_science_analysis`. The rms of the significance map of the resulting mosaics (see Figure 8.15), is large, due to the lack of background correction, for revolution 0758 a rms of $s_{\mathrm{rms}} = 1.35$ is found and for revolution 0876 a rms of $s_{\mathrm{rms}} = 1.43$. In the significance map of the mosaic of revolution 0876 the bar-like structures are present, whereas the significance map of revolution 0758 shows a structure, but not the bands we see in the final mosaic. This would indicate that the bar-like structure we see in the later revolutions, and the final mosaic, is not due to the background subtraction.

Figure 8.14: Significance maps of the mosaics of revolutions 0758 (left) and 0876 (right). These mosaics were created using a custom catalogue to study the source cleaning. The images are scaled to [-2, 2] to increase the visibility and have been centred at the same point.

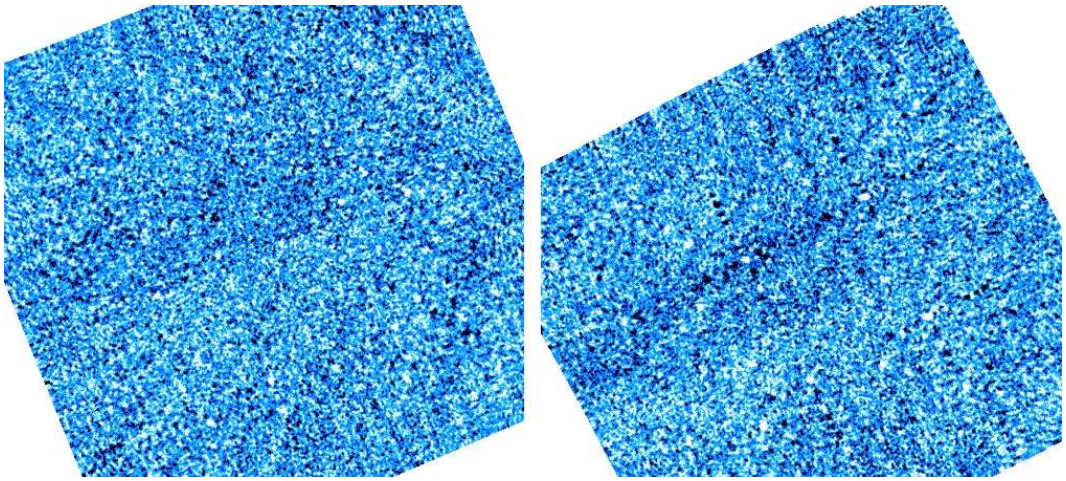

Figure 8.15: Significance maps of the mosaics of revolutions 0758, left, and 0876, right. The mosaics have not been background corrected, resulting in a stronger structure for both revolutions. The images are scaled to [-2, 2] to increase the visibility and have been centred at the same point.

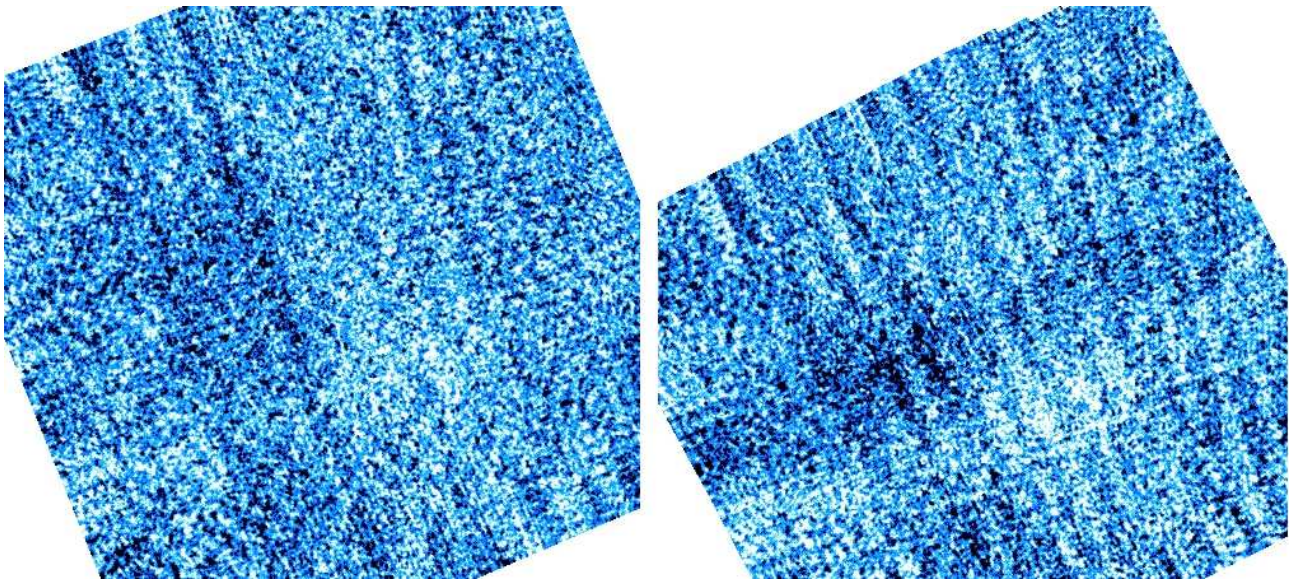

Figure 8.16: Mosaic of the region around M87. Shadowgram cutting has been applied to the revolutions with a significance rms of $s_{\rm rms} > 1.1$. The significant sources, and the position of M87, are indicated in this image. The grid is in J2000.0 coordinates.

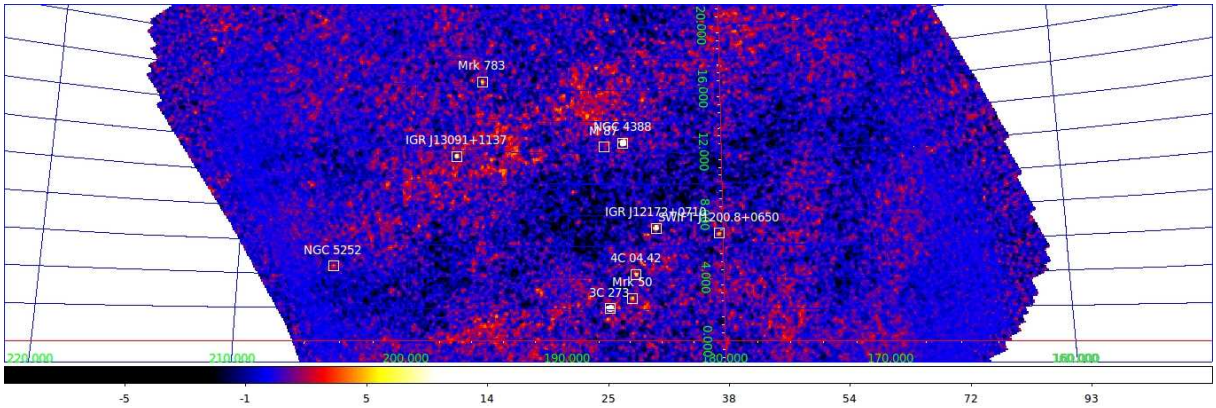

Conclusions

The analysis of the M87 field using the standard ISGRI analysis resulted in a noise-dominated image. We investigated the structures by applying selections to the data, and changes in the analysis software. We found that the structures are not caused by ghosts of bright sources, source cleaning, nor background subtraction. However, with our own tests we reduced the rms of the significance of the full mosaic from $s_{\rm rms} = 1.85$ using OSA-9, to $s_{\rm rms} = 1.08$ using OSA-10, with selected science windows, and adapted software. The best image (see Figure 8.16) yielded a 3σ upper limit flux for M87 of $f < 3.3 \times 10^{-12}\,{\rm erg\,cm^{-2}\,s^{-1}}$ between 20 keV and 60 keV.

8.4.2 INTEGRAL/JEM-X

Analysis

In addition to the *INTEGRAL*/IBIS detector, we also analysed data from the soft X-ray instrument JEM-X (see Section 6.2.1). The analysis of JEM-X coded mask data is similar to the analysis for IBIS/ISGRI, however JEM-X consists of two detectors of which only one had been switched on during the observations of the M87 field. Care must be taken to analyse the data of each detector independently, and to use only the science windows from the same detector in a mosaic. Another difference is that the JEM-X coded mask has an almost non-cyclic pattern, so ghosts of sources are rare.

We used all public data available with pointing direction within a radius of 2.5° from M87, where we selected only the observations with a good time of at least 500 seconds. The searching radius is significantly smaller for JEM-X compared to ISGRI, due to the much smaller field of view (5° for JEM-X, 9° by 9° for ISGRI). In addition we used the private data we obtained through a successful *INTEGRAL* data rights proposal, which gives a total of 212 scw used in the final mosaic.

Similar to the IBIS/ISGRI analysis we processed every scw one by one using `jemx_science_analysis` (OSA 9), from the corrected level (COR) to the spectral (SPE) level, such that in each scw a spectrum of the source is created. During this analysis the energy and position of the detected events are corrected, dubious events are flagged, and transient problems such as problems with the detector are determined. Then the events are filtered according to the good time intervals, and dead-time corrected. We performed the analysis in three energy bins: 46–129, 130–196 and 46–196, which correspond to energies of 3–10.2 keV, 10.2–25.2 keV and the full band 3–25.2 keV. The sources from the input catalogue are selected, and a search for significant sources is performed. The shadowgrams and sky images are created, and lastly the spectra are extracted and responses for the spectra are produced. Creating the spectra at this step will make possible to sum all spectra to get a good flux estimate. By changing in the catalogue for M87 FLAG=1, the flux at the source position will be extracted. Then we constructed two mosaics, for both JEM-X detectors, by running the `jemx_science_analysis` from level IMA2 to IMA2, where we centred the mosaics around the position of M87, using the parameters IMA2_RAcenter and IMA2_DECcenter, a step that allows a subsequent combination of the two mosaics.

In the JEM-X1 mosaic (consisting of 131 scw for an exposure is 247 ks), M87 was significantly detected at 13.2σ in the 3–10.2 keV, and at 9.8σ in the full 3–25.2 keV band. In the band between 10.2–25.2 keV, the source was not detected, with a significance at the source position below 3σ. The JEM-X2 mosaic consists of 90 scw, with an exposure of 199 ks, M87 is detected in the JEM-X2 3–10.2 keV band, with a significance of 9.8σ. Between 10–25.2 keV, and in the full energy band 3–25.2 keV the source is not detected.

We combined the two JEM-X mosaics, using the `j_ima_mosaic` tool. The significance maps of the 3–10.2 keV and 10.2–25.2 keV bands are shown in Figure 8.17. Between 3 and 10.2 keV M87 has a significance of 15.1σ, while between 10.2 and 25.2 keV M87 is not detected. In the full energy band from 3 to 25.2 keV, M87 has a significance of 10.1σ.

We used `mosaic_spec` to extract a flux at the position of M87. We have also tried to sum all the spectra created in the individual scw using `spe_pick`, but due to the source being faint the spectrum is dominated by background noise. Using the count rate from `mosaic_spec` and the appropriate Crab count rate and flux for normalization, we found a flux of $f = (1.6 \pm 0.2) \times 10^{-11}\,\mathrm{erg\,cm^{-2}\,s^{-1}}$ between 3 and 10.2 keV. Between 10.2–25 keV we found a $3-\sigma$ upper limit to the flux of $f < 1.2 \times 10^{-11}\,\mathrm{erg\,cm^{-2}\,s^{-1}}$. From the 3–10.2 keV detection, a power law index of $\Gamma > 2.0$ would be necessary to be consistent with the upper limit in the 10.2–25.2 keV range. Comparing the JEM-X detection to the IBIS/ISGRI $3-\sigma$ UL of $f < 3.3 \times 10^{-12}\,\mathrm{erg\,cm^{-2}\,s^{-1}}$ in the 20–60 keV band, a power law index of $\Gamma > 2.85$ is required. This power law index is steep compared to other *INTEGRAL* detected AGN. In fact, the second *INTEGRAL* catalogue showed that only 2 out of 22 sources (both BL Lac objects) with combined JEM-X and ISGRI fitting, have a power law index $\Gamma > 2.5$ (Beckmann et al. 2009).

Core emission

Due to the limited angular resolution of JEM-X, with a full-width at half maximum (FWHM) of 3 arcminutes, we cannot resolve the components of M87, which has a total size of 7'x7' on the sky. In the case of IBIS/ISGRI, the angular resolution is even worse, with a FWHM

Figure 8.17: Significance maps of the mosaic of the two JEM-X detectors combined. The left image shows the significance map between 3–10.2 keV, right image the significance map between 10.2–25.2 keV. The image is centred on M87, which can be seen in the middle of the left image. The bright source next to M87 is NGC 4388, which has a significance of $\sim 33\sigma$ between 3–10.2 keV and a flux of $f = 1.6 \times 10^{-11}\,\mathrm{erg\,cm^{-2}\,s^{-1}}$, and $\sim 38\sigma$ between 10 and 25 keV, and a flux of $f = 5.4 \times 10^{-11}\,\mathrm{erg\,cm^{-2}\,s^{-1}}$.

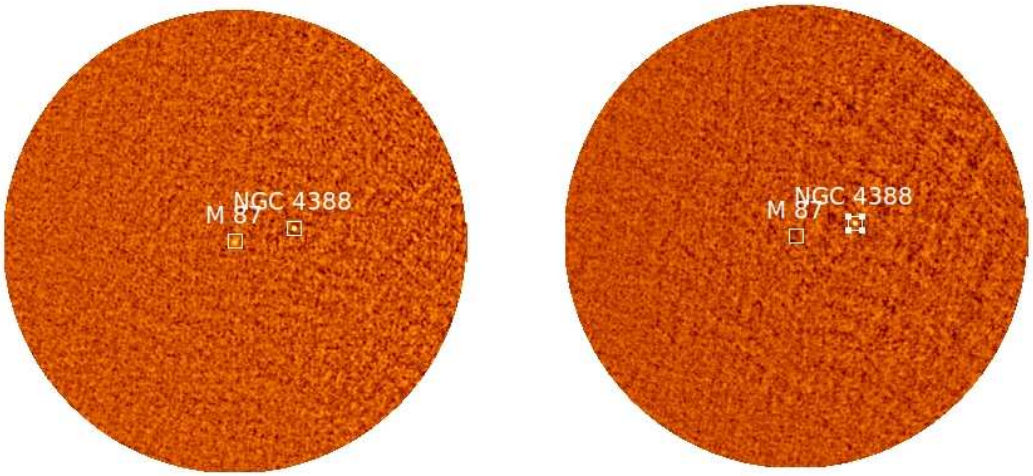

of ∼12', but since few hard X-ray missions (e.g. *NuSTAR*) have an angular resolution which allows to distinguish the different components in M87, there is no measurement up to now of the hard X-ray flux from the core to compare with the full flux observed with IBIS/ISGRI. *INTEGRAL* observations of the nearby source Centaurus A have shown that the hard X-ray emission up to 1000 keV coincides with the core and no extended emission is detectable from the radio lobes (Beckmann et al. 2011).

For soft X-rays the situation is different. Instruments such as *Chandra*, which have a high angular resolution of 0.5" (Weisskopf et al. 2000), have observed M87 and have shown that soft X-ray emission arises from the core, the jet and a diffuse extended region (see for example Wilson & Yang 2002). For our analysis of M87 we are interested in the origin of the high-energy emission, emitted from, or close to, the core. Earlier results, for example by extrapolating *XMM-Newton* UV observations taken in 2010, suggest a core flux is $f = 1.3 \times 10^{-12}\,\mathrm{erg\,cm^{-2}\,s^{-1}}$ between 3-10 keV (Sabra et al. 2003).

An issue with detecting the core flux of M87 using instruments such as *Chandra* but also *XMM-Newton* is pile-up (González-Martín et al. 2009). The contents of a CCD (charge-coupled device) detector is read out at regular intervals, with this read out being also called a frame (Ballet 2001). A detection, or event, is the result of a photon causing an excess in the charge content, where the charge is connected to the energy of the photon. Pile-up in bright sources then happens if two or more photons are detected within the same read-out and thus observed as one event. This causes loss of information both of detected energy, since the sum

Figure 8.18: *Chandra*/ACIS image of M87. The green circle shows the FWHM of JEM-X (2.5'). The core, which is piled-up in this observation, and the jet are visible in the middle of the image.

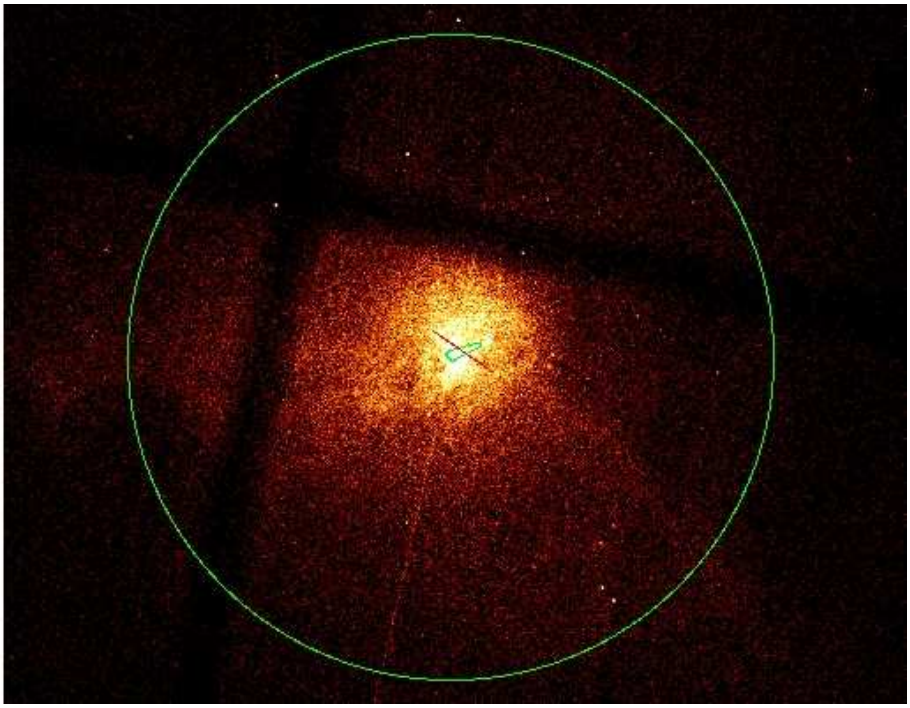

of two photon energies is detected as a single photon, and also spectral changes due to the transfer of low energy photons to higher energies, resulting in an hardening of the spectrum.

To properly estimate the core emission using the JEM-X detection, we used *Chandra* observations (see Section 6.2.4 for the instrument description), to estimate the diffuse extended emission. The ACIS (Advanced CCD Imaging Spectrometer) onboard of *Chandra* is sensitive between 0.2–10 keV, and has a spatial resolution of < 1 arcsecond. The observations we used were made between 3 to 5 May 2005, with an on-time exposure of 123 ks. First we imaged the events file with DS9, where we defined two regions, one corresponding to the FWHM of JEM-X, where we used a 2.5 arcmin radius centred on the core of M87, in which the core (which is piled-up) and jet are excluded (see Figure 8.18), and the other one for the estimation of the background. Then we extract a spectrum from the event file in these regions using SPECEXTRACT, which also builds associated response and ancillary response files. The resulting spectrum is rebinned to increase the significance of the data points at higher energies. We fitted the 1 to 10 keV spectrum with an absorbed model for the emission of hot diffuse gas (mekal, Mewe et al. 1985, 1986; Kaastra 1992; Liedahl et al. 1995). The fit has a goodness of $\chi^2_\nu = 2.9$ for 266 d.o.f., due to higher bins being less defined (see Figure 8.19), and a flux between 3 and 10 keV of $f_{\rm ext} = 9 \times 10^{-12}\,{\rm erg\,cm^{-2}\,s^{-1}}$ is derived.

The jet emission is dominated by the knots in the jet. The closest, 0.85" from the core, is HST-1, which is variable and was in outburst between 2003 to 2007, with a peak luminosity in

Figure 8.19: *Chandra*/ACIS count spectrum of the M87 diffuse emission, modelled with a spectrum for diffuse hot gas (mekal). The bottom panel shows the residuals.

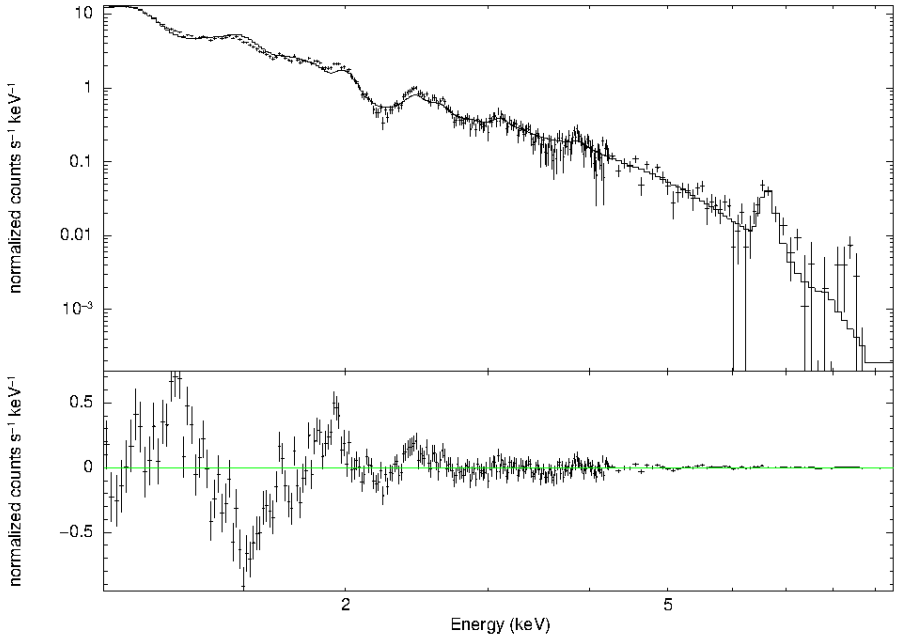

2005. Most of the JEM-X observations have been made after 2008, so this outburst does not have any influence on the luminosity derived with JEM-X. Using *Chandra*/ACIS observations from 29-30 July 2009, Perlman & Wilson (2005) fit the HST-1 data with an absorbed power law model between 0.3–5 keV. Using the fit parameters in `xspec`, we were able to derive a flux of $f_{\mathrm{HST-1}} \sim 2 \times 10^{-13}\,\mathrm{erg\,cm^{-2}\,s^{-1}}$ between 3 and 10 keV.

The knots at a larger distance from the core, D ,E, F, A, B and C, also contribute to the jet flux. Using *Chandra*/ACIS during an observation of M87 on 20 April 2000, Wilson & Yang (2002) obtained spectra for the knots in the jet. Using these in `xspec` yielded the flux for these knots. The brightest knot between 3–10 keV is A with a flux of $f_{\mathrm{A}} \sim 3 \times 10^{-13}\,\mathrm{erg\,cm^{-2}\,s^{-1}}$, similar to HST-1. Adding all the fluxes gives a total flux for the jet of $\sim 10^{-12}\,\mathrm{erg\,cm^{-2}\,s^{-1}}$ between 3 and 10 keV.

The core flux for M87 using JEM-X is $f \simeq 6 \times 10^{-12}\,\mathrm{erg\,cm^{-2}\,s^{-1}}$ between 3 and 10 keV, which is higher than the estimate by Sabra et al. (2003).

8.4.3 Fermi/LAT

M87 is reported in the first and second *Fermi*/LAT catalogue (Abdo et al. 2010a; Nolan et al. 2012), with a significance between 100 MeV to 100 GeV of 10.8σ and 16.7σ, respectively.
In Section 7.3 a description of the *Fermi*/LAT data reduction and likelihood analysis is provided. We downloaded all available Pass 7 data from 4th August 2008 to 29 May 2012, see Figure 8.20 for a light curve.For the Pass 7 data the event classes have been redefined compared to the Pass 6 data. The default for non-transient sources is class 2, this was the diffuse class in Pass 6. The classes 3 and 4, Clean and UltraClean are only recommended for very

Figure 8.20: Light curve of all *Fermi*/LAT used, between 100 MeV and 100 GeV. The light curve has been binned with month.

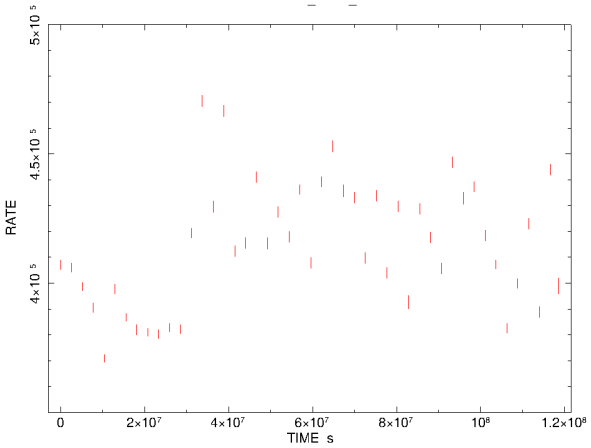

bright sources, since the photon selection is very restricted. For our analysis, we selected the event class 2, source events, the default recommended by the instrument team. We selected events in a radius of 30°around the source, since we intended to use the binned likelihood analysis (see Section 7.3). The region selection in this step is conical, and must fully contain 3D counts map spatial boundary, which is square. We also selected a maximum zenith angle of 100°, as recommended by the LAT instrument team. The photons coming from the Earth limb introduce a strong background, and setting the angle to 100 °provides a buffer of 13 degrees between the region of interest (ROI) and the Earth's limb. We chose events with an energy range between 100 MeV to 100 GeV. Then we filtered the events with the good time intervals, based on the spacecraft file, selected time, ROI, event class and zenith angle. The standard cuts include for example the data quality and the instrument configuration. A count map of the region is shown in Figure 8.21

For the binned analysis we created a 3D binned counts cube, which has an energy axis in addition to the spatial axes. The spatial size of the cube has to fit in the circular ROI, we choose a 40° by 40° map. The binning of the count map determines the binning of the exposure calculation, we used 30 logarithmically uniform bins.

The number of counts detected from a source depends on the inclination angle of the instrument, and the time passed during this inclination angle. It also depends on the livetime, the accumulated time during which the detector was taking data, which depends on the sky position and inclination angle. Now, using the spacecraft file and the time range in the events file, we computed a livetime cube to cover the entire sky. For practical reasons, the cubes are calculated on a grid, and the inclination angle is binned.

Using the livetime cube we generated the binned exposure map, with the exposure at each position in the sky. To ensure that the contribution of all sources, even those outside the ROI are accounted for, the exposure map should include sources up to 10° outside the ROI. This is necessary due to the large point spread function (PSF) of the detector, especially at lower energies. We made an exposure map for the whole sky, $360° \times 180°$, since there is only a small increase in processing power necessary compared to a map covering the intended section of the sky.

Figure 8.21: *Fermi*/LAT counts map summed over the total energy range around M87 (60° x40°). The background is 10-20 counts, M87 has about 35 counts. For comparison, the bright source 4C +21.35, just above M87 has about 400 counts, and 3C 273, below M87 has about 200 counts.

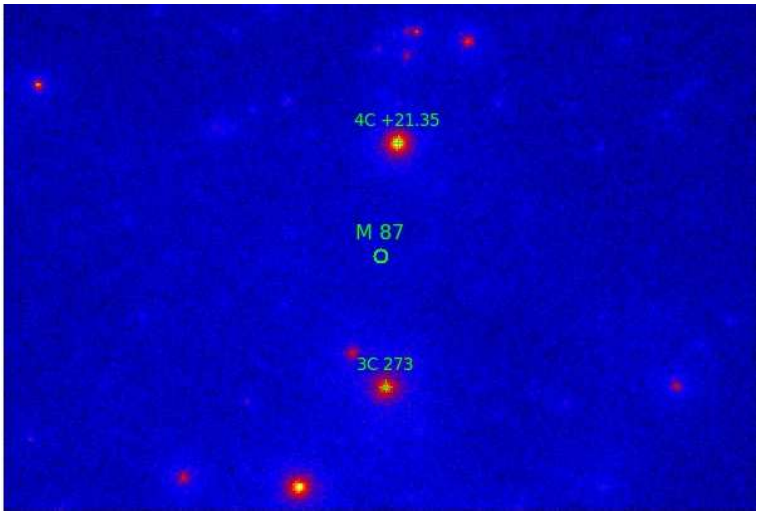

It is necessary to create model count maps which are used for the binned analysis. The model count maps need each spectrum in the model, which is multiplied with the exposure at the source position, and then convolved with the effective PSF. To do this the source model, livetime cube, the counts cube, the exposure map, and the spacecraft file are needed. As demonstrated in Section 7.3, finding a model which represents the data properly is important to deduce physical parameters of the source.

For this we used a user-contributed python tool[3]. This tool creates an xml model file for a given ROI from the catalogue, either first or second. We used the second catalogue, which created a model with 228 point sources in the 30°radius. We froze the parameters of all sources outside of a 10° radius of M87. The -log likelihood of the fit is $L = 438682.4$. We found for M87 a TS value of 370, which is 19σ, a flux of $2.2 \times 10^{-8}\,\mathrm{ph\,cm^{-2}\,s^{-1}}$ and a power law index of $\Gamma_\gamma = 2.16 \pm 0.06$. The significance we found is higher than the catalogue value of 16.7σ, but the flux and power law index are consistent. To study if the model properly represents the data we create model map, which shows the count map in the ROI based on the model fit. Then, we make a counts map with the same field of view as the model map, and subtract the model map to create a residual map. The residual map shows structures, mostly negative count rates. This would indicate that the model does not attribute enough counts to these regions. The features on the residual map coincide with the position of bright sources, which are outside the 10° radius of M87, so the parameters have been fixed in the analysis.
To improve the model we free also four bright sources 4C +21.35, 3C 279, BZB J1230+2518 and 3C 273. The -log likelihood of the fit is $L = 437437.9$, a decrease compared to the previous fit. This yielded very similar values for M87, a significance of TS=370, a flux of

[3]Created by T. Johnson, can be found here: http://fermi.gsfc.nasa.gov/ssc/data/analysis/user

.

Table 8.4: Results of the binned likelihood in 5 energy bins. The energy bins are chosen logarithmically between 100 MeV and 100 GeV. The errors are given with $1-\sigma$ significance.

Bin	Emin [GeV]	Emax [GeV]	TS	Flux [$\mathrm{ph\,cm^{-2}\,s^{-1}}$]	Power law index
1	0.1	0.4	35.6	$(1.5 \pm 0.5) \times 10^{-8}$	1.9 ± 0.6
2	0.4	1.6	125.7	$(3.2 \pm 0.4) \times 10^{-9}$	1.9 ± 0.3
3	1.6	3.0	105.1	$(6.2 \pm 1.0) \times 10^{-10}$	2.7 ± 0.5
4	3.0	10.0	87.0	$(3.2 \pm 0.3) \times 10^{-10}$	1.47 ± 0.05
5	10.0	100.0	11.6	$(4.3 \pm 1.0) \times 10^{-11}$	2.29 ± 0.06

$f = (2.2 \pm 0.3) \times 10^{-8}\,\mathrm{ph\,cm^{-2}\,s^{-1}}$ and a spectral index of $\Gamma_\gamma = 2.16 \pm 0.06$. The residual map seemed slightly improved, but there were still indications that the bright sources are not properly modelled. However, since the values we derived for M87 are stable and consistent with the catalogue values, we decided to use these values.

Since M87 is detected with a significance of $> 10\sigma$ the source is bright enough to study the spectral behaviour. For this we created 5 logarithmic energy bins, similar to those used in the catalogue. It is necessary to redo the analysis from the start with the chosen energy ranges. Also the livetime cube and exposure map have to be calculated within the chosen energy range. Then source models were created and the likelihood analysis is applied. We used the model with the bright sources and near ($< 10^\circ$) sources free. The result of the analysis can be found in Table 8.4. As can be seen, the highest significance of the source is in the second bin, 0.4–1.6 GeV, where the significance is TS=125.7, or 11.2σ, and third bin, 1.6–3.0 GeV, with TS=105.1, or 10.2σ. This is similar to the *Fermi* catalogue, where the significance is highest in the 1–3 GeV bin with 11σ. Between 0.3–1 GeV a significance of 8.2σ is given. The power law indices in the first 3 bins, up to 3 GeV, are consistent with each other and the overall power law index of $\Gamma_\gamma = 2.2$. In the 4th bin, from 3 to 10 GeV, the spectrum is flatter, with a spectral index of $\Gamma_\gamma = 1.47 \pm 0.05$. Then in the last bin there is a turn-over, from 10-100 GeV the index is steep with $\Gamma_\gamma = 2.29 \pm 0.06$.

8.4.4 Suzaku

Suzaku has observed M87 from 29 November to 2 December 2006 (see section 6.2.2 for information about the instrument), with an elapsed time of 187 ks. Since this instrument has both a soft X-ray detector (the X-ray Imaging Spectrometer, XIS) and a Hard X-ray detector (HXD), the data will be useful to compare with the *INTEGRAL* IBIS/ISGRI upper limit and the JEM-X detection.

XIS

The imaging instrument XIS consists of three detectors and is sensitive to ∼0.2–12 keV. When inspecting the cleaned event files visually, a strong striped structure is visible. Therefore, we re-analysed the data using the `aepipeline`, which duplicates the *Suzaku* processing. This pipeline performs calibration, for example by corrected the arrival time of the events, and by screening, for example by removing flickering pixels. Unfortunately the striped structure remained, see Figure 8.22, rendering the observations not usable. It is not clear what caused

Figure 8.22: *Suzaku*/XIS-1 events. A strong striped structure can be seen. (Image size 0.2° by 0.3°).

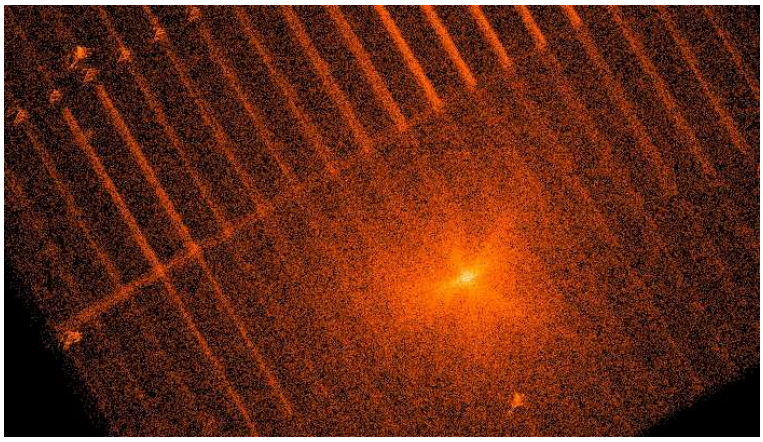

this. According to the observation log, during the observation no problems occurred, however 20 days before the observation of M87 was made, the XIS-2 detector became unstable and suffered damage. After this, the detector was only used for diagnostic observations.

HXD

The HXD detector of *Suzaku* consists of two components, the PIN silicon diodes and GSO (Gadolinium Silicate) phoswich counters. The PIN diodes are sensitive to lower energies, ~ 3 keV to $\sim$ 60keV, whereas the GSO detectors are sensitive from ~ 40 keV up to almost 600 keV.

The *Suzaku* instrument team suggests reprocessing if the data if the data have been processed using version 2.0.X.X, and the observations have been made after 28 July 2007 for PIN. For GSO reprocessing is always recommended. The observations used have been taken before 28 July 2007, but the processing version indicates reprocessing of the data might be necessary.
First we extracted spectra from the clean events provided by the *Suzaku* team using XSELECT. As described in Section 7.4.1, the background for the PIN data consists of a non-X-ray background (NXB), which is due to the detector, and the Cosmic X-ray background (CXB). The NXB file is distributed by the instrument team, where the event rate is 10 times higher than the real background to suppress Poisson errors, so we multiplied the exposure time with a factor of 10. The CXB, which is ∼5% of the background, needs to be simulated in XSPEC. For this the flat PIN response file, which is used for large extended sources, from the corresponding epoch is used (see Section 7.4.1). Then the background files are added, where for the exposure the NXB exposure multiplied by 10 is used.
For the GSO background only the NXB file is necessary, since the CXB is <0.1% of the total background rate. In addition, the exposure of the NXB does not have to be multiplied with 10. For the GSO the backgrounds have been grouped, so it is necessary to group the spectra the same.
Then we merged the GTI files, of the cleaned event and the background files for both PIN and GSO, into a new GTI file. Using XSELECT we extracted spectra from the event and

background files, which are filtered with the GTI file. The GSO spectrum is grouped using the same bins as the background spectrum. Then, the event and GSO background spectra are dead-time corrected. This is not necessary for the PIN background.
For the spectral fitting we needed appropriate, so depending on the epoch and pointing, response files for the PIN and GSO. For the GSO spectral analysis a correction arf file is required. These files are prepared by the instrument team.
The PIN data have enough counts to extract a significant spectrum between 15 and 70 keV, and a flux of $f = 6.5 \times 10^{-12}\,\mathrm{erg\,cm^{-2}\,s^{-1}}$ between 20–60 keV, and a power law index of $\Gamma = 3.3 \pm 0.2$.

After this we decided to reprocess the data from the raw files to confirm the flux and power law index. The re-analysis starts from the two 'well' files, or detector files. At this point, there is not difference between PIN and GSO. First, `hxdtime` is used, which corrects for the arrival times. The arrival time of each event is calculated from the HXD internal time and data processor time into aetime, the Suzaku time coordinate. Then we used `hxdpi` to determine the event pulse height values, based on the gain history, PIN individual gain variation, and other calibration data. By using `hxdgrade` we filter the 5 grade columns. For the first column holds the grade_quality, and the next two columns the origin of the event, either PMT triggered or PIN triggered. The fourth column relates to the GSO and the last column the hit pattern grade.
With XSELECT we screened the files with the cleaned GTI files, for example to exclude intervals during the transition through the SAA, and 500 seconds after, to keep the pointing is constrained within 1.5' of the mean, and the elevation of the target is constrained to at least 5 degrees above the Earth's limb. Now we filtered the detector file to differentiate between the PIN and GSO events, and we added both detector files, also using XSELECT. The keyword DETNAM in the header is left to WELL so we change this to WELL_PIN or WELL_GSO, to indicate which detector is used. For the PIN files, the TIMEDEL has to be set manually to 61μs to avoid problems later in the analysis. From here we used the background spectra and dead-time correction as described before.

The GSO spectrum showed a negative count rate, and the spectrum showed some data points between 30 and 50 keV, and some at 700 keV. We didn't use this spectrum, since it showed only noise.

The PIN spectrum showed significant points between 10 and 23 keV, so we regrouped the spectrum. Between 22–38 keV we grouped the spectrum with a factor of 10, and above 38 keV we grouped with a factor of 20. We fitted the spectrum with an absorbed power law model, $\chi^2_\nu = 1.3$ (27 d.o.f.). Here, the equivalent hydrogen column density is fixed to $N_\mathrm{H} = 2 \times 10^{20}\,\mathrm{cm^{-2}}$. The power law index found is $\Gamma = 2.8^{+0.5}_{-0.4}$ (90% errors). The flux between 20 and 60 keV is $f = 1.3^{+0.1}_{-0.2} \times 10^{-11}\,\mathrm{erg\,cm^{-2}\,s^{-1}}$. The resulting spectrum and fit can be found in Figure 8.23. At the higher energies the model seems to represent the data less well, as the deviation from $\chi^2 = 0$ increases. Due to the low count rate, and lack of significant points, it is not clear if the deviation is due to noise or due to physical processes.

Since the 20–60 keV flux found using PIN is about three times the upper limit to the flux set by *INTEGRAL* IBIS/ISGRI, we used ISGRI data near the *Suzaku* detection to confirm if the detection is consistent with the UL found. Unfortunately there is no simultaneous observation, but during July 2006 ISGRI has observed M87, with an on-source time of 67

Figure 8.23: *Suzaku*/PIN spectrum between 15 and 70 keV with an absorbed power law model. The bottom panel shows the residuals of the fit in terms of the standard deviation with error bars one sigma.

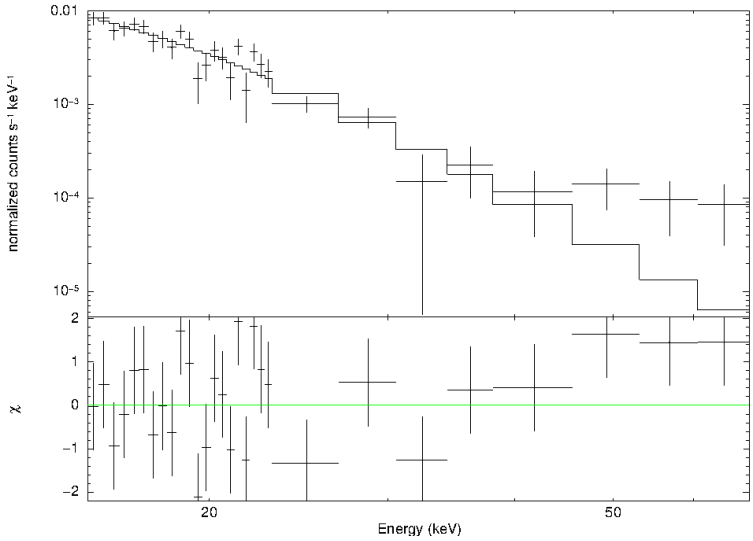

ks. Using `mosaic_spec` we found a 3σ upper limit to the flux between 20 and 60 keV of $f = 3 \times 10^{-11}\,\mathrm{erg\,cm^{-2}\,s^{-1}}$, which is consistent with the flux found using *Suzaku*/PIN.

8.5 SED modelling

To understand the origin of the gamma-ray emission and VHE emission from M87, and the understand the hard X-ray upper limit and detection, we want to create an spectral energy distribution (SED), similar to what we did for 3C 111 (see Section 7.6). We found that for the gamma-ray bright radio galaxy 3C 111 a blazar-type model represented the data properly.

Blazars show a typical SED with two branches, see for example Figure 4.6. To model blazars often a synchrotron self-Compton (SSC) model is used, which reproduces the two-humped SED, with the first hump being caused due to synchrotron emission and the second by inverse Compton of the synchrotron population. A full description of the model is given in Section 7.6.1.

Fossati et al. (1998) showed, using a sample of 126 blazars, both BL Lac and flat spectrum radio sources (FSRQ), that a significant correlation (>90%) between the jet power and the synchrotron peak frequency exists. Weak sources typically show higher peak frequencies than more luminous sources, the least luminous sources, high-peak BL Lacs, show a peak in the synchrotron branch at UV or soft X-rays, and the peak of the inverse Compton branch lies in the gamma-ray to VHE regime. There are several explanations for this phenomena. It is for example thought that low-luminous sources, which have a weak external radiation field, are less influenced by cooling processes, enabling particles to reach high energies, resulting in high peak frequencies for the synchrotron and inverse Compton branch. For the luminous sources, the strong external radiation field contributes to the cooling processes, preventing particles from reaching the highest energies which causes lower peak frequencies of the synchrotron and

inverse Compton branch (Ghisellini et al. 1998). Meyer et al. (2011) proposed an advanced scenario, based on a sample with over 600 blazar SEDs. The population can be divided into a group which shows strong jets without velocity gradients or deceleration, which exhibits radiatively efficient accretion, and a group which shows weak jets, which do show deceleration, and which exhibits radiatively inefficient accretion. They found that the jet power does not completely determine the peak frequencies, and the alignment, or jet angle, also plays a role.

Since M87 is a FR-I type source, it would be natural to model it as a BL Lac, since these sources are thought to be similar in the unification scheme. In addition, M87 has been observed in gamma-rays and beyond, a possible indication for a high-peaked object. In that case, the absence of the hard X-ray emission in the average state could point to the dip between the synchrotron and inverse Compton branch. Abdo et al. (2009c) applied an SSC model to M87, and found that using a jet angle of $\theta = 30°$, the model gave a good representation of the data. Since the jet angle of M87 is known to be 30°we wish to apply an SSC model using this larger jet angle.

8.5.1 Building the SED

We created two SEDs, an average SED using the *INTEGRAL* IBIS/ISGRI and JEM-X, and *Fermi*/LAT observations, and a 2006 SED around the *Suzaku*/PIN detection, since it is not possible to account for both the IBIS/ISGRI upper limit to the flux and the PIN detection. It is likely the difference in flux in the 20–60 keV band during the PIN detection is due to a flare of some kind, and using simultaneous observations can help understand the change in the SED during the flare.

We used the *INTEGRAL* IBIS/ISGRI and JEM-X detection and upper limits and calculated the monochromatic flux at the logarithmic centre. For the *Fermi*/LAT observations we used the 5 bins. For the average SED we also used all available core observations from NED[4] in the radio and infra red band. We also used observations from *Chandra*/ACIS-S, taken between November 2008 and May 2009 (Abdo et al. 2009c). For the TeV regime we used data from H.E.S.S. observations taken between 2003 and 2006 (Aharonian et al. 2006).

For the 2006 PIN detection we tried to find simultaneous observations, however during the small-time frame of 3 days there were no observations in other wavebands available. Instead, we searched for observations that were made during the same year, which yielded four different detections, with the largest time gap being 8 months (see Table 8.5). Compared to the average observations, the *Suzaku* point and the observation at 18.7μm deviate, and the other observations seem to be consistent, see Figure 8.24.

8.5.2 SSC codes used

To model the SED of M87 we used two SSC codes. One, developed by Krawczynski et al. (2004), which is described in section 7.6.3. Second, we used a code developed by Andrea Tramacere[5] (Tramacere et al. 2009, 2011; Massaro et al. 2006). The code developed by Andrea Tramacere (hereafter AT) is based on the same principles as the code developed by Krawczynski. An electron plasma is confined in a spherical, homogeneously emitting, region with radius R_s and a randomly oriented magnetic field B. This region moves down the relativistic jet with a bulk Lorentz factor Γ, and the jet has an angle θ to the line of sight, which yields a

[4] http://ned.ipac.caltech.edu/

[5] The code can be found here: http://isdc-web00.isdc.unige.ch/sedtool/SED_Web_tool/html_js/SED_Web_tool/SED_start_test.html

Figure 8.24: Spectral energy distribution of M87. The green stars in the NED data points, the red diamonds the 2006 observations. The blue square is the JEM-X core flux, the blue triangles show the JEM-X and IBIS/ISGRI upper limits to the flux. The red square is the PIN detection from 2006. The blue circles are the *Fermi*/LAT detections, and the green boxes show the H.E.S.S. observations.

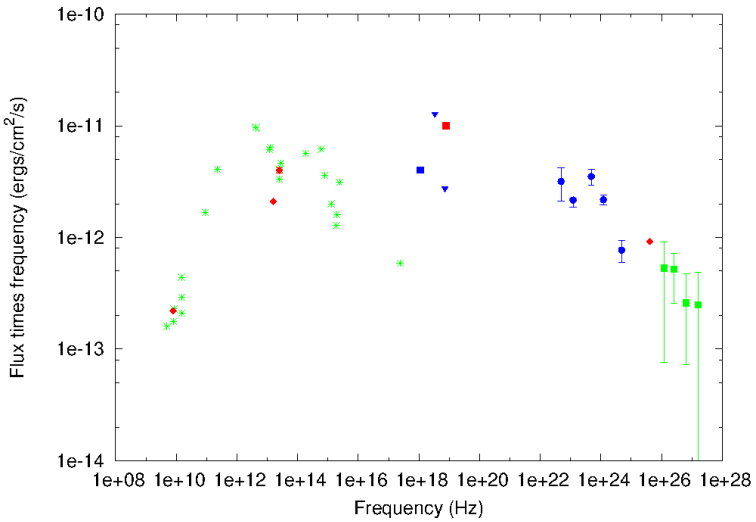

.

Table 8.5: List of observations used in the 2006 SED.

Observation date	Instrument	Waveband	Flux	Reference
December 2006	MAGIC	>100 GeV	6×10^{-12} ph cm^{-2} s^{-1}	(Berger 2011)
29-11-2006 to 2-12-2006	*Suzaku*/PIN	20-60 keV	1.3×10^{-11} erg cm^{-2} s^{-1}.	this work
9-3-2006	VISIR	11.9 μm	16 ± 0.8 mJy	(Reunanen et al. 2010)
9-3-2006	VISIR	18.7 μm	$\lesssim 18$ mJy	(Reunanen et al. 2010)
17-4-2006	VLA	8.4 GHz	2726 mJy	(Capetti et al. 2009)

Doppler factor of $\delta = [\Gamma(1 - \beta\cos\theta)]^{-1}$. The electrons emit synchrotron radiation which is then inverse Compton upscattered to higher energies. The electron energy distribution can be described in several ways, the most common is a broken power law, as utilized in the Krawczynski code, but the SSC code developed by AT has more options, for example a log parabolic function, or a power law with an exponential cut-off. (see Section 7.6.1 for a more extensive description).
The different codes have a different implementation. The Krawczynski code uses the input parameters to simulate a spectrum. The AT code uses the input parameters within certain bounds, and then uses a fitting routine to model the spectrum. The advantage is that the fit has a quantifiable goodness, and that the parameters are fine-tuned to get the best representation of the emission. A disadvantage is that data points with smaller error bars, most the lower energy observations, in the SED can dominate the fitting. Also additional information, from spectral analysis for example, can not be used to enforce a certain shape in the final SED.

8.5.3 SED for the average state

For the modelling we have applied the code developed by Andrea Tramacere. This code has a fitting routine, which searches for a minimum in the χ^2-space. Since the parameters are interconnected, finding a low χ^2 for the fit is not trivial. In certain cases we fixed the parameters to the best fit value, or a value is chosen based on literature.

To model the SED of M87 we used a broken power law distribution to characterise the electron energy distribution, and we added an additional host galaxy component, which shows a peak in the optical. The host galaxy contribution is $\nu f(\nu) = (4 \pm 2) \times 10^{-12}\,\mathrm{erg\,cm^{-2}\,s^{-1}}$. First we fixed the Doppler factor to $\delta = 5$, the bulk Lorentz factor Γ and the jet angle θ can vary within this limit. A Doppler factor of $\delta = 5$ is consistent with the apparent motion observed of $\sim 0.5c$ (Kellermann et al. 2007). The fit yields a $\chi^2_\nu = 2.5$ (20 d.o.f.). The magnetic field of $B = 3.8 \times 10^{-3}\,\mathrm{G}$, the radius of $R_s = 1.3 \times 10^{17}\,\mathrm{cm}$ and the minimum energy of the electron distribution of $E_{\mathrm{min}} = 2.9 \times 10^6\,\mathrm{eV}$ are fixed to the best-fit values. For the maximum energy of the electron distribution a value of $E_{\mathrm{max}} = 4.5 \times 10^{13}\,\mathrm{eV}$ is found, this is similar to the maximum energy used to model the blazar Mrk 421 in Figure 4.6 (Abdo et al. 2011). The break energy is $E_{\mathrm{br}} = 2 \times 10^9\,\mathrm{eV}$, similar to the model used by Abdo et al. (2009c) to model the SED of M87. The indices of the broken power law used to characterise the electron energy distribution are $p_1 = 1.2$ and $p_2 = 3.5$, similar to the values used by Abdo et al. (2009c). The electron density for the jet is found to be $n = 4.6\,\mathrm{cm^{-3}}$.

Next we fixed the jet angle at $\theta = 10°$. The fit has a $\chi^2_\nu = 3.3$ (17 d.o.f.). A bulk Lorentz factor of $\Gamma = 2.5$ is found, which indicates a Doppler factor of $\delta = 4.1$. For the magnetic field of the emitting region $B = 8.0 \times 10^{-3}\,\mathrm{G}$ is used. The radius of the emitting region is $R_s = 8.7 \times 10^{16}\,\mathrm{cm}$, smaller than the previous fit, allowing less particles in the emitting region and as such decreasing the overall power in the SED. This can be linked to the smaller magnetic field B in this fit, compared to the previous one, since a lower magnetic field decreases the synchrotron power and thus lowers the overall power in the SED. The minimum energy of the electron distribution is now $E_{\mathrm{min}} = 1.0 \times 10^7\,\mathrm{eV}$, the maximum power is $E_{\mathrm{max}} = 1.2 \times 10^{13}\,\mathrm{eV}$ and the break energy is $E_{\mathrm{br}} = 1.7 \times 10^9\,\mathrm{eV}$. The minimum energy E_{min} and the break energy E_{br} are similar to those found in the previous fit with the fixed Doppler factor to $\delta = 5$, but the maximum energy E_{max} increased. The power law indices of the electron energy distribution are similar to the previous fit with $p_1 = 1.0$ and $p_2 = 3.5$.

.

Table 8.6: Results of the SSC modelling of the SED of M87. The first column shows the parameters of the SSC code, the second, third and fourth column the results of fitting the data with the code developed by A. Tramacere, for the instances of a jet angle of a fixed Doppler factor of $\delta = 5$, a fixed jet angle of θ=10°, and θ =30°. The fifth column shows the results using the same code on the 2006 SED, which includes the *Suzaku*/PIN detection, with a fixed Doppler factor of $\delta = 5$. The sixth column shows the result of the SED modelling using the SSC code developed by Krawczynski et al. (2004), based on the 2006 data points. The last column shows the results derived by Abdo et al. (2009c) on the SED of M87, using a jet angle of θ=10°.

Parameter	AT fixed beam	AT 10°	AT 30°	AT 2006	Krawczynski 2006 [d]	Abdo 2009
θ	-[c]	10°[a]	30°[a]	-[c]	30°	10°
B [G]	3.8×10^{-3} [b]	8.0×10^{-3} [b]	1.0×10^{-2} [b]	1.3×10^{-2}	4.0×10^{-2}	5.5×10^{-2}
R_s [cm]	1.3×10^{17} [b]	8.7×10^{16}	4.3×10^{17} [b]	3.3×10^{16} [b]	4.3×10^{17}	1.4×10^{16}
Γ	-[c]	2.5	3.5	-[c]	3	2.3
$E_{\rm min}$ [eV]	2.9×10^{6} [b]	1.0×10^{7}	2.0×10^{7} [b]	2.9×10^{7}	2.0×10^{7}	5×10^{5}
$E_{\rm max}$ [eV]	4.5×10^{13}	1.2×10^{13}	5.9×10^{12}	5.4×10^{12}	6.3×10^{12}	5×10^{12}
$E_{\rm br}$ [eV]	2.0×10^{9}	1.7×10^{9}	2.0×10^{9}	8.3×10^{8}	2.0×10^{11}	2×10^{9}
p_1	1.2	1.0	1.0	0.9	2.2	1.6
p_2	3.5	3.5	3.5	3.5	3.8	3.6
$n\,[{\rm cm}^{-3}]$	4.6	5.0	0.6	38.4	-	-
χ^2_ν	2.5 (20 d.o.f.)	3.3 (17 d.o.f.)	3.1 (19 d.o.f.)	3.0 (18 d.o.f.)	-	-

[a] The parameter is fixed.

[b] The parameter is fixed to best-fit value or literature values.

[c] The Doppler factor is fixed to $\delta = 5$.

[d] Parameters can not vary.

Figure 8.25: Results of the AT code on the average SED where a jet angle of 30°is used, see text for parameters. The black arrows show the *INTEGRAL* upper limits derived. The blue curve shows the SSC model and the purple line shows the host galaxy component.

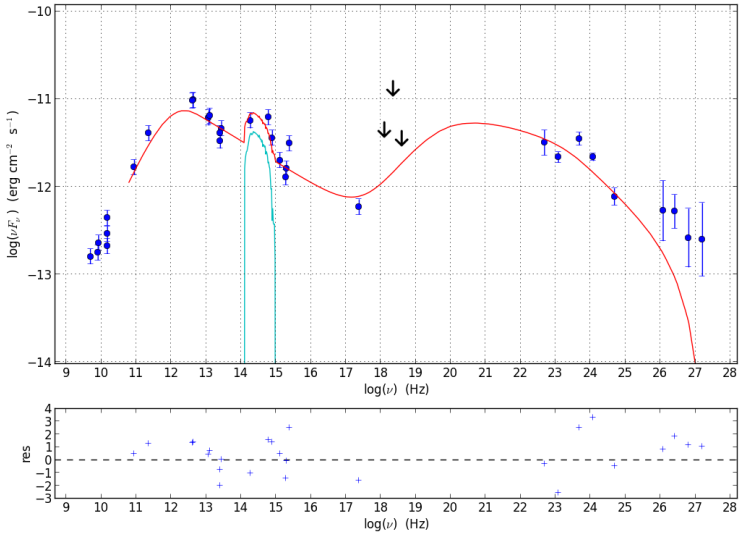

The electron density is also at a similar level of $n = 5.0\,\mathrm{cm}^{-3}$.

Lastly, the angle of the jet is fixed to $\theta = 30°$, as known from literature (see Section 8.2). The fit yielded $\chi^2_\nu = 3.1$ (19 d.o.f.), see Figure 8.25. The bulk Lorentz factor increased to $\Gamma = 3.5$ compared to the fit with a jet angle of $\theta = 10°$. This gives a Doppler factor of $\delta = 1.7$. Since the Doppler factor δ is now lower as before, both the magnetic field $B = 1.0 \times 10^{-2}\,\mathrm{G}$ and the radius $R_s = 4.3 \times 10^{17}\,\mathrm{cm}$ (both are fixed to the best-fit value) increased to compensate for the decrease in power caused by the lower Doppler factor. The electron distribution has a minimum energy fixed to $E_{\mathrm{min}} = 2.0 \times 10^7\,\mathrm{eV}$. The maximum energy of $E_{\mathrm{max}} = 5.9 \times 10^{12}\,\mathrm{eV}$ is lower than for the previous fits, but close to the value derived by Abdo et al. (2009c). The break energy of $E_{\mathrm{br}} = 2.0 \times 10^9\,\mathrm{eV}$ is the same as before, which would indicate this parameter is not dependent on the angle. Similarly the indices of the broken power law that characterise the electron energy distribution are $p_1 = 1.0$ and $p_2 = 3.5$. The electron density decreased in this fit to $n = 0.6\,\mathrm{cm}^{-3}$.

8.5.4 2006 SED

The main change in the 2006 data points compared to the average state is in the X-ray emission. The radio and infra red observations are not distinguishable from the average observations. The MAGIC observation seems to follow the line between the *Fermi*/LAT and H.E.S.S. observations. However, since the SED is clearly under sampled, it is possible that the broad-band spectrum does show a different shape compared to the average state, similar to blazars in outburst. During a flaring episode the luminosity increases, and the peak frequencies of the synchrotron and inverse Compton in the SED increase as well, resulting in a different broad-band emission compared to a low-flux state, see for example Figure 12 in Błażejowski et al. (2005), which shows the source Mrk 421 at different flux states.

Figure 8.26: Results of the AT code on the 2006 SED, see text for parameters. The blue curve shows the SSC model and the purple line shows the host galaxy component.

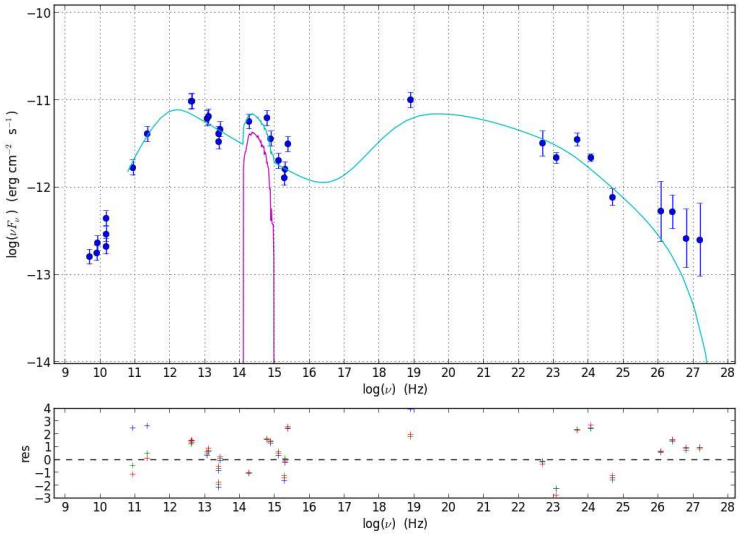

First we used the AT code, using a fixed Doppler factor of $\delta = 5$. The radius in this fit is fixed to $R_s = 3.3 \times 10^{16}$ cm, see the entry AT 2006 in Table 8.6 for the resulting parameters. The magnetic field for this fit is $B = 1.3 \times 10^{-2}$ G, which is higher than the magnetic field found for the smaller jet angles. For the minimum energy a value of $E_{\rm min} = 2.9 \times 10^7$ eV is found, which is higher than the value found for the average SED with a fixed Doppler value of $\delta = 5$. The maximum energy, $E_{\rm max} = 5.4 \times 10^{12}$ keV, is similar to the value found for average SED with a fixed angle of θ =30°, but lower than found for the average SED with smaller jet angles. The break energy $E_{\rm br} = 8.3 \times 10^8$ eV is smaller to the values found as before. Overall the energy distribution of the electrons is different than for the other configurations. The power law indices stay the same however, with $p_1 = 0.9$ and $p_2 = 3.5$. The electron density increased to $n = 38.5\,{\rm cm}^{-3}$. Figure 8.26 shows the model and data points. The model does not properly represent the SED in the X-ray regime, since the power law index in the band is known to be $\Gamma = 2.8$ (see Section 8.4.4). This would result in a steep shape in the SED, possibly the declining synchrotron branch. Therefore, we decide to also use the code of Krawczynski et al. (2004) on this SED, which allows more control over the output due to the absence of a fitting routine.

For this model a jet angle of $\theta = 30°$ is used, and we started to tune the parameters from the results for the average SED. The parameters can be found in Table 8.6, and Figure 8.27. For the bulk Lorentz factor a value of $\Gamma = 3$ is used, which is similar to for the average SED. The magnetic field, $B = 4.0 \times 10^{-2}$ G increased, which is natural since the peak frequency for the synchrotron branch, which depends on the magnetic field B, increased. We found the radius of the emitting region to remain the same as during the average SED, at $R = 4.3 \times 10^{17}$ cm. The minimum energy of the electrons also does not need to change to fit this SED, $E_{\rm min} = 2.0 \times 10^7$ eV. The maximum energy increased to $E_{\rm max} = 6.3 \times 10^{12}$ eV to accommodate better the end of the Compton branch. The break energy increased to $E_{\rm br} = 2.0 \times 10^{11}$ eV, since the peak frequencies of both the synchrotron and the inverse

Figure 8.27: Results of the Krawczynski code on the 2006 SED, see the text for parameters. The fitting is focussed on the green, 2006 data points. The red data points show the average state of the source for comparison.

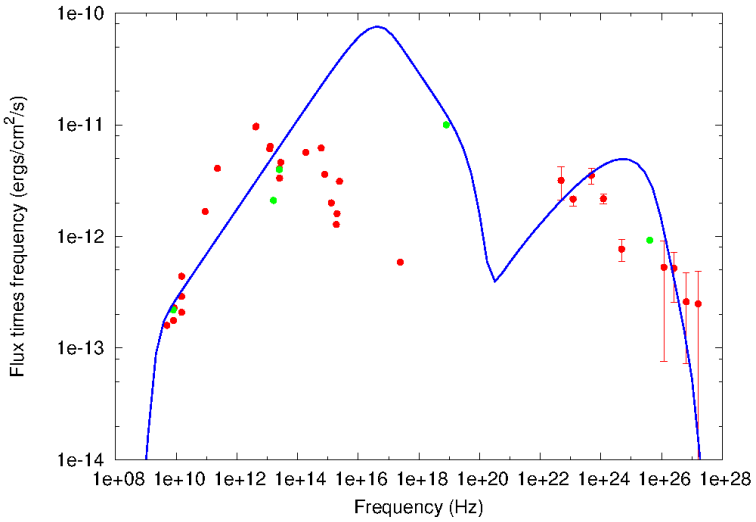

Compton are dependent on this parameter. Lastly, the power law indices of that characterise the electron energy distribution are $p_1 = 2.2$ and $p_2 = 3.8$, showing a change from previous results which might indicate that during the flaring the physical properties of the emission changed.

8.6 Discussion

8.6.1 Hard X-ray

Using all available *INTEGRAL* IBIS/ISGRI, with a total exposure time of 1.7 Ms, we find no significant detection of M87 between 20 and 60 keV. The $3-\sigma$ upper limit to the flux we found is $f < 3 \times 10^{-12}\,\mathrm{erg\,cm^{-2}\,s^{-1}}$. This is not consistent with a 5.1σ detection found earlier using IBIS/ISGRI observations, where a flux of $f = (8.6 \pm 1.8) \times 10^{-12}\,\mathrm{erg\,cm^{-2}\,s^{-1}}$ was found (Walter & Neronov 2008). This can be due for example to the newer software used in our analysis, which has improved the image cleaning. We created a mosaic using a similar data set as Walter & Neronov (2008), we did not detect M87, and found a 3σ upper limit to the flux of $f < 8 \times 10^{-12}\,\mathrm{erg\,cm^{-2}\,s^{-1}}$, which is not consistent with the earlier detection claim.

We also analysed *Suzaku*/PIN observations from the end of November to early December 2006, with an elapsed time of 187 ks. The observation yielded a detection of $f = 1.3 \times 10^{-11}\,\mathrm{erg\,cm^{-2}\,s^{-1}}$ between 20 and 60 keV, which is about three times as high as the average upper limit to the flux. This indicates that M87 was flaring during the time the observation was made, and as such the flux increased significantly.

8.6.2 Spectral energy distribution

In the soft X-ray emission of M87, no thermal features such as the iron K-α line are observed. This indicates that, in addition to the radio and gamma-ray emission, also in the soft X-ray band the jet emission dominates. Therefore, the use of a SSC model, based on jet emission, to represent the broad-band SED is a natural choice for M87. Similar to the 3C 111 SED in the previous chapter, the SED analysed for M87 is not simultaneous and this might result in a biased measurement if an object is variable since several spectral states can contribute to the data. Abramowski et al. (2012) showed light curves of the core of M87 from 2001 to 2011, in radio, optical, X-ray and VHE band. These light curves show a variability in the radio and optical domain, of a factor of $\sim$2, which does not significantly affect the physical parameters derived from the SED. The observations used in the SED are averaged over several years and show a similar trend. A similar approach of using time-averaged SEDs has been applied succesfully to M87 (Abdo et al. 2009c), and also other radio galaxies such as Pictor A (Brown & Adams 2012) and 3C 111 (de Jong et al. 2012b).

The high flux detected by *Suzaku*/PIN in 2006 indicates flaring of M87. Flaring behaviour has been observed in most BL Lac objects, such as Mrk 501 (Tavecchio et al. 2001). During the outburst the overall luminosity increases, and the peak frequencies of the synchrotron and inverse Compton branch increase as well. Tavecchio et al. (2001) show for Mrk 501 that the parameter which varies for the different states to be the break energy, which is interpreted as a change in the acceleration process of the moving electrons. In this frame, the steep power law in the hard X-rays can be interpreted as the tail of the synchrotron branch, in the time-averaged SED the absence of detection rather points to the dip between the synchrotron and inverse Compton branch. In the model for the 2006 SED we find the parameters to be similar to the time-averaged SED with exception of the break energy of the electron distribution, which might indicate flaring. However, due to the low sampling of the 2006 SED it is not possible to discern the typical flaring behaviour as described in Tavecchio et al. (2001).

Another gamma-ray bright FR-I radio galaxy is Centaurus A. The SED of this sources has also been modelled with a SSC code (Abdo et al. 2010c). For Cen A a Doppler factor $\delta = 1.0$ was used, and for M87, when using a jet angle of $\theta = 30^\circ$ for the time averaged SED, the Doppler factor is $\delta = 1.7$. For the radius of the emitting region, Abdo et al. (2010c) used $R_s = 3 \times 10^{15}\,\mathrm{cm}$, where we found for M87 a radius of $R_s = 4 \times 10^{17}\,\mathrm{cm}$. The magnetic field used to model Cen A is $B = 6,2\,\mathrm{G}$, compared to $B = 10^{-2}\,\mathrm{G}$ for M87. Both the radius R_s and magnetic field B influence the overall power in de SED, so the larger magnetic field used for Cen A is compensated by the lower radius of the emitting region. The magnetic field B also influences the frequencies of the synchrotron branches.

BL Lacs are thought to be FR-I sources, when viewed directly into the jet (Urry & Padovani 1995). Comparing the SED of M87 to a BL Lac source, such as Mrk 421, shows a large difference in the Doppler factor δ. For the modelling of M87 we used a Doppler factor $\delta = 1.7$, for Mrk 421 a Doppler factor of $\delta = 10$ is used (Błażejowski et al. 2005). The Doppler factor influences the power in the SED, so a larger Doppler factor to model Mrk 421 is natural. For Mrk 421 a magnetic field $B = 0.405\,\mathrm{G}$ and a radius of the emitting region of $R_s = 2 \times 10^{15}\,\mathrm{cm}$ are used, where the smaller radius is negated by the larger magnetic field for the more luminous source.

8.7 Conclusion

In this chapter we have analysed 1.7 Ms of *INTEGRAL* IBIS/ISGRI observations of the region around the FR-I radio galaxy M87, to set an upper limit to the 20–60 keV flux from this source. The standard analysis showed a mosaic image (the image of all pointing combined) to have an underlying structure. Therefore, we have shown several techniques beyond the standard OSA analysis to improve the image. We derive a 3σ upper limit to the 20–60 keV flux of $f < 3 \times 10^{-12}\,\mathrm{erg\,cm^{-2}\,s^{-1}}$.

We have detected, for the first time M87 at hard X-rays using *Suzaku*/PIN observations made end 2006. The flux between 20 and 60 keV is $f = 1.3^{+0.1}_{-0.2} \times 10^{-11}\,\mathrm{erg\,cm^{-2}\,s^{-1}}$. The spectrum, between 10 and 70 keV, has a steep power law with an index of $\Gamma = 2.8^{+0.5}_{-0.4}$ (90% error). The fit has a goodness of $\chi^2_\nu = 1.3$ (27 d.o.f.), but at higher energies (>50 keV) the model deviates from the data, indicating this fit does not represent the higher energies of the spectrum.

To understand the broad-band emission we model the complete SED from radio to TeV. Here we distinguish between the average SED, using the *INTEGRAL* observations, and a high-flux state SED, using the 2006 *Suzaku*/PIN detection. The overall SED can be modelled with a one-zone synchrotron self-Compton model, similar to blazars. The SED parameters show that M87 can be considered a weak BL Lac source, consistent with an advection dominated accretion flow for the core (ADAF, Ptak et al. 1998; Reynolds et al. 1996). The 2006 observations where likely taken during a flaring episode, during which the source brightened and the peak frequencies of the synchrotron and inverse Compton branches increased. This is also evidenced by the steep PIN spectrum, showing the edge of the synchrotron branch. Unfortunately the 2006 SED is badly sampled, especially at high energies, creating a difficulty to properly represent the inverse Compton branch.

The SED parameters, and the likely ADAF flow, are also consistent with the Unification model (see for example Urry & Padovani 1995), which dictates that FR-I radio galaxies are BL Lac sources seen with a large angle to the jet. The more luminous FSRQ sources are linked to the FR-II radio galaxies, like 3C 111, which have powerful jets. To model the SED of a BL Lac type source, only a SSC model is necessary, whereas the FSRQ object require an additional external Compton component (Ghisellini et al. 1998). For M87 we could model the SED with only SSC, in line with the prediction by the Unification model. But for the FR-II radio galaxy 3C 111 we found that no external component was required to model the SED (de Jong et al. 2012b), unlike the FSRQ counter parts. This might indicate that the accretion in 3C 111 is radiatively inefficient, similar to M87.

Astronomy & Astrophysics manuscript no. M87_draft_theis
September 5, 2013

High-energy Emission Processes in M 87

S. de Jong[1], V. Beckmann[1], S. Soldi[1], and A. Tramacere[2] ea

[1] François Arago Centre, APC, Université Paris Diderot, CNRS/IN2P3, CEA/Irfu, Observatoire de Paris, Sorbonne Paris Cité, 10 rue Alice Domon et Léonie Duquet, 75205 Paris Cedex 13, France
[2] ISDC Data Centre for Astrophysics, 16. ch. d'Écogia, 1290 Versoix, Switzerland

September 5, 2013

ABSTRACT

Aims. We study the contribution of thermal and non-thermal processes to the inverse Compton emission of the radio galaxy M 87 by modelling the broad-band emission. Through this we aim to derive insight into where in the AGN the X-ray, gamma-ray, and VHE emission is produced.
Methods. We use all available *INTEGRAL* IBIS/ISGRI data on M 87 to set an upper limit to the flux in hard X-rays. To do this we have used several techniques beyond the standard analysis: using selected revolutions and by cutting the borders of the shadowgrams to provide a custom background. In addition we analyse data from *Fermi*/LAT, *INTEGRAL*/JEM-X, and *Suzaku*/PIN. We then create a spectral energy distribution of this source using multi-wavelength observations, and model the SED applying various single-zone SSC models with a large jet angle of $\theta = 30^\circ$.
Results. We have detected M 87 using *Suzaku*/PIN data taken late November 2006 with a flux of $f(20-60\,\mathrm{keV}) = 10^{-11}\,\mathrm{erg\,cm^{-2}\,s^{-1}}$. For the average X-ray emission we have set a new upper limit using 1.7 Ms *INTEGRAL* IBIS/ISGRI data resulting in $f \lesssim 3 \times 10^{-12}$ $\mathrm{erg\,cm^{-2}\,s^{-1}}$. We present a summary of the techniques used and the results yielded. We have also analysed data from *INTEGRAL* JEM-X and *Fermi*/LAT, and combined this with historical radio/IR/optical data and VHE data from H.E.S.S., to create a broad-band spectral energy distribution. We model this SED with a synchrotron self-Compton model and show that using this type of model the spectral energy distribution of M 87 can be represented.
Conclusions. We show that modelling the core emission of M 87 using a single-zone synchrotron self-Compton model does represent the SED, suggesting that the core is dominated by a BL Lac type AGN core.

Key words. galaxies: active – galaxies: individual: M 87 – X-rays: galaxies – gamma rays: galaxies

1. Introduction

Radio galaxies are a subclass of AGN, which display jets which are observed with a large angle of $\theta > 10^\circ$ with respect to the line of sight, enabling a view of both the jet and the core. In the unification model of AGN, they are thought to be the radio-loud counterparts of Seyfert galaxies (Antonucci 1993; Urry & Padovani 1995; Beckmann & Shrader 2012). In the case of blazars γ-ray emission is expected due to the small jet angle and the resulting relativistic beaming towards the observer. The relativistic jet will dominate the emission, and due to Doppler boosting this emission can reach into the γ-ray and TeV range. Several non-blazar AGN have also been detected in the γ-ray (see for example the 2FGL catalogue Ackermann et al. (2011)), and a few of these sources have been observed at energies > 100 GeV (Perkins et al. 2012). The mechanism driving this high-energy emission in radio galaxies is still under discussion.

M 87 is a FR-I radio galaxy (Fanaroff & Riley 1974; Laing et al. 1983), with a central supermassive black hole of mass $M_{bh} = (3-6) \times 10^9\,M_\odot$ (Macchetto et al. 1997; Gebhardt & Thomas 2009), at a distance of 16 Mpc (Tonry 1991). The jet is observed to have an angle of $\theta = 30^\circ$ (Bicknell & Begelman 1996) with respect to the line of sight. M 87 has been detected by *Fermi*/LAT (Abdo et al. 2009), making it the third radio galaxy to be detected in γ-rays, after Centaurus A and NCG 1275. M 87 has also been detected at VHE energy ranges during flares, e.g. by *HEGRA* (Aharonian et al. 2003). M 87 shows variable emission in the soft X-ray regime, and extrapolating from high flux states observed by *Chandra* (f$\simeq 2 \times 10^{-12}\,\mathrm{erg\,cm^{-2}\,s^{-1}}$), a flux of $f \simeq 10^{-12}\,\mathrm{erg\,cm^{-2}\,s^{-1}}$ can be expected between 20 and 60 keV. Walter & Neronov (2008) reported a detection with $f = (8.6 \pm 1.8) \times 10^{-12}\,\mathrm{erg\,cm^{-2}\,s^{-1}}$ between 20–60 keV using *INTEGRAL*/ISGRI data.

The proximity of M 87 allows us to image the core separately from the jet and the diffuse extended emission in several wavelengths like radio, optical, and soft X-rays, but not in hard X-rays nor at higher energies. By studying the spectral energy distribution (SED) it is possible to test whether the high-energy emission originates from the core, the jet, or from the extended diffuse emission. Earlier SEDs of M 87 have been represented with a synchrotron self-Compton (SSC) type model, see for example Abdo et al. (2009). SSC models are often used to represent blazars, but they have also been applied to other gamma-ray detected radio galaxies such as Centaurus A (Abdo et al. 2010a). The latter study was inconclusive, though, on the question whether the X-ray domain is dominated by the non-thermal jet emission, or arises rather from a Seyfert type core.

In this paper we present an upper limit on the average long-term hard X-ray emission of M 87 using 1.7 Ms of *INTEGRAL* IBIS/ISGRI data and different techniques for performance enhancement of *INTEGRAL* IBIS/ISGRI. We have also analysed *Suzaku*/PIN data from November 2006, where we have detected M 87 between 20–60 keV. This is combined with other data in soft X-rays by *INTEGRAL*/JEM-X, gamma-rays by *Fermi*/LAT, historical radio, infrared and optical emission of the core, and

VHE data from H.E.S.S. to create an average spectral energy distribution (SED).

2. Data analysis

2.1. INTEGRAL

In this study we used all data on M 87 available data taken by the *INTEGRAL* mission (Winkler et al. 2003) since its launch. Observations are performed in dithering mode with pointed observations, so-called science windows, lasting between 2000s and 4000s. The data cover the time from 2003 to 2011, and most of the observations are taken after 2008. We analysed data from the X-ray monitor JEM-X and from the IBIS/ISGRI imager. JEM-X is a coded-mask instrument consists of 2 indentical coaligned telescopes and operates in the 3 to 35 keV band (Lund et al. 2003). We created images in the energy ranges of 3–10 keV and 10–25 keV for each pointing and combined these into a single mosaic for both the JEM-X detectors. In the energy band 3–10 keV we detect M 87 with a significance of 15.1σ and a flux with $f = 1.6 \times 10^{-11}\,\mathrm{erg\,cm^{-2}\,s^{-1}}$. In the energy band 10–25 keV M 87 is not detectable, with a 3σ upper limit of $f \lesssim 1.2 \times 10^{-11}\,\mathrm{erg\,cm^{-2}\,s^{-1}}$.

The *INTEGRAL* Soft Gamma-Ray Imager (ISGRI) is part of the Imager on Board *INTEGRAL* Spacecraft (IBIS), which is also a coded-mask instrument. ISGRI is sensitive between 15 keV to 1 MeV (Lebrun et al. 2003).
We have used all available IBIS/ISGRI data from the beginning of the mission until 2011 (see Fig. 1), resulting in an effective on-source exposure time of 1.7 Ms. Using the standard Offline Scientific Analysis (OSA) package version 9.0 provided by the ISDC (Courvoisier et al. 2003) we created images for each pointing in the energy range 20–60 keV and combined them together into a mosaic. For M 87 we derived a detection significance of 3.9σ and a flux of $f \simeq 3 \times 10^{-12}\ \mathrm{erg\,cm^{-2}\,s^{-1}}$. However, the mosaic image shows strong noise features in the vicinity of M 87, and thus the detection cannot be deemed as trustworthy. To improve the quality of the image we applied several techniques, a summary of which can be found in Table 1.

In order to quantify the quality of the mosaic images, we determined histograms of the significance image and the root mean square (*rms*) of this histogram, where in the ideal case the mean should be 0 and the $rms = 1$. Using the *rms* we can track the improvement of the mosaic quality. For the mosaic created using OSA 9 we derived $rms = 1.75$. To improve the image we started by excluding those science windows from the mosaic analysis which showed a high noise level, i.e. we removed all science windows with $rms > 1.2$ ($\sim$ 4% of the total). The image quality improved, and the M 87 detection is no longer significant (see Tab. 1). We have also processed the good science windows with the more recent OSA 10 software. We found a detection significance of 1.32 for M 87 and derive an upper limit of $f =\lesssim 3.3 \times 10^{-12}\,\mathrm{erg\,cm^{-2}\,s^{-1}}$, and the mosaic has a $rms = 1.38$ (OSA 10 in Tab. 1).

We then created mosaics per revolution (a revolution lasts about 3 days and has an effective exposure time of $\sim$ 200 ks) to judge their quality based on the *rms* value of the significance map. For the mosaics we set the *rms* threshold to 1.1, because the fluctuations in the mosaics are more averaged out compared to the single science windows. Most of the revolutions that have $rms < 1.1$ are within the first 6.5 years of the mission ($rev < 800$), see Fig. 1. We then combined those images based on revolutions where the rms is < 1.1. The rms of the combined mosaic is 1.18 and we derive for M 87 a 3σ upper limit of $f < 4.2 \times 10^{-12}\,\mathrm{erg\,cm^{-2}\,s^{-1}}$ (Tab. 1: OSA 10 selected revolutions). We also made a mosaic with the combined revolutions with rms >1.1, the upper limit to the flux is $4.9 \times 10^{-12}\,\mathrm{erg\,cm^{-2}\,s^{-1}}$ and the mosaic $rms = 1.39$. In order to increase the image quality, and thus derive a more reliable upper limit on the flux of M 87, we have also modified the *ghost busters* module inside the OSA software. This module has been developed by D. Eckert (ISDC) and removes artifacts in the ISGRI shadowgrams related to bright sources. Here, we fixed the source positions and applied the *ghost busters* corrections also for fainter sources in the field of view, like NGC 4388. This was done on several revolutions, but no significant improvements was detectable applying these techniques.

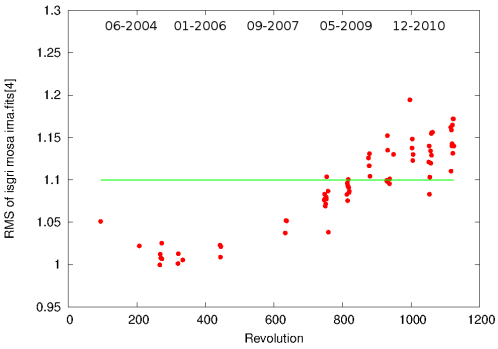

Fig. 1. The evolution of the *rms* of the significance image of the mosaic per revolution. The line shows the cut for $rms = 1.1$. Later revolutions, starting around revolution 800 (2009), have on average a higher *rms*.

Lastly we used a technique which required changes to the program `ii_shadow_ubc`, which is part of the OSA 10 pipeline. This routine performs the background correction using the detector images (shadowgrams). To decrease the noise in the mosaic image we removed pixels from the borders of the shadowgrams, because they can be affected by uncertainties in the exact detector mask thickness and geometry (Soldi et al. 2013). After testing several configurations on single revolutions we used a cut of the 3 outmost pixels to create 3 mosaics containing all available observations: one mosaic contains the non-modified science windows (control), one mosaic where all science windows had been modified, and one mosaic where cuts where applied only for those revolutions with a high *rms* value. To quantitatively judge these mosaics we calculate the rms of the significance extension, where we now considered only the inner $10^\circ x 10^\circ$ and excluding the area around bright sources in the field, since the borders of the mosaics show noise features due to the cutting procedure of the shadow grams. The rms for the modified mosaic is the lowest, $rms = 1.40$, and for the unmodified mosaic the highest, $rms = 1.54$. However, we found that these techniques did not alter the upper limit on the flux of M 87.

2.2. Suzaku/HXD

Suzaku has observed M 87 from 29 November 2006 to 2 December 2006 with an elapsed time of 187 ks in HXD nominal pointing mode. We analysed data from both the X-ray Imaging Spectrometer (XIS, Koyama et al. 2007) and the Hard X-ray Detector (HXD, Takahashi et al. 2007). The XIS instrument operates between ~0.2–12.0 keV and consists of three separate CCD detec-

Table 1. Results of IBIS/ISGRI analysis on the field of M 87 applying different data selection criteria.

Method	Mosaic rms	Detection significance M 87 [σ]	count rate [s^{-1}]	M 87 3σ upper limit [10^{-12} erg cm^{-2} s^{-1}]	Detection significance NGC 4388 [σ]
OSA 10	1.38	1.35	2.20±0.02	3.3	113.5
OSA 10: selected revolutions	1.18	1.70	2.33±0.03	4.2	89.4
OSA 10: borders cut	1.42	1.16	2.20±0.02	3.2	111.3

tors. The XIS data were reprocessed applying the standard event cuts, but the resulting image exhibited strong structures and can therefore not be used. The HXD is a collimated detector which consists of two independent detector systems, silicon PIN diodes that operate in the range ∼10–60 keV and GSO scintillation counters that function between ∼ 30 – 600 keV. We reprocessed the data applying the standard event cuts. Due to the low count rate in the GSO band no significant spectrum could be extracted from this detector. For the PIN detector we extracted a significant spectrum between 15 and 70 keV (Fig. 2). The spectrum can be represented by an absorbed power law with a fixed column column density $N_{\rm H} = 2\times10^{-20}$ cm^{-2} and a power law index of $\Gamma = 2.8^{+0.5}_{-0.4}$ (90% errors) giving a reduced $\chi^2_\nu = 1.17$ (for 12 degrees of freedom). The model flux is $f = 10^{-11}$ erg cm^{-2} s^{-1} between 20 and 60 keV.

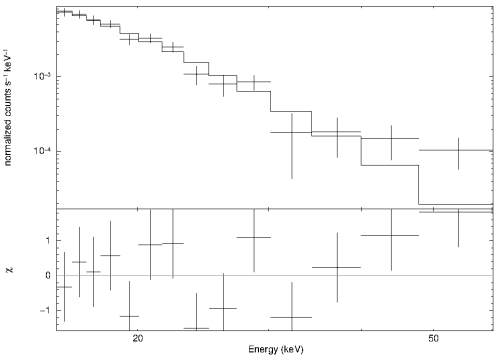

Fig. 2. Suzaku/PIN count spectrum between 15 and 70 keV with an absorbed power law model fit. The bottom panel shows the residuals of the fit in terms of the standard deviation with error bars of size one sigma.

2.3. Fermi/LAT

The Large Area Telescope (LAT, Atwood et al. 2009) aboard the *Fermi* satellite is a pair-conversion instrument with an energy range between 20 MeV and 300 GeV. We have used all available data taken between August 2008 and May 2012, with a total effective exposure of XX Ms. We have selected source-class-events (P7SOURCE_V6) between 100 MeV and 100 GeV in a circular region of 30° around M 87. The large extraction radius is necessary for the binned analysis we performed. Events with a zenith angle of more than 100° were excluded, and we used the standard cuts proposed by the *Fermi* team based on the data quality of the events and on the instrument configuration. In order to get a reliable result for the source of interest, we included in the maximum likelihood fitting procedure all sources which had been report in the second *Fermi* catalogue (2FGL) within 45° around the position of M 87.

Table 2. Results of the binned likelihood analysis off the *Fermi*/LAT data in 5 bins between 0.1–100 GeV with a power law of photon index Γ. The errors are given with a 1σ significance.

bin	energy range [GeV]	flux [10^{-12}ergs cm^{-2} s^{-1}]	TS	Γ
1	0.1–0.4	4.4 ± 1.5	36	1.9±0.6
2	0.4–1.6	3.9 ± 0.5	126	1.9 ± 0.3
3	1.6–3.0	2.1 ± 0.3	105	2.7±0.5
4	3.0–10	2.8 ± 0.3	87	1.47± 0.05
5	10–100	1.6 ± 0.4	12	2.29 ±0.06

Between 100 MeV and 100 GeV we derived a flux for M 87 of $f = (2.2 \pm 0.3) \times 10^{-8}$ ph cm^{-2} s^{-1} and a power law index of 2.16 ± 0.06, with a test statistic $TS = 370$, which corresponds to a detection significance of $\sim 19\sigma$. Since the source is bright in γ-rays, we divided the energy range 100 MeV to 100 GeV into 5 logarithmic bins to track the spectral evolution with energy. The results are summarized in Tab. 2, where we give the significance, flux and power law index per energy range.

3. Spectral energy distribution modelling

In order to derive a spectral energy distribution (SED) over the whole electromagnetic waveband, we included radio to UV data from the literature. We use the *INTEGRAL* IBIS/ISGRI upper limit between 20–60 keV, the *INTEGRAL*/JEM-X detection between 3–10 keV and the 10–25 keV upper limit together with the *Fermi*/LAT data to build the spectral energy distribution. We combine this with core detections from radio to infrared from NED [1] and VHE data from H.E.S.S., which has observed M 87 between 2003 and 2006 (Aharonian et al. 2006).

To represent the broad-band SED we applied a one-zone synchrotron self-Compton (SSC) model. This model assumes an isotropic population of high-energy electrons that emit synchrotron radiation followed by inverse Compton scattering of the synchrotron photons to higher energies (Maraschi et al. 1992). In this simplified model the electron population is contained in a spherical volume with radius R and randomly orientated magnetic field B. The volume moves relativistically with a bulk Lorentz factor of Γ_b towards the observer in the jet with an angle θ to the line of sight. The emission is Doppler-shifted with a Doppler factor $\delta = [\Gamma_b(1-\beta\cos\theta)]^{-1}$. The electron energy distribution in the jet-frame is assumed to follow a broken power-law, with index p_1 between the minimum energy $E_{\rm min}$ and the break energy $E_{\rm br}$ and index p_2 between $E_{\rm br}$ and the maximum energy $E_{\rm max}$. The peak frequencies are dependent on the break energy via $\nu_s = \frac{4}{3}\gamma_{br}^2 \frac{eB}{2\pi m_e c}\frac{\delta}{1+z}$, with $\gamma_{br} = (\frac{E_{br}}{m_e c^2})^2$ for the synchrotron peak and $\nu_{IC} = \frac{4}{3}\gamma_{br}^2\nu_b$ with ν_b the break in the electron power law spectrum, where we assume that the dominant synchrotron power is emitted at the break. Here, γ is the Lorentz factor of the relativistic electron in the plasma blob.

[1] http://ned.ipac.caltech.edu/

For some objects, such as the bright flat spectrum radio quasars, the SSC model does not properly represent the SED. In addition to the inverse Compton scattering of synchrotron photons, external seed photons from e.g. the broad-line region, that are Compton upscattered to higher energies can be contribute to the inverse Compton emission (external Compton component, Dermer & Schlickeiser 1993). When using an external Compton component, the geometry of the emitting region is important, since the emission does not arise in a single zone as with SSC.

For the modelling of M 87 we have used two different single-zone SSC codes, the publicly available code by Krawczynski et al. (2004) and an online code developed by A. Tramacere[2] (Massaro et al. 2006; Tramacere et al. 2009, 2011). In the following sections we describe the results of the two models, see Table 3 for the best-fit results.

3.1. SSC model for the average low-flux state

We used a SSC model developed by A. Tramacere (hereafter AT). This code has the possibility to apply several different electron energy distribution shapes, and we choose the broken power law shape to compare the result of the fitting with previous work. In addition to the SSC emission there is also a host galaxy component in the model, which shows a peak in the optical that is consistent with the data. For this component, the luminosity of the host galaxy, converted into a value of $\nu f_{host}(\nu) = (4 \pm 2) \times 10^{-12}\,\mathrm{erg\,cm^{-2}\,s^{-1}}$ for all fits presented below.

First we keep the angle θ and the bulk Lorentz factor Γ free with a fixed beaming factor δ of 5. This value is consistent with the apparant motion of $\sim 0.5c$ (Kellermann et al. 2007). The model has a χ^2 of 2.5 (20 d.o.f.), see Table 3. The magnetic field B, radius R and minimum energy $E_{\rm min}$ have been fixed. This gives a value of $E_{\rm max} = 4.5 \times 10^{13}$ eV for the maximum energy of the electrons and $E_{\rm br} = 2 \times 10^9$ eV for the break energy. The indices of the broken power law are $p_1 = 1.2$ and $p_2 = 3.5$.

Then we have fixed the angle at $\theta = 10°$, an angle that is closer to that of blazars, although the apparent angle as seen in the large scale radio jet appears to be rather $\theta = 30°$. In a first approach, we fix the magnetic field strength B, the radius of the emission region R, and the minimum energy of the electron distribution to the best-fit values in order to vary the remaining parameters. The fit gives a reduced $\chi^2_\nu = 3.3$ (17 d.o.f.) with $B = 10$ mG and $R = 8.7 \times 10^{16}$ cm (Tab. 3). A bulk factor $\Gamma = 2.5$ is found which is consistent with the value $\Gamma = 2.3$ derived by Abdo et al. (2009). The maximum energy is $E_{max} = 1.3 \times 10^{13}$ eV and the break energy $E_{\rm br} = 1.7 \times 10^9$ eV, both consistent with the previous model using a free angle and the values used by Abdo et al. (2009). The power law indices found are $p_1 = 1.0$ and $p_2 = 3.5$ are both similar to the previous fit and the model by Abdo et al. (2009).
Lastly we fixed the angle at $\theta = 30°$, the jet angle known from literature (Bicknell & Begelman 1996). The best-fit model has a reduced $\chi^2_\nu = 3.1$ (19 d.o.f.), see Fig. 3, and the parameters are reported in the first column of Tab. 3. The maximum energy is $E_{\rm max} = 5.8 \times 10^{12}$ eV, similar to the model by Abdo et al. (2009) but lower than the values found with a smaller jet angle. The break energy is $E_{\rm br} = 2.0 \times 10^9$ eV, the same as for the previous models and the model by Abdo et al. (2009). The power law indices $p_1 = 1.0$ and $p_2 = 3.$ are consistent with the previous models, and the findings of Abdo et al. (2009). These parameters produce a similar model when applied with the Krawczynski code.

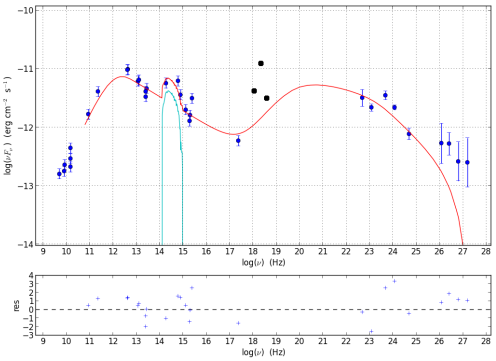

Fig. 3. SED of M 87 modelled using the code provided by Tramacere. The blue points are historical data, the black dots indicate the *INTEGRAL* upper limits.

3.2. SSC model for the high flux state in 2006

Since the *Suzaku*/PIN data taken in 2006 indicates a flux level which is 3 times as high as the upper limit determined from the average 2003-2011 data provided by *INTEGRAL* IBIS/ISGRI, we also included additional 2006 data in order to derive a simultaneous SED for this period. We added VHE data provided by *MAGIC* (Berger 2011), *VLT* (Reunanen et al. 2010) and *VLA* (Capetti et al. 2009) which are taken within 8 months of the PIN observation. These fluxes, in the radio infra red and VHE band, seem to be consistent with the overall, time averaged SED.

Therefore we considered the 2006 SED unchanged, except for the high-state in the X-ray band, and applied the *Suzaku*/PIN detection instead of the *INTEGRAL* upper limits and applied the SSC code. The results are reported in Tab. 3 (column `AT 2006`) and in Figure4. The Doppler factor δ is fixed to 5, and the radius to $R = 3.3 \times 10^{16}$ cm. The fit gives $\chi^2_\nu = 3.0$ with 18 d.o.f., which is slightly worse than the $\chi^2 = 2.5$ (20 d.o.f.) when using the average *INTEGRAL* points. The magnetic field strength for this model is $B = 1.3$ mG. The indices of the broken power law describing the electron energy distribution are $p_1 = 0.9$ and $p_2 = 3.5$. The first index is lower than found for the previous models, and the second index is similar to previous models. The minimum energy of the electron population is $E_{\rm min} = 2.7 \times 10^7$ eV, the maximum energy $E_{\rm max} = 5.4 \times 10^{12}$ eV and the break energy is at $E_{\rm br} = 8.3 \times 10^8$ eV. The minimum and maximum energy are similar to the previous models, but the break energy is lower.

The model is not in accordance with the spectrum derived from the *Suzaku*/PIN data, which dictates a steep power law in the X-ray regime. This suggests that this data point lies in fact on the tail of the synchrotron branch and not on the inverse Compton branch. In order to test this, we produced a model using the Krawczynski code, see Figure 5. Here we focused on modelling the 2006 observations, and to reproduce the hard X-ray emission, which shows a steep power law which should translate as a decrease of flux in the SED. We started from the parameters found using the AT code on the average low-flux state SED. We found that a higher magnetic field $B = 4.0 \times 10^{-2}$ G represents the data better. The radius of the emitting region remains

[2] http://isdc-web00.isdc.unige.ch/sedtool/SED_Web_tool/html_js/SED_Web_tool/SED_start_test.html

Table 3. The results of the fitting of the SED of M 87 using two different SSC models. The errors quoted estimated using a covariance matrix.

Parameter	AT 30°	AT fixed beam	AT 10°	AT 2006	Kraw 2006	Abdo 2009[d]
θ	30° [a]	-[c]	10° [a]	-[c]	30°	10° [a]
$B[G]$	1.0×10^{-2} [b]	3.8×10^{-3} [b]	8.0×10^{-3} [b]	1.3×10^{-3}	4.0×10^{-2}	5.5×10^{-2}
$R[cm]$	4.3×10^{17} [b]	1.3×10^{17} [b]	8.7×10^{16}	3.3×10^{16} [b]	4.3×10^{17}	1.4×10^{16}
Γ	3.5	-[c]	2.5	-[c]	3	2.3
$E_{\rm min}[eV]$	2.0×10^{7} [b]	2.9×10^{6} [b]	1.0×10^{7}	2.7×10^{7}	2.0×10^{7}	5×10^{5}
$E_{\rm max}[eV]$	5.8×10^{12}	4.5×10^{13}	1.2×10^{13}	5.4×10^{12}	6.3×10^{12}	5×10^{12}
$E_{\rm br}[eV]$	2.0×10^{9}	2.0×10^{9}	1.7×10^{9}	8.3×10^{8}	2.0×10^{11}	2×10^{9}
p_1	1.0	1.2	1.0	0.9	2.2	1.6
p_2	3.5	3.5	3.5	3.5	3.5	3.6
$n[cm^{-3}]$	0.6	4.6	5.0	38	-	-
χ^2_ν	3.1 (19 d.o.f.)	2.5 (20 d.o.f.)	3.3 (17 d.o.f.)	3.0 (18 d.o.f.)	-	-

Notes. *a)* parameter fixed; *b)* parameter fixed to best-fit value or literature value; *c)* beaming factor θ fixed to 5, see text; *d)* see Abdo et al. (2009)

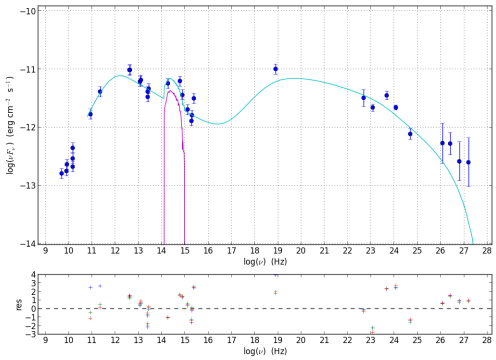

Fig. 4. SED of M 87 using the 2006 *Suzaku*/PIN detection, modelled with the AT code.

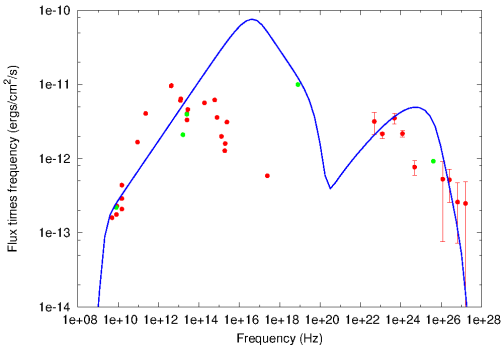

Fig. 5. 2006 SED with Krawczynski code, see text for parameters. For the modelling we focused on representing the 2006 observations, which are plotted as green points.

at $R = 4.3\times10^{17}$ cm. The bulk Lorentz factor found is $\Gamma = 3$, which increases the Doppler factor slightly to $\delta = 1.9$, compared to $\delta = 1.7$ for the average low-flux state. We find that the minimum energy of the electrons remains $E_{\rm min} = 2.0\times10^{7}$ eV, same as for the average low-flux state SED. The maximum energy of the electrons increased slightly to $E_{\rm max} = 6.3\times10^{12}$ eV. The break energy increased to $E_{\rm br} = 2.0\times10^{11}$ eV. The power law indices that characterise the electron energy distribution are $p_1 = 2.2$ and $p_2 = 3.8$, showing a change compared to the average SED.

4. Discussion

In the following we discuss first the discuss the possible origin site of the emission seen in *INTEGRAL*/JEM-X, before we turn to the hard X-ray variability and the spectral energy distribution. Finally, we discuss the possible source type at the origin of the high-energy emission in M 87.

4.1. JEM-X: core emission

Due to the the angular resolution of JEM-X (FWHM=3 arcmin), the flux of M 87 observed by JEM-X is the sum of core, jet and extended diffuse emission. We are interested only in the core emission, because we want to investigate the origins of the high-energy emission which is emitted from, or close to the core. In addition, the measured JEM-X flux is an average over several years. The knot HST-1 is also known to be variable, and was in outburst during 2003 to 2007, and the luminosity of the knot peaked in 2005. For a light curve of the X-ray emission of HST-1 see Fig. 1 in Abramowski et al. (2012). Since the JEM-X observations we used are taken mostly after 2008, and none during 2005, we assume that we did not include data during which the know was in outburst. Therefore, the flux observed in JEM-X is likely to be dominated by the core of M 87.

Using literature values from observations of the knot HST-1 made with *Chandra*/ACIS by Perlman & Wilson (2005) and by Wilson & Yang (2002) for other jet knots, we find the combined jet flux is about $f(3-10\,{\rm keV}) = 10^{-12}\,{\rm erg\,cm^{-2}\,s^{-1}}$. For the extended emission we used observations from *Chandra*/ACIS, taken beginning of May 2005. We analysed the data, with an exposure of 123 ks in total, and extracted a spectrum in a region of 2.5 arcminutes centered around the core of M 87. The core and jet are excluded. This spectrum yielded a flux of $f(3-10\,{\rm keV}) = 9\times10^{-12}\,{\rm erg\,cm^{-2}\,s^{-1}}$. This implies that the core emission, is about $f = 5\times10^{-12}\,{\rm erg\,cm^{-2}\,s^{-1}}$, with a variability by a factor of two in X-rays (Hilburn & Liang 2012).

4.2. Hard X-ray variability

We found an overall 3σ upper limit to the flux of $f(20 - 60\,\mathrm{keV}) \simeq 3 \times 10^{-12}\,\mathrm{erg\,cm^{-2}\,s^{-1}}$ using all available *INTEGRAL* data for a total effective exposure time of 1.7 Ms. Apart from a spurious detection by *INTEGRAL* of 5.1σ, corresponding to a flux of $f(20 - 60\,\mathrm{keV}) = (9 \pm 2) \times 10^{-12}\,\mathrm{erg\,cm^{-2}\,s^{-1}}$ (Walter & Neronov 2008), M 87 had not been detected in hard X-rays. Using the same data set as Walter & Neronov (2008) but applying the latest analysis software OSA 10 we derived a 3σ upper limit flux of $f(20 - 60\,\mathrm{keV}) = 8 \times 10^{-12}\,\mathrm{erg\,cm^{-2}\,s^{-1}}$, inconsistent with the earlier detection claim. This does not mean, however, that the hard X-ray flux of M 87 never exceeds this average flux. We found that, during a *Suzaku*/PIN observation at the end of November 2006, M 87 is detected with a flux of $f(20 - 60\,\mathrm{keV}) = 10^{-11}\,\mathrm{erg\,cm^{-2}\,s^{-1}}$. There is no *INTEGRAL* IBIS/ISGRI observation at this time to confirm the detection, but in July 2006 *INTEGRAL* has observed M 87 for 23 ks giving a $3-\sigma$ upper limit of $f(20 - 60\,\mathrm{keV}) < 3\,\mathrm{times}10^{-11}\ \mathrm{erg\,cm^{-2}\,s^{-1}}$, consistent with the flux measured by *Suzaku*/PIN.

4.3. Spectral energy distribution

The data used in the SED have been taken at different times, which might result in a biased measurement in the case of a variable object since several spectral states might contributed to the data. Abramowski et al. (2012) showed lightcurves of M 87 from 2001 to 2011 based on radio, optical, X-rays and VHE observations. The VHE band shows increased activity in 2005, 2008 and 2010, during which the X-ray emission also increased. During these periods the radio emission from the jet base did not increase, which indicates the VHE emission is likely produced near the SMBH. The VHE observation used in the SED was taken in 2004 when M 87 was in a low state. The radio and optical detections of the core used in the SED are averaged over several years, and the light curves show variations by a factor of ~ 2. Variability at this level will not significantly alter the physical parameters derived from modelling the SED. A similar approach of using time-averaged SEDs has been applied already succesfully to M 87 (Abdo et al. 2009) and other radio galaxies, for example Pictor A (Brown & Adams 2012) and 3C 111 (de Jong et al. 2012).

The high flux detected by *Suzaku*/PIN can indicate a flaring state of the source. In 2005, the increase in VHE, X-ray and optical emission coincided with the expulsion of the jet knot HST-1 from the core. During the *Suzaku* observations end 2006 the light curves presented in Abramowski et al. (2012) do not show increased activity in the VHE or optical band, so the *Suzaku* observation is likely not to be connected to this HST-1 flare.

Flaring behaviour has been observed in BL Lac objects such as Mrk 501 (Tavecchio et al. 2001). During a flare the overall luminosity increases, and in the SED this also results in an increase of the peak frequencies of the synchrotron and inverse Compton branch.

The 2006 *Suzaku*/PIN observation of M 87 can be interpreted as a flare. The steep spectrum observed in the hard X-ray data with $\Gamma \simeq 2.8$ can be interpreted as being the high-energy tail of the synchrotron branch, whereas in the time-averaged SED this energy range is rather dominated by inverse Compton emission. The SED parameter that changed significantly to represent the 2006 SED compared to the average low-flux state SED is the break energy E_{br}. Tavecchio et al. (2001) show that for the high and low flux states in Mrk 501 it is also the break energy rather than any other parameters, which might indicate a change in the acceleration process of electrons.

Due to the lack of simultaneous observations in 2006 this cannot be confirmed. Because of the non-imaging character of the *Suzaku*/PIN observations, we are also not able to determine whether the enhanced emission results rather from the core of M 87 or for example from a knot in the jet, such as HST-1.

The physical parameters derived from the spectral energy distribution can be compared to other gamma-ray bright radio galaxies. Another FR-I radio galaxy of this class is Cen A, where the overall SED can also be modelled by a simple SSC process (Abdo et al. 2010b), although a strong Seyfert contribution is visible in the X-rays and optical domain (Beckmann et al. 2013). Abdo et al. (2010b) present several SED fits to the core of Cen A. Comparing the results for M 87 to the model for Cen A using a jet angle fixed at $\theta = 30\,^{\circ}$, M 87 displays a slightly higher Doppler factor of $\delta = 1.7$, compared to the Doppler factor used for Cen A of $\delta = 1$, a lower Doppler factor causes the emission to appear less boosted. The magnetic field B and radius of the emitting region R are quite different for both sources, for Cen A a value of $B = 6.2$ G was found for the magnetic field, and a much lower value of $B = 10^{-2}$ G for M 87. Since the synchrotron emission depends on the magnetic field, a larger magnetic field will show a higher flux. The radius of the emitting region is reported to be $R = 4.3 \times 10^{17}$ cm for M 87 and $R = 3 \times 10^{15}$. The radius R defines the amount of particles, increasing the amount of radiating particles increases the flux. The lower magnetic field B used to model M 87, combined with the larger radius R compared to Cen A results in a similar overall power in the SED.

Comparing the SED parameters with the luminous FR-II galaxy 3C 111 shows the differences between these two types of sources. The Doppler factor used to model 3C 111 is $\delta = 14$, compared to $\delta = 1.7$ used for M 87. For the radius of the emitting region $R = 2 \times 10^{16}$ cm and the magnetic field $B = 4 \times 10^{-2}$ G are used (de Jong et al. 2012). The smaller region used to model 3C 111 compared to M 87 yields a lower flux, but the strong Doppler factor δ and larger magnetic field B of 3C 111 increase the flux strongly.

The SED of the low state of Mrk 421, a BL Lac source, can also be represented with an SSC model (Błażejowski et al. 2005). To do this a Doppler factor of $\delta = 10$ is used, strongly boosting the emission compared to M 87. For the emitting region a radius of $R = 7.0 \times 10^{15}$ cm and a magnetic field of $B = 0.405$ G are used. The radius of the emitting region used is smaller for Mrk 421, compared to M 87. However, the magnetic field is again stronger, which together with the strong Doppler boosting increases the flux.

In the overall context of SED models of gamma-ray bright sources, we can compare the derived values with the average ones for Fermi/LAT detected BL Lacs and FSRQs. As the FR-I radio galaxies can be understood as the parent population of the BL Lacs (e.g. Urry & Padovani 1995), also their SED parameters are closer to the ones found for BL Lacs than for the brighter FSRQ class. As pointed out by Ghisellini et al. (2010) , the average BL Lacs appear to have similar masses as the FSRQs, with values around $10^8 - 10^9\,\mathrm{M_\odot}$. The SMBH in M 87 has a similar mass but its bolometric luminosity of $L_{\mathrm{bol}} \simeq 10^{42}\,\mathrm{erg\,s^{-1}}$ giving an Eddington ratio of only $\lambda = L_{\mathrm{bol}}/L_{\mathrm{Edd}} \simeq 10^{-2}$ (Owen et al. 2000). Nevertheless, a similar jet model can be applied to the SED as in the case of BL Lacs.

4.4. M 87, a radio galaxy with a low luminous BL Lac core

In the case of M 87 we know that the base of the jet visible in the radio domain is less than 20 Schwarzschild radii from the core (Hada et al. 2011). Because the acceleration time scale goes with $t_{\rm acc} \propto m^{-1}$ and the cooling time scale is proportional to m^2, the jet emission visible and resolvable in the radio, optical, and soft X-rays is likely to be dominated by leptons rather than by hadrons.

The properties of M 87's central engine are closer to that of BL Lacs than to FSRQs. The strength of the magnetic field, the bulk Lorentz factor of the jet and also the electrons' Lorentz factor distribution indicate rather a BL Lac type emission. Also the overall bolometric luminosity of $L_{\rm bol} \simeq 10^{41}\,{\rm erg\,s^{-1}}$ giving Eddington ratio of only $\lambda = L_{\rm bol}/L_{\rm Edd} \simeq 10^{-3}$ (Di Matteo et al. 2003) points in this direction. The observed physical properties of this AGN put it in a low luminous BL Lac class. The low power jet can be explained by the low accretion rate, rather than by the large mass, although the finding by Laor (2000), that AGN with black hole masses larger than $M_{\rm BH} > 10^9\,{\rm M}_\odot$ are radio-loud, seems to hold also in the case of M 87. The low Eddington ratio can be understood in the context that the M 87 core likely not fed by an accretion disk but by a radiative inefficient accretion flow (RIAF) or advection dominated accretion flow (ADAF; Reynolds et al. 1996; Di Matteo et al. 2003). The assumption that the accretion is radiative inefficient also explains why in the case of M 87 we do not see a significant thermal inverse Compton component in the X-rays, and an optical spectrum consistent with that of a LINER. This is different to other gamma-ray bright radio galaxies which show an optical Seyfert core as e.g. Cen A (Beckmann et al. 2011) and 3C 111 (de Jong et al. 2012).

5. Conclusion

We report, for the first time, a hard X-ray detection of the FR-I radio galaxy M 87 using *Suzaku*/PIN data. The observations were made between 29 November to 2 December 2006 with an elapsed time of 187 ks, resulting in a flux of $f = 10^{-11}\,{\rm erg\,cm^{-2}\,s^{-1}}$ between 20 and 60 keV. In addition, we derive a 3-σ upper limit of $f(20-60\,{\rm keV}) < 3\times10^{-12}\,{\rm erg\,cm^{-2}\,s^{-1}}$ for the multi-year time averaged emission, based on 1.7 Ms of *INTEGRAL*IBIS/ISGRI data.

By studying the broad-band energy distribution we connect the hard X-ray and γ-ray emission to the core emission. For the modelling we used a one-zone SSC model. The SED parameters show that M 87 can be considered a weak BL Lac object, consistent with the advection dominated accretion flow model for the core (Ptak et al. 1998; Reynolds et al. 1996) and the overall low-luminous FR-I nature of this galaxy. The high X-ray flux detected with *Suzaku*/PIN at the end of 2006 seems to indicate the source was undergoing an outburst or flaring episode. The steep slope of the spectrum, with a power law index of $\Gamma = 2.8^{+0.5}_{-0.4}$ between 20–60 keV, indicates that the emission was likely the high-energy tail of the synchrotron branch, indicating that the overall luminosity as well as the the peak frequencies of both synchrotron and inverse Compton branch increased.

In the Unification model for AGN, radio galaxies are the counterparts of blazars, where the lower luminosity BL Lacs are linked to FR-I galaxies and the more powerful flat spectrum radio quasars (FSRQ) to the FR-II sources. In the SED BL Lacs can be represented by only an SSC model. To model FSRQ SEDs in addition to the SSC model there is the need for an external Compton component (Ghisellini et al. 1998). The SSC model for the overall SED appears to be valid for this class of *Fermi*/LAT detected radio galaxies. Also in the cases of the brighter FR-II objects, like 3C 111, no external Compton component seems to be necessary to represent the SED, which is not in line with the Unification model. Thus, in all these cases the dominating emission region is either far from a strong field of seed photons like the broad line region (as in the case of 3C 111), or the broad line region itself is weak because of radiatively inefficient accretion, as might be the case in M 87. This hypothesis, that EC is not significant in gamma-ray detected radio galaxies, should be tested in the case of the *Fermi*/LAT detected radio galaxy 3C 207.0, which hosts a Seyfert 1.2 core. At a redshift of $z = 0.68$ this object has a luminosity of $f(2-10\,{\rm keV}) = 2.3\times10^{45}\,{\rm erg\,s^{-1}}$, and the strong Seyfert core which displays an iron Kα line with $EW \simeq 60\,{\rm eV}$, should give rise to a significant photon field able to provide ample seed photons for inverse Compton processes in this case.

Acknowledgements. The authors thank Juan Antonio Zurita Heras, Fabio Mattana, and Alexandra Gros for their support in the *INTEGRAL* analysis. This research is based on data provided by *INTEGRAL*, an ESA project funded by ESA member states (especially the PI countries: Denmark, France, Germany, Italy, Spain, Switzerland), Czech Republic, Poland, and with the participation of Russia and the USA. We acknowledge the use of public data from the Swift data archive. This research has made use of the NASA/IPAC Extragalactic Database (NED), which is operated by the Jet Propulsion Laboratory, California Institute of Technology, under contract with the National Aeronautics and Space Administration. This research has made use of NASA's Astrophysics Data System Bibliographic Services. We acknowledge the financial support from the UnivEarthS Labex program of Sorbonne Paris Cité (ANR-10-LABX-0023 and ANR-11-IDEX-0005-02) within the project "Impact of black holes on their environment"

References

Abdo, A. A., Ackermann, M., Ajello, M., et al. 2009, ApJ, 707, 55
Abdo, A. A., Ackermann, M., Ajello, M., et al. 2010a, ApJ, 719, 1433
Abdo, A. A., Ackermann, M., Ajello, M., et al. 2010b, ApJ, 719, 1433
Abramowski, A., Acero, F., Aharonian, F., et al. 2012, ApJ, 746, 151
Ackermann, M., Ajello, M., Allafort, A., et al. 2011, ApJ, 743, 171
Aharonian, F., Akhperjanian, A., Beilicke, M., et al. 2003, A&A, 403, L1
Aharonian, F., Akhperjanian, A. G., Bazer-Bachi, A. R., et al. 2006, Science, 314, 1424
Antonucci, R. 1993, ARA&A, 31, 473
Atwood, W. B., Abdo, A. A., Ackermann, M., et al. 2009, ApJ, 697, 1071
Beckmann, V., de Jong, S., Mattana, F., Saez, D., & Soldi, S. 2013, ArXiv e-prints
Beckmann, V., Jean, P., Lubiński, P., Soldi, S., & Terrier, R. 2011, A&A, 531, A70
Beckmann, V. & Shrader, C. R. 2012, Active Galactic Nuclei
Berger, K. 2011, in International Cosmic Ray Conference, Vol. 8, International Cosmic Ray Conference, 153
Bicknell, G. V. & Begelman, M. C. 1996, ApJ, 467, 597
Błażejowski, M., Blaylock, G., Bond, I. H., et al. 2005, ApJ, 630, 130
Brown, A. M. & Adams, J. 2012, MNRAS, 421, 2303
Capetti, A., Kharb, P., Axon, D. J., Merritt, D., & Baldi, R. D. 2009, AJ, 138, 1990
Courvoisier, T. J.-L., Walter, R., Beckmann, V., et al. 2003, A&A, 411, L53
de Jong, S., Beckmann, V., & Mattana, F. 2012, A&A, 545, A90
Dermer, C. D. & Schlickeiser, R. 1993, ApJ, 416, 458
Di Matteo, T., Allen, S. W., Fabian, A. C., Wilson, A. S., & Young, A. J. 2003, ApJ, 582, 133
Fanaroff, B. L. & Riley, J. M. 1974, MNRAS, 167, 31P
Gebhardt, K. & Thomas, J. 2009, ApJ, 700, 1690
Ghisellini, G., Celotti, A., Fossati, G., Maraschi, L., & Comastri, A. 1998, MNRAS, 301, 451
Ghisellini, G., Tavecchio, F., Foschini, L., et al. 2010, MNRAS, 402, 497
Hada, K., Doi, A., Kino, M., et al. 2011, Nature, 477, 185
Hilburn, G. & Liang, E. P. 2012, ApJ, 746, 87
Kellermann, K. I., Kovalev, Y. Y., Lister, M. L., et al. 2007, Ap&SS, 311, 231
Koyama, K., Tsunemi, H., Dotani, T., et al. 2007, PASJ, 59, 23
Krawczynski, H., Hughes, S. B., Horan, D., et al. 2004, ApJ, 601, 151
Laing, R. A., Riley, J. M., & Longair, M. S. 1983, MNRAS, 204, 151
Laor, A. 2000, ApJ, 543, L111
Lebrun, F., Leray, J. P., Lavocat, P., et al. 2003, A&A, 411, L141

Lund, N., Budtz-Jørgensen, C., Westergaard, N. J., et al. 2003, A&A, 411, L231
Macchetto, F., Marconi, A., Axon, D. J., et al. 1997, ApJ, 489, 579
Maraschi, L., Ghisellini, G., & Celotti, A. 1992, ApJ, 397, L5
Massaro, E., Tramacere, A., Perri, M., Giommi, P., & Tosti, G. 2006, A&A, 448, 861
Owen, F. N., Eilek, J. A., & Kassim, N. E. 2000, ApJ, 543, 611
Perkins, J. S., for the VERITAS Collaboration, & for the Fermi LAT Collaboration. 2012, ArXiv e-prints
Perlman, E. S. & Wilson, A. S. 2005, ApJ, 627, 140
Ptak, A., Yaqoob, T., Mushotzky, R., Serlemitsos, P., & Griffiths, R. 1998, ApJ, 501, L37
Reunanen, J., Prieto, M. A., & Siebenmorgen, R. 2010, MNRAS, 402, 879
Reynolds, C. S., Di Matteo, T., Fabian, A. C., Hwang, U., & Canizares, C. R. 1996, MNRAS, 283, L111
Soldi, S., Lebrun, F., Gros, A., et al. 2013, ArXiv e-prints
Takahashi, T., Abe, K., Endo, M., et al. 2007, PASJ, 59, 35
Tavecchio, F., Maraschi, L., Pian, E., et al. 2001, ApJ, 554, 725
Tonry, J. L. 1991, ApJ, 373, L1
Tramacere, A., Giommi, P., Perri, M., Verrecchia, F., & Tosti, G. 2009, A&A, 501, 879
Tramacere, A., Massaro, E., & Taylor, A. M. 2011, ApJ, 739, 66
Urry, C. M. & Padovani, P. 1995, PASP, 107, 803
Walter, R. & Neronov, A. 2008, in Proceedings of the 7th INTEGRAL Workshop
Wilson, A. S. & Yang, Y. 2002, ApJ, 568, 133
Winkler, C., Courvoisier, T. J.-L., Di Cocco, G., et al. 2003, A&A, 411, L1

9 Detection of two new X-ray sources using *Swift*

For our research on gamma-ray bright AGN which are not bona-fide blazers we have requested the *INTEGRAL* data rights for three *Fermi*/LAT detected sources. For the source 2FGL J1551.9+0855, which was detected with 5σ by *Fermi*/LAT, we have also requested successfully a dedicated observation by *Swift* to complete the simultaneous *INTEGRAL* observations of this source. In the error circle of 2FGL J1551.9+0855, two new X-ray sources were discovered: the Seyfert 1 galaxy LSBC F727–V01 and the blazar BZB J1552+0850 (Described in ATel #4551, de Jong et al. 2012a).

9.1 Introduction

The source 2FGL J1551.9+0855 (RA=237.975, Dec=8.925) was detected by *Fermi*/LAT with a photon flux $(6 \pm 1) \times 10^{-10}\,\mathrm{ph\,cm^{-2}\,s^{-1}}$ between 1 GeV and 100 GeV (Nolan et al. 2012). The power law photon index between 100 MeV and 100 GeV is $\Gamma = 2.0 \pm 0.2$. The source was also included in the first *Fermi*/LAT catalogue, with a significance of 4.4σ and a 1–100 GeV photon flux of $(6 \pm 3) \times 10^{-10}\,\mathrm{ph\,cm^{-2}\,s^{-1}}$ and a 100 MeV–100 GeV power law index of $\Gamma = 2.2 \pm 0.2$ (Abdo et al. 2010a). In the first and second catalogue the source is tentatively associated with the source CRATES J1552+0850, which is a BL Lac object at $z = 1.015$ (Plotkin et al. 2008).

9.2 2FGL J1551.9+0855 as observed by *INTEGRAL*/ISGRI

We have analysed the *INTEGRAL* IBIS/ISGRI data from two revolutions simultaneous to the *Swift* observations of the 2FGL J1551.9+0855 (see Table 9.1 and Table 9.2). The *INTEGRAL*/ISGRI observations were processed via a science window-by-science window routine, which is described in Section 7.4.2. In both revolutions 2FGL J1551.9+085 was not significantly detected between 20 and 60 keV, with a 3-σ upper limit to the flux of

Table 9.1: *Swift* observation log, including the corresponding *INTEGRAL* revolution. Times are given in UT.

No.	Begin	End	Target Name	Exposure time [s]	*INTEGRAL* revolution
1	2011-09-19 08:39:00	2011-09-19 08:51:00	CRATESJ155202+085051	604.7	-
2	2012-07-29 03:29:00	2012-07-29 06:49:00	CRATESJ155202+085051	1056.4	1196
3	2012-08-01 08:22:00	2012-08-01 11:50:00	CRATESJ155202+085051	2457.3	1198

Figure 9.1: *INTEGRAL* IBIS/ISGRI significance maps of the region around 2FGL J1551.9+0855 for revolution 1196 (left) and revolution 1198 (right). The grid shows J2000.0 coordinates.

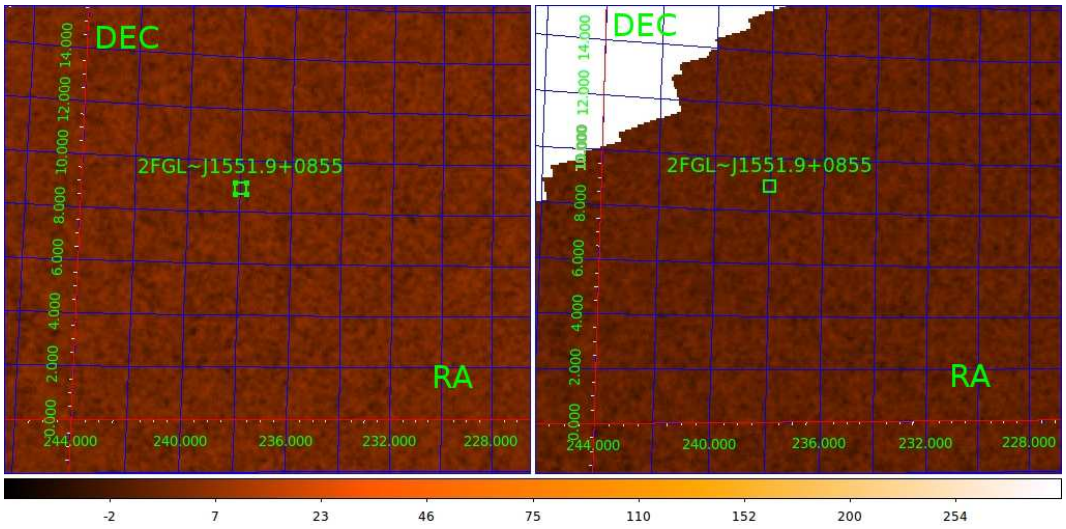

Table 9.2: Details of the *INTEGRAL* observations of 2FGL J1551.9+0855 and results.

Revolution	No. scw	Exposure [ks]	3-σ upper limit flux 2FGL J1551.9+0855 [erg cm^{-2} s^{-1}]
1196	68	89.0	4×10^{-11}
1198	36	6.9	3×10^{-10}

$f \lesssim 4 \times 10^{-11}$ erg cm^{-2} s^{-1} for revolution 1196, and of $f \lesssim 3 \times 10^{-10}$ erg cm^{-2} s^{-1} for revolution 1198. The significance maps for these revolutions are shown in Figure 9.1.

9.3 *Swift* analysis

The *Swift* observations are listed in Table 9.1 (see Section 6.2.3 for more information about the mission and its instruments). For each observations we analysed the data of the XRT and UVOT narrow field instruments.

9.3.1 XRT analysis

First we have analysed the data from the *Swift* X-ray Telescope (XRT). This soft X-ray instrument (0.2–10 keV) has a field of view of 23 arcmin, with a resolution of 18". We inspected the cleaned event files using `ximage` and none of the observations showed a clustering of events at the source position. Searching for 3-σ excesses gives two potential sources (see Figure 9.2) at RA=238.014, DEC=8.846 (observations 2 and 3) and at RA=237.918, DEC=8.875 (observation 3). The positions coincide with a BL Lac object, BZB J1552+0850 ($z > 1.015$), and a Seyfert 1 galaxy, LSBC F727-V01 ($z = 0.071$), respectively. The 95% confidence region

Figure 9.2: Third *Swift*/XRT observation of the region around 2FGL J1551.9+0855 (1 pixel is 2.4" by 2.4"). Two excesses of 3σ are indicated.

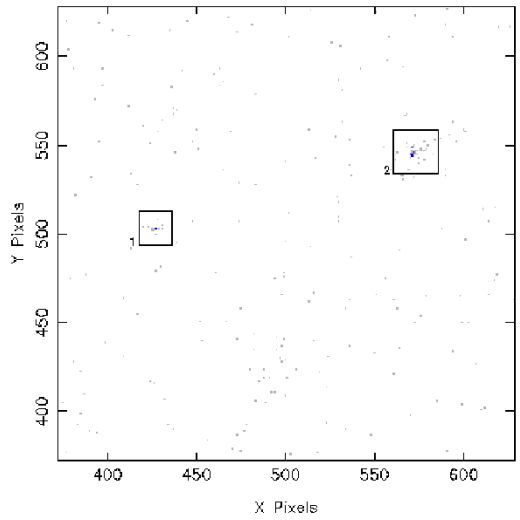

of 2FGL J1551.9+0855 is comparably large, with a semi-major axis of $\theta_1 = 0.121°$ and a semi-minor axis of $\theta_2 = 0.099°$, so both of the potential sources are positioned within this error circle and are thus potential counter parts for the gamma-ray emission. In the second *Fermi*/LAT catalogue, the BL Lac BZB J1552+0850 is listed as a potential counterpart of the 2FGL source.

To determine the exact position and 90% positional uncertainty of these sources in the 2012 XRT observations, we used the `xrtcentroid` routine on the event files. This routine calculates the source centroid in a box region, whose starting position is determined by the user. The error on the position is a combination of systematic and statistical errors, and in this case using `xrtcentroid` gives a systematic error of 3.5 arcsec. Using `xrtcentroid` the position for BZB J1552+0850 was determined in all three XRT observations. For LSBC F727–V01 positional information could be extracted with `xrtcentroid` in observation 2 and 3 only. Due to the low exposure of observation 1, LSBC F727–V01 was not detected in this data set. The results can be found in Table 9.3. Using `xrtcentroid` shows a scatter in the position of both sources, but the values are consistent within the errors.

Spectra

Spectra were extracted from the XRT event files with `xselect`. The event files were filtered with the source and background regions. Then an exposure map was created, to correct for the loss of flux due to several CCD pixels not collecting data. Using the exposure map and the extracted spectrum, an ancillary response file was extracted. The relevant response files were prepared by the instrument team.

Using observation 3, the spectrum extracted for BZB J1552+0850 contained only a few sig-

Table 9.3: Position of *Swift*/XRT sources found by `xrtcentroid`, potential counter parts of the BL Lac BZB J1552+0850 and the Seyfert 1 galaxy LSBC F727–V01.

Source, Observation	RA	DEC	Error radius ["]
BZB J1552+085,1	238.011	8.845	12.2
BZB J1552+085,2	238.014	8.846	6.9
BZB J1552+085,3	238.015	8.847	6.7
LSBC F727–V01,1	–	–	–
LSBC F727–V01,2	237.979	8.925	16.6
LSBC F727–V01,3	237.981	8.920	11.0

nificant bins, so it was not possible to fit a model to it. From the count rate of $(5\pm1)\times10^{-3}$ c/s (98.3 % total) a significance of 3.4σ could be calculated. Using the HEASARC WebPIMMS tool[1] we estimated a flux based on the count rate. Assuming a Galactic hydrogen column density of $N_{\rm H} = 3.24 \times 10^{20}\,{\rm cm}^{-2}$, and a power law index of $\Gamma = 2$, a 0.1–2.4 keV flux of $2\times10^{-13}\,{\rm erg\,cm^{-2}\,s^{-1}}$ was estimated. This is consistent with the *ROSAT* all-sky survey upper limit of $f \lesssim 5 \times 10^{-13}\,{\rm erg\,cm^{-2}\,s^{-1}}$ in this region.

In observation 3, LSBC F727–V01 has a count rate of $(1.3 \pm 0.2) \times 10^{-2}$ c/s (92.3 % total), which corresponds to a significance of 6.5σ. The data can be represented by a power law model with a photon index of $\Gamma = 1.9 \pm 0.4$, and fixed Galactic hydrogen column density $N_{\rm H} = 3.24 \times 10^{20}\,{\rm cm}^{-2}$. The 2–10 keV flux is $f = 3 \times 10^{-13}\,{\rm erg\,cm^{-2}\,s^{-1}}$. In the 0.1–2.4 keV RASS band, the flux is $f = 4 \times 10^{-13}\,{\rm erg\,cm^{-2}\,s^{-1}}$, consistent with the aforementioned upper limit to the flux in this region.

9.3.2 UVOT analysis

Next we analysed the UV and optical data based on the *Swift*/UVOT observations. The UVOT is sensitive between $\lambda = 170\,{\rm nm}$ and 650 nm, and has 6 filters: v (centred on 546.8nm), b (439.2 nm), u (346.5 nm), uvw1 (260.0 nm), uvm2 (224.6 nm) and uvw2 (192.8 nm). The field of view is smaller than that of the XRT with 17" by 17". The event files used have been processed, for example by correcting for bad pixels, by the instrument team.
For every filter three different event files exist: raw, co-added sky (RA/DEC coordinates) and co-added exposure. We used the co-added sky event file. In the cases where this file included several images, they were added. Using `ds9` the source extraction and background region were defined (see Figure 9.3). Then, using `uvotsource` a detection significance and coincidence-corrected count rate, magnitude and flux density were derived. In Table 9.4 the significances and count rates of LSBC F727–V01 in the different filters are shown. BZB J1552+085 was detected in observation 2 with a significance of 13.8σ in the uvw2-band and in observation 3 with 35.2σ in the u-band.

Earlier measurements of LSBC F727–V01 have shown a brightness of 19.69 ± 0.04 magnitudes (AB) in the u band (based on the Sloan digital sky survey, e.g. Abazajian et al. 2003). In the first observation the source was not significantly detected in the u-band, with a 3σ

[1] http://heasarc.gsfc.nasa.gov/Tools/w3pimms.html

Figure 9.3: *Swift*/UVOT region around LSBC F727–V01 in the uvw2 filter (central wavelength $\lambda = 192.8\,\mathrm{nm}$). The source has a count rate of ~ 10 c/s, the background 0–2 c/s.

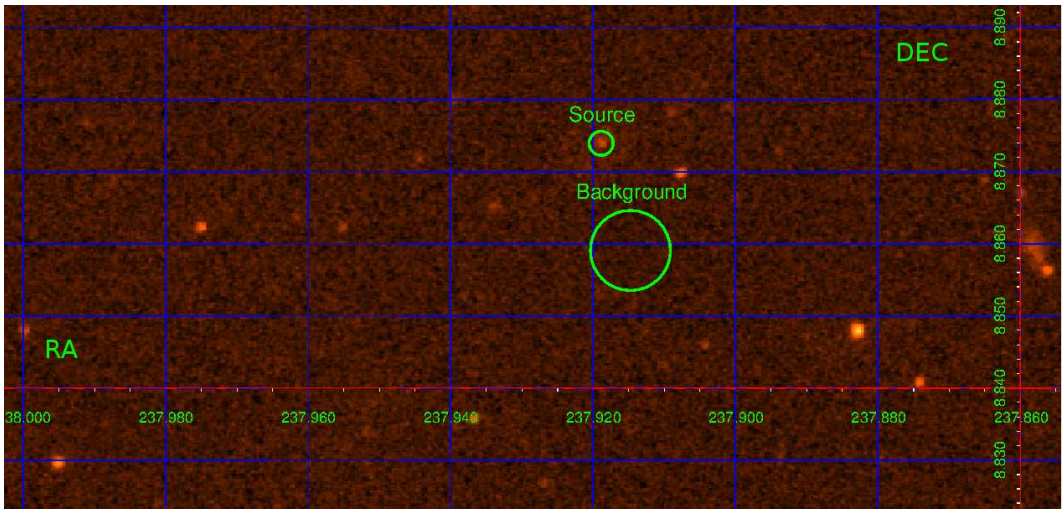

Table 9.4: Results of the UVOT analysis of LSBC F727–V01, the significances in the different bands and the corrected count rate. If the source is not significant compared to the background, the count rate is the 3σ upper limit. The quoted errors are 1σ.

Obs.	Significance v [σ]	Significance v [σ]	Significance u [σ]	Significance uvw1 [σ]	Significance uvm2 [σ]	Significance uvw2[σ]
1	8.4	7.4	4.2	5.5	4.1	5.6
2	-	-	-	-	-	13.2
3	-	-	37.8	-	-	-
Obs.	**count rate v [c/s]**	**count rate b [c/s]**	**count rate u [c/s]**	**count rate uvw1 [c/s]**	**count rate uvm2 [c/s]**	**count rate uvw2 [c/s]**
1	2.6 ± 0.3 (stat)	2.7 ± 0.4(stat)	< 1.2	0.8 ± 0.1 (stat)	< 0.3	0.36 ± 0.07 (stat)
2	-	-	-	-	-	0.24 ± 0.02 (stat)
3	-	-	1.34 ± 0.04 (stat)	-	-	-

Table 9.5: Infrared magnitudes of the WISE counter parts to BZB J1552+0850 and LSBC F727–V01 (Massaro et al. 2012).

Source	3.4 micron [mag]	4.6 micron [mag]	12 micron [mag]	22 micron [mag]
BZB J1552+0850	12.27 ± 0.02	11.30 ± 0.02	8.60 ± 0.02	6.41 ± 0.05
LSBC F727-V01	13.02 ± 0.03	12.76 ± 0.03	10.75 ± 0.09	8.7 ± 0.4

upper limit of > 19.2 mag (AB), excluding the SDSS detection. In the third observation the brightness in the u-band was 19.04 ± 0.04 (stat)$\pm$0.02 (sys) mag (AB), lower than the earlier observations.
BZB J1552+085 has also been included in the SDSS with a brightness of 18.89 ± 0.03 mag (AB). In the first observation this source was not significant in the u band, with a 3σ upper limit of > 19.2 mag (AB), and in the third observation the source was detected with 19.14 ± 0.04 (stat) $\pm$0.02 (sys) mag (AB). The SDSS detection was not consistent with our findings. A difference in brightness can, for example, be introduced by the extraction radius or source variability.

9.4 IR follow up

Shortly after we published the Astronomer's Telegram (ATel) on the X-ray counter parts, an infrared follow up was presented by Massaro et al. (2012) using the Wide-field Infrared Survey Explorer (WISE, Wright et al. 2010) catalogue[2].
For the BL Lac BZB J1552+0850 a WISE gamma-ray blazar candidate was found, consistent with the VLBA position of BZB J1552+0850 with an offset of 0.17". This infrared counter part was also consistent with the position we had derived in the X-ray band (offset of 6.3"). The infrared magnitudes can be found in Table 9.5.
Also for LSBC F727-V01 an infrared WISE counter part was found, with an offset of 0.44" to the optical position, and an offset of 3.5" to the X-ray position derived in this work.

Using an infrared colour-colour diagram as described in D'Abrusco et al. (2012), Massaro et al. (2012) shows that the infrared behaviour of LSBC F727-V01 is not consistent with a gamma-ray bright blazar. Therefore it is more likely that the BL Lac BZB J1552+0850 is the counter part of the *Fermi*/LAT detected source 2FGL J1551.9+0855.

9.5 Conclusion

We have found two X-ray sources, up to now undetected in this band, in the error circle of the *Fermi*/LAT detected source 2FGL J1551.9+0855. The position of one of the sources, at RA=237.9181 and DEC=8.8744 with 2.7 arcsec uncertainty (90% confidence radius), is consistent with the Seyfert 1 galaxy LSBC F727-V01 ($z = 0.071$). The other X-ray source is consistent with the BL Lac BZB J1552+0850 ($z > 1.015$) at RA=238.0153 and DEC=8.8456 with an error circle of 4.1 arcsec (90% confidence radius). Even though both sources are positioned in the error circle of 2FGL J1551.9+0855, it is more likely that BZB J1552+0850

[2] http://wise2.ipac.caltech.edu/docs/release/allsky/

is the X-ray counter part of the *Fermi*/LAT detected source. BL Lac objects are known to be possible gamma-ray bright sources, the second *Fermi*/LAT AGN catalogue contains 395 BL Lac objects out of a total of 886 AGNs (Ackermann et al. 2011b), whereas Seyfert galaxies are only rarely gamma-ray emitters (Ackermann et al. 2012a). This result was confirmed by Massaro et al. (2012), who did an infrared follow-up on LSBC F727–V01 and BZB J1552+0850 and used infrared colour analysis to show that LSBC F727-V01 does not have the characteristics of a gamma-ray emitter.

10 Search for possible dark matter annihilation around M87

In addition to my work on radio galaxies, I have also collaborated with Dmitry Prokhorov (MPA Munich, Germany) on morphological analysis of extended emission with *Fermi*/LAT. In this section, I will describe the frame work of this research and my contribution to the collaboration. A paper describing the research will be submitted to MNRAS.

10.1 Introduction

In the current cosmological paradigm, the universe consists largely of undetected matter and energy. Baryonic matter, the ordinary observable matter, consists of only 4.9% of the mass-energy content of the universe. About ∼27% of the matter is non-baryonic, and the dark energy (linked to the acceleration of the expansion of the universe) accounts for the largest part of the total mass-energy budget, with about 68%.

In 1932 the presence of dark matter (DM) was first observed. Oort (1932) measured the velocities of stars in the Milky Way using spectroscopy, and found that the stars moved faster as expected from gravitational force calculated from the visible mass in the Galaxy indicating an unseen additional mass component (but the conclusions were disputed later, see e.g. Kuijken & Gilmore 1989). In clusters of galaxies the presence of additional mass was found in a similar way. The individual galaxies display a velocity larger than expected from the gravity as calculated using the cluster visible mass (Zwicky 1933). Later work has shown the presence of DM in galaxies using rotation curves, where the velocities of stars is plotted against their distance from the centre. Assuming Newtonian dynamics, the velocity of stars is the highest in the bulge, where most of the mass is located, and decreases toward the outskirts. However, it was found that the rotation curves show a rather flat profile, showing that stars follow a constant velocity profile even at the edges of galaxies (e.g. Babcock 1939). This indicates the presence of more mass than visible throughout the whole galaxy.

The composition of DM is still a topic of debate. An example of a popular candidate for DM are the WIMPs, or weakly interacting massive particles. The mass of WIMPs should be more than $\sim$ keV (Porter et al. 2011), such that it is 'cold', meaning that it was non-relativistic at the time of structure formation such that the DM can gravitationally clump to form galaxies. The upper limit to the WIMP mass is $\lesssim 300\,\mathrm{TeV}$, to account for the observed WIMP density in the universe (Griest & Kamionkowski 1990). These particles are thought to be thermal relics from the early universe. The WIMPs interact via gravity and the weak force, but they cannot be observed since they do not interact via electromagnetic processes. WIMPs also do not interact with atoms via the strong nuclear force (e.g. Edsjö & Gondolo 1995). In the early universe, the interactions with WIMPs and standard model particles, by annihilation and formation, kept them in a thermal equilibrium at the existing high temperature. Then,

Figure 10.1: Residual count map of the region around M87, between 1–3 GeV. The colours show the galactic diffuse model, and the contours correspond to 0.6, 1.0, 1.4, and 1.8 counts per pixel. A ring-like structure is visible in the galactic diffuse emission.

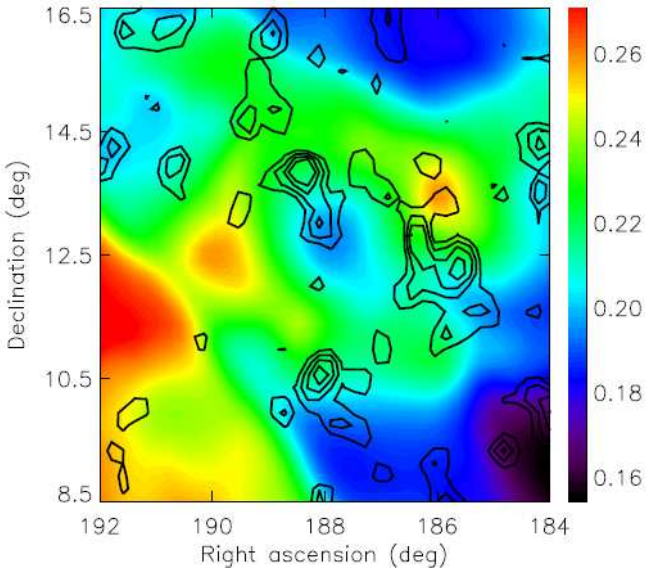

as the universe expanded, the rate of the interactions decreased and the abundance of WIMPs did not change significantly. The annihilation processes continued, but since the WIMPs are still postulated to exist in the present time, the annihilation rate should be very low.

Galaxy clusters can hold hundreds of galaxies, and as such are the largest gravitationally bound objects in the universe. The cluster mass is of the order of $M \simeq 10^{14} - 10^{15}\,\mathrm{M}_{\odot}$, and the DM contributes $\simeq$80% to the total mass. The Virgo Cluster, with a distance of 16.5 Mpc, is a nearby galaxy cluster which contains, among others, M87. Han et al. (2012) have reported signals consistent with DM annihilation lines in the Virgo cluster, using 3 years of *Fermi*/LAT observations (for a description of the instrument see Section 6.2.5). This signal, reported with a significance of 4.4σ, is consistent with a particle of mass 20–60 GeV annihilating via b-quarks, or a particle with mass between 2–10 GeV or a mass >1 TeV, annihilating via muons.

10.2 Fermi analysis

We have analysed *Fermi*/LAT observations, obtained from 4 August 2008 to 12 June 2012, within a radius of 20° of M87. We have selected the source events with an energy range between 0.1–100 GeV in 30 bins. Then we performed the event selection as recommended by the instrument team, and created a counts cube for the binned analysis. After this the lifetime cube and exposure map were created. We applied the binned likelihood analysis, with the model same as used in Section 8.4.3, which contains all sources as reported from the second *Fermi*/LAT catalogue, with the bright and nearby ($d < 10°$) sources in addition to the

Figure 10.2: Templates used to model the extended emission.

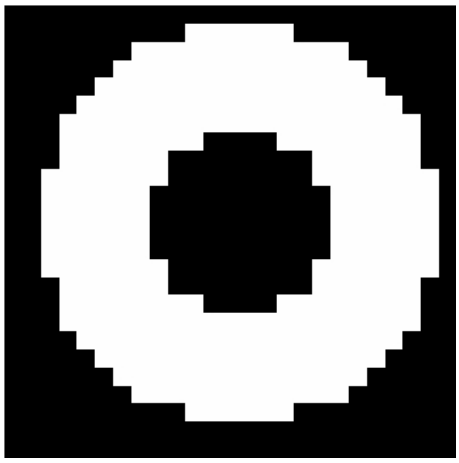

(a) The ring-shaped template used in the analysis, with an outer radius is 2.3°, and an inner radius is 1°.

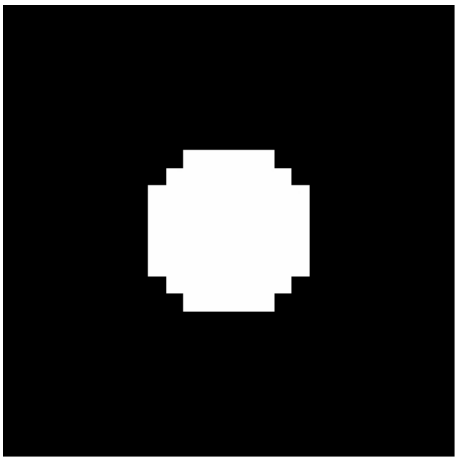

(b) The inside of the ring-shaped template.

galactic and extragalactic diffuse emission (model 1). We also applied just the galactic diffuse emission model to the data, which shows a ring-like structure around M87. The resulting 1–3 GeV map can be found in Figure 10.1 which shows the galactic diffuse model and the residuals of the model.

In the following sections the analysis used to study the structure in the 1–3 GeV residual map is described. In Section 7.3 the likelihood analysis is described in more detail. The goodness of the fit is evaluated based on $L = -\log$ Likelihood.

10.2.1 Extended emission results

We created a template for the ring-like excess found in the galactic diffuse emission map, shown on the left in Figure 10.2. During the fitting the background models are kept free, since the observed feature is likely to be caused by background emission. We used model 1 (see Section 8.4.3) where we added the template as a diffuse emission component. For each model we only need to generate the source maps, which are model dependent.

Using the base model 1, where the background normalization is left free, yields a -log likelihood of $L = 437378.5$. Then, the ring-like template is added to the model, where we used an exponential cut-off power law, with all parameters fixed except the normalization. This yields a -log likelihood of $L = 437373.4$, with one additional degree of freedom (d.o.f.). This means the ring-like structure is significant with a TS value of 10.2, which corresponds to a significance of $\sim 3\sigma$.

First we use an exponential cut-off power law, which is often used to model pulsars but also approximates the annihilation spectrum of WIMPs (Ackermann et al. 2012c). This yielded a -log likelihood $L = 437373.5$ (5 d.o.f. more than with the standard model), so the ring-shape

has a significance of 1.8σ. The fit shows a power law index of $\Gamma_1 = 1.2 \pm 0.9$ and a cut-off energy of $3.1 \pm 0.6\,\mathrm{GeV}$, as expected. Another exponentially cut-off broken power-law gave a similar -log likelihood of $L = 437378.0$ (4 additional d.o.f.). However, the parameters are not well constrained in this fit. Using a simple power law model yielded a -log likelihood of $L = 437367.8$ (2 additional d.o.f.), with a power law index of $\Gamma = 1.8 \pm 0.2$. We also applied a log-parabola spectrum, which is often used for bright blazars (e.g. Landau et al. 1986). This yielded a -log likelihood of $L = 437367.3$ (4 additional d.o.f.).

An exponential cut-off power law gives the best representation of the data when using the ring-shaped template.

10.2.2 Morphology results

We have also used different templates to find the shape which best represents the 1–3 GeV excess found in the galactic diffuse emission.
First we used the disk template shown on the right of Figure 10.2 together with the original ring-shape to better understand the 1–3 GeV excess. The addition of the disk template yielded a -log likelihood $L = 437373.2$, with 1 additional d.o.f., using an exponentially cut-off power law with the values fixed to the spectrum found using the ring-shaped template. The additional component does not significantly improve the fit. It should be noted, however, that the disk template covers a surface area almost three times less than the ring-shaped template.

To investigate asymmetry in the ring profile we used two different templates, shown in Figure 10.2.2. We used the same model as before, with an exponentially cut-off power law where the parameters have been left free. The model with the petals1 shape yielded a -log likelihood of $L = 437371.3$ (5 additional d.o.f.). The model without the additional source has a -log likelihood of $L = 437378.5$, so the source modelled with the petals1 template has a significance of 2.5σ. Using the petals2 template, the fit shows a -log likelihood of $L = 437377.2$ (5 additional d.o.f.), which corresponds to a significance of 0.3σ.

10.2.3 Point source identification

In the counts map of the M87-region, several points sources lie on or near the ring-shaped structure. The sources have not been included in the second *Fermi*/LAT catalogue, since with 2 years of data the significance threshold, TS=25, was not reached. The data set used contains almost 4 years of *Fermi*/LAT data, and the undetected sources have reached a significance of TS>25. This has been shown in a recent work by Macías-Ramírez et al. (2012).

We have tried to identify counter parts of these sources. Due to the large positional *Fermi*/LAT error, it is not trivial to locate a single counter-part. Table 10.1 shows the number of sources from the 2MASS survey (2 μm, e.g. Skrutskie et al. 2006), RASS catalogue (soft X-ray e.g. Voges et al. 1999), and the associations using the radio catalogue from HEASARC[1] in the 95% error circle of the point sources. In addition, we used the 13th AGN and quasar catalogue compiled by Véron-Cetty and Véron (Véron-Cetty & Véron 2010). The fourth IBIS catalogue did not show a match with any of the sources (Bird et al. 2010).

[1] http://heasarc.gsfc.nasa.gov/cgi-bin/W3Browse/w3table.pl?MissionHelp=radio_catalog

Figure 10.3: Templates used to model the extended emission, combined they form the ring-shape in Figure 10.2 (left).

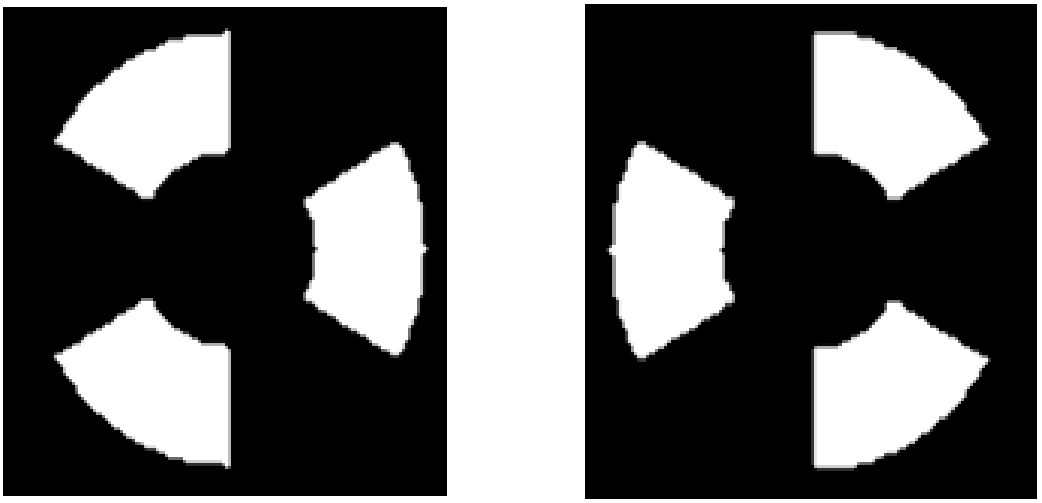

(a) Template petals1.

(b) Template petals2.

Figure 10.4: TS map of the region around M87, showing the new point sources. Image is centred at on the same position as Figure 10.1 and has the same size.

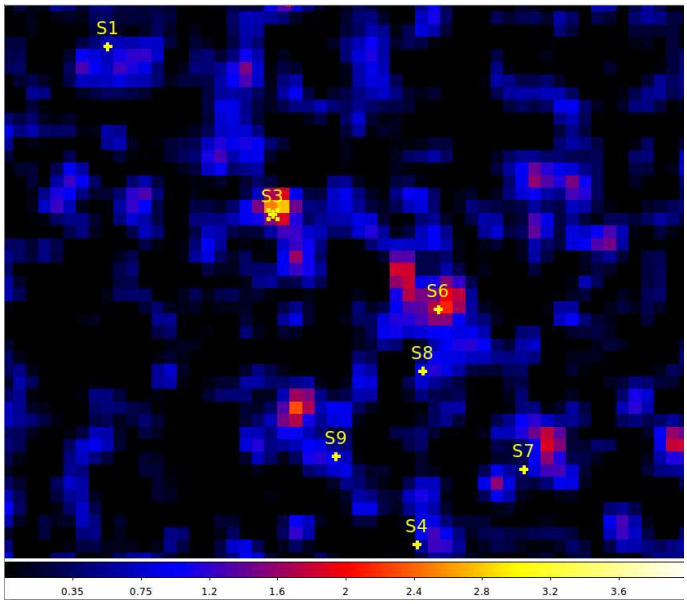

Table 10.1: Unidentified point sources near the GeV excess ring. Due to the large *Fermi*/LAT 95% error circle, column 4, several potential counter parts can be identified. Position and error circles from Macías-Ramírez et al. (2012).

source	RA [degrees]	DEC [degrees]	95% Error radius [degrees]	2MASS	RASS	Radio[a]	AGN cat[b]
S1	190.92	16.21	0.07	32	-	3	-
S2	187.91	16.88	0.09	41	-	21	-
S3	188.18	13.56	0.11	56	-	26	-
S4	185.85	8.30	0.05	9	-	2	-
S5	186.68	6.68	0.04	3	1	2	1
S6	185.48	12.04	0.11	45	-	1	-
S7	184.12	9.48	0.06	17	-	1	-
S8	185.74	11.06	0.09	33	1	3	1
S9	187.15	9.71	0.09	36	-	3	-

[a] HEASARC archive [b] 13$^{\text{th}}$ AGN and quasar catalogue (Véron-Cetty & Véron 2010)

Due to the large amount of possible counter parts, it is not possible for all sources to determine the true corresponding source. For two sources we found a *ROSAT* counter part. We found for S5 a positional coincidence with a blazar, BZB J1226+0638 (Massaro et al. 2009). This source also coincides with the RASS source 1RXS J12267+0639 and SDSS J12265+0640, which are included in the 13th AGN and quasar catalogue. This might indicate that this source can be positively connected to this blazar. Also the source S8 has a counter part in the 13th AGN and quasar catalogue, namely the source SDSS J12231+1100 (a BL Lac source at z=1.065). The SDSS J12231+1100 source is located 0.4' distance from the *ROSAT* source 1RXS J122308.4+110054, and is suggested to be an optical counter part for this X-ray source (Anderson et al. 2007).

10.3 Conclusion

In this Chapter I have described my contribution to the study of a possible DM signal observed by *Fermi*/LAT in the M87 region. A DM signal was reported by Han et al. (2012), who found an 4.4σ excess between 1–3 GeV using *Fermi*/LAT observations of the M87 region. The excess at $\sim 1-3$ GeV is consistent with annihilation of WIMPs with a mass of $\backsimeq 28$ GeV. The analysis performed by Han et al. (2012) included all point sources reported in the second *Fermi*/LAT catalogue (Nolan et al. 2012), with the parameters fixed to the catalogue values. In our analysis we have used 3.8 years of *Fermi*/LAT observations. We include these sources, 16 in total including M87, but with the parameters free to vary, since the second *Fermi*/LAT catalogue describes the two-year data, and the observations used exceed those two years. We have applied several models to the extended emission, and used the residuals to get the best representation of the data. We found the extended emission has an irregular shape, and is best modelled with an exponentially cut-off power law. The reported 1–3 GeV excess is more likely to be caused by the contribution of point sources (see Macías-Ramírez et al. 2012), since the significance of the potential DM emisson decreased from 4.4σ to $\sim 3\sigma$ using 3.8 years of data. Also uncertainties in the galactic diffuse emission might contribute to the signal.

Mon. Not. R. Astron. Soc. **000**, ??–?? (2012) Printed 26 August 2013 (MN LATEX style file v2.2)

A morphological analysis for searches of possible extended γ-ray sources associated with dark matter annihilation

D. A. Prokhorov[1⋆], S. de Jong[2]

[1] *Max-Planck-Institut für Astrophysik, Karl-Schwarzschild-Strasse 1, 85741 Garching, Germany*
[2] *François Arago Centre, APC, Université Paris Diderot, CNRS/IN2P3, CEA/Irfu, Observatoire de Paris, Sorbonne Paris Cité, 10 rue Alice Domon et Léonie Duquet, 75205 Paris Cedex 13, France*

Accepted ..... Received ..... ; in original form .....

ABSTRACT
We propose a morphological analysis for searches of extended γ-ray emission associated with dark matter annihilation. Our approach is based on the likelihood analysis including the spatial templates produced by taking into account the residual count maps in the energy band in that the dark matter annihilation spectrum has a prominent spectral feature. The approach is tested on the example of the possible dark matter annihilation signal from the Virgo cluster of galaxies.

Key words:

1 INTRODUCTION

Model selection is an important part of any statistical analysis (Burnham & Anderson 2002). One needs to make assumptions about the completeness of a model taking into account relevant physical processes. Residual count maps, obtained from the subtraction of the modelled count map (obtained as the result of a likelihood analysis) from the observational data, can contain spatial or spectral structures. These structures are more likely due to imperfections of the selected model rather than the evidence for a new physical process. In this paper, we analyse the data taken by the *Fermi* Large Area Telescope (LAT) from the region including the Virgo cluster of galaxies and propose a method to test the presence of a possible extended γ-ray source.

A number of astrophysical source classes including supernova remnants, pulsar wind nebulae, molecular clouds, normal galaxies, and clusters of galaxies are expected to be spatially extended and resolvable by the *Fermi*-LAT. Normal galaxies and galaxy clusters contain large amounts of dark matter. An analysis of extended objects is more complex compared with that of point-like objects because the extension of an object is an additional degree of freedom in the model. The LAT has firmly detected twelve extended γ-ray sources (including three normal galaxies), during the first 2 years of the *Fermi* mission (for a catalog, see Nolan et al. 2012), see also Lande et al. (2012) for observations of other extended objects. Galaxy clusters are promising candidates to γ-ray emitting sources which can potentially be discovered by *Fermi*-LAT(e.g., see Miniati 2003). While the nature of dark matter is still unknown, a weakly interacting massive particle (WIMP) is a popular candidate. γ-ray emission produced through dark matter annihilation may be detectable by *Fermi*-LAT. Thus, galaxy clusters can be diffuse sources associated with dark matter annihilation (e.g., see Ackermann et al. 2010a).

To search for an extended object on the maps of *Fermi*-LAT, one needs to assume its spatial morphology and spectrum. One of the methods to make such assumptions is to adopt a spatial template associated with emission in a different energy band (e.g. at radio or X-ray frequencies), however this is no guarantee that the spatial morphologies are similar since different radiative processes can give contributions at different frequencies. Another method is to choose the shape of the photon spectrum, e.g. a power-law, but the photon spectrum of a candidate source is *a priori* unknown. The likelihood ratio test allows us to compare candidate models to determine which one gives a better description of the data, but the set of models can never be totally complete and the likelihood ratio test can be applied only for a comparison of nested candidate models (one candidate model is a special case of the other).

Residual count maps can be used to produce spatial templates and to determine shapes of spectra for new extended γ-ray source candidates. This technique can be successfully used if foreground and background emission is perfectly modelled. However, there are some uncertainties in the determination of foreground and background emission. The method that we present below and that will be applied for testing the presence of extended objects is based on the

⋆ E-mail:phdmitry@gmail.com

analysis of assumptions on the spectral and spatial properties of an extended object which adopted in the model in which candidates to extended objects are supposed (and their presence is consistent with observations at the high statistical significance). If the modification to the assumptions (e.g., of spatial symmetry) results in a strong decrease of the statistical significance of a candidate extended object then the model should be reconsidered. Below we discuss how to search for the presence of extended emission from the Virgo cluster that could potentially be produced via the annihilation of dark matter particles. The presented method will allow us to study the presence of an extended object associated with the Virgo cluster and can be applied for a search for extended objects associated with high dark matter concentrations, such as the Galactic Centre and Andromeda, in the future.

2 APPARENT EXTENDED EMISSION FROM THE DARK MATTER HALO IN VIRGO

Clusters of galaxies are the largest gravitationally bound structures in the Universe, with sizes of $\simeq$1-3 Mpc, containing hundreds of galaxies and a hot ($\simeq$1-10 keV) diffuse plasma which sets in equilibrium in the potential wells of the clusters (for a review, see Sarazin 1986). The presence of non-baryonic matter, known as Dark Matter (DM), was inferred from its gravitational effects on visible matter. The DM component contributes $\simeq$80% to the total mass of a galaxy cluster, $M \simeq 10^{14} - 10^{15} M_{\odot}$. The nature of DM remains unknown. Weakly interacting massive particles (WIMPs) are hypothetical particles serving as one possible solution to the dark matter problem and are predicted by many new physics models beyond the standard model of particle physics (for a review, see Bertone et al. 2005). γ-rays from annihilation of WIMPs in galaxy clusters could potentially be detected by *Fermi*-LAT (for a review of the present status of searches for particle DM by astronomical instruments, see Porter et al. 2011). The search for GeV emission from clusters of galaxies using data collected by the LAT from 2008 August to 2010 February has been reported by Ackermann et al. (2010b), who derived γ-ray flux upper limits from galaxy clusters under the assumption that galaxy clusters are γ-rays point-like (i.e., non-extended) sources.

The Virgo cluster is located about 16.5 Mpc away and is the nearest large galaxy cluster. This cluster of galaxies is an excellent target for γ-ray observations and can spatially be resolved by *Fermi*-LAT at GeV energies because of Virgo's proximity. Recently, a signal consistent with that expected from DM annihilation in the DM halo of the Virgo cluster has been discussed by Han et al. (2012a), who have analysed the first 3 years of data from *Fermi*-LAT. The reported signal is at a significant level of 4.4σ for a model in which WIMPs, with mass $M \simeq 28$GeV, annihilate into the $b\bar{b}$ channel. Note that a large boost factor, $\sim 10^3$, is required for the consistency between the observational data and DM interpretation. Recent Phoenix simulations by Gao et al. (2012) suggest the large enhancement of a flux (a boost of $\simeq$1000) due to substructures in galaxy clusters.

As was shown by Macías-Ramírez et al. (2012) and Han et al. (2012b), the tentative evidence for a γ-ray excess from the Virgo cluster is mainly due to the appearance of a population of γ-ray point sources with power-law spectra near the Virgo cluster that are not part of the LAT 2-year point source (2FGL) catalog (Nolan et al. 2012). The 2FGL catalog contains significant γ-ray point sources detected by the LAT in the first 24-months of the *Fermi* mission. The new γ-ray point sources are found to be above the standard detection significance threshold when more than two years of LAT data is included. The inclusion of the 7 new point sources in the original model of Han et al. (2012a), that are above the test-statistics (Mattox et al. 1996) of TS=25 threshold for the four year data, decreases the significance of the possible DM signal from the $\simeq 5\sigma$ level to $\simeq 3\sigma$ level (Macias-Ramirez et al. 2012).

Note that the presence of the central galaxy of M87, that is also a γ-ray source (Abdo et al. 2009), in the Virgo cluster makes the analysis of this cluster more complex, since the subtraction of M87 from the data is necessary for studying the possible extended component associated with the DM halo of the Virgo cluster. The separation of these two γ-ray emission components can be performed by analysing the emission with energies of $\gtrsim$1 GeV at which the FWHM of the point spread function (PSF) is less than the expected angular size of the DM halo. Annihilation of WIMPs of $M \simeq 28$GeV should produce a γ-ray signal resulting in an excess at energies of $\simeq$1-3 GeV over the total emission from point sources, diffuse galactic foreground, and isotropic background (this excess should be owing to the specific spectral shape of emission from DM annihilation occured via the $b\bar{b}$ channel, see Sect. 4). The excess of γ-ray emission from the Virgo cluster at $\simeq$1-3 GeV energies over that expected from 2FGL sources, diffuse galactic foreground, and isotropic background was demonstrated by Han et al. (2012a, see the right panel of their Fig. 12). The presence of this excess in the spectrum leads us to the idea that the analysis of residual count maps at energies of a few GeV can be useful for studying the morphology of extended emission from the Virgo cluster. In this paper, we will prove the importance of a morphological analysis for the study of extended γ-ray sources.

3 OBSERVATION AND DATA REDUCTION

Fermi was launched on 2008 June 11 into a nearly circular Earth orbit with an altitude of 565 km and inclination of 25.6°, and an orbital period of 96 minutes. The principal instrument on *Fermi* is the LAT (Atwood et al. 2009), a pair-production telescope with a large effective area ($\sim$8000 cm^2 at 1 GeV) and field of view (2.4 sr), sensitive to γ-rays between 20 MeV and >300 GeV. After the commissioning phase, the *Fermi*-LAT began routine science operations on 2008 August 4. The *Fermi*-LAT normally operates in sky-survey mode which provides a full-sky coverage every 3 hours (i.e., 2 orbits).

For the data analysis, we use the Fermi Science Tools v9r27p1 package[1] and P7V6 instrument response functions (IRFs). Events $\geqslant$100 MeV arriving within 20° of M87 (region of interest – ROI) and satisfying the SOURCE event selection are taken. To reduce the contamination by the

[1] `http://fermi.gsfc.nasa.gov/ssc/data/analysis/`

Table 1. The list of the sixteen strong sources in the ROI

2FGLJ1158.8+0939	2FGLJ1204.2+1144
2FGLJ1209.7+1807	2FGLJ1214.6+1309
2FGLJ1214.8+1653	2FGLJ1222.4+0413
2FGLJ1224.9+2122	2FGLJ1229.1+0202
2FGLJ1230.8+1224	2FGLJ1231.6+1417
2FGLJ1239.5+0443	2FGLJ1239.5+0728
2FGLJ1251.2+1045	2FGLJ1256.1-0547
2FGLJ1301.5+0835	2FGLJ1305.0+1152

γ-ray emission coming from cosmic-ray interactions in the Earth's upper atmosphere our selection is refined by choosing events with zenith angles $<100^\circ$. We remove events that occur during manoeuvres when the *Fermi*-LAT rocking angle was larger than 52°. For this analysis, we have accumulated events obtained from 2008 August 4 to 2012 June 12.

Our aim is to study the morphologies of spatial structures on the residual count map of the Virgo cluster at energies of a few GeV. The residual count map is the result of the subtraction of the modelled count map based on the result of a likelihood analysis from the observational data. To demonstrate the approach for studying extended objects, we include the 2FGL point sources and the diffuse foreground and background in the model. Our model includes the 2FGL sources located within the ROI. Their spectral shapes are taken from the 2FGL catalog (Nolan et al. 2012), while the normalizations and spectral parameters of sixteen strong point sources (including M87) are derived from the likelihood analysis (the list of the sixteen strong sources are shown in Table 1). The normalizations of fainter point sources are held fixed at the 2FGL catalog values. The galactic diffuse foreground and isotropic diffuse background[2] are included in the model by the templates, gal_2yearp7v6_v0.fits and iso_p7v6source.txt, respectively. The normalizations of the galactic and isotropic components are allowed to vary during the fitting. Note that our model is more detailed than that of Han et al. (2012a), because the parameters of only three 2FGL point sources (within the Virgo's virial radius of 4.6°) have been allowed to vary in their analysis. As shown in Fig. 1 of Han et al. (2012a), the three point sources within the Virgo's virial radius are faint and, therefore, the residuals are dominated by the contribution from stronger γ-ray sources which are outside the virial radius. This is because their spectral parameters are not perfectly described by the values taken from the 2FGL catalog, while the data from a longer *Fermi*-LAT observation is analysed. Since the values of the spectral parameters of the sixteen strong point sources are derived from the likelihood analysis in our study, the calculated residual count maps (see Sect. 4) are more suitable for the morphological analysis. We will discuss a population of γ-ray point sources near the Virgo cluster (that are not part of the 2FGL catalog) in Sect. 5, where the results of our likelihood analysis will be presented.

[2] `http://fermi.gsfc.nasa.gov/ssc/data/access/lat/BackgroundModels.html`

4 LIKELIHOOD ANALYSIS AND RESIDUAL COUNT MAP BETWEEN 1 AND 3 GEV

We analyse the first 3.8 years of *Fermi*-LAT observations using the binned maximum likelihood mode of the gtlike routine, which is part of the Science Tools[1]. The test-statistic (TS) (Mattox et al. 1996) was employed to evaluate the significance of the γ-ray fluxes coming from the sources. The TS value is defined as twice the difference between the log-likelihood function maximised by adjusting all the parameters of the model, with and without the source. The choice of the free and fixed parameters in the analysis is described in Sect. 3. The list of the sixteen 2FGL point sources that spectral parameters were free in the fit is shown in Table 1. We set the energy binning to 30 logarithmic bins between 100 MeV and 300 GeV.

From the resulting best-fit we construct the model counts map in the 1-3 GeV band using the gtmodel tool from the Science Tools. We choose this energy interval because it corresponds to photon energies at which the γ-ray emission from DM annihilation of WIMPs with $M \simeq 28$ GeV via the $b\bar{b}$ channel should strongly contribute to the total signal (see, e.g., Baltz et al. 2007). Note that the photon spectrum, dN/dE, corresponding to annihilation of WIMPs with $M \simeq 25$ GeV via the $b\bar{b}$ channel can be approximated as an exponentially cutoff power-law function with Γ=1.22 and $E_{\rm cut} = 1.8$ GeV (see, Ackermann et al. 2012)

$$\frac{dN}{dE} = N_0 \left(\frac{E}{E_0}\right)^{-\Gamma} \exp\left(\frac{-E}{E_{\rm cut}}\right), \qquad (1)$$

where N_0 and E_0 are a prefactor and a scale factor. The value of the exponential cut-off, $E_{\rm cut} = 1.8$ GeV, lies in the energy interval of (1 GeV, 3 GeV) and the spectral index, Γ, is very hard at energies below the exponential cut-off compared with a typical spectral index of 2FGL point sources. Therefore, the flux excess in the 1-3 GeV energy range can be interpreted as the exponential break in the exponentially-cutoff-power-law spectrum of an additional component produced by DM annihilation. The additional component that could be consistent with possible annihilation emission of DM particles with $M \simeq 28$ GeV was found by Han et al. (2012a) in their likelihood analysis adopting the specific spatial DM template based on high resolution cosmological simulations by Gao et al. (2012), assuming DM annihilation spectra, and including only point sources from the 2FGL catalog in the original model. Therefore, we suppose that this component can potentially also be revealed on the residual count map at 1-3 GeV by studying morphology of residuals.

Figure 1 shows the residual count map of size $8^\circ \times 8^\circ$ (2.3 Mpc×2.3 Mpc) for the energy range 1-3 GeV by contour lines. The pixel size is 0.1°. This map is derived from the observed LAT count map by subtracting the model obtained from the likelihood analysis and is centred on the position of M87. The residual map was smoothed with a 2D Gaussian kernel of $\sigma = 0.4^\circ$. The contour levels correspond to 0.6, 1.0, 1.4, and 1.8 counts per pixel. The residual count map reveals three prominent structures near the Virgo cluster that have approximate coordinates $\simeq$ (188°, 13.5°), $\simeq$(188°, 10.5°), and $\simeq$(186°, 12°). We also show the galactic diffuse foreground model in the energy band of 1-3 GeV in Fig. 1 by colour. The galactic diffuse model is taken from the spa-

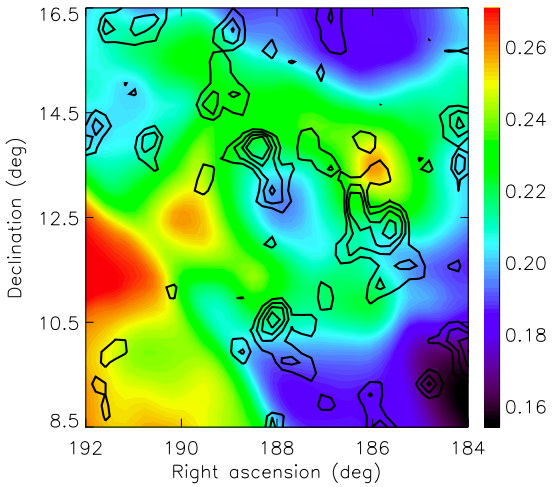

Figure 1. The residual count map for the energy range 1-3 GeV is shown by contour lines. The residual map was smoothed with a 2D Gaussian kernel of $\sigma = 0.4^\circ$. The contour levels correspond to 0.6, 1.0, 1.4, and 1.8 counts per pixel.

tial and spectral template, gal_2yearp7v6_v0.fits, provided by the *Fermi*-LAT collaboration[3]. This model for the Galactic diffuse emission was developed using spectral line surveys of HI and CO (as a tracer of H2) to derive the distribution of interstellar gas in Galactocentric rings. Infrared tracers of dust column density were used to correct column densities in directions where the optical depth of HI was either over- or underestimated. The model of the diffuse γ-ray emission was constructed by fitting the γ-ray emissivities of the rings in several energy bands to the LAT observations after removal of the point sources. In the southeastern quadrant of this map, the North Polar spur (the rim of a hot galactic superbubble) is contributing to the foreground galactic diffuse emission model.

In the next section, we attempt to understand the origin of these three prominent structures on the 1-3 GeV residual count map and to discuss whether or not their origin can be caused by DM annihilation emission from the dark matter halo of the Virgo cluster. The aim of the following study is to demonstrate that the residuals at the exponential break energy of the assumed additional spectral component can be used for producing templates and that it is useful to include the spatial templates in the analysis in order to interpret the observations by means of a likelihood analysis.

5 LIKELIHOOD ANALYSIS AND MORPHOLOGY OF RESIDUALS

In this Section, we make various spatial templates for the additional γ-ray component coming from the region of the Virgo cluster. We take the morphology of the residual count map at energies of 1-3 GeV into account and compare the models associated with the spatial templates using the likelihood ratio test for goodness of fit.

The dominant foreground γ-rays are produced by the neutral pion decay originating from interactions of CR protons with the interstellar medium (ISM). The γ-ray intensity from neutral pion decay is proportional to the integral along the line of sight of the product of the ISM density and the cosmic ray (CR) proton density. The resulting γ-ray distribution produced via neutral pion decay should be morphologically correlated with other maps of spatial tracers of the ISM, such as spectral lines of HI and CO, and dust continuum.

Figure 1 shows that the galactic diffuse emission is inhomogeneous in the region of the Virgo cluster and that the galactic diffuse emission map of this region contains the spatial structure. This structure has the shape of a doughnut and its centre coincides with M87. The three prominent structures on the residual count map at 1-3 GeV lie approximately on this γ-ray "doughnut" structure (see Fig. 1). To clarify the origin of the "doughnut" structure on the diffuse galactic emission map, we use the HI gas map obtained by the *Leiden/Argentine/Bonn* Survey of Galactic HI (Kalberla et al. 2005). We checked and found that the HI map contains a similar "doughnut" structure and that the positions of the HI gas "doughnut" and of the diffuse emission "doughnut" structure are spatially coincident. **Further evidence for the gas "doughnut" in the direction of the Virgo cluster comes from far infrared observations. The *Herschel* Virgo Cluster Survey observed four 4×4 sq deg regions towards the Virgo cluster (Davies et al. 2010; Auld et al. 2013). At a wavelength of 250 μm, the Galactic dust cirrus is seen in the 4×4 sq deg map centred on M87 and is doughnut-shaped (see the left-bottom panel of Fig. 1 in Auld et al. 2013). The observations of both the HI and dust emission show a prominent doughnut-shaped structure towards the Virgo cluster.** Therefore, we conclude that the presence of the "doughnut" structure on the galactic diffuse emission map is owing to the particular shape of the ISM gas spatial distribution in this sky region. Note that the residuals in the 1-3 GeV energy band for this $8^\circ \times 8^\circ$ region are highest on the "doughnut" structure and, therefore, the *Fermi*-LAT observations of this region are not described properly by the galactic diffuse template and 2FGL point sources.

5.1 Spatial templates

We create the first spatial template, dubbed *doughnut*, taking into account the approximate spatial coincidence of the locations of the foreground emission "doughnut" structure and of the high residuals at 1-3 GeV. This template is shown on the upper left panel in Fig. 2. The radii of the inner and outer circular boundaries of the *doughnut* are $R_{\rm inner} = 1^\circ$ and $R_{\rm outer} = 2.2^\circ$, respectively, and were choosen according to the morphology of the structure on the galactic diffuse emission map shown by colour in Fig. 1. The normalization coefficient, X, shown on the map, is derived by using the rule, $X = 1{\rm sr}/(\pi R^2_{\rm outer} - \pi R^2_{\rm inner})$. Note that the template, *doughnut*, is homogeneous and, therefore, the possible variations of the gas column density over the HI gas "doughnut" are not taken into account.

[3] http://fermi.gsfc.nasa.gov/ssc/data/access/lat/Model_details/Pass7_galactic.html

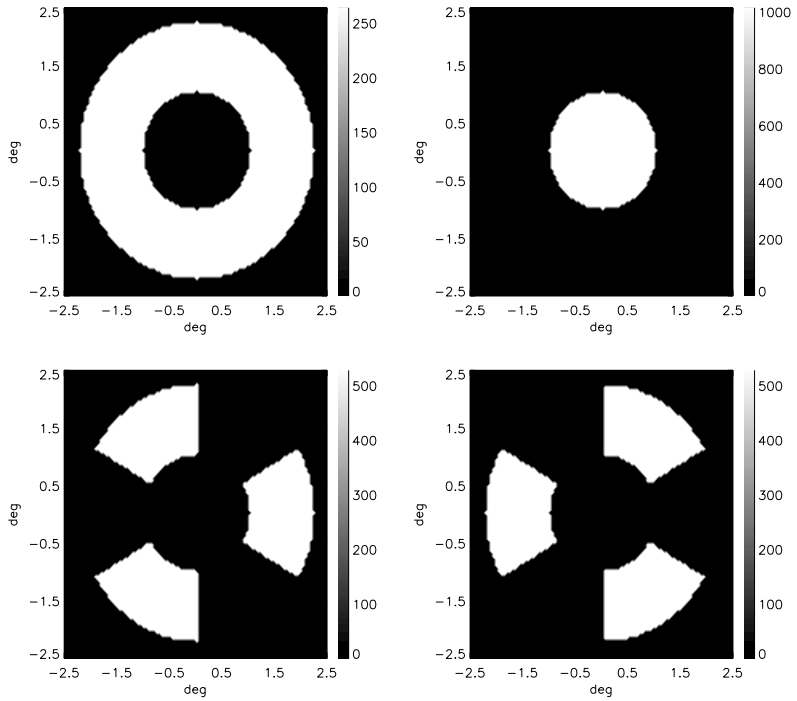

Figure 2. Templates which we use for the comparison of different models of the origin of the excess between 1-3 GeV from Virgo

The second spatial template is associated with the "disk" inside the foreground emission "doughnut" structure in Fig. 1 (i.e., the "disk" corresponds to the hole of the "doughnut"). This template, dubbed *disk*, corresponds to the inner region with a size of 1° of the Virgo cluster and is shown on the upper right panel in Fig. 2. The values, X, on the map were derived by using the rule, $X = 1\mathrm{sr}/(\pi R^2_{\mathrm{inner}})$. Note that the surface area of the *disk* template is ≈ 3.8 times smaller than that of the *doughnut* template. The number of *Fermi*-LAT photon events (as well as the incoming photon flux) associated with a spatial template, is expected to be proportional to the surface area of a template. Therefore, the DM annihilation signal from the *doughnut* template might be stronger than that from the *disk* template. However, the γ-ray signal from DM annihilation is proportional to the integral along the line of sight of the squared mass density of dark matter, $J = \int \rho^2_{\mathrm{DM}} dl$ and can depend on the spatial DM distribution (thus, a cusped DM profile can increase the DM annihilation signal from the inner part of the Virgo cluster).

The third and fourth spatial templates (dubbed *petals1* and *petals2* owing to their spatial shapes) are each composed of three distinct parts of equal surface areas. The centres of the three parts belonging to each of these spatial templates are located at the apices of an equilateral triangle. The third and fourth templates are shown on the lower left and lower right panels, respectively, in Fig.2. The values, X, on the map were derived by using the rule, $X = 1\mathrm{sr}/(\pi R^2_{\mathrm{outer}}/2 - \pi R^2_{\mathrm{inner}}/2)$. The sum of the third and fourth templates (with equal weighting factors) is identical to the first template, *doughnut*, multiplied by a factor of 2. The template, *petals1*, covers the three prominent structures on the 1-3 GeV residual count map, while the template, *petals2*, does not spatially overlap with these prominent structures on the 1-3 GeV residual map. The DM distribution in the halos of relaxed clusters is expected to be roughly spherically symmetrical and, therefore, the *petals1* and *petals2* templates should be useful to test the possible deviation from the continuous spherical symmetry of the DM distribution. Note that a large part of the mass of the Virgo cluster is centred on the galaxy M87, with smaller concentrations around M86 (at RA$\approx$186.55°, DEC$\approx$12.95°) and M49 (at RA$\approx$187.44°, DEC$\approx$8.00°), see, e.g., Böhringer et al. (1994). The mass concentration around M86 is part of a small group of galaxies that is merging with the main galaxy cluster and is covered by the spatial template *petals2*. Thus, if the DM distribution is the same as described by Böhringer et al. (1994), we expect that the model including the two spatial templates, *disk* and *petals2*, should be the more statistically significant than that includes the spatial template *petals1*.

5.2 Morphological analysis

Morphological analysis is a problem-structuring technique of combining parameters into new combinations for the later review. Below we apply the morphological analysis to the study of the *Fermi*-LAT observations of the Virgo cluster in order to show that the residuals at the energy band at

that the dark matter annihilation spectrum has a prominent spectral feature can be successfully used for the search for extended γ-ray sources associated with DM annihilation.

We assume the presence of the possible additional components with different spatial distributions, which have not been included in the likelihood analysis in the previous section, and perform a likelihood analysis for various models. The results of likelihood analyses are shown in Table 2. The model, M0, is identical to that considered in the previous section and includes 2FGL sources, galactic foreground, and isotropic background. The model, M1, is nested with the model, M0, and includes the additional template, *doughnut*, with the photon spectrum given by Eq. 1 and mimicking the possible DM annihilation spectrum. The models, M2, M3, M4, are also nested with the model, M0, and include the additional spatial templates, *disk*, *petals1*, and *petals2*, respectively, and their spectral distributions are taken from Eq. 1. The models, M1, M2, M3, and M4, each include one additional free parameter, compared with the model M0, that corresponds to the normalization of an additional component. The models, M5 and M6, are more complex and include two additional templates, *petals1* + *petals2*, and, *petals2* + *disk*, respectively. The spectral shapes of each of these components are given by Eq.1 and their normalizations are independent free parameters in likelihood analyses. The model, M5, is nested with the models, M0, M1, M3, and M4, whereas the model, M6, is nested with the models, M0, M2, and M4. The calculated log-likelihood values for the described models are shown in the fourth column of Table 2. The difference, multiplied by two, between the log-likelihood function maximised by adjusting all the parameters of the model, with (L) and without (L_0) the additional component, are shown in the fifth column of Table 2 (note that the model without any additional component is M0).

The model with an additional component (with free normalization) will always fit at least as well (have a greater log-likelihood) as the model without additional component. Whether it fits significantly better and should thus be preferred is determined by deriving the probability of the difference in the log-likelihoods. Where the null hypothesis represents a special case of the alternative hypothesis (i.e., the case of nested models), the probability distribution of the test statistics is approximately a chi-squared distribution with degrees of freedom equal to df_2 - df_1, where df_1 and df_2 represent the number of free parameters of two candidate models. If we take the model, M0, as a null model then using the fifth column of the table we find that the models, M1, M3, and M5, significantly better describe the observational data than the model, M0, does. Comparing the model M1 with M0, we find that the significance of the presence of the DM "doughnut" structure is 3.4σ. Comparing the models M3 and M5 with M0, we find that the presence of the template, *petals1*, strongly improves the fit and its significance is 4.3σ for the model M3 and is 4.0σ for the model M5. As for the models M2 and M4, our analysis demonstrates that the inclusion of either *disk* or *petals2* templates do not significantly improve the fit. Therefore, the observational data supports the presence of the spatial structure associated with the template, *petals1*, and has no evidence for the presence of other additional spatial structures with the DM spectrum given by Eq.1.

The models M1 and M5 are nested and their comparison with the observational data permits us to check if the model M5 provides a significantly better fit than the model M1. Since the template for the model M5 is produced by using the high 1-3 GeV residuals, this template is not continuously symmetric with respect to the axis passed through the centre of the count map (i.e., the position of M87) along the line of sight (although this template has a discrete rotational symmetry of the 6th order, i.e. rotation by an angle of $360^\circ/6=60^\circ$ does not change the template), while the template for the model M1 is continuously symmetric about this central axis. The comparison of these models is a test of the assumption about the continuously symmetry that has been made by Han et al. (2012a). Twice the difference between the log-likelihood of the models, M1 and M5, is 7.52 (see, the fourth column in Table 2). Therefore, the significance of the improvement of the fit by taking into account the two templates, *petals1* or *petals2*, instead of the template, *doughnut*, is 2.7σ. At 2.7σ there is only one chance in nearly 150 that a random fluctuation would yield the result. Note that the two sources from a new γ-ray population of seven point sources, proposed by Macías-Ramírez et al. (2012), and nearest to the centre of the Virgo cluster are covered by the spatial template, *petals1*. The coordinates of these two point sources are (RA, DEC)=(188.18, 13.56) and (185.48, 12.04). This shows correspondence between the derived high significance of the spatial structure associated with the template, *petals1*, and the tentative point sources beyond the 2FGL catalog. Although the template, *disk*, covers the central part of the Virgo cluster and that the template, *petals2*, covers the mass concentration around M86, the inclusion of these templates in the analysis (the model M6) does not significantly improve the fit compared with that of the original model M0, see the fifth column of Table2.

Thus, we have demonstrated that the residuals at 1-3 GeV allowed us to create the template, *petals1*, which significantly improves the fit to the data and is not associated with the largest mass concentration. Using a prominent feature of WIMP annihilation spectra and creating the spatial templates (covering the highest residuals in the energy band corresponding to the WIMP annihilation spectral feature), we have shown that the presented morphological analysis is a powerful approach for studying extended γ-ray sources and their possible association with signals from WIMP annihilation.

Table 2. The results of likelihood analyses

Model	Template	d.o.f.	-log(L)	-2 log(L/L_0)
M0	-	-	312042.20	-
M1	doughnut	1	312036.37	11.66
M2	disk	1	312040.88	2.64
M3	petals1	1	312032.61	19.18
M4	petals2	1	312041.35	1.7
M5	petals1+petals2	2	312032.61	19.18
M6	petals2+disk	2	312040.55	3.3

Table 3. The results of likelihood analyses of the 5-year data

Model	Template	d.o.f.	-2 log(L/L$_0$)
M0	-	-	-
M1	doughnut	1	20.1
M3	petals1	1	33.4
M4	petals2	1	2.8
M5	petals1+petals2	2	33.4

6 LIKELIHOOD ANALYSIS USING FIVE YEARS OF DATA

The previous Sections have been completed in December 2012. Later we re-wrote one paragraph in Sect. 5 to include information on the Herschel observation of the Galactic dust cirrus. The result of the analysis presented above shows that the additional extended gamma-ray source in the region of the ISM doughnut-shaped gas structure, that is located in the direction of the Virgo cluster, is statistically significant at 3.4σ level. This emission can be attributed to DM annihilation in the halo of the Virgo cluster or to non-2FGL point sources near the Virgo cluster (see Han et al. 2012b; Macías-Ramírez et al. 2012). It can also be caused by imperfections of the Galactic foreground model describing the ISM doughnut-shaped structure towards the Virgo cluster. To check these possibilities, we compared the two models, M1 and M5, in Sect. 5.2 and found that the additional extended gamma-ray source is spatially inhomogeneous under the assumption that the Galactic foreground model is perfectly modelled. If these results hold then we expect that:

1. the significance of the doughnut template, *doughnut*, **should increase with observation time, and**

2. the relative likelihood of the model M5 (based on the template *petals1+petals2*) **with respect to the model M1 (based on the template** *doughnut*) **should increase with time.**

We were waiting since December 2012 while the *Fermi*-**LAT is collecting the data. In the end of July 2013, we repeated the likelihood analyses using the data collected from August 4, 2008 to July 25, 2013. The results of the likelihood analyses are shown in Table 3. The models and parameters shown in this Table are the same as those shown in Table 2 and are described in the second paragraph of Sect. 5.2.**

Using the fourth column of Table 3 and applying the Wilks theorem, we found that the statistical significance of the template *doughnut* **is 4.5σ. We also found that the statistical significance of the template** *petals1* **is 5.8σ and the statistical significance of the template** *petals2* **is only 1.7σ. The significance of the improvement of the fit by taking into account the two templates,** *petals1* **or** *petals2*, **instead of the template,** *doughnut*, **is 3.7σ. At 3.7σ there is only one chance in nearly 3800 that a random fluctuation would yield the result. This provides strong evidence that a possible additional extended source, located in the region of the ISM doughnut-shaped structure, is spatially inhomogeneous. Therefore, the results reported in the previous Sections hold when the first five years of the** *Fermi*-**LAT data are analysed.**

7 CONCLUSION

In this paper we develop and demonstrate how to apply the morphological analysis for the search for the possible extended gamma-ray sources associated with dark matter annihilation. Our approach is based on an analysis of morphology of residual count maps using spatial templates and taking into account a prominent spectral feature of WIMP annihilation. We chose the photon spectrum produced via annihilation of WIMPs with a mass of 25 GeV as an example, since the possible signals from annihilation of WIMPs with such masses have recently been discussed by Hooper & Linden (2011) and Han et al. (2012a) in their analyses of the *Fermi*-LAT observations.

The *Fermi*-LAT (Atwood et al. 2009) is a pair-production telescope with a large effective area ($\simeq$8000 cm^2 at 1 GeV) and field of view (2.4 sr), which is sensitive to γ-rays between 20 MeV and >300 GeV. The point spread function (PSF) for on-axis γ-rays has a 68% containment radius of about 3° at 100 MeV and 0.04° at 100 GeV. The PSF is about 1° at 1 GeV and *Fermi*-LAT allows us to spatially resolve the nearest clusters of galaxies. The detection of the nearest galaxy clusters, such as Virgo and Coma, is one of goals of the *Fermi* mission. A γ-ray signal from galaxy clusters can be dominated by photons produced via dark matter annihilation. Other extended γ-ray sources on the sky, that can partially be contributed by WIMP annihilation photons, are the Galactic centre and the DM halo of the Andromeda galaxy.

DM particles annihilation in astrophysical sources allows us to perform indirect searches for dark matter. We consider the process $\chi\chi \rightarrow b\bar{b}$, the annihilation of pairs of dark matter particles to pairs of b quarks. Spectrum of photons from hadronic processes has a peak which occurs at an energy of $E_{\rm peak} \approx m_\chi/25$ (e.g., see Baltz et al. 2007). If a dark matter particle mass is 25 GeV, then we expect the peak in the photon spectrum at $\simeq$ 1 GeV. Therefore, the residual count map at the peak energy, that is produced by the subtraction of the model (without the inclusion of a WIMP annihilation source) from the observational data, could give valuable information about the spatial morphology of a possible WIMP annihilation source. Note that point like γ-ray sources with hard spectra at low energies and with a spectral exponential cut-off at a high energy equally well describe pulsar and WIMP annihilation spectra in γ-rays. Therefore, the extended γ-ray sources associated with a high concentration of DM provide us with a unique possibility to search for WIMP annihilation γ-ray signals.

We applied a morphological analysis to the study of the Virgo cluster initially assuming the presence of 2FGL sources, galactic diffuse foreground, and extragalactic diffuse background. We derived the 1-3 GeV residual count map and found that the high residuals at 1-3 GeV are confined in three spatial regions, and that the morphology of residuals is clumpy rather than continuously spherically symmetric. **Using the first 3.8 years of** *Fermi*-**LAT observations,** we performed a likelihood analysis using different spatial

templates, dubbed *doughnut, disk, petals1, and petals2*, obtained by taking into account the morphology of the high 1-3 GeV residuals. Our analysis demonstrates that the presence of the template, *petals1*, covering the high 1-3 GeV residuals and having the photon spectrum provided by WIMP annihilation, strongly improves the fit and its significance is 4.3σ. The template, *doughnut*, is continuously spherically symmetric, spatially covers the high 1-3 GeV residuals, and its surface is two times larger than the surface of a *petals1* template. The significance of the improvement of the fit by taking into account the two templates, petals1 or petals2, (with equal surface areas) instead of the continuously symmetric template, *doughnut*, is 2.7σ. This shows that the γ-ray signal which could be associated with WIMP annihilation is not continuously symmetric in the inner part of the Virgo cluster. Therefore, the morphology of residuals at the energy peak of photon spectra corresponding to those of WIMP annihilation provides an interesting diagnostics of a dark matter distribution. **In Sect. 6, we demonstrated that the conclusion on inhomogeneity of the possible extended source towards the Virgo cluster holds when the first five years of *Fermi*-LAT observations are analysed.** Studying of the morphology of residual count maps at such energies can be used for a search for extended γ-ray signals from WIMP annihilation.

REFERENCES

Abdo A. A. et al., 2009, ApJ, 707, 55
Ackermann M. et al., 2010a, JCAP, 5, 25
Ackermann M. et al., 2010b, ApJ, 717, L71
Ackermann M. et al., 2012, ApJ, 747, 121
Atwood W. B. et al., 2009, ApJ, 697, 1071
Auld R. et al., 2013, MNRAS, 428, 1880
Baltz E. A., Taylor J. E., Wai L. L., 2007, ApJ, 659, L125
Bertone G., Hooper D., Silk J., 2005, Phys. Rep., 405, 279
Böhringer H., Briel U. G., Schwarz R. A., Voges W., Hartner G., Trümper J., 1994, Nature, 368, 828
Burnham K. P., Anderson D. R., 2002, Model Selection and Multimodel Inference: A Practical Information-Theoretic Approach, Springer, 2002, 488 p. ISBN 0-387-95364-7
Davies J. I. et al., 2010, A&A, 518, L48
Gao L., Frenk C. S., Jenkins A., Springel V., White S. D. M., 2012, MNRAS, 419, 1721
Han J., Frenk C. S., Eke V. R., Gao L., White S. D. M., 2012a, ArXiv e-prints 1201.1003
Han J., Frenk C. S., Eke V. R., Gao L., White S. D. M., Boyarsky A., Malyshev D., Ruchayskiy O., 2012b, ArXiv e-prints 1207.6749
Hooper D., Linden T., 2011, Phys. Rev. D., 84, 123005
Kalberla P. M. W., Burton W. B., Hartmann D., Arnal E. M., Bajaja E., Morras R., Pöppel W. G. L., 2005, A&A, 440, 775
Lande J. et al., 2012, ApJ, 756, 5
Macías-Ramírez O., Gordon C., Brown A. M., Adams J., 2012, Phys. Rev. D., 86, 076004
Mattox J. R., et al., 1996, ApJ, 461, 396
Miniati F., 2003, MNRAS, 342, 1009
Nolan P. L. et al., 2012, ApJS, 199, 31
Porter T. A., Johnson R. P., Graham P. W., 2011, ARA&A, 49, 155
Sarazin C. L., 1986, Reviews of Modern Physics, 58, 1

11 Discussion

In this work we have studied two gamma-ray bright radio galaxies, the FR-II source 3C 111 and the FR-I galaxy M87. Both sources showed very different properties, for example in gamma-ray brightness and in the X-ray band. In this section we will discuss the results in the context of general characteristics of gamma-ray bright radio galaxies and how these sources fit into the Unification model of AGN (described in Section 4.3).

11.1 Origin of the gamma-ray emission

Most sources cannot be spatially resolved in gamma-rays, due to technical limitations which constrain the angular resolution at high energies. For example, *Fermi*/LAT has an angular resolution of 3.5° at 100 MeV (single photon, on-axis, Atwood et al. 2009). Therefore, the emission region cannot be constrained from gamma-ray observations alone. In the case of blazars, the gamma-ray emission is likely to arise in the relativistic jet, which is pointed towards the observer. The emission is Doppler boosted, explaining the high luminosity and the energetic emission observed. The rapid variability of the gamma-ray emission ($\Delta t < 2-3$ hrs, e.g. Foschini et al. 2011) suggests a compact emitting region, near the central engine. The broad-line region (BLR) causes the spectral breaks observed in blazars, due to pair absorption on the He Lyman recombination continuum and lines (Poutanen & Stern 2010). Gamma-ray emission can be produced in the BLR by inverse Compton scattering of the BLR UV seed photons, in the Klein-Nishina regime. The cooling time of the electrons is energy-independent in this case (Dotson et al. 2012). An emission region placed at a distance $\lesssim 10^{16}$ cm of the central engine, where the accretion disk photons dominate, cannot reproduce the observed emission, due to high opacity caused by pair production (Ghisellini & Tavecchio 2009). Multi-waveband observations have shown that the gamma-ray emission is connected to the optical and radio emission (e.g. Marscher et al. 2010). This would place the gamma-ray emitting region even further down the jet, at parsec scale distance from the central engine. The gamma-ray emission can also originate from the inverse Compton scattering of infrared photons from the dusty torus. This process takes place in the Thompson regime, producing again energy-dependent electron cooling times (Dotson et al. 2012).

Radio-quiet sources are not expected to show gamma-ray emission, due to the absence of a strong relativistic jet. However, some starburst galaxies, such as the nearby M82 (distance 2.4 Mpc), have been observed in the GeV band with *Fermi*/LAT (Ackermann et al. 2012b). In this case the gamma-ray emission is possibly connected to supernova activity, where particles can be accelerated in the supernova remnant shock waves, and interact with the radiation fields, magnetic fields and dense gas. Electrons and positrons will lose energy via synchrotron and inverse Compton radiation, whereas accelerated protons can emit gamma-rays via proton-proton interaction (Voelk et al. 1989). Similarly, gamma-ray emission connected to star formation in the host galaxy might be observed in Seyferts. Since the bulk of the hard X-ray emission is produced in the disk coronae, this might also be a potential

gamma-ray emission site (Zdziarski & Lightman 1985). Also proton-proton interactions in the inner accretion disk could generate gamma-ray emission, if a rapidly spinning black hole is present and the accretion flow is advection dominated (Niedzwiecki et al. 2009).
Ackermann et al. (2012a) used *Fermi*/LAT to study a hard X-ray selected sample of 120 Seyfert galaxies. Only two sources showed a significance of $> 4.6\sigma$, but these are thought to be false positives due to chance spatial coincidences. A mean value for the 95% upper limit to the >100 MeV photon flux was found of $f \lesssim 4 \times 10^{-9}\,\mathrm{erg\,cm^{-2}\,s^{-1}}$, where a power law index of $\Gamma_\gamma = 2.5$ is assumed. If gamma-ray emission is produced via proton-proton interactions in the inner accretion disk, it is expected to be $\gtrsim 10\%$ of the disk or disk corona X-ray luminosity, assuming a maximally spinning black hole. However, the upper limit found for the gamma-ray emission excludes this hypothesis.

Most radio galaxies, where the jet is pointed away from the observer with an angle $\theta > 10^\circ$ are not gamma-ray bright. So far, only about 15 radio galaxies have been detected in gamma-rays, using *Fermi*/LAT (Abdo et al. 2010a; Nolan et al. 2012). Kataoka et al. (2011) used a sample of 18 X-ray selected radio galaxies to explore the gamma-ray emission of these sources. Analysing 2 years of *Fermi*/LAT observations of these sources showed that most sources are not significantly detected in the gamma-ray band. Only two sources, 3C 111 and 3C 120, which are also included in the *Fermi*/LAT catalogue, are detected with a significance $> 5\sigma$. The source Pictor A is tentatively detected with a significance of $\sim 3\sigma$ (using 3 years of *Fermi*/LAT observations, this source is detected with $\sim 5.8\sigma$ Brown & Adams 2012). Furthermore, the gamma-ray emission is likely to be variable on time scales of months to years.

The nearby (distance 3.7 Mpc; Ferrarese et al. 2007) FR-I radio galaxy Centaurus A shows spatially extended gamma-ray emission, which coincides with the radio core, but also with the extended radio lobes (Abdo et al. 2010d). The radio lobes have an angular size of $\sim 10^\circ$ (Shain 1958), and are detected at $> 100\,\mathrm{MeV}$, with significances of 10σ for the northern lobe, and 20σ for the southern lobe, using 3 years of *Fermi*/LAT observations (Yang et al. 2012). The combined $> 100\,\mathrm{MeV}$ flux from the lobes is $f \sim 1.9 \times 10^{-7}\,\mathrm{ph\,cm^{-2}\,s^{-1}}$, whereas the flux from the core is $f \sim 1.5 \times 10^{-7}\,\mathrm{ph\,cm^{-2}\,s^{-1}}$ (Abdo et al. 2010d). The gamma-ray emission from the radio lobes can be explained with a synchrotron self-Compton model (SSC, see Section 7.6.1). Another gamma-ray detected radio galaxy is the FR-II source Pictor A, (z=0.034 Liu & Zhang 2002), which has a significance of 5.8σ in the >200 MeV band, using 3 years of *Fermi*/LAT observations. Brown & Adams (2012) showed that the gamma-ray flux of this source cannot be reproduced using an SSC model for the radio lobes. An additional external Compton component might be necessary to fit the SED, or the gamma-ray emission of Pictor A does not arise from the radio lobes but rather from the core.

The X-ray spectrum of blazars is thought to be dominated by jet emission. Using a long-term (1996 to 2001) spectral variability study of the FSRQ 3C 273 ($z = 0.158$), Grandi & Palumbo (2004) showed that the X-ray spectrum cannot be properly represented by a simple power law. By fitting the X-ray spectrum with a Seyfert-like model, which included a cut-off power law spectrum, reflection and an iron K$-\alpha$ line, it was shown that the emission is rather a mix of thermal and non-thermal contributions. The spectrum is dominated by non-thermal emission, which overwhelms the Seyfert contribution. The ratio between the jet flux and the thermal component flux is about 1.2–3 in the soft X-ray 2–10 keV band, up to a factor of 7 in the hard X-ray band >20 keV. Applying a similar method to several radio galaxies, Grandi

Table 11.1: Sample of *Fermi*/LAT radio galaxies, the FR-I sources. Flux, power law index and significance from the *Fermi*/LAT second source catalogue (Nolan et al. 2012), except for 3C 78 and 3C 120 (Abdo et al. 2010e), and M87 (this work).

Object	0.1–100 GeV Flux $[\times 10^{-12}\,\mathrm{erg\,cm^{-2}\,s^{-1}}]$	Power law index 100 MeV–100 GeV	Significance $[\sigma]$ 100 MeV–100 GeV	log (Luminosity) $[\mathrm{ergs\,s^{-1}}]$
M87	17.3 ± 0.9	2.16 ± 0.06	19	41.91
Cen A	65 ± 3	2.76 ± 0.05	27	41.67
NGC 1275	174 ± 6	2.03[a]	65	44.08
3C 78	5.9 ± 0.2	2.0 ± 0.1	35	43.04
PKS 0625-354	17 ± 2	1.93 ± 0.09	13	42.04
NGC 6251	13 ± 1	2.20 ± 0.07	12	43.26
3C 120	11.2 ± 0.4	2.7 ± 0.4	32	43.46
Cen B	23 ± 4	2.3 ± 0.1	5	42.93
IC 310	10 ± 3	2.1 ± 0.2	4	42.89
Fornax A	6 ± 1	2.2 ± 0.2	6	41.66

[a] Logparabola fit

Table 11.2: Sample of *Fermi*/LAT radio galaxies, FR-II sources. Flux, power law index and significance from the *Fermi*/LAT second source catalogue (Nolan et al. 2012), except for 3C 111 (this work) and Pictor A (Brown & Adams 2012)

Object	0.1–100 GeV Flux $[\times 10^{-12}\,\mathrm{erg\,cm^{-2}\,s^{-1}}]$	Power law index 100 MeV–100 GeV	Significance $[\sigma]$ 100 MeV–100 GeV	log (Luminosity) $[\mathrm{ergs\,s^{-1}}]$
3C 111	6 ± 2	2.4 ± 0.2	3	43.76
3C 207	10 ± 1	2.4 ± 0.1	8	46.38
3C 380	17 ± 2	2.34 ± 0.07	14.1	46.65
PKS 0943–76	10 ± 2	2.4 ± 0.1	5	45.40
Pictor A	7 ± 2	2.93 ± 0.03	6	43.33

& Palumbo (2007) showed that the jet contribution does not dominate the emission, with a factor of < 0.7 in the 2–10 keV band. We found that the X-ray emission from 3C 111 is dominated by thermal inverse Compton components. The overall spectral energy distribution of 3C 111, on the other hand, can be represented by a jet model, showing that the gamma-ray emission might arise similarly to that observed in blazars. In the case of M87, we could extract an X-ray spectrum when the source was in a bright state. A flare would indicate the variable jet emission dominates, overwhelming any thermal components. Additionally, due to the noise in the spectrum, components apart from a power law are difficult to discern.

Neither of the sources studied in this work can be resolved by *Fermi*/LAT. Due to their distance they appear as point sources in the gamma-ray band. In the case of the FR-II source 3C 111 (z=0.049, Sargent 1977), Grandi et al. (2012) have argued, based on multi-wavelength observations and variability arguments, that the gamma-ray emission arises at a distance of 0.3 pc from the central black hole. For the FR-I source M87, with its distance of D=16 Mpc (Tonry 1991), it is not certain if there is any contribution to the gamma-ray emission from the radio lobes, based on *Fermi*/LAT observations alone (Abdo et al. 2009c).

Figure 11.1: The redshifts of the FR-I (red squares) and FR-II (green dots) galaxies plotted versus the flux between 0.1–100 GeV. The high flux is from NGC 1275.

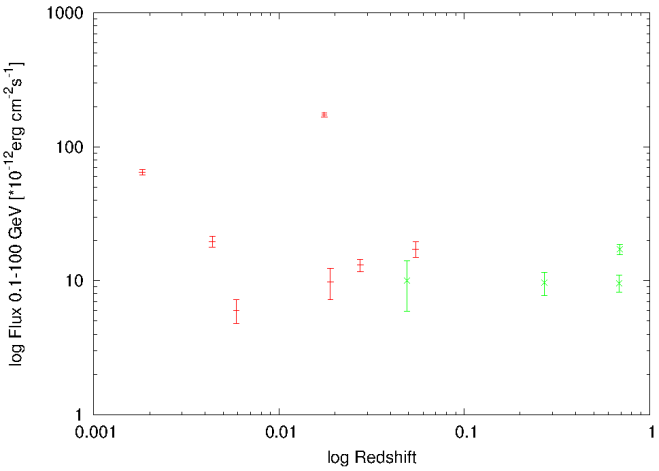

11.2 Proximity

In the second *Fermi*/LAT AGN catalogue, the peak of the redshift distribution of flat spectrum radio quasars (FSRQ) is located at $z = 1$, with the largest observed redshift at $z = 3.10$ (Ackermann et al. 2011a). More than half of the BL Lac sources do not have an associated redshift, due to the featureless optical spectrum where no lines are present which can be used for redshift determination. Using a complete sample of blazars from the 3-year *Swift*/BAT survey, Ajello et al. (2009) showed a different redshift distribution, where 40% of the FSRQ have a redshift z>2. This might indicate that the gamma-ray emission from high redshift sources is too weak to be observed with *Fermi*/LAT, or that the population of FSRQ probed with *Fermi*/LAT differs from the population observed in the *Swift*/BAT hard X-ray sample.

Table 3.1 lists the redshifts of the gamma-ray detected radio galaxies, showing that all these sources are observed at low redshift compared to the *Fermi*/LAT detected FSRQ population. The bright FR-II radio galaxy 3C 380 has the highest redshift of this group, with $z = 0.692$. A possible explanation for this is that all radio galaxies emit gamma-rays, but due to sensitivity limits we only observe those nearby. For example, compared to FR-II galaxies the FR-I sources are weaker gamma-ray emitters, with a luminosity of $L_\gamma \sim 10^{44}\,\mathrm{erg\,s^{-1}}$ (Ackermann et al. 2011a), and the FR-I source with the highest redshift is PKS 0625-35 with $z = 0.0546$. The FR-II sources are observed to have higher gamma-ray luminosities, of the order of $L_\gamma \sim 10^{45} - 10^{46}\,\mathrm{erg\,s^{-1}}$, and for gamma-ray bright FR-II sources the highest redshift observed is $z = 0.692$ for 3C 380. In Figure 11.1 the gamma-ray flux of the radio galaxies is plotted versus the redshift. The brightest sources are observed at low redshifts, and at high redshifts only low luminosity objects are found.

A setback for the proximity argument is also that it does not account for the luminous FR-II radio galaxy Cygnus A, which has a redshift of $z = 0.0561$ and has not yet been detected by *Fermi*/LAT. Cygnus A is brighter in the soft X-ray band compared to 3C 111. For example,

Figure 11.2: Comparison of the X-ray luminosity of the gamma-ray detected radio galaxies and their gamma-ray luminosity.

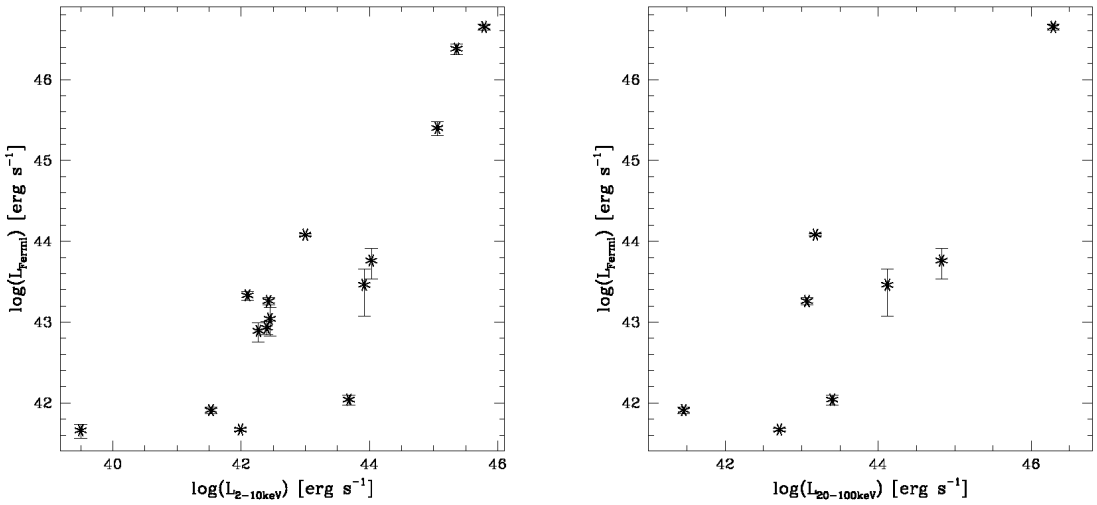

(a) The soft X-ray (2–10 keV) luminosity versus the gamma-ray luminosity show a >99.9% probability for a positive correlation.

(b) The hard X-ray (20–100 keV) luminosity versus the gamma-ray luminosity also indicates a trend, with a probability for a positive correlation of >98%.

Chandra/ACIS observed a flux of $f = 1.8 \times 10^{-11}\,\mathrm{erg\,cm^{-2}\,s^{-1}}$ between 2 and 10 keV (Shi et al. 2005), where we found for 3C 111 a 2–10 keV flux of $f = 2.0 \times 10^{-12}\,\mathrm{erg\,cm^{-2}\,s^{-1}}$ using *Suzaku*/XIS and PIN. In the hard X-ray band, the sources show a similar flux. In the 58-month *Swift*/BAT survey, Cygnus A has a flux of $f = 1.2 \times 10^{-10}\,\mathrm{erg\,cm^{-2}\,s^{-1}}$, and 3C 111 has a flux of $f = 1.1 \times 10^{-10}\,\mathrm{erg\,cm^{-2}\,s^{-1}}$ (Baumgartner et al. 2010). As can be seen in Figure 11.2, sources which are brighter in the soft X-ray band and hard X-ray band tend to have higher gamma-ray luminosities. Therefore, if all radio galaxies would be gamma-ray bright, and we observe only those nearby due to sensitivity limits, a detectable flux in the *Fermi*/LAT band would be expected for Cygnus A. Since this source is not detected by *Fermi*/LAT, it is more likely that the gamma-ray emission from radio galaxies is caused by specific inherent properties. Another possibility is that the gamma-ray emission in radio galaxies, like the one from blazers, has a certain duty cycle, in the sense that these sources can be active for a limited amount of time and then be gamma-ray silent again.

Thus, even though the proximity of a source obviously is important concerning the question whether or not a radio galaxy is detectable in the gamma-ray band, it cannot be the only factor.

11.3 Physical properties

Blazars, in a large sample, show an anti-correlation between luminosity and the peak frequencies of the synchrotron and inverse Compton branches, the so-called blazar sequence (see Section 4.3.1 and Figure 4.8). In the sample of radio galaxies, most of the *Fermi*/LAT detected sources are of the FR-I type, see Tables 11.1 and 11.2. Since FR-I types radio galaxies

Figure 11.3: SED peak luminosity derived from parabolic fits against the radio luminosity. The ratio of the peak frequencies of the synchrotron and inverse Compton branch is constant.

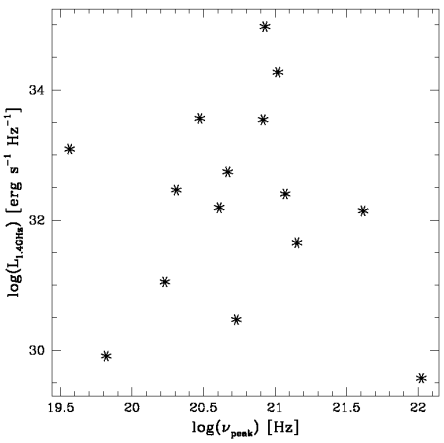

(a) Radio luminosity (1.4 GHz) against the inverse Compton peak frequency for the radio galaxy sample. The Spearman rank test shows no correlation between these parameters.

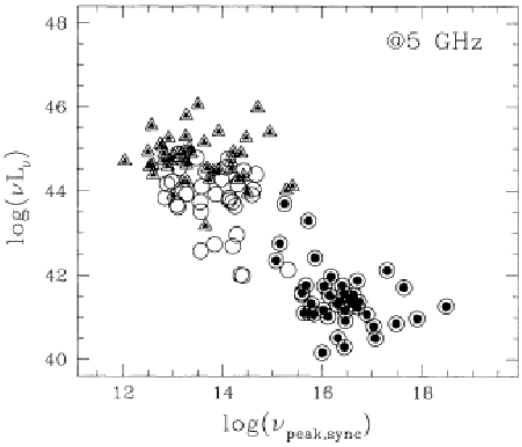

(b) Radio luminosity (5 GHz) versus the synchrotron peak frequency of a large sample of 126 sources, containing FSRQ (triangles), LBL (open circles) and HBL (filled circles). Image from Fossati et al. (1998).

are connected to BL Lacs, and FR-II with FSRQ, it is possible that there is also an anti-correlation visible between luminosity and peak frequencies of these sources. For this we have modelled the inverse Compton branch by using a simple parabolic representation based on the 2–10 keV X-ray and *Fermi*/LAT gamma-ray data. While this is not a physical model, it provides an easy way to estimate the luminosity in the inverse Compton branch and the peak frequency. With three known points a parabola is completely defined, and here 2 keV, 10 keV, and 200 MeV data points are used (see Section refparabola in the appendix). Figure 11.3 shows the results, the plot on the right showing for comparison a sample of radio galaxies taken from Fossati et al. (1998). In the right panel the sample consists of 126 sources, and a trend can be distinguished, where the FSRQ occupy a different part of the parameter space than the HBL. In the case of the gamma-ray detected radio galaxies such a trend is not visible. Applying the Spearman rank test to these parameters of the radio galaxy sample, a Pearson correlation-coefficient of $r_\mathrm{s} = -0.09$ is found, the probability for a negative correlation is <80%, meaning there is no correlation. It has to be pointed out, though, that the the LAT detected sample covers only $\Delta \log \nu_\mathrm{peak} = 2.5$, while the sample presented by Fossati covers peak frequencies within a range of $\Delta \log \nu_\mathrm{peak} = 6$. Taking a subset of the Fossati sample with $\Delta \log \nu_\mathrm{peak} = 2.5$ would also not allow to detect the trend of the blazer sequence.

In order to understand why some radio galaxies are gamma-ray bright and some are not, we need to study the common properties of the sample of gamma-ray bright sources. To characterise the sources we searched for correlations between luminosities in different wavebands, both visually and by applying a statistical test, see Section 13.2. As can be seen in Figure 11.2 there seems to be a correlation between the X-ray luminosity (both in the soft,

Figure 11.4: The X-ray jet luminosity as measured using high-resolution *Chandra* observations of nearby radio galaxies shows a correlation with the luminosity in the *Fermi*/LAT band.

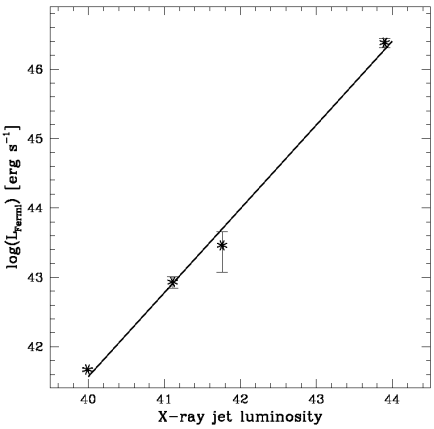

$L_{2-10\mathrm{keV}}$ and the hard $L_{20-100\mathrm{keV}}$ bands) and the luminosity in the *Fermi*/LAT band L_{LAT}. Using the Spearman rank test, we find a Pearson correlation-coefficient $r_{\mathrm{s}} = 0.86$, which gives a probability for a positive correlation of >99.9% between the soft X-ray luminosity $L_{2-10\mathrm{keV}}$ and the LAT luminosity L_{LAT}. Between the hard X-ray luminosity $L_{20-100\mathrm{keV}}$ and the LAT luminosity L_{LAT}, the Pearson correlation-coefficient $r_{\mathrm{s}} = 0.79$, giving a probability for a positive correlation of >98%. The gamma-ray luminosity L_{LAT} is likely due to inverse Compton scattering, which also plays a role in the X-ray band as we found applying the SSC modelling in the case of 3C 111 and M87. For some sources, such as 3C 111, the luminosity in the soft X-ray band $L_{2-10\mathrm{keV}}$ includes a contribution by thermal Seyfert-like processes, which might explain the scatter present in this correlation. Often it is not possible to view only the non-thermal jet emission, due to lack of angular resolution for sources at higher distances. For a few nearby sources this is possible using *Chandra* observations, showing a tight correlation between the 2–10 keV jet luminosity and the gamma-ray luminosity, as can be seen in Figure 11.4. In the hard X-ray band any thermal component should not have a large influence and here the scatter might be due to different spectral shapes of the SEDs. Also the radio luminosity correlates with the gamma-ray luminosity, as shown in Figure 11.5. The Spearman rank test yields a Pearsons correlation-coefficient of $r_{\mathrm{s}} = 0.89$, showing a probability of a positive correlation of >99.9%. In general, radio galaxies that are luminous in the radio and X-ray band are also more luminous in gamma-rays when compared to other gamma-ray bright radio galaxies.

11.4 Unified scheme

In the previous section we have seen that gamma-ray bright radio galaxies are likely to belong to the same class of objects, rather than following a sequence as suggested by the unified scheme. Due to the presence of both, FR-I and FR-II type sources, a sample with both BL Lac cores and FSRQ cores might be expected. Of the four FR-II sources in the sample, 3C 111 seems to have a BL Lac core, as its gamma-ray luminosity of $\log L_\gamma = 43.8$ lies far

Figure 11.5: The radio luminosity at 1.4 GHz is correlated with the luminosity in the *Fermi*/LAT band, with a probability of >99.9%.

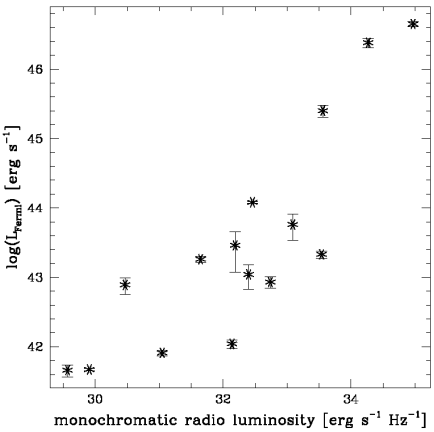

below the FSRQ range, as shown in Figure 11.6.

One of the differences between the blazar types is the Compton dominance. To model FSRQ sources, an external Compton component in addition to the SSC emission is often necessary to represent the data. For BL Lacs, the SSC model alone provides a good representation. We found that this holds for the FR-I source M87. However, for 3C 111, an FR-II galaxy, there is no need for external Compton to represent the data. This is in agreement with our finding that 3C 111 most likely hosts a BL Lac core. BL Lacs are thought to show an inefficient accretion flow (ADAF, RIAF), whereas the FSRQ have efficient accretion via a disk (Beckmann & Shrader 2012). In terms of the Eddington ratio $\lambda_{\rm Edd} = L_{\rm bol}/L_{\rm Edd}$, FSRQ show an accretion efficiency of $\lambda_{\rm Edd} > 0.01$, while for BL Lac sources this ratio is $\lambda_{\rm Edd} < 0.01$. A similar observation was made for radio galaxies, where the FR-II types have efficient accretion while FR-I sources do not. In the case of M87 we have shown that the accretion is not efficient. For 3C 111, the Eddington ratio is $\lambda_{\rm Edd} \sim 0.02$ (assuming a black hole mass of $M_{\rm BH} = 2.4^{+0.6}_{-0.5} \times 10^8\,{\rm M}_\odot$ Chatterjee et al. 2011). This would put the source just in the transition zone between FSRQ and BL Lac type blazers.

When considering their luminosity, the class of gamma-ray bright radio galaxies appear to host a BL Lac core, rather than a FSRQ type central engine. For some FR-I sources an SED is available and modelled, such as for M87 (this work) and for Cen A (Abdo et al. 2010c). As expected if these sources host a BL Lac core, the SEDs of these sources can be represented by an SSC model without adding an external Compton component. In the case of the FR-II sources, 3C 111 shows a luminosity closer to that of a BL Lac source, and the SED requires only an SSC model. Unfortunately, for the other FR-II sources the SED has not yet been modelled. Thus, it is unclear if the absence of an external Compton component for 3C 111 is a trend for all gamma-ray bright FR-II sources.

Figure 11.6: This histogram shows the luminosity distribution of gamma-ray bright sources. The radio galaxies are shown in the upper panel, FR-I with the red continuum line and FR-II with the green dashed line. The lower panel shows the distribution for blazars, BL Lac objects – blue continuum line; FSRQs – black dashed region. 3C 111 is the only FR-II source outside the FSRQ luminosity range (image from Abdo et al. 2010e) .

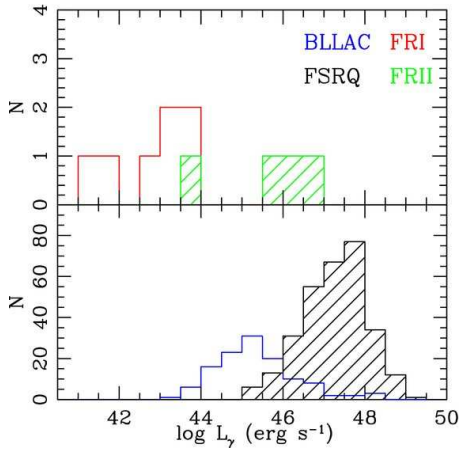

11.5 Gamma-ray emission site

Ever since the first radio galaxy was observed in gamma-rays, the question is how exactly the emission is produced. As described in Section 11.1, the dominant emission from blazar sources originates from the jet. In the case of radio galaxies, the emission is not always jet-dominated due to the jet being observed at an angle $\theta > 10°$. Since we observe thermal components in the emission of gamma-ray bright radio galaxies, for example in 3C 111 and Cen A, the broad-band emission is (partially) due to thermal processes (Beckmann et al. 2012). In case of M87, we likely see only jet emission, due to the absence of thermal signatures in the soft X-ray band.

Several theories exist on the emission sites and processes of gamma-ray emission in radio galaxies. In an early model the gamma-ray photons are thought to be the result of inverse Compton scattering of starlight photons fields and the cosmic microwave background by ultra-relativistic electrons in the FR-I jets of radio galaxies (Stawarz et al. 2003, 2006). However, the emission produced via this process underestimates the flux detected. In the SED we derived for M87, and for FR-I sources in general, an external Compton component is not necessary to properly represent the broad-band flux.
Tavecchio & Ghisellini (2008) proposed a model for M87 where the jet consists of a fast spine surrounded by a slower outer layer. In the spine the magnetic field B is higher, and the break energy $E_{\rm br}$ lower compared to the outer layer (see Section 7.6.1). The spine is where the MeV to GeV emission is produced. The particles in the outer layer, which might be energized by turbulent acceleration, can be responsible for the TeV emission. We found in our analysis that the SED of M87 can be represented by a single-zone model, disfavouring this theory at least in the case of this specific radio galaxy.
Another theory assumes that the gamma-ray emission originates near the central engine and

that this region is filled with several plasma blobs moving in the large opening angle of the jet formation zone creating a multi-zone SSC spectrum (Lenain et al. 2008). While one blob is travelling down the jet along the line of sight, other blobs move with an angle to the line of sight. For M87 this model showed a blob size of radius $R \sim 10^{14}$ cm, assuming 6 blobs. This can be compared to our results, where we found an emission region with a radius $R \sim 10^{16}$ cm using a one-zone SSC model. Assuming all blobs emit similar SSC emission, the SED is not distinguishable from a one-zone SSC model. This multi-blob approach solves the gamma-ray emission from misaligned jets, but a large jet opening angle is necessary. In the case of M87 the opening angle of the jet is 60°near the centre, and collimation sets in at larger distances from the core, at about ∼30–100 Schwarzschild radii (Junor et al. 1999).

Gamma-ray emission can also originate from a hot accretion flow near the central black hole via neutral pion production and decay (Niedźwiecki et al. 2013). Here, an advection-dominated accretion flow (ADAF) is assumed, with a two-temperature structure. In this model, the spin of the black hole is an important parameter. The model has been applied to M87, and it provides a good representation of the data, assuming that there are no outflows which can reduce the accretion rate.

From this we conclude that it is most likely that the bulk of the gamma-ray emission originates in the jet, near the central black hole. Then the emission can be viewed along the line of sight with a mechanism such as reflection via a corona, or multiple blobs in the jet with a large opening angle. Even though the accretion disk might produce gamma-ray emission, the disk is not always visible in radio galaxies, as for example in the case of M87.

11.6 Future

It is likely that more gamma-ray bright radio galaxies will be found as the sensitivity of the *Fermi*/LAT survey increases with on-going observations. This will allow for better understanding of this specific class. From the current sample it seems most likely that new gamma-ray bright galaxies will preferentially belong to the FR-I class. Also the ground-based observatories, such as CTA, will contribute to our understanding of radio galaxies, since several of these objects have been observed at TeV energies and with the next generation Cherenkov telescopes the coverage might reach down to energies as low as a few dozen GeV. This will help constrain the spectra at high energies.
Multi-wavelength observations, with the improved contribution to the hard X-ray band of new instruments such as *NuSTAR*, will help with the SED studies necessary to study the broad-band emission of radio galaxies. Improved angular resolution in this band will constrain the hard X-ray emission site(s), for example in nearby sources such as M87. A properly-sampled SED will help to disentangle jet emission and thermal core emission, and will allow us to discern between pure SSC and SSC with external Compton component.
The contribution of these sources to the isotropic gamma-ray background might be significant. Di Mauro et al. (2013) calculated a contribution up to 10%, derived from the gamma-ray luminosity function from the gamma-ray bright radio galaxies observed by *Fermi*/LAT up to now. Future studies can help understanding the origin of the isotropic background, and the role of radio galaxies.

PROCEEDINGS OF SCIENCE

Gamma-ray emitting radio galaxies at hard X-rays: Seyfert core or jet emission?

Volker Beckmann*, **Sandra de Jong, Fabio Mattana, Dounia Saez, & Simona Soldi**
François Arago Centre, APC, Université Paris Diderot, CNRS/IN2P3, CEA/Irfu, Observatoire de Paris, Sorbonne Paris Cité, 13 rue Watt, 75013 Paris, France
E-mail: beckmann@apc.univ-paris7.fr

A number of radio galaxies has been detected by Fermi/LAT in the gamma-ray domain. In some cases, like Cen A and M 87, these objects have been seen even in the TeV range by Cherenkov telescopes. Whereas the gamma-ray emission is likely to be connected with the non-thermal jet emission, dominating also the radio band, the situation is less clear at hard X-rays. While the smoothly curved continuum emission and the overall spectral energy distribution indicate a non-thermal emission, other features such as the iron line emission and the low variability appear to be rather of Seyfert type, i.e. created in the accretion disk and corona around the central black hole.

We investigate several prominent cases using combined X-ray and gamma-ray data in order to constrain the possible contributions of the jet and the accretion disk to the overall spectral energy distribution in radio galaxies. Among the three sources we study, three different origins of the hard X-ray flux can be identified. The emission can be purely non-thermal and caused by the jet, as in the case of M 87, or thermal inverse Compton emission from the Seyfert type core (Cen A), or appears to be a superposition of non-thermal and thermal inverse Compton emission, as we observe in 3C 111. Gamma-ray bright radio galaxies host all kinds of AGN cores, Seyfert 1 and 2, BL Lac objects, and also LINER.

"An INTEGRAL view of the high-energy sky (the first 10 years)" 9th INTEGRAL Workshop and celebration of the 10th anniversary of the launch,
October 15-19, 2012
Bibliotheque Nationale de France, Paris, France

*Speaker.

1. Introduction

Among the radio loud objects, radio galaxies present the cases where the central engine is hidden by circumnuclear mattter, but the object produces bright radio jets, sometimes with prominent extended lobes [1]. In order to be detectable as a radio galaxy, the jet angle with respect to the line of sight has to be large, i.e. $\gg 10^\circ$ because for smaller angles the object would appear as a blazar in which we assume to look right down the jet. The main emission component we see in the extended images of radio galaxies is produced by synchrotron emission of the charged particles interacting with the magnetic field of the jet. The inverse Compton component of radio galaxies is expected to appear rather as that of Seyfert galaxies. The emission should not be efficiently beamed toward the observer, as the jet is not pointing towards us, resulting in a component decreasing rapidly in the X-ray domain, with a high-energy cut-off in the range 50–200 keV.

One exception from this rule has been known since the observations of the *Compton Gamma-Ray Observatory* (*CGRO*) in the 1990s: Cen A was detected by *CGRO*/COMPTEL and EGRET up to $\sim 1\,\mathrm{GeV}$. With *Fermi*/LAT the number has increased and there are now more than a dozen gamma-ray bright radio galaxies known. Four radio galaxies, all of them of type FR-I, are detectable up to the TeV range (3C 66B, NGC 1275, M 87, Cen A). This raises the question, how the high photon energies $E \gg 100\,\mathrm{keV}$ are achieved in these cases, and what makes a radio galaxy gamma-ray bright [2]. For example, the apparently brightest extragalactic radio source, the FR-II Cygnus A is not a gamma-ray emitter, although it displays a hard X-ray flux of $f_{20-100\,\mathrm{keV}} = 8 \times 10^{-11}\,\mathrm{erg\,cm^{-2}\,s^{-1}}$ [3]. Gamma-ray loud radio galaxies are of further interest as they might be responsible for a large fraction of the cosmic background above 1 MeV [4].

In this work we use X-ray data and the overall spectral energy distribution (SED) to investigate the characteristics of 3 gamma-ray bright radio galaxies: Cen A, 3C 111, and M 87. In the X-rays we want to clarify whether the observed spectrum has thermal or non-thermal characteristics, i.e. whether it is produced by inverse Compton scattering close to the central engine in a electron plasma cloud (e.g. a hot corona on top of the accretion disk) or in a jet.

2. Centaurus A

Centaurus A is a FR-I radio galaxy that has been detected all the way from the radio domain up to the TeV region. Its brightness and small distance ($D = 3.8\,\mathrm{Mpc}$) makes it an ideal target to clarify in which energy bands the emission is thermal and where it appears to be dominated by non-thermal processes. The double hump structure of the SED with an apparently continuous inverse Compton emission from the X-rays to the TeV domain suggests that this emission is of non-thermal origin. Analysis of *CGRO* data shows that the emission from 50 keV up to 1 MeV is well represented by a double broken power-law model [5], which could be a simplification of the smoothly curved continuous inverse Compton emission of a blazar and therefore caused by the jet. One has to keep in mind though, that in the range $0.9 - 3\,\mathrm{MeV}$, the *CGRO* data provided only upper limits on the source flux. A transition from a thermal inverse Compton (IC) dominated process to a non-thermal component could therefore occur in this energy range and would have passed unnoticed.

In order to clarify the situation we performed an in-depth analysis of all the available *INTEGRAL* data [6]. The analysis of the 3–1000 keV data showed that the overall spectrum can be fit by a physical model of thermal Comptonisation (compPS) giving a plasma temperature of $kT_e = 206 \pm 62\,\mathrm{keV}$ within the optically thin corona with Compton parameter $y = 0.42^{+0.09}_{-0.06}$. A reflection component with a reflection strength $R = 0.12^{+0.09}_{-0.10}$ has been measured. Therefore, the data are consistent with $R = 0$ on the 1.9σ level, and a strength of $R > 0.3$ can be excluded on a 3σ level. Extending the cut-off power-law or the Comptonisation model to the gamma-ray range shows that they cannot account for the high-energy emission. On the other hand, a broken or curved power-law model can also represent the data, therefore a non-thermal origin of the X-ray to GeV emission could not be ruled out.

We then studied the extended, jet, and core emission in the 2–10 keV band as observed and resolved by *Chandra* (Fig. 1). Extrapolating the phenomenological models we fit to the core and jet spectra in the *Chandra* band to the 20–100 keV energy range covered by *INTEGRAL* IBIS/ISGRI, we find that the expected flux for the core emission of Cen A is $f_{20-100\,\mathrm{keV}} \simeq 6 \times 10^{-10}\,\mathrm{erg\,cm^{-2}\,s^{-1}}$, while the expected flux of the jet is about two orders of magnitude lower with $f_{20-100\,\mathrm{keV}} \simeq 7 \times 10^{-12}\,\mathrm{erg\,cm^{-2}\,s^{-1}}$. It turns out that the extrapolated core spectrum gives indeed the flux we measure in IBIS/ISGRI [6]. Thus, we can conclude that the emission in the hard X-ray band is still dominated by the Seyfert-type core and can be described as thermal inverse Compton process.

The transition to the non-thermal, jet dominated spectral energy distribution has then to take place somewhere between a few 100 keV and $\sim 10\,\mathrm{MeV}$. This underlines the need for a dedicated satellite mission in this up to now poorly explored energy range of $1 - 100\,\mathrm{MeV}$ [7].

3. 3C 111

3C 111 is a FR-II radio galaxy at redshift $z = 0.049$ ($D = 205 Mpc$), which displays a broad line region in the optical and iron Kα emission in the X-rays, similar to Seyfert galaxies. The radio jet has an angle of 18° to the line of sight. This object has been first detected by *Fermi*/LAT in the gamma-rays, with a photon index of $\Gamma = 2.4 \pm 0.2$ in the range $0.1 - 200\,\mathrm{GeV}$ and a flux of $f \simeq 10^{-8}\,\mathrm{ph\,cm^{-2}\,s^{-1}}$ [8]. This low flux level allows only for a low significant detection of $\sim 3\sigma$. In both, the soft and the hard X-rays, the source is fainter than Cen A, with $f_{20-200\,\mathrm{keV}} \simeq 10^{-10}\,\mathrm{erg\,cm^{-2}\,s^{-1}}$.

In order to determine whether the (hard) X-ray data are dominated by non-thermal or thermal emission, we analysed combined *Suzaku* XIS and PIN, *Swift*/BAT, and *INTEGRAL* IBIS/ISGRI data. The overall spectrum in the $0.4 - 200\,\mathrm{keV}$ band shows an absorbed exponential cut-off power-law with reflection from neutral material with a photon index $\Gamma = 1.68 \pm 0.03$, a high-energy cut-off at $E_{\mathrm{cut}} = 230^{+140}_{-70}\,\mathrm{keV}$, a reflection component with $R = 0.7 \pm 0.3$ and an iron Kα line with an equivalent width of $EW = 85 \pm 11\,\mathrm{eV}$ [8]. Thus, in the case of 3C 111 we see indication for both, thermal and non-thermal inverse Compton emission in the X-rays. The measured high-energy cut-off can occur in a thermal IC emission, or can be the signature of a smoothly curved hard X-ray spectrum. The iron line and the Compton reflection hump are clear indications for a thermal IC process, but at the same time the iron line is rather weak compared to the continuum emission and the overall spectral energy distribution can be fit by a one-zone synchrotron self-Compton model as typical for blazars. This seems to suggest that although there is compelling evidence for Seyfert-

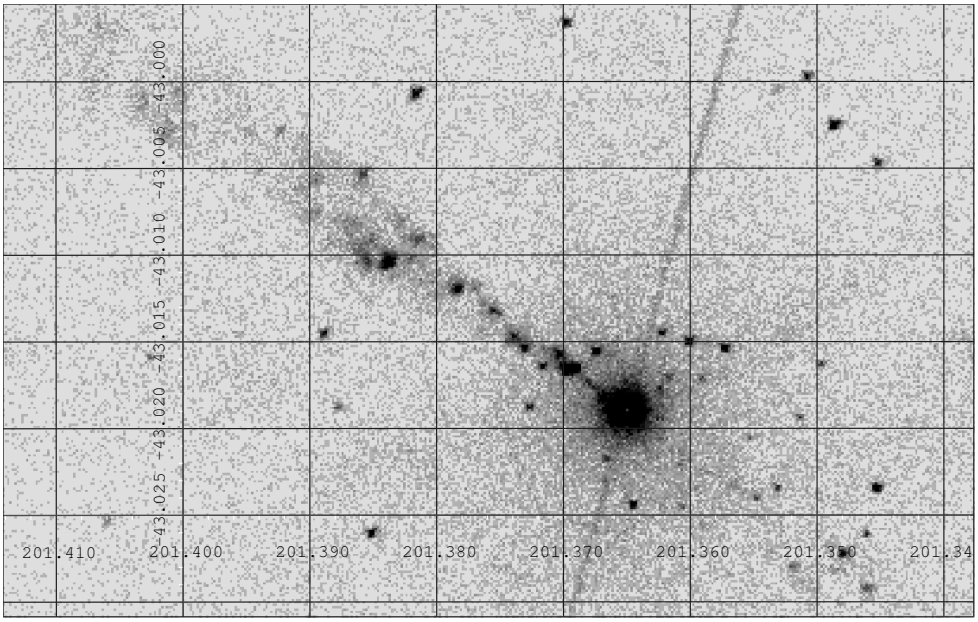

Figure 1: *Chandra*/ACIS-I image of Centaurus A based on a 98 ksec exposure taken in May 2007. The core, which is piled-up in this image, shows a 100 times higher flux level than the combined extended and jet emission (including the hot spots). For comparison: in M 87, which is another gamma-ray detected radio galaxy, the jet emits about 4 times as much as the core in the 2–10 keV band [10].

like emission from 3C 111, the X-rays are most likely also influenced by non-thermal jet emission. This is further supported by the fact that the equivalent width of the iron line and the continuum emission are variable, and we observe a highly-significant anti-correlation between the equivalent width and the continuum flux. It seems, that the variations of the underlying continuum by a factor of ~ 4 are driven by the variable non-thermal emission, while the Seyfert core remains persistent.

Thus, for 3C 111 we conclude that the X-rays show contribution of both, non-thermal jet emission and thermal inverse Compton emission similar to that in Seyfert galaxies. Also here, like in the other radio galaxies, we assume that the gamma-ray emission can be entirely attributed to jet emission, because the thermal IC component with its exponential cut-off in the hard X-rays will not contribute significantly beyond $\simeq 500\,\mathrm{keV}$.

4. M 87

The third radio galaxy we studied in this work is the FR-I M 87 at a distance of $D = 16\,\mathrm{Mpc}$. In this case, similar as for Cen A, the different components can be resolved in the optical and X-ray regime. The jet of M 87 has an angle to the line of sight of 30°, and several knots can be distinguished in the X-rays based on Chandra data [9]. The source is detectable up to the TeV range, but so far has escaped detection in the hard X-rays above 10 keV, with a 3σ upper limit of $f < 3 \times 10^{-12}\,\mathrm{erg\,cm^{-2}\,s^{-1}}$ [10]. Different than in the case of Cen A and 3C 111, this source shows a dominance of the jet over the core emission in the 2–10 keV band: the jet emission is on

	FR type	jet angle	core type	$f_{>100\,\mathrm{MeV}}$ $[\mathrm{ph\,cm^{-2}\,s^{-1}}]$	$f_{20-60\,\mathrm{keV}}$ $[\mathrm{erg\,cm^{-2}\,s^{-1}}]$	X-rays
M 87	FR-I	30°	LINER	2.4×10^{-8}	$<3\times10^{-12}$	jet
Cen A	FR-I	$50^\circ-80^\circ$	Seyfert 1.5	2.1×10^{-7}	6×10^{-10}	core
3C 111	FR-II	18°	Seyfert 1	4×10^{-8}	8.5×10^{-11}	core+jet

Table 1: Selected parameters of the three gamma-ray bright radio galaxies studied here.

average about a factor of 4 brighter than the core. This ratio depends on the time of observation, as the jet emission is highly variable. In addition, there is no iron Kα emission detectable from the core. Studying the hard X-ray light curve as derived from 1.7 Msec effective on-source observation with *INTEGRAL* IBIS/ISGRI, there is no detection achievable in the hard X-rays at any given time. The overall spectral energy distribution can be modeled, like in the case of 3C 111, by a one-zone synchrotron self-Compton model with parameters typical for high-frequency peaked BL Lac object.

Further investigations on the nature of the SED and the possibility to detect M 87 at hard X-rays are performed and will be presented soon (de Jong et al. 2013, in preparation). But the picture which emerges for M 87 is that of a radio galaxy with no sign of Seyfert-type activity in the core detectable in X-rays, with this energy range entirely dominated by non-thermal emission. Considering that the core has been classified as that of a LINER in the optical domain [11], the lack of strong thermal inverse Compton emission in the X-rays can be expected because of the low power output of the central engine, and LINER are also known for not displaying an iron Kα line [12]. In summary, it seems that the X-ray emission of M 87 is dominated by non-thermal inverse Compton emission arising from the jet.

5. Fermi/LAT detected radio galaxies in the X-rays

Although we have investigated only three particular cases, already in this small sample we find three different types of X-ray emission in gamma-ray bright radio galaxies. The hard X-rays are either dominated by non-thermal emission from the jet (M 87; FR-I), by thermal inverse Compton emission arising from the Seyfert type core (Cen A; FR-I), or a composite of core and jet emission is visible in this band (3C 111; FR-II). Summarizing some of the parameters of interest in Table 1, it might be that the core dominance in the X-rays in the case of Cen A can be attributed to the large jet angle with respect to the line of sight. The fact that the thermal inverse Compton component is not visible in the case of M 87 could be caused by the relatively weak AGN core.

Three objects are not sufficient in order to draw any firm conclusions here. In a next step we will investigate the hard X-ray spectra of other gamma-ray detected radio galaxies, in order to see whether a trend emerges in which certain physical parameters of the objects determine the gamma-ray brightness. Already a glance at the optical core classification of these galaxies seems to indicate that the type of AGN at the center does not give a hint whether or not a radio galaxy can become gamma-ray bright. Radio quiet AGN do not seem to be significant gamma-ray emitters [13]. For example, among 491 *Swift*/BAT detected Seyfert galaxies, only NGC 4945 and NGC 1068 were detected by *Fermi*/BAT, and in these cases the star burst component in the host galaxy is likely

to be the origin of the high-energy emission [14]. Among the *Fermi*/LAT detected radio galaxies, there are cores with BL Lac spectra (IC 310), of type Seyfert 2 (NGC 1275, NGC 6251), Seyfert 1.5 (3C 380.0, Cen A), Seyfert 1.2 (3C 207.0), Seyfert 1 (3C 111), several LINER (Fornax A, OH -342, M 87), and even an apparently optically non-active elliptical galaxy (Cen B). Gamma-ray bright radio galaxies are also observed in a large redshift range, from Cen A at a distance of $D = 3.8\,\mathrm{Mpc}$ out to $2,400\,\mathrm{Mpc}$ ($z = 0.68$) in the case of 3C 207.0, and thus we observe objects which are very different in terms of luminosity.

Acknowledgements: This work has been supported by the LabEx UnivEarthS[1] project "Impact of black holes on their environment". We thank the anonymous referee for the constructive comments which helped to improve this paper.

References

[1] Beckmann, V. & Shrader, C. R. 2012, "Active Galactic Nuclei", Wiley-VCH, Berlin, 380 pages, ISBN-13: 978-3527410781

[2] Rieger, F. M. 2012, American Institute of Physics Conference Series, 1505, 80

[3] Beckmann, V., Soldi, S., Ricci, C., et al. 2009, A&A, 505, 417

[4] Inoue, Y. 2011, ApJ, 733, 66

[5] Steinle, H., Bennett, K., Bloemen, H., et al. 1998, A&A, 330, 97

[6] Beckmann, V., Jean, P., Lubiński, P., Soldi, S., & Terrier, R. 2011, A&A, 531, A70

[7] Lebrun, F., Aharonian, F., Beckmann, V., et al. 2010, 8th Integral Workshop "The Restless Gamma-ray Universe", PoS, 115, 34

[8] de Jong, S., Beckmann, V., & Mattana, F. 2012, A&A, 545, A90

[9] Wilson, A. S., & Yang, Y. 2002, ApJ, 568, 133

[10] de Jong, S., Beckmann, V., Soldi, S., Zurita Heras, J. A., & Mattana, F. 2013, PoS(INTEGRAL2012), 70

[11] Sabra, B. M., Shields, J. C., Ho, L. C., Barth, A. J., & Filippenko, A. V. 2003, ApJ, 584, 164

[12] Younes, G., Porquet, D., Sabra, B., & Reeves, J. N. 2011, A&A, 530, A149

[13] Ackermann, M., et al. 2012, ApJ, 747, 104

[14] Teng, S. H., Mushotzky, R. F., Sambruna, R. M., et al. 2012, ApJ, 742, 66

[1] http://www.univearths.fr/en

12 Conclusions

In this work we have studied AGN and the properties of gamma-ray bright radio galaxies in particular. In the case of blazars the relativistic jet is pointed towards the observer, Doppler-boosting the emission. This provides a straight-forward explanation for the high luminosity and the observed emission in the gamma-ray and TeV band for this class of objects. Since radio galaxies are observed with an angle of $> 10°$ to the line of sight, the gamma-ray emission is not easily explained. In order to understand the origin of the gamma-ray emission, we have analysed X-ray and gamma-ray data of two gamma-ray bright radio galaxies, 3C 111 and M87. These sources, though both radio galaxies, show different behaviour in the high-energy branch.

3C 111 ($z = 0.049$) belongs to the FR-II type radio galaxies, which have large extended jets. We analysed data from several instruments: *Suzaku*/XIS and PIN, *INTEGRAL*/ISGRI and *Swift*/BAT to create an X-ray spectrum between 0.4–200 keV. The spectrum could be fit best with an absorbed (column density $N_{\rm H} = (9.0 \pm 0.2) \times 10^{21}\,{\rm cm}^{-2}$), power law with index $\Gamma = 1.68 \pm 0.03$, and a cut-off at $E_{\rm cut} = 230^{+140}_{-70}\,{\rm keV}$, a reflection component $R = 0.7 \pm 0.3$ and a Gaussian profile for the redshifted iron K-α line at $E_{\rm line} = 6.11 \pm 0.02\,{\rm keV}$ with an equivalent width $EW = 85 \pm 11\,{\rm eV}$. The reflection and iron line are Seyfert-like, thermal features, originating near the central black hole. The X-ray spectrum is a mixture of core and jet emission, due to the large distance to 3C 111 the different components can not be distinguished. In the *Fermi*/LAT band this source has shown variability (Kataoka et al. 2011). From analysing *Fermi*/LAT data, we found that 3C 111 has a low > 100 MeV flux of $f = (6 \pm 2) \times 10^{-12}\,{\rm erg\,cm^{-2}\,s^{-1}}$. We combined the X-ray spectrum and *Fermi*/LAT observations to build a spectral energy distribution (SED). The SED of 3C 111 can be represented by a synchrotron self-Compton (SSC) model, showing that the broad-band emission of the source is rather originating in the jet. This implies that for 3C 111 that the jet emission contributes to all wavebands. In the radio domain the jet emission is dominant, but in the optical and X-ray band signatures of thermal processes have been observed (de Jong et al. 2012b).

The second source we studied in great detail is the nearby FR-I galaxy M87 ($z = 0.0044$). FR-I radio galaxies have weaker jets compared to FR-II sources. In the case of M87 we have analysed ~ 5.1 Ms of *INTEGRAL* IBIS/ISGRI observations. Using the standard analysis produced an image that was dominated by noise patterns. Investigating and developing several additional techniques, such as science window (scw, a pointing) selection and noise reduction through specific treatment of the ISGRI shadowgrams before their deconvolution, we were able to extract a 3σ upper limit to the hard X-ray flux of M87 between 20–60 keV of $f \lesssim 3 \times 10^{-12}\,{\rm erg\,cm^{-2}\,s^{-1}}$. Using a *Suzaku*/PIN observation, taken end of November 2006, we were able to detect M87 for the first time in the hard band with a flux of $f = 1.3 \times 10^{-11}\,{\rm erg\,cm^{-2}\,s^{-1}}$ between 20–60 keV. This indicates significant variability in the hard X-ray band.

We have also analysed *INTEGRAL*/JEM-X data. Due to the imaging resolution of the instrument of ~ 3 arcmin, the observed flux of $f_{3-10\,\mathrm{keV}} = (1.6 \pm 0.2) \times 10^{-11}\,\mathrm{erg\,cm^{-2}\,s^{-1}}$ is a superposition of the core and the extended emission. By subtracting the flux of the jet, estimated from the flux of the individual jet knots (Wilson & Yang 2002; Perlman & Wilson 2005), and the flux of the extended emission by using *Chandra*/ACIS observations, we determined the 3–10 keV core flux of $f_{\mathrm{core}} \simeq 6 \times 10^{-12}\,\mathrm{erg\,cm^{-2}\,s^{-1}}$. We also analysed the *Fermi*/LAT data of this source, which is detected with a significance of 19σ, and a > 100 MeV photon flux of $f = (2.2 \pm 0.3) \times 10^{-8}\,\mathrm{ph\,cm^{-2}\,s^{-1}}$.
For this source we created two spectral energy distributions: an average state SED using the upper limit in the hard X-rays based on the *INTEGRAL* observations and a high-state SED considering the *Suzaku*/PIN detection. In both cases the SED can be well represented by an SSC model, with a difference of the magnetic field B and of the properties of the relativistic electron population. The SED parameters of M87 are consistent with those of a weak BL Lac object and the radiatively inefficient accretion flow expected for BL Lac objects.

The sample of gamma-ray bright radio galaxies is small, containing so far only 15 sources. Therefore population studies can derive only limited insight into this class of objects. In the case of 3C 111 thermal processes from the core are observed in X-rays, whereas for M87 the emission in X-rays is jet-based. We have concluded that the gamma-ray brightness is not solely dependent on proximity, but that these sources are rather a separate class of radio galaxies. The gamma-ray emission is likely to be produced in the jet, near the central compact object, similar as in the common model assumed for blazars. Then, this inner jet emission can be observed, even if the jet angle is large, for example due to reflection or because of a wide opening angle of the jet.
To fully understand the gamma-ray origin of these sources, a larger sample of radio galaxies, both gamma-ray bright and non-gamma-ray bright, should be studied in the X-ray and gamma-ray band. In the X-ray band, both the thermal contribution of the core and the non-thermal jet contribution can be observed. Using the new generation of X-ray instruments, such as *NuSTAR* and *ASTRO-H* will help with their superior angular and spectral resolution and through their high sensitivity. Using simultaneous multi-wavelength observations, SEDs can be created to study the broad-band emission of these sources. We found that M87 has shown a flare in 2006, and it is possible that other radio galaxies also display this type of variable behaviour. For 3C 111 we found the SED could be properly modelled with a SSC model. Using properly sampled SEDs it is possible to test if the gamma-ray bright FR-II galaxies can be properly represented with only SSC or if there is an external Compton component necessary. This is a test for the AGN unification scheme, which connects radio galaxies to blazars, where the FR-II sources are connected to FSRQ. To model the SED of FSRQs an external Compton component is necessary to properly represent the data.
Lastly, the addition of TeV data is important for this study, since several sources in this sample have been observed in the TeV band already. Using for example HESS or CTA, both detections and flux upper limits can help to understand the emission from these radio galaxies by constraining the inverse Compton branch.

In addition to this, we have documented the first X-ray detection using *Swift*/XRT of two sources in the error circle of the *Fermi*/LAT detected source 2FGL J1551.9+0855: the Seyfert 1 galaxy LSBC F727–V01 ($z = 0.071$) and the blazar BZB J1552+0850 ($z > 1.015$) (de Jong et al. 2012a). We analysed the *INTEGRAL* IBIS/ISGRI observations, for which we

had successfully applied for, and simultaneous *Swift*/XRT and UVOT data, also requested per proposal. Due to the low exposure within IBIS/ISGRI, the sources were not detected in the hard X-ray band. Even though both sources are located within the error circle of 2FGL J1551.9+0855, it is the BL Lac BZB J1552+0850 which is likely to be the counter part of the gamma-ray source, since Seyfert 1 galaxies do not emit gamma-rays. Massaro et al. (2012) did an infrared follow-up on LSBC F727–V01 and BZB J1552+0850, and found that the behaviour of LSBC F727–V01 in the infrared did not match that of gamma-ray emitting sources, confirming BZB J1552+0850 as the counterpart of 2FGL J1551.9+0855.
Due to the large positional error on many gamma-ray detected sources, often several potential counter parts exist. Here, multi-wavelength observations are a useful tool to find the proper counter parts of the *Fermi*/LAT detected sources.

13 Appendix

13.1 Parabola calculation

A parabola can be completely defined using 3 points. Given these three points $[x_i, y_i]; i = [1..3]$, the parameters for a parabola $y = a \cdot x^2 + b \cdot x + c$ are :

$$a = \frac{y_3 - y_1 - \frac{y_2 - y_1}{x_2 - x_1} \cdot x_3 + x_1 \cdot \frac{y_2 - y_1}{x_2 - x_1}}{((x_3^2 + x_1^2 \cdot \frac{x_3}{x_2 - x_1} - x_2^2 \cdot \frac{x_3}{x_2 - x_1} - x_1^2) - x_1^3) \cdot (x_2 - x_1)} + \frac{x_1 \cdot x_2^2}{x_2 - x_1} \tag{13.1}$$

$$b = \frac{y_2 - y_1 + a \cdot x_1^2 - a \cdot x_2^2}{x_2 - x_1} \tag{13.2}$$

$$c = y_1 - a \cdot x_1^2 - b \cdot x_1 \tag{13.3}$$

And the peak of the parabola occurs at the point x_{peak}:

$$x_{peak} = \frac{-b}{2a} \tag{13.4}$$

with a peak value

$$y_{peak} = \frac{a \cdot b^2}{4} - \frac{b^2}{2a} + c \tag{13.5}$$

13.2 Spearman rank test

To evaluate a possible correlation between two variables, the Spearman rank test can be used. This estimates how well the relationship between the variables can be described using a monotonic function (a function between ordered sets that preserves the order).

Assuming n observed pairs with parameters $[X_i, Y_i]_{i=1..n}$, the hypothesis H_0 is tested, if the two parameters are *not* correlated. The Pearsons correlation-coefficient r_{XY}, a measure of linear correlation between two variables X and Y, can be used for this test. This gives a value between $[-1; +1]$, where 1 is a total positive correlation, 0 means no correlation, and -1 is a negative correlation. Assuming that X and Y are normal distributed then r_{XY} can be used to test if X and Y are independent. If the (unknown) correlation coefficient $\rho = 0$ then

$$t = \frac{r_{XY} \cdot \sqrt{n-2}}{\sqrt{1 - {r_{XY}}^2}} \tag{13.6}$$

is the realization of a t-distributed random variable with $n - 2$ degrees of freedom. The t-distribution, also called Students distribution, is tabulated for different n and t values. This results in a significance level on which the assumption that X and Y are uncorrelated can be rejected.

14 Publications

- de Jong, Beckmann & Mattana, "The non-thermal core of 3C 111", PoS(Extremesky2011) 076

- Walter, Bordas, Bozzo, Beckmann, de Jong & Panessa, "IGRJ 12580+0134, a flaring Seyfert 2 galaxy", ATel 3108 (2011)

- Soldi, Beckmann, Gehrels, de Jong & Lubiński, "High-energy emission from NGC 5506, the brightest hard X-ray Narrow Line Seyfert 1 galaxy', PoS(NLS12011), 063

- de Jong, Beckmann & Mattana, "The nature of the multi-wavelength emission of 3C 111", A&A. 545, 90, 2012

- de Jong, Beckmann, Kennea, Soldi, Shrader & Gehrels, "Detection of two X-ray sources in the error circle of the Fermi/LAT source 2FGL J1551.9+0855", ATel 4551 (2012)

- de Jong, Beckmann, Soldi, Zurita Heras & Mattana, "M87 in hard X-rays: an INTEGRAL view", PoS(INTEGRAL workshop 2012)

- Beckmann, de Jong, Mattana, Soldi & Saez, "Gamma-ray emitting radio galaxies at hard X-rays: Seyfert core or jet emission", PoS(INTEGRAL workshop 2012)058

- de Jong, Beckmann, Soldi & Tramacere, "High-energy emission processes in M87", in prep. (2013)

- Prokhorov & de Jong, "A morphological analysis for searches of possible extended gamma-ray emission sources associated with dark matter annihilation", in prep. (2013)

15 Accepted proposals

- 2010, 2011, INTEGRAL data rights on three Fermi-detected sources, PI (de Jong, Beckmann, Soldi, Shrader& Gehrels)

- 2010, 2011, INTEGRAL data rights on M87, Co-I (Beckmann, de Jong, Soldi, Shrader & Gehrels)

- 2012, Swift TOO on 2FGL J1551.9+0855, as addition to the INTEGRAL data rights on the observations of the three Fermi-detected sources PI

- 2011, INTEGRAL data rights on NGC 5506 Co-I (Soldi, Beckmann, de Jong, Gehrels & Lubiński)

- 2012, INTEGRAL data rights on NGC 2110 Co-I (Beckmann, de Jong, Gehrels, Lubiński & Soldi)

- 2012, INTEGRAL data rights on GRS 1734-292 Co-I (Beckmann, de Jong, Gehrels, Lubiński & Soldi)

- 2013, INTEGRAL Target-of-Opportunity proposal on NGC 2110, Co-I (Beckmann, de Jong, Gehrels, Lubiński, Petrucci, Ricci, Shrader & Soldi)

16 Conference presentations

- de Jong, Beckmann & Mattana, "The non-thermal core of 3C 111", The X-ray Universe, 27-30 June 2011, Berlin, Germany (poster presentation)

- de Jong, Beckmann & Mattana, "The non-thermal core of 3C 111", The Extreme and Variable High Energy Sky, 19-23 September 2011, Chia Laguna (Cagliari) Italy (poster presentation and proceedings)

- de Jong, Beckmann & Mattana, "The non-thermal core of radio galaxy 3C 111", 29 November-2 December 2011, Elbereth, Paris, France (oral presentation)

- de Jong, Beckmann & Mattana, "The hybrid AGN core of 3C 111", 29 May-8 June 2012, Fermi Summer School, Lewes, USA (oral presentation)

- Saez, de Jong & Beckmann, "Jet versus core of Cen A in *Chandra* X-ray data", 14–22 July, 2012, 39th COSPAR Assembly, 2012, Mysore, India (poster presentation)

- Beckmann, de Jong, Li Cavoli, et al., "Gamma-ray emitting radio galaxies: Seyfert core or jet emission", 14–22 July, 2012, 39th COSPAR Assembly, 2012, Mysore, India (oral presentation)

- de Jong, Beckmann, Soldi, Zurita Heras & Mattana, "M87 in hard X-rays: an INTEGRAL view", 15-19 October 2012, 9th INTEGRAL workshop, Paris, France (poster presentation and proceedings)

- de Jong, Beckmann, Soldi, Zurita Heras & Mattana, "M87 in hard X-rays", 11-14 December 2012, Elbereth, Paris, France (oral presentation)

- de Jong, Beckmann, Tramacere, Soldi, "M87 in hard X-rays", 29 April-8 May 2013, School for Cosmic Accelerators, Cargèse, Corsica, (oral presentation)

List of Figures

List of Tables

Bibliography

Abazajian, K., Adelman-McCarthy, J. K., Agüeros, M. A., et al. 2003, AJ, 126, 2081

Abdo, A. A., Ackermann, M., Atwood, W. B., et al. 2008, Science, 322, 1218

Abdo, A. A., Ackermann, M., Ajello, M., et al. 2009a, ApJS, 183, 46

Abdo, A. A., Ackermann, M., Ajello, M., et al. 2009b, ApJ, 700, 597

Abdo, A. A., Ackermann, M., Ajello, M., et al. 2009c, ApJ, 707, 55

Abdo, A. A., Ackermann, M., Ajello, M., et al. 2010a, ApJS, 188, 405

Abdo, A. A., Ackermann, M., Ajello, M., et al. 2010b, ApJS, 187, 460

Abdo, A. A., Ackermann, M., Ajello, M., et al. 2010c, ApJ, 719, 1433

Abdo, A. A., Ackermann, M., Ajello, M., et al. 2010d, Science, 328, 725

Abdo, A. A., Ackermann, M., Ajello, M., et al. 2010e, ApJ, 720, 912

Abdo, A. A., Ackermann, M., Ajello, M., et al. 2010f, ApJ, 714, L73

Abdo, A. A., Ackermann, M., Antolini, E., et al. 2010g, ApJ, 715, 429

Abdo, A. A., Ackermann, M., Ajello, M., et al. 2011, ApJ, 736, 131

Abramowski, A., Acero, F., Aharonian, F., et al. 2012, ApJ, 746, 151

Ackermann, M., Ajello, M., Allafort, A., et al. 2011a, ApJ, 743, 171

Ackermann, M., Ajello, M., Allafort, A., et al. 2011b, ApJ, 743, 171

Ackermann, M., Ajello, M., Allafort, A., et al. 2012a, ApJ, 747, 104

Ackermann, M., Ajello, M., Allafort, A., et al. 2012b, ApJ, 755, 164

Ackermann, M., Albert, A., Baldini, L., et al. 2012c, ApJ, 747, 121

Aharonian, F., Akhperjanian, A., Beilicke, M., et al. 2003, A&A, 403, L1

Aharonian, F., Akhperjanian, A. G., Bazer-Bachi, A. R., et al. 2006, Science, 314, 1424

Ajello, M., Costamante, L., Sambruna, R. M., et al. 2009, ApJ, 699, 603

Anderson, S. F., Margon, B., Voges, W., et al. 2007, AJ, 133, 313

Antón, S., Browne, I. W. A., Marchã, M. J. M., Bondi, M., & Polatidis, A. 2004, MNRAS, 352, 673

Antonucci, R. R. J. & Miller, J. S. 1985, ApJ, 297, 621

Antonucci, R. 1993, ARA&A, 31, 473

Arnaud, K. A. 1996, in Astronomical Society of the Pacific Conference Series, Vol. 101, Astronomical Data Analysis Software and Systems V, ed. G. H. Jacoby & J. Barnes, 17

Atwood, W. B., Abdo, A. A., Ackermann, M., et al. 2009, ApJ, 697, 1071

Babcock, H. W. 1939, Lick Observatory Bulletin, 19, 41

Baldwin, J. A. 1977, ApJ, 214, 679

Balick, B. & Brown, R. L. 1974, ApJ, 194, 265

Ballet, J. 2001, in Astronomical Society of the Pacific Conference Series, Vol. 238, Astronomical Data Analysis Software and Systems X, ed. F. R. Harnden, Jr., F. A. Primini, & H. E. Payne, 381

Ballo, L., Braito, V., Reeves, J. N., Sambruna, R. M., & Tombesi, F. 2011, MNRAS, 418, 2367

Barr, P., Mushotzky, R., Giommi, P., Clavel, J., & Wamsteker, W. 1986, in IAU Symposium, Vol. 119, Quasars, ed. G. Swarup & V. K. Kapahi, 269

Barthelmy, S. D., Barbier, L. M., Cummings, J. R., et al. 2005, Space Sci. Rev., 120, 143

Baumgartner, W. H., Tueller, J., Markwardt, C., & Skinner, G. 2010, in Bulletin of the American Astronomical Society, Vol. 42, AAS/High Energy Astrophysics Division #11, 675

Baumgartner, W. H., Tueller, J., Markwardt, C. B., et al. 2013, ApJS, 207, 19

Beckmann, V., Bade, N., & Wucknitz, O. 1999, A&A, 352, 395

Beckmann, V., Barthelmy, S. D., Courvoisier, T. J.-L., et al. 2007, A&A, 475, 827

Beckmann, V., Soldi, S., Ricci, C., et al. 2009, A&A, 505, 417

Beckmann, V., Jean, P., Lubiński, P., Soldi, S., & Terrier, R. 2011, A&A, 531, A70

Beckmann, V. & Shrader, C. R. 2012, Active Galactic Nuclei (Wiley-VCH)

Beckmann, V., De Jong, S., Mattana, F., Saez, D., & Soldi, S. 2012, in Proceedings of "An INTEGRAL view of the high-energy sky (the first 10 years)" - 9th INTEGRAL Workshop and celebration of the 10th anniversary of the launch (INTEGRAL 2012). 15-19 October 2012. Bibliotheque Nationale de France, Paris, France.

Berger, K. 2011, in International Cosmic Ray Conference, Vol. 8, International Cosmic Ray Conference, 153

Bicknell, G. V. & Begelman, M. C. 1996, ApJ, 467, 597

Bignami, G. F., Boella, G., Burger, J. J., et al. 1975, Space Science Instrumentation, 1, 245

Bird, A. J., Bazzano, A., Bassani, L., et al. 2010, ApJS, 186, 1

Blandford, R. D. & Payne, D. G. 1982, MNRAS, 199, 883

Blandford, R. D. & Znajek, R. L. 1977, MNRAS, 179, 433

Błażejowski, M., Blaylock, G., Bond, I. H., et al. 2005, ApJ, 630, 130

Boella, G., Butler, R. C., Perola, G. C., et al. 1997, A&AS, 122, 299

Boldt, E. 1987, in IAU Symposium, Vol. 124, Observational Cosmology, ed. A. Hewitt, G. Burbidge, & L. Z. Fang, 611–615

Bondi, M., Marchã, M. J. M., Dallacasa, D., & Stanghellini, C. 2001, MNRAS, 325, 1109

Bridle, A. H. & Perley, R. A. 1984, ARA&A, 22, 319

Bridle, A. H., Hough, D. H., Lonsdale, C. J., Burns, J. O., & Laing, R. A. 1994, AJ, 108, 766

Brown, A. M. & Adams, J. 2012, MNRAS, 421, 2303

Burrows, D. N., Hill, J. E., Nousek, J. A., et al. 2005, Space Sci. Rev., 120, 165

Caballero, I., Zurita Heras, J. A., Mattana, F., et al. 2012, in Proceedings of "An INTEGRAL view of the high-energy sky (the first 10 years)" - 9th INTEGRAL Workshop and celebration of the 10th anniversary of the launch (INTEGRAL 2012). 15-19 October 2012. Bibliotheque Nationale de France, Paris, France.

Capetti, A., Kharb, P., Axon, D. J., Merritt, D., & Baldi, R. D. 2009, AJ, 138, 1990

Caroli, E., Stephen, J. B., Di Cocco, G., Natalucci, L., & Spizzichino, A. 1987, Space Sci. Rev., 45, 349

Chatterjee, R., Marscher, A. P., Jorstad, S. G., et al. 2011, ApJ, 734, 43

Chatterjee, R., Bailyn, C. D., Bonning, E. W., et al. 2012, ApJ, 749, 191

Chaty, S. 2005, in Proceedings of Rencontres de Moriond, Very High Energy Phenomena in the Universe, La Thuile, Italy (March 12-19, 2005).

Chávez, R., Terlevich, E., Terlevich, R., et al. 2012, MNRAS, 425, L56

Clavel, J., Reichert, G. A., Alloin, D., et al. 1991, ApJ, 366, 64

Combes, F. 2001, in Advanced Lectures on the Starburst-AGN, ed. I. Aretxaga, D. Kunth, & R. Mújica, 223

Courvoisier, T. J.-L., Walter, R., Beckmann, V., et al. 2003, A&A, 411, L53

Courvoisier, T. J.-L. & Türler, M. 2005, A&A, 444, 417

Courvoisier, T. J.-L. 2013a, in Proceedings of "An INTEGRAL view of the high-energy sky (the first 10 years)" - 9th INTEGRAL Workshop and celebration of the 10th anniversary of the launch (INTEGRAL 2012). 15-19 October 2012. Bibliotheque Nationale de France, Paris, France.

Courvoisier, T. J.-L. 2013b, High Energy Astrophysics (Springer-Verlag Berlin Heidelberg)

D'Abrusco, R., Massaro, F., Ajello, M., et al. 2012, ApJ, 748, 68

Dadina, M. 2007, A&A, 461, 1209

Dadina, M. 2008, A&A, 485, 417

de Jong, S., Beckmann, V., & Mattana, F. 2011, in Extreme and Variable High Energy Sky (Extremesky 2011)

de Jong, S., Beckmann, V., Kennea, J., et al. 2012a, The Astronomer's Telegram, 4551, 1

de Jong, S., Beckmann, V., & Mattana, F. 2012b, A&A, 545, A90

de Jong, S., Beckmann, V., Soldi, S., Zurita Heras, J. A., & Mattana, F. 2012c, in Proceedings of "An INTEGRAL view of the high-energy sky (the first 10 years)" - 9th INTEGRAL Workshop and celebration of the 10th anniversary of the launch (INTEGRAL 2012). 15-19 October 2012. Bibliotheque Nationale de France, Paris, France.

Detmers, R. G., Kaastra, J. S., & McHardy, I. M. 2009, A&A, 504, 409

Di Mauro, M., Calore, F., Donato, F., Ajello, M., & Latronico, L. 2013, ArXiv e-prints

Doeleman, S. S., Fish, V. L., Schenck, D. E., et al. 2012, Science, 338, 355

Dotson, A., Georganopoulos, M., Kazanas, D., & Perlman, E. S. 2012, ApJ, 758, L15

Eckart, A. & Genzel, R. 1997, MNRAS, 284, 576

Edge, D. O., Shakeshaft, J. R., McAdam, W. B., Baldwin, J. E., & Archer, S. 1959, MmRAS, 68, 37

Edsjö, J. & Gondolo, P. 1995, Physics Letters B, 357, 595

Ekers, J. A. 1969, Australian Journal of Physics Astrophysical Supplement, 7, 3

Elitzur, M. & Shlosman, I. 2006, ApJ, 648, L101

Eracleous, M., Sambruna, R., & Mushotzky, R. F. 2000, ApJ, 537, 654

Fabian, A. C., Iwasawa, K., Reynolds, C. S., & Young, A. J. 2000, PASP, 112, 1145

Falceta-Gonçalves, D., Caproni, A., Abraham, Z., Teixeira, D. M., & de Gouveia Dal Pino, E. M. 2010, ApJ, 713, L74

Fanaroff, B. L. & Riley, J. M. 1974, MNRAS, 167, 31P

Feenberg, E. & Primakoff, H. 1948, Physical Review, 73, 449

Ferrarese, L., Mould, J. R., Stetson, P. B., et al. 2007, ApJ, 654, 186

Finke, J. D. 2013, ApJ, 763, 134

Forman, W., Jones, C., Cominsky, L., et al. 1978, ApJS, 38, 357

Foschini, L., Ghisellini, G., Tavecchio, F., Bonnoli, G., & Stamerra, A. 2011, A&A, 530, A77

Fossati, G., Maraschi, L., Celotti, A., Comastri, A., & Ghisellini, G. 1998, MNRAS, 299, 433

Frontera, F., Costa, E., dal Fiume, D., et al. 1997, A&AS, 122, 357

Gammie, C. F., Shapiro, S. L., & McKinney, J. C. 2004, ApJ, 602, 312

Gebhardt, K. & Thomas, J. 2009, ApJ, 700, 1690

Gehrels, N., Chincarini, G., Giommi, P., et al. 2004, ApJ, 611, 1005

Ghez, A. M., Klein, B. L., Morris, M., & Becklin, E. E. 1998, ApJ, 509, 678

Ghez, A. M., Salim, S., Weinberg, N. N., et al. 2008, ApJ, 689, 1044

Ghisellini, G., Celotti, A., Fossati, G., Maraschi, L., & Comastri, A. 1998, MNRAS, 301, 451

Ghisellini, G. & Tavecchio, F. 2008, MNRAS, 387, 1669

Ghisellini, G. & Tavecchio, F. 2009, MNRAS, 397, 985

Giacconi, R., Gursky, H., Paolini, F. R., & Rossi, B. B. 1962, Physical Review Letters, 9, 439

Gillessen, S., Eisenhauer, F., Trippe, S., et al. 2009, ApJ, 692, 1075

González-Martín, O., Masegosa, J., Márquez, I., Guainazzi, M., & Jiménez-Bailón, E. 2009, A&A, 506, 1107

Grandi, P. & Palumbo, G. G. C. 2004, Science, 306, 998

Grandi, P., Malaguti, G., & Fiocchi, M. 2006, ApJ, 642, 113

Grandi, P. & Palumbo, G. G. C. 2007, ApJ, 659, 235

Grandi, P., Torresi, E., & Stanghellini, C. 2012, ApJ, 751, L3

Greenstein, J. L. & Schmidt, M. 1964, ApJ, 140, 1

Griest, K. & Kamionkowski, M. 1990, Physical Review Letters, 64, 615

Grossberger, C., Kadler, M., Wilms, J., et al. 2012, Acta Polytechnica, 52, 010000

Hada, K., Doi, A., Kino, M., et al. 2011, Nature, 477, 185

Han, J., Frenk, C. S., Eke, V. R., et al. 2012, MNRAS, 427, 1651

Harrison, F. A., Boggs, S., Christensen, F., et al. 2010, in Society of Photo-Optical Instrumentation Engineers (SPIE) Conference Series, Vol. 7732

Hartman, R. C., Bertsch, D. L., Bloom, S. D., et al. 1999, ApJS, 123, 79

Hartman, R. C., Kadler, M., & Tueller, J. 2008, ApJ, 688, 852

Hazard, C., Mackey, M. B., & Shimmins, A. J. 1963, Nature, 197, 1037

Henri, G., Pelletier, G., Petrucci, P. O., & Renaud, N. 1999, Astroparticle Physics, 11, 347

Hill, G. J. & Lilly, S. J. 1991, ApJ, 367, 1

Ho, L. C. 2002, ApJ, 564, 120

Ichimaru, S. 1977, ApJ, 214, 840

Ishibashi, W. & Courvoisier, T. J.-L. 2009, A&A, 495, 113

Ishibashi, W. & Courvoisier, T. J.-L. 2010, A&A, 512, A58

Iwasawa, K. & Taniguchi, Y. 1993, ApJ, 413, L15

Jaffe, W., Meisenheimer, K., Röttgering, H. J. A., et al. 2004, Nature, 429, 47

Jahoda, K., Swank, J. H., Giles, A. B., et al. 1996, in Society of Photo-Optical Instrumentation Engineers (SPIE) Conference Series, ed. O. H. Siegmund & M. A. Gummin, Vol. 2808, 59–70

Jansen, F., Lumb, D., Altieri, B., et al. 2001, A&A, 365, L1

Jennison, R. C. & Das Gupta, M. K. 1953, Nature, 172, 996

Jorstad, S. G., Marscher, A. P., Lister, M. L., et al. 2005, AJ, 130, 1418

Junor, W., Biretta, J. A., & Livio, M. 1999, Nature, 401, 891

Kaastra, J. 1992, Internal SRON-Leiden Report, updated version 2.0

Kaastra, J. S., Petrucci, P.-O., Cappi, M., et al. 2011, A&A, 534, A36

Kanbach, G., Bertsch, D. L., Fichtel, C. E., et al. 1988, Space Sci. Rev., 49, 69

Kataoka, J., Stawarz, Ł., Takahashi, Y., et al. 2011, ApJ, 740, 29

Kellermann, K. I., Sramek, R., Schmidt, M., Shaffer, D. B., & Green, R. 1989, AJ, 98, 1195

Kellermann, K. I., Kovalev, Y. Y., Lister, M. L., et al. 2007, Ap&SS, 311, 231

King, A. L., Miller, J. M., Gültekin, K., et al. 2013, ApJ, 771, 84

Kniffen, D. A., Fichtel, C. E., & Hartman, R. C. 1973, NASA Special Publication, 339, 139

Koski, A. T. 1978, ApJ, 223, 56

Koyama, K., Tsunemi, H., Dotani, T., et al. 2007, PASJ, 59, 23

Kraushaar, W., Clark, G. W., Garmire, G., et al. 1965, ApJ, 141, 845

Kraushaar, W. L., Clark, G. W., Garmire, G. P., et al. 1972, ApJ, 177, 341

Krawczynski, H., Hughes, S. B., Horan, D., et al. 2004, ApJ, 601, 151

Krolik, J. H. & Begelman, M. C. 1986, ApJ, 308, L55

Krolik, J. H. & Begelman, M. C. 1988, ApJ, 329, 702

Kuijken, K. & Gilmore, G. 1989, MNRAS, 239, 651

Labanti, C., Di Cocco, G., Ferro, G., et al. 2003, A&A, 411, L149

Laing, R. A., Riley, J. M., & Longair, M. S. 1983, MNRAS, 204, 151

Laing, R. A. & Bridle, A. H. 1987, MNRAS, 228, 557

Landau, R., Golisch, B., Jones, T. J., et al. 1986, ApJ, 308, 78

Laor, A. 2000, ApJ, 543, L111

Lebrun, F., Leray, J. P., Lavocat, P., et al. 2003, A&A, 411, L141

Lenain, J.-P., Boisson, C., Sol, H., & Katarzyński, K. 2008, A&A, 478, 111

Lense, J. & Thirring, H. 1918, Physikalische Zeitschrift, 19, 156

Lewin, W. H. G., van Paradijs, J., Jansen, F., et al. 1985, IAU Circ., 4101, 2

Lewis, K. T., Eracleous, M., Gliozzi, M., Sambruna, R. M., & Mushotzky, R. F. 2005, ApJ, 622, 816

Lichti, G. G., Bottacini, E., Ajello, M., et al. 2008, A&A, 486, 721

Liedahl, D. A., Osterheld, A. L., & Goldstein, W. H. 1995, ApJ, 438, L115

Linfield, R. & Perley, R. 1984, ApJ, 279, 60

Liu, F. K. & Zhang, Y. H. 2002, A&A, 381, 757

Lund, N., Budtz-Jørgensen, C., Westergaard, N. J., et al. 2003, A&A, 411, L231

Lynden-Bell, D. 1969, Nature, 223, 690

Macchetto, F., Marconi, A., Axon, D. J., et al. 1997, ApJ, 489, 579

Macías-Ramírez, O., Gordon, C., Brown, A. M., & Adams, J. 2012, Phys. Rev. D, 86, 076004

Magdziarz, P. & Zdziarski, A. A. 1995, MNRAS, 273, 837

Magorrian, J., Tremaine, S., Richstone, D., et al. 1998, AJ, 115, 2285

Makino, F. 1987, Astrophys. Lett., 25, 223

Malzac, J. 2001, MNRAS, 325, 1625

Maraschi, L., Ghisellini, G., & Celotti, A. 1992, ApJ, 397, L5

Marscher, A. P., Jorstad, S. G., Larionov, V. M., et al. 2010, ApJ, 710, L126

Mas-Hesse, J. M., Giménez, A., Culhane, J. L., et al. 2003, A&A, 411, L261

Massaro, E., Tramacere, A., Perri, M., Giommi, P., & Tosti, G. 2006, A&A, 448, 861

Massaro, E., Giommi, P., Leto, C., et al. 2009, A&A, 495, 691

Massaro, F., Cowperthwaite, P. S., Paggi, A., & D'Abrusco, R. 2012, The Astronomer's Telegram, 4555, 1

Matthews, T. A. & Sandage, A. R. 1963, ApJ, 138, 30

Mayer, W. F. 1975, Johns Hopkins APL Technical Digest, 14, 14

Meegan, C., Lichti, G., Bhat, P. N., et al. 2009, ApJ, 702, 791

Mewe, R., Gronenschild, E. H. B. M., & van den Oord, G. H. J. 1985, A&AS, 62, 197

Mewe, R., Lemen, J. R., & van den Oord, G. H. J. 1986, A&AS, 65, 511

Meyer, E. T., Fossati, G., Georganopoulos, M., & Lister, M. L. 2011, ApJ, 740, 98

Mitsuda, K., Bautz, M., Inoue, H., et al. 2007, PASJ, 59, 1

Molina, M., Bassani, L., Malizia, A., et al. 2009, MNRAS, 399, 1293

Moran, J. M., Greenhill, L. J., & Herrnstein, J. R. 1999, Journal of Astrophysics and Astronomy, 20, 165

Murray, S. S., Austin, G. K., Chappell, J. H., et al. 2000, in Society of Photo-Optical Instrumentation Engineers (SPIE) Conference Series, ed. J. E. Truemper & B. Aschenbach, Vol. 4012, 68–80

Nandra, K., George, I. M., Mushotzky, R. F., Turner, T. J., & Yaqoob, T. 1997, ApJ, 477, 602

Narayan, R. & Yi, I. 1994, ApJ, 428, L13

Narayan, R., Igumenshchev, I. V., & Abramowicz, M. A. 2003, PASJ, 55, L69

Neronov, A. & Aharonian, F. A. 2007, ApJ, 671, 85

Niedzwiecki, A., Xie, F. G., & Zdziarski, A. A. 2009, in The Extreme Sky: Sampling the Universe above 10 keV

Niedźwiecki, A., Xie, F.-G., & Stepnik, A. 2013, MNRAS, 432, 1576

Nixon, C. & King, A. 2013, ApJ, 765, L7

Nolan, P. L., Bertsch, D. L., Fichtel, C. E., et al. 1992, IEEE Transactions on Nuclear Science, 39, 993

Nolan, P. L., Abdo, A. A., Ackermann, M., et al. 2012, ApJS, 199, 31

Oort, J. H. 1932, Bull. Astron. Inst. Netherlands, 6, 249

Owen, F. N. & Ledlow, M. J. 1994, in Astronomical Society of the Pacific Conference Series, Vol. 54, The Physics of Active Galaxies, ed. G. V. Bicknell, M. A. Dopita, & P. J. Quinn, 319

Owen, F. N., Eilek, J. A., & Kassim, N. E. 2000, ApJ, 543, 611

Padovani, P. & Giommi, P. 1995a, MNRAS, 277, 1477

Padovani, P. & Giommi, P. 1995b, ApJ, 444, 567

Padovani, P., Giommi, P., & Fiore, F. 1997, MNRAS, 284, 569

Padovani, P., Costamante, L., Ghisellini, G., Giommi, P., & Perlman, E. 2002, ApJ, 581, 895

Pariev, V. I. & Bromley, B. C. 1998, ApJ, 508, 590

Penrose, R. 1969, Nuovo Cimento Rivista Serie, 1, 252

Perlman, E. S. & Wilson, A. S. 2005, ApJ, 627, 140

Plotkin, R. M., Anderson, S. F., Hall, P. B., et al. 2008, AJ, 135, 2453

Plucinsky, P. P., Schulz, N. S., Marshall, H. L., et al. 2003, in Society of Photo-Optical Instrumentation Engineers (SPIE) Conference Series, ed. J. E. Truemper & H. D. Tananbaum, Vol. 4851, 89–100

Porter, T. A., Johnson, R. P., & Graham, P. W. 2011, ARA&A, 49, 155

Poutanen, J. & Svensson, R. 1996, ApJ, 470, 249

Poutanen, J. & Stern, B. 2010, ApJ, 717, L118

Ptak, A., Yaqoob, T., Mushotzky, R., Serlemitsos, P., & Griffiths, R. 1998, ApJ, 501, L37

Ptak, A., Terashima, Y., Ho, L. C., & Quataert, E. 2004, ApJ, 606, 173

Rees, M. J. 1966, Nature, 211, 468

Reunanen, J., Prieto, M. A., & Siebenmorgen, R. 2010, MNRAS, 402, 879

Reynolds, C. S., Fabian, A. C., Celotti, A., & Rees, M. J. 1996, MNRAS, 283, 873

Reynolds, C. S., Heinz, S., Fabian, A. C., & Begelman, M. C. 1999, ApJ, 521, 99

Risaliti, G., Harrison, F. A., Madsen, K. K., et al. 2013, Nature, 494, 449

Rivers, E., Markowitz, A., & Rothschild, R. 2011, ApJS, 193, 3

Roming, P. W. A., Kennedy, T. E., Mason, K. O., et al. 2005, Space Sci. Rev., 120, 95

Rybicki, G. B. & Lightman, A. P. 1979, Radiative processes in astrophysics

Ryle, M. & Sandage, A. 1964, ApJ, 139, 419

Sabra, B. M., Shields, J. C., Ho, L. C., Barth, A. J., & Filippenko, A. V. 2003, ApJ, 584, 164

Salpeter, E. E. 1964, ApJ, 140, 796

Sandage, A. 1964, ApJ, 139, 416

Sargent, W. L. W. 1977, ApJ, 212, L105

Schlegel, D. J., Finkbeiner, D. P., & Davis, M. 1998, ApJ, 500, 525

Schmidt, M. 1963, Nature, 197, 1040

Schönfelder, V., Diehl, R., Lichti, G. G., et al. 1984, IEEE Transactions on Nuclear Science, 31, 766

Seyfert, C. K. 1943, ApJ, 97, 28

Sguera, V., Bassani, L., Malizia, A., et al. 2005, A&A, 430, 107

Shain, C. A. 1958, Australian Journal of Physics, 11, 517

Shakura, N. I. & Sunyaev, R. A. 1973, A&A, 24, 337

Shi, Y., Rieke, G. H., Hines, D. C., et al. 2005, ApJ, 629, 88

Shu, X. W., Yaqoob, T., & Wang, J. X. 2010, ApJS, 187, 581

Sikora, M. & Begelman, M. C. 2013, ApJ, 764, L24

Skrutskie, M. F., Cutri, R. M., Stiening, R., et al. 2006, AJ, 131, 1163

Smith, E. P., Heckman, T. M., Bothun, G. D., Romanishin, W., & Balick, B. 1986, ApJ, 306, 64

Soldi, S., Lebrun, F., Gros, A., et al. 2012, in Proceedings of "An INTEGRAL view of the high-energy sky (the first 10 years)" - 9th INTEGRAL Workshop and celebration of the 10th anniversary of the launch (INTEGRAL 2012). 15-19 October 2012. Bibliotheque Nationale de France, Paris, France.

Sreekumar, P., Bertsch, D. L., Dingus, B. L., et al. 1996, ApJ, 464, 628

Stawarz, Ł., Sikora, M., & Ostrowski, M. 2003, ApJ, 597, 186

Stawarz, Ł., Kneiske, T. M., & Kataoka, J. 2006, ApJ, 637, 693

Su, M., Slatyer, T. R., & Finkbeiner, D. P. 2010, ApJ, 724, 1044

Swanenburg, B. N., Hermsen, W., Bennett, K., et al. 1978, Nature, 275, 298

Takahashi, T., Abe, K., Endo, M., et al. 2007, PASJ, 59, 35

Takahashi, T., Mitsuda, K., Kelley, R., et al. 2010, in Society of Photo-Optical Instrumentation Engineers (SPIE) Conference Series, Vol. 7732

Tanaka, Y., Inoue, H., & Holt, S. S. 1994, PASJ, 46, L37

Tavecchio, F., Maraschi, L., & Ghisellini, G. 1998, ApJ, 509, 608

Tavecchio, F., Maraschi, L., Pian, E., et al. 2001, ApJ, 554, 725

Tavecchio, F. & Ghisellini, G. 2008, MNRAS, 385, L98

Taylor, B. G., Andresen, R. D., Peacock, A., & Zobl, R. 1981, Space Sci. Rev., 30, 479

Tombesi, F., Sambruna, R. M., Reeves, J. N., et al. 2010, ApJ, 719, 700

Tombesi, F., Sambruna, R. M., Reeves, J. N., Reynolds, C. S., & Braito, V. 2011, MNRAS, 418, L89

Tonry, J. L. 1991, ApJ, 373, L1

Tramacere, A., Giommi, P., Perri, M., Verrecchia, F., & Tosti, G. 2009, A&A, 501, 879

Tramacere, A., Massaro, E., & Taylor, A. M. 2011, ApJ, 739, 66

Truemper, J. 1982, Advances in Space Research, 2, 241

Tueller, J., Baumgartner, W. H., Markwardt, C. B., et al. 2010, ApJS, 186, 378

Ubertini, P., Lebrun, F., Di Cocco, G., et al. 2003, A&A, 411, L131

Uchiyama, Y., Maeda, Y., Ebara, M., et al. 2008, PASJ, 60, 35

Urry, C. M. & Padovani, P. 1995, PASP, 107, 803

Vedrenne, G., Roques, J.-P., Schönfelder, V., et al. 2003, A&A, 411, L63

Véron-Cetty, M.-P. & Véron, P. 2010, A&A, 518, A10

Voelk, H. J., Klein, U., & Wielebinski, R. 1989, A&A, 213, L12

Voges, W., Aschenbach, B., Boller, T., et al. 1999, A&A, 349, 389

Walter, R. & Neronov, A. 2008, in Proceedings of the 7th INTEGRAL Workshop

Wehrle, A. E., Piner, B. G., Unwin, S. C., et al. 2001, ApJS, 133, 297

Weisskopf, M. C., O'dell, S. L., & van Speybroeck, L. P. 1996, in Society of Photo-Optical Instrumentation Engineers (SPIE) Conference Series, ed. R. B. Hoover & A. B. Walker, Vol. 2805, 2–7

Weisskopf, M. C., Tananbaum, H. D., Van Speybroeck, L. P., & O'Dell, S. L. 2000, in Society of Photo-Optical Instrumentation Engineers (SPIE) Conference Series, ed. J. E. Truemper & B. Aschenbach, Vol. 4012, 2–16

Wilson, A. S. & Colbert, E. J. M. 1995, ApJ, 438, 62

Wilson, A. S. & Yang, Y. 2002, ApJ, 568, 133

Winkler, H. 1992, MNRAS, 257, 677

Winkler, C., Courvoisier, T. J.-L., Di Cocco, G., et al. 2003, A&A, 411, L1

Woltjer, L. 1959, ApJ, 130, 38

Wright, E. L., Eisenhardt, P. R. M., Mainzer, A. K., et al. 2010, AJ, 140, 1868

Yang, R.-Z., Sahakyan, N., de Ona Wilhelmi, E., Aharonian, F., & Rieger, F. 2012, A&A, 542, A19

Yates, M. G. & Garden, R. P. 1989, MNRAS, 241, 167

Zdziarski, A. A. & Lightman, A. P. 1985, ApJ, 294, L79

Zhang, J., Sun, X.-N., Liang, E.-W., et al. 2013, ArXiv e-prints

Zwicky, F. 1933, Helvetica Physica Acta, 6, 110